LEABHARLANN CHOLÁISTE NA TRÍONÓIDE, BAILE ÁTHA CLIATH | TRINITY COLLEGE LIBRARY DUBLIN
Ollscoil Átha Cliath | The University of Dublin

Terms and Conditions of Use of Digitised Theses from Trinity College Library Dublin

Copyright statement

All material supplied by Trinity College Library is protected by copyright (under the Copyright and Related Rights Act, 2000 as amended) and other relevant Intellectual Property Rights. By accessing and using a Digitised Thesis from Trinity College Library you acknowledge that all Intellectual Property Rights in any Works supplied are the sole and exclusive property of the copyright and/or other IPR holder. Specific copyright holders may not be explicitly identified. Use of materials from other sources within a thesis should not be construed as a claim over them.

A non-exclusive, non-transferable licence is hereby granted to those using or reproducing, in whole or in part, the material for valid purposes, providing the copyright owners are acknowledged using the normal conventions. Where specific permission to use material is required, this is identified and such permission must be sought from the copyright holder or agency cited.

Liability statement

By using a Digitised Thesis, I accept that Trinity College Dublin bears no legal responsibility for the accuracy, legality or comprehensiveness of materials contained within the thesis, and that Trinity College Dublin accepts no liability for indirect, consequential, or incidental, damages or losses arising from use of the thesis for whatever reason. Information located in a thesis may be subject to specific use constraints, details of which may not be explicitly described. It is the responsibility of potential and actual users to be aware of such constraints and to abide by them. By making use of material from a digitised thesis, you accept these copyright and disclaimer provisions. Where it is brought to the attention of Trinity College Library that there may be a breach of copyright or other restraint, it is the policy to withdraw or take down access to a thesis while the issue is being resolved.

Access Agreement

By using a Digitised Thesis from Trinity College Library you are bound by the following Terms & Conditions. Please read them carefully.

I have read and I understand the following statement: All material supplied via a Digitised Thesis from Trinity College Library is protected by copyright and other intellectual property rights, and duplication or sale of all or part of any of a thesis is not permitted, except that material may be duplicated by you for your research use or for educational purposes in electronic or print form providing the copyright owners are acknowledged using the normal conventions. You must obtain permission for any other use. Electronic or print copies may not be offered, whether for sale or otherwise to anyone. This copy has been supplied on the understanding that it is copyright material and that no quotation from the thesis may be published without proper acknowledgement.

3-Dimensional Solder Paste Inspection using Structured Light Techniques

Cecilia Ka Yuk Chan

Department of Electronic and Electrical Engineering
Trinity College Dublin
Ireland

Thesis submitted for the degree of Ph.D.

September 2001

TRINITY COLLEGE
18 MAR 2003
LIBRARY DUBLIN
THESIS
7191

Declaration

I, Cecilia Ka Yuk Chan, declare that this thesis is entirely my own work, except where otherwise accredited, and that it has not been previously submitted for a degree at this or any other university or institution. I agree that the Library may lend or copy the thesis upon request.

Signed: Cecilia Chan .
Cecilia Ka Yuk Chan

Date: 21-11-2002 .

Summary

Re-modelling of three-dimensional solder paste constructed from optical profilometry has gathered ever-increasing attention in different inspection and process control sectors of the electronics Printed Circuit Board manufacturing industry. It has been shown that *50%* to *80%* of the solder defects encountered are usually a direct consequence of variations in the quality of board printing. Since the amount and shape of solder paste on pad affects primarily the quality of joints, a highly accurate control system is necessary to correct process drift before the value-adding process in the form of integrated circuits and microprocessor chips has been added to the board. The process control systems commercially available today are either low-cost equipment which operate on a statistical basis, and have certain degree of limitations on the inspection of the system, or are based on laser scan technologies which are exceptionally expensive. In the existing market for solder paste inspection equipment, systems must be capable of achieving inspection rates in real-time, delivering area, height, and volume of solder paste deposits. In order to attain zero defects, every paste deposit on the board should be monitored. The aim of this work is to investigate the feasibility of a low cost, non-contact, high-speed, on-line system for the inspection of low attitude objects such as Surface Mount Technology (SMT) component solder-joints.

The research began by continuing further investigations on the study of a phase profilometry technique using binary encoded structured light pattern that had previously been developed by former colleagues at Trinity College. The main objective of this part of the research was to investigate the factors and problems which might influence the accuracy and the overall effectiveness of the developed phase profilometry and compared the results with other known phase profilometry techniques namely Fourier Transform and Signal Domain Profilometry. A system called Dual Projection was also developed to demonstrate some inaccuracies caused by one-dimensional structured light technique. The work was then expanded by looking at several range-imaging techniques for general applications and also other Automated Optical Inspection systems. However, it was found that structured light technique was by far the most suitable if it is to satisfy the criteria of a low cost and real time solder paste inspection system.

During the study of the phase profilometry with binary encoded structured light pattern, it was found that the height of the object being inspected is greatly limited by the grating frequency. To overcome this problem, a new approach was adopted. This approach uses a Colour Encoded Structured Light pattern (CESL) and image processing methods to extract the appropriate colours and to filter out the unwanted data to allow computation of the relative pixel shift due to the topography of the object. The strategy is named as Geometric Profilometry with Colour Encoded Structured Light Pattern Recognition.

The accuracy was then further improved by combining the advantages of the phase profilometry and of the colour encoded structured light technique. This final part of the research brings about the methodology - Rectangular Phase Profilometry with Colour Encoded Structured Light Pattern Recognition.

Step by step simulations and experimental implementations are presented for all the studies in this research and the effectiveness of the results is assessed.

To

Mum and Dad,
Ka Yee and Ka Po.

"For always be there for me."

Acknowledgements

In this thesis, there are pages and pages of ideas and results, which may or may not make a difference in this world. But among all, these two particular pages are possibly the most meaningful out of the entire thesis as they are dedicated to those who I have received a great amount of time, advice and goodwill from in the duration of my research.

Firstly, I would like to thank my supervisor Frank during my time at Trinity College. His conversation was always inspiring, informative and full of encouragement. It is his persuasive power that I allowed myself a chance from being a Mechanical Engineer to a semi Computer Electronic Engineer. And I am glad that I took that chance.

Thanks to Joe, who I am greatly indebted to. Without him, this thesis may never be completed. His extensive knowledge on a wide variety of subjects is most admirable, I would always be grateful for his tremendous advice and input, but above all, his guidance in life as a friend for which I am most grateful.

Anybody who is even an acquaintance of mine would know about all those late nights or early mornings that I have spent in the lab. For this, an exceptional individual must be mentioned – Ed, my New Zealander whom I might have never understood but who has kept me company for many dark scary nights.

I would like to thank and acknowledge everyone in the Electronic Department of Trinity College for all their help and advice, especially Ludvic for his Matlab programming expertise and his good ideas; Robbie Dempsey who would just drop everything to help you no matter what it is; Shane who is so nice that would help you finish demonstrate the lab if you just ask; I just want to say "I really appreciate you guys, thanks".

To everyone in the lab, both past and present, thanks for all the good times and fun we had especially all those crazy Christmas parties and not forgetting those countless coffee breaks, I have enjoyed every minute of it. A special mention to Devendra and Lorcan, who I had plenty of fun and serious talk about life with, without them in the lab, things were just not the same. And of course, there are

Pauline, the one who was there for me when I was most in need of a friend, our little smiley Chinese girl - Yanming, Siobhan who is always full of social ideas, our serious but not so serious Conor N, the genius Hugh with plenty of great ideas, and Andreas who is full of complimenting remarks.

To all my friends, who have been there for me all these years and kept me from insanity. Their tireless companionship and kindness was a source of great encouragement. Big mention to Anne Griffin and Anne O'Brien, who I have known since I was young, may our friendship last in all future years to come, well and of course, endless amount of fun! To those friends that I might not have been able to keep in touch as much due to my personal dilemma, Kevin, Mark O'C, Niamh, Aoife, Mark M, and Paddy. Thanks for being around still.

A very special person who deserve a special mention, my good friend Tom, for being always there for me no matter where you are in the world, and always had a spare ear to listen to my moaning, and a kind word to pick me up when I am down.

To my father, my mother and my two sisters, Ka Yee and Ka Po, to whom this work is dedicated to, for their endless love, patience and understanding, even when I was in my mood swings. Ka Yee, for your insights in life and just talking to you once about my problem is better than talking to thousands, as despite our differences, you understand me and teach me how to be positive and for that I admire you. And as for Ah Po, you are just the best, your wittiness and your humour are just character, having you around lighten up the room.

Finally, to someone who has taught me and allowed me to realise the meaning of love, no matter how many years of research and study I do, I would have never learnt until I met you, I will always remember you and your smile.

To those who I have loved and loved me.

Contents

Part III of the Thesis

Chapter 7

Rectangular Pulse Phase Profilometry and Colour Encoded Structured light Pattern Recognition

Chapter 8

Overall Discussions and Suggestions for Future Work

Appendix A – System Hardware

Appendix B – 32 Fringe Image Implementation and Windows Interface

Appendix C – Correction of Non Uniform Illumination

List of Figures

Figure No.

List of Figures

Figure No.

List of Figures

Figure No.

List of Figures

Figure No.

List of Figures

Figure No.

List of Figures

Figure No.

List of Figures

Figure No.

List of Figures

Figure No.

List of Figures

Figure No.

List of Tables

Table No.

Chapter 1

Introduction to Printed Circuit Boards Inspection and Surface Mount Technology

1.1 Introduction

Printed circuit board assembly has became one of the fastest growing sectors in the electronics manufacturing industry especially since the advent of Surface Mount Technology (SMT). Surface Mount Technology enables electronics manufacturers to reduce circuit board size, improve reliability and increase throughput. The ever-increasing number of products utilising surface mount components is evidence of the worldwide interest in surface mount technology on circuit boards [1].

In the manufacturing world of electronics, there is continual pressure to reduce costs, reduce time to volume, improve quality, miniaturise and react to changes. With the effects of the advances in miniaturisation technology on the physical dimensions of parts and patterns of PCB assembly [2], and the continuous increase in density of the component boards, it has become more and more difficult to carry out adequate inspection and parts measurement with the traditional inspection techniques. Automated Optical Inspection (AOI) offers a good alternative solution. In fact, the SMT automated inspection market has grown dramatically in the last few years; it has tripled in size between 1992 and 1997 and the market in 1999 exceeded $150M [3,4]. It has been estimated that there are 30,000 SMT lines world wide, and out of these manufacturing lines, 3,000 of them are actually utilising some type of in-line SMT AOI equipment, while most others are supported by off-line measurement systems. With 90% of the present market as targets and not counting the future demand, it seems to be a good idea to provide a state-of-the-art in-line inspection technology to improve process control in electronic circuit-pack assembly.

In 1998, about 80% of all automated inspection systems sold were for post-reflow inspection[i]. Although it seems to be the optimum solution to place one inspection machine at the end of the process rather than having a combination of machines between the printer and the soldering oven, it is impossible to find an efficient post-

[i] post-reflow systems are printed circuit boards inspection systems used to examine the circuit boards at the finishing line after component soldering.

reflow machine capable of supplying all the necessary information for a full in-line PCB inspecting assembly. Figure 1.1 shows the step by step SMT production line and the required inspections. In fact, a columnist in *the European Test Industry Journal* [5] has concluded that for post-reflow inspection to work effectively, the following preconditions need to exist:

- *'Inspectability'* - needs to be designed in, that is, board layout guidelines need to incorporate technology requirements like optimum lead to pad ratio, minimal shadowing so that no components are in the shadow of tall connectors and new silk screen requirements.
- *'Standardised'* - components need to be designed with inspectability in mind. For example, standard connector footprints, standard colours and materials.
- *'Stability'* - minimal mechanical vibrations. The system needs to be stable, no profile tweaking, no stencil changes, and few changeovers.

In addition to the above conditions, inspection after reflow soldering means defects are only detected at the final stage after full value in the form of integrated circuits and microprocessor chips has been added to the board. This indicates that most defective boards would be discarded, as rework is time-consuming and costly. Based upon these facts, it would be preferable that more attention should be directed towards ensuring that faults do not occur, rather than detecting faults after they occur, or at least detecting faults at an early stage before the value-adding process. Due to the economics of high production yields, uniformly strong quality is absolutely essential at an early stage of SMT process. The way to achieve a controlled process is to build quality into a circuit board during production rather than to discard a defective board

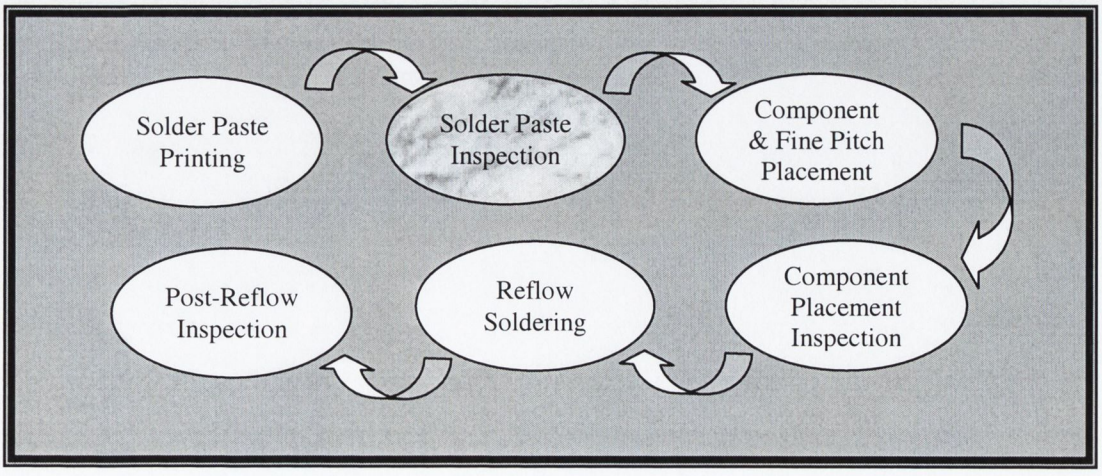

Figure 1.1: SMT Inspection Production Line

during quality control at end of the process. In the case of solder paste printing this means directly after the printing process, which is what this research is mainly concerned with.

1.2 Surface Mount Technology Production line

In conventional board assembly technology, the component leads are inserted into holes through the PC board and connected to the solder pads by wave soldering on the reverse side. This is known as the **Through-hole** technology [1]. Another assembly technology is the **Hybrid** technology, which consists of thick and thin film circuits. Leadless components are reflow soldered onto the ceramic or glass substrate in addition to the components already integrated on the substrate. Surface Mounting is an assembly technology that evolved from these two techniques. In surface mount technology, the components can be assembled on both sides of the PCB. The components are first attached to the PCB by solder paste or non-conductive glue and then soldered.

The SMT Production line in printed circuit board assembly consists of three main steps as shown in Figure 1.2. More detailed treatment of SMT can be found in [6], including various soldering and glue dispensing techniques.

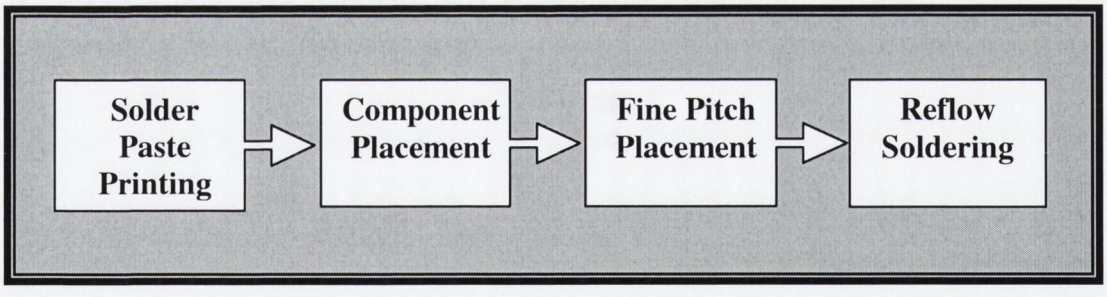

Figure 1.2: SMT Production Line

Solder Paste Printing

The first step in SMT assembly process involves the printing of solder paste onto the pads of a logic board. The accurate deposition of the solder paste on these pads is without doubt one of the most critical parts of the entire assembly process. Since the Surface Mount Technology components placed on each solder paste pad are very small, a significant proportion of all SMT assembly problems is related to the solder paste quality. In fact, experience [7] has shown that between 50% to 80% of the solder defects encountered are usually a direct consequence of variations in the

quality of board printing. This includes all types of solder defects such as open joints, bridging, tombstoning or billboarding.

Component and Fine Pitch Placement

After the solder paste is screen printed onto the circuit board, the small surface mount components are placed onto the solder pads. Surface Mounted Devices (SMD) are components especially designed for the surface mount assembly line with soldering pads or leads that are much smaller than their original through hole components counterparts. Furthermore, in contrast to the conventional components, the leads of which must be inserted into the holes, SMDs are directly attached to the surface of the PCB and then soldered[ii]. The component placement procedure is usually done by robotic pick-and-place machines at high production speeds. Following the placement of small surface mount components such as integrated circuits, fine pitch placements of larger components such as microprocessor chips are then applied to the printed circuit boards. These fine pitch components may consist of leads on all four edges that require soldering to the circuit board. During the component and fine pitch placement processes, many potential defects may occur, such as component misplacement, misalignment, bending or damaged leads, possibly resulting in missed electrical connections, open circuits and ultimately a defective product. A placement inspection machine can highlight these potential errors by accurately measuring and monitoring the positional and related failures before the PCB is passed to the reflow process. Pre-reflow inspection has an advantage over post-reflow inspection in that defects are much easier to repair, and most systems have built-in repair stations.

Reflow Soldering

In the stage of reflow soldering, after the components have been electrically and mechanically attached to the PCB, a heat-induced phase transition of the solder from solid to liquid and then back to solid is performed to achieve the finished assembled PCB. A post-reflow inspection process is ideal here to examine the quality of the finished product.

[ii] It should be noted that not all component types are available as surface mount version at present, mixed assemblies (i.e.) a combination of leaded and surface mounted components is an appropriate replacement.

1.3 Printed Circuit Board Inspection

The advent of Surface Mount Technology has brought significant successes in the miniaturisation of electronic printed circuit boards (PCB) for many sophisticated devices. It has overcame the difficulties that the traditional "Through-Hole" technique [1] encounters such as interconnecting components in highly dense configurations, while increasing the overall quality and reducing manufacturing costs. However, these successes do not come without penalties; as the size of the electronic components and the spacing between interconnections is reduced, the probability of short circuits and leads with insufficient solder increases at the same time. All these deficiencies must be corrected via process monitoring and inspection.

In PCB manufacturing, a mechanical assembly consisting of layers of fiberglass sheet is laminated with etched copper patterns onto which the electronic parts are mounted. It is also known as a Printed Wiring Board (PWB). There are several board materials and layers to choose from. Among the board types, Fibreglass and Phenolic are the most popular, Phenolic being the cheaper laminate material. After deciding on the board and layer type, the PCB layout must be drawn. The board is then etched. Etching is probably the easiest and most cost effective methods for constructing PCBs. Etching is the process of chemically removing the unwanted copper from a plated board, where a mask or photo-resistive solution must be placed on the portions of the copper that are to remain after the etch. These portions that remain on the board are the traces that carry electrical current between devices. However, such a process can lead to many problems with the final circuit pattern, e.g. the circuit path may be broken, it may be too wide or too thin, or there may be spurious copper remaining on the PCB.

There are many different aspects of the printed circuit board manufacturing process that require inspection [8,9,10]. The most common aspects are listed below.

1) Verify that components have been inserted in the correct places.
2) Check for defects (e.g. non-uniform bends) in the leads attaching components to the board.
3) Check the circuit paths to ensure they are perfectly printed and there are no broken connections.
4) Check the circuit paths for any short circuits due to solder debris.

5) Verify that there are sufficient solder joints and that they have been correctly formed.

The first three problems require two-dimensional geometric inspection and crack detection [9,10]. They can be solved by simple image processing techniques such as dark field illumination, image subtractions, template matching and feature matching used in conjunction with thresholding methods. Testing for components being inserted in the correct place and for bent leads does not require a very complicated two-dimensional inspection task. Most inspection techniques make a comparison to an ideal model of some kind. A model of the printed circuit board and its components is first derived and the board is then scanned for the occurrence of components in order to verify the correct placements. These template matching systems must be tolerant of a small amount of misalignment and must allow for minor differences along the edges. On the other hand, they must also be sensitive to cracks and bridges of any solder joints. A drawback of the method is the fact that most PCBs do not match point-by-point identically because of shrinking or swelling of the board. But with a feature matching strategy, the sensitivity of input intensity data can be reduced, and the storage of the image data greatly compressed. In the early 1980s, *Hara et al.* [11] developed a referential system to isolate surface PCB defects. The methodology involved extracting local features from the board under inspection and comparing these with an ideal template model. Initially, boundary line extraction was performed in four directions using shape operators to detect salient features. Comparatively wide defects were detected by demarcating boundaries running in a direction differing from that of the boundaries of the reference pattern. This method was useful for matching defects of a width greater than a fixed value and for the detection of local features. Narrow defects, such as fine wiring, were subsequently detected using shape operators in a manner similar to the original boundary extraction stage. The system was successfully installed on a PCB production line yielding higher quality inspection at a much lower cost.

Checking for breaks in circuit boards is usually performed before components have been inserted, but checks for short circuits due to solder debris obviously have to be carried out after components have been inserted and soldered in place. However, the basic processes used to detect such defects are similar. For conventional electrical testing, these potential faults (shorts and breaks) are impossible to detect but

automated optical and image processing techniques can greatly assist for such inspection. Image subtraction techniques can again be used to compare an ideal image of the circuit from the image of the current board, although, it requires a certain amount of processing time. The ideal and the actual images must be aligned. This can be achieved by matching features from both images and estimating the relative position and orientation of the boards. Another two very basic image-processing methods of checking for breaks and shorts are erosion and dilation. They are two simple operators derived from the area of mathematical morphology [9]. The basic effect of the erosion operator is to erode away the boundaries of regions, removing each object pixel having a neighbour in the background according to the law of connectivity. Dilation is the opposite of erosion. It expands each object pixel with its neighbouring pixels. Erosion and dilation techniques are extremely effective for detecting tracks with extraneous copper or tracks with a neck. If the tracks or pads consist of extraneous copper attached (Figure 1.3a), then by dilating the image several times causes the two tracks to merge (Figure 1.3b) and a subsequent analysis of the tracks' connectivity will identify this potential fault. Conversely, a track which is too thin or has a neck (Figure 1.4a) will break when eroded (Figure 1.4b), and again, the connectivity analysis can identify this potential circuit break.

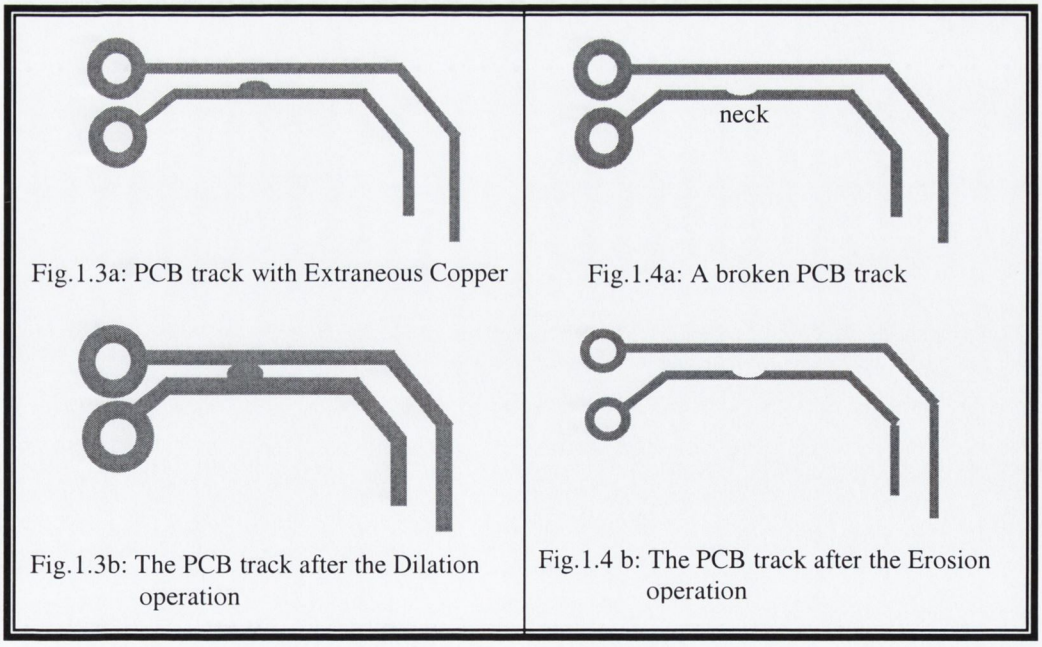

Fig.1.3a: PCB track with Extraneous Copper

Fig.1.4a: A broken PCB track

Fig.1.3b: The PCB track after the Dilation operation

Fig.1.4 b: The PCB track after the Erosion operation

Fig.1.3: Dilation Operation on PCB track

Fig.1.4: Erosion Operation on PCB track

The inspection of solder joints and solder pads, however, presents a printed circuit board inspection system with a quite different set of problems. The printing of the

solder paste is a crucial process and the measurement of its volume is most vital for the quality of the board, since the amount and shape of solder paste on component pads primarily affect the quality of joints. Studies have shown that over 50% of the solder defects encountered can be caused by problems during solder paste printing [2]. The understanding of how these defects correlate to the numerous variables in the printing process is a problem faced by all SMT manufacturers. An inspection of the solder paste printing is therefore important since repairing defects is not only uneconomical, (it has been estimated to increase by an order of magnitude at each successive level of electronic assembly), but there is a high degree of possibility that repairing can damage the components or the PC board. During the whole process, poor solder joints may be the result of insufficient or excessive solder, an inappropriate reflow soldering temperature, or incorrect placement of assemblies. The ideal gauging system should be capable of measuring the height of the solder paste before reflowing and before mounting the SMDs. At this stage, the paste is dull and the reflectance is low. After reflowing, the solder will appear shiny and it is much more difficult to obtain images that are not over-exposed. This deeply saturated colour will cause problems in pattern identification as the colour balance of the solder paste is disturbed. In a recent article in the Test & Measurement World Journal, *Owen* [12] from MV Technology has listed a table which identifies specific types of solder paste defects and the possible corrective actions to deal with these defects. In brief, a 2D video camera system can usually measure characteristics such as paste area and paste position and a 3D triangulation system can measure paste characteristics such as height and volume.

1.4 Past and Present Trends on Solder Paste Inspection Industry

In this section, the past and current exploitation of the solder paste inspection industry are briefly reviewed [13,16]. The most ineffective and traditional PCB inspection system was the 'Manual Inspection', that is a group of highly trained workers visually inspecting each board manually. This was the universal norm; in fact, up to relatively recently all defects and flaws of the PCB boards were almost exclusively assessed by human inspection [10,16]. However, the combination of fine

pitch board technology and high yield requirements means that manual inspection is no longer acceptable as a quality control solution. Although in limited circumstances such as large surface flaws, or misalignments of a board, visual inspection tasks can still be accomplished by human inspection. However, in the examination of small scale flaws (often with dimensions below 2mm), and repetitive tasks which require tedious inspections, the accuracy and consistency of manual inspection is poor. Davy [14] has composed a survey on the consistency of some highly trained inspectors and to summarise the report conclusions: manual inspection is very variable and it does not improve with time. On the other hand, non-contact automated optical inspection (AOI) is becoming more widely accepted as a technology adding significant advantages to the production line in recent years [13]. AOI has the ability to improve inspection consistency and provide more reliable results with its high magnification in optics and better lighting equipment than manual inspection and in the long term, the cost factor is reduced. In fact, it is necessary as an in-process inspect facility for SMT, to help understand why, how, and where the defects or quality losses occur, and ultimately, to stimulate improvement of the process itself. In the existing market for solder paste inspection equipment, systems must be capable of achieving inspection rates in real-time, delivering area, height, and volume of solder paste deposits. In order to attain zero defects, every paste deposit on the board should be monitored. The current industry [15] uses several different techniques to try to achieve the above goals and these techniques are usually based on one of the three proven methods: X-ray, Laser triangulation and Structured light technique[iii].

Below shows a list of the companies or industrial research groups which are currently in the market of solder paste inspection.

Company Name	**Inspection System**
Philips	Triscan
SVS	8100 System
Esprit	EU Esprit system
MV Technology	SP1
CyberOptics	CyberSentry

[iii] As this research is principally focusing on the topics of solder paste inspection, details on post reflow soldering and component placement inspection will not be discussed. However relevant materials maybe found in [21].

I Systems Inc.	SMD-3D
Texas Instruments	TI DSEG's MPS

Table 1.1: PCB Inspection System manufacturers

The Philips Triscan, SP1 and SVS 8100 System employ a scanning laser-based triangulation technique to yield the required solder paste height measurements. These systems exploit the use of more than one light source to compensate the occlusions that may arise when using triangulation techniques. The system developed by Esprit [21] is also based on advanced laser technology. Solder pattern formations are scanned using a specially-developed high speed 3-D microscope, each board is scanned twice. In the forward stroke, board dimensions are recorded and checked against CAD data for translation, rotation and stretch. During the backward stroke, the board is scanned at up to 1000 scan lines per second and the solder paste deposit parameters are calculated with minute accuracy. The CyberSentry and I Systems Inc.'s SMD-3D systems utilise structured light imaging in conjunction with laser light projection to compute the local geometry; this allows multiple laser stripes per pad (up to 5 lines). The TI DSEG's MPS [17] uses Hewlett Packard's Four Pi X-Ray Laminography System [18] to measure the volume of solder paste applied to a circuit board. The Four Pi X-Ray system uses a variable focal point technique to take X-ray images of slices of solder joints for a circuit board under test. An x-ray beam and an x-ray detector move synchronously to form a focal plane through a cross-sectional area of an object. This synchronous movement creates a slice image through an object. Features above and below the thin focal plane are averaged into the focal plane. HP sell this system mainly for post-reflow soldering inspection.

These solder paste inspection systems commercially available today are either low-cost equipment which process data using statistical methods, or are based on laser scan technologies which are exceptionally expensive [6]. The lack of a robust, on-line, high-speed, non-contact, cost effective sensing system is a major barrier to improved process control in electronic circuit-pack assembly. The aim of this work is to investigate the feasibility of such system for the inspection of Surface Mount Technology components solder-joints based on structured light using computer vision and digital signal processing.

1.4.1 X-ray Techniques

The X-ray technique uses an X-ray [15] source on one-side of the board and a special sensor on the other side of the board to measure the level of X-rays transmitted through the board. The lead in solder paste absorbs X-rays and the level of absorption is proportional to the height of paste. Therefore, the darker the paste area appears, the more paste is present. There are two different types of X-ray inspection systems, one is the 2D X-ray Image by Transmission [17] and the other is 3D X-ray Image by Laminography [17,18]. 2D systems do not allow for double sided boards while 3D systems can separate the bottom and top side board for inspection. X-ray systems are the only systems which can examine hidden features or joints, like the solder joints on array packages. They are, however, much more expensive compared to the other inspection systems and the X-ray tube must be replaced every 6 to 24 months depending on the amount of usage. An X-ray inspection system also requires a longer period of time to capture the image and, moreover, special safety precautions must be taken when operating the X-ray machines.

1.4.2 Laser Triangulation

The laser based technique [20] uses laser scan cameras which project points, lines or other structured light patterns onto the scene for determining the height gradient from the interferograms of the beams. The light source is projected at an angle to the board and the sensor is placed directly above the PCB so that the resulting image is offset, with the amount of offset being based on the height of the solder paste. Laser line scan cameras are normally quite accurate and they provide very high resolution images for depth measurements. However, in order to correspond the actual position of the scene with the 3D wire frame model determined by the laser system, a second camera is required to capture the actual image so as to overlap this image with the 3D frame model. The main advantage of a laser line scan camera is its distinct separation lines which are remarkably easy to identify. But because the image must be scanned point by point or line by line across the board, the procedure for acquiring an image is quite time consuming compared to other depth extraction techniques. The laser based method is also sensitive to specular reflection. Thus, wetter solder paste tends to reflect a huge amount of light at a tangent to the surface, that is away from the sensor,

while with drier solder paste, the light is more scattered, and a high level of light is reflected back to the sensor.

1.4.3 Structured Light Technique

Structured light technique [19,20] uses a controlled light source of regular grating patterns (grids, stripes, elliptical, etc) to illuminate the scene. The grating pattern is perturbed according to the topography of the object. The 2D modulated image pattern, which carries 3D information, is then captured by a CCD camera. Surface shapes are then deduced from the distortion of the patterns that are produced when the light is reflected from the surfaces of the object. Knowing relevant camera and projector geometry, depth can be inferred by triangulation. The difficulty does not lie in the apparatus set-up but on the profilometry to extract the depth measurements from the 2D modulated image pattern. With only video cameras needed for the capturing of two dimensional images of reflected light intensity, structured light technique is the simplest, fastest and least expensive imaging technology among the known inspection methods.

1.5 History on 3D measurements

Apart from the three AOI techniques mentioned in the previous section which were mainly developed for the specific PCB inspection, there are other volumetric inspection methods constructed from optical profilometry which have gathered ever-increasing attention in industrial applications. Such topographic information is needed in high speed on-line inspection, quality control, medical diagnostics, solid modelling, robotics, CAD/CAM and many manufacturing applications. Regardless of the specific applications or context, the use of non-contact, non-destructive automated surface measurement is a desirable alternative to the conventional micrometers, callipers and dial gauges.

Several optical techniques toward the general volumetric measurement have been reported in the last thirty years. To date, four main papers have reviewed the field of range measurements. The first was by *Jarvis* [22], who investigated a variety of techniques, with emphasis on the details of particular implementations. *Nitzan* [23] later used a more structured approach, proposing a general taxonomy for the

classification of vision techniques, and also proposed a four stage model for range data acquisition involving image transduction, pre-processing, feature extraction and feature interpretation. *Besl* [24] reviewed a large number of techniques, and produced performance comparisons based on range accuracy, pixel location, time, and depth of field. Most recently, *Poussart* and *Laurendeau* [25] compiled a review of all 3D sensing techniques with full details.

All these optical range measurements can be categorised into two basic classifications; namely, *time-of-flight* [22] and *triangulation*. Depending on the medium used, there are two types of time-of-flight techniques. The first usually consists of a transmitter that emits a light beam and a receiver that detects the portion of reflected light on the target. In 1977, *Nitzan et al* [26] presented a model which modulated a laser beam in amplitude and measured the phase shift of reflected light. The range was obtained from the time needed for the light to travel from the transmitter to the object and back. The second type of time-of-flight technique is Ultrasonic ranging.

Triangulation can be subdivided into *passive* and *active* methods. For the passive method, scene illumination is usually provided by ambient light, while for the active method a special lighting device is used to illuminate the scene. Among the active triangulation methods the Moiré Shadow Contouring technique was proposed by *Takasaki* [27] and *Meadows et al* [28] in 1970. Moiré topography is generated by observing two grating patterns superimposed on each other and analysing the interferograms between the demodulated grating shadow and the original reference-grating pattern in two dimensions. The resultant Moiré pattern produces a constant height contour of equal separation on the object. The positions of these contours are then used to determine the shape of the surface. However, ambiguities often arise in interrogating the fringe patterns. With the Moiré contouring strategy, it is often not possible to determine whether a contour line is higher or lower than the adjacent contour line, i.e. the moiré fringe order. The Moiré Shadow Contouring technique is described in more detail in Chapter 2.

Other improved metrologies based on Moiré contouring have also been investigated by previous researchers. *Duncan T. Moore and B. E. Traux* [29] presented a practical improvement by oscillating the phase of the Moiré pattern by a small amount so as to distinguish the depression and elevation of the object. This is

achieved by moving the grating in the observation system. Compared to the conventional Moiré contouring method proposed in [27,28], the slope ambiguity problem of the contour lines is eliminated. Various applications have also been developed using Moiré Contouring method and can be found in the literature [30].

Since Moiré Contouring is a shadow method, it has no physical contact with the inspected object, therefore no deformation will occur in the measuring process. Another well-known active triangulation computer vision technique for three-dimensional scene information is the Structured Light Technique, which is the technique this research is based on. The Structured light technique uses a controlled light source of regular patterns to illuminate the scene, and hence it creates artificial features on the surface of objects that are easy to extract. It involves projecting a grating (grids, stripes, elliptical, etc) pattern onto an object's surface. The grating pattern is perturbed according to the topography of the object. The 2-D modulated imaged pattern, which carries 3-D information, is then recorded. Surface shapes are then deduced from the distortion of the patterns that are produced when the light is reflected from the surfaces of the object. Knowing relevant camera and projector geometry, depth can be inferred by triangulation, the main task being the extraction of the topographic information from the 2-D modulated imaged pattern.

Several demodulation and extraction profilometries based on the structured light techniques have been developed. *Takeda and Mutoh* [31,32] employed fast-Fourier Transform Phase Profilometry (FTP) to demodulate the phase deviation from the variations introduced by non-uniform reflectivity, that is the 3-D height information data from the 2-D perturbed image. It is accomplished by suitably modifying the frequency spectrum of the grating image to generate a complex image in which the local phase embodies the desired information and reflectivity variations act only upon the amplitude. FTP is free from all the complications associated with Moiré Contouring technique, as it does not utilise Moiré fringes. However, the system hardware is complex and the computational process is relatively expensive. Another phase profilometry is the Signal Domain Phase Profilometry (SDP) presented by *S. Tang and Y. Hung* [33]. In contrast to FTP, it processes the fringe pattern in the real-signal domain rather than the frequency domain by using demodulation and convolution operations. For demodulation, the 2D data is multiplied by sine and cosine terms, the low frequency components are then extracted by a low-pass FIR

filter yielding the phase deviation. These phase profilometries are discussed in more detail in chapter 3.

1.6 Overview of the Thesis

In this research, several familiar and novel volumetric-extraction profilometries based on the structured light technique for infinitesimal objects such as solder paste are thoroughly studied. The research can be divided into 3 main parts. In the first part of the research, three range extraction techniques based on measuring the amount of phase modulation in the fringe image were examined. Two of these phase extraction profilometry techniques were already introduced above - namely, the fast-Fourier Transform Profilometry (FTP) and the Signal Domain Profilometry (SDP). The other phase extraction profilometry technique is the New Fast Phase Profilometry (NFP) proposed *by L.Di Stefano and F.Boland* [34, 35]. The main objective of this part of the research is to investigate the factors and problems which might influence the accuracy and the overall effectiveness of the phase profilometry. During the investigations, it was discovered and proved mathematically, by using a 2D reference image, that the camera-grating misalignment problem arising from an optical set-up error can be compensated. Comparisons were made to investigate the effectiveness of each of the three phase profilometries. During this part of the study, an apparatus with two projection systems was built to demonstrate the inaccuracies of the solder paste profile which lies at the edges of the fringes. This system was named as the Dual Projection System.

The second part of the research contains a novel strategy which was developed to address the problems and drawbacks in the implementations of the Phase Profilometry techniques. This approach adopted the colour encoded structured light pattern which was first introduced by *Boyer and Kak* [36] in 1987 and uses image processing methods to extract the appropriate colours so as to filter out the unwanted data to allow computation of the relative pixel shift due to the topography of the object. The strategy is named as Geometric Profilometry with Colour Encoded Structured Light Pattern Recognition. The algorithm is presented and verified experimentally.

In the final part of the research, a novel approach which combines some of the advantageous algorithms of the phase profilometry and the colour encoded structured light technique is presented. It seems to be most ideal, by investigating the problems

and drawbacks from the study of all the profilometries that were examined in the first two parts of the research and combine the efficient parts of the two algorithms. The potential to design a solder paste inspection system that would provide accurate, low-cost and real time measurements does appear to be possible.

There are 8 chapters in the thesis, each chapter starts with a brief summary of the chapter itself. Chapter 1 brings about the objective of the research and the history of the subject. Chapter 2 presents several range-imaging techniques for general applications and the mathematical principle for structured light technique will be fully described. Chapters 3 and 4 present the first part of the research. Chapter 3 gives a complete description of the three Phase Profilometry methods with particular emphasis on the underlying theories. Chapter 4 illustrates the effectiveness from the implementations and the results of the three phase profilometries. Chapters 5 and 6 present the second part of the research. The complete methodology of the Geometric Profilometry with Colour Encoded Structured Light Pattern Recognition including the manufacturing process of suitable colour grating is presented in Chapter 5. The implementations and drawbacks of the algorithm are then displayed in Chapter 6. Chapter 7 begins with the purposes for the final part of the research. All experimental results are verified and presented in details. The step by step simulations and implementations of the technique are illustrated and the effectiveness of the results is concluded. An overall critical view of all profilometry techniques researched, together with a look at possible future work are concluded in the final chapter.

Chapter 2

Range Imaging Techniques

2.1 Introduction

The basic purpose of computer vision is to extract useful information from a scene efficiently. The information can then be used to guide various processes such as robotic manipulation, automatic inspection and industrial manufacturing. The image processing strategy in a computer vision application may differ depending on the type of image data available and the objectives of the application. From a two-dimensional image only a limited amount of information can be deduced about the physical shape and size of an object in a scene. If volumetric measurements are required, the 3D structure of the scene must be known and a 3D range sensing method must be implemented. In some situations, a small amount of three dimensional data is all that is required to understand a scene, while in others, dense three dimensional data are necessary. If such three-dimensional description is needed, view integration must be performed on multiple partial views of the object.

This Chapter begins with a brief introduction to some terminology used in computer vision. Several range-imaging techniques for general applications are then presented. Finally, methods for range-imaging based on the structured light technique will be fully described.

2.2 Depth Maps and Range Imaging

A *depth map* is an image that contains depth measurements taken from a scene. A depth map consists of a two-dimensional array where the x and y co-ordinate information corresponds to the rows and columns of the array as in an ordinary image, and the corresponding depth readings (z values) are stored in the array's elements (pixels). It can be a difficult task to capture a depth map as it typically requires at least two simultaneous views. In practice, methods of capturing three-dimensional data may result in a partially filled depth map, where only certain pixels contain valid depth values, and other pixels are set to some signal value such as zero to indicate there is not a valid reading for that pixel [37].

The measurement of a depth map is known as *range imaging*. There are two basic optical techniques to measure range; namely, *time-of-flight* and *triangulation*. Time-of-flight techniques can be subdivided into ultrasonic and light ranging according to the type of medium the measurements are engaged in. Triangulation is subdivided into *passive* and *active* methods. For the passive method, the scene illumination is usually provided by ambient light, while for the active method a special lighting device is used to illuminate the scene. A selective review of time-of-flight techniques and passive methods is first presented. The remainder of the Chapter will then be solely focused on the active triangulation ranging method, with emphasis on the structured light technique, which is most relevant to the work in this thesis.

2.2.1 Time of Flight Optical Measurements

2.2.1.1 Time-Of-Flight: Ultrasonic Ranging

Ultrasound [38] has been used extensively in many applications. It dates back to 1822, when a Swiss physicist used an underwater bell in an attempt to calculate the speed of sound in waters of Lake Geneva. With the use of ultrasound, the time of flight measured as the ultrasound to travel from the transmitter to and back from a target can be determined relatively easy, since the velocity of ultrasound is much slower than that of light. Ultrasound ranging measurements have the advantage that they can be carried out under natural lighting.

The basic procedure for ultrasound involves transmitting a short ultrasonic pulse towards an object. Some of its energy is reflected back to the transmitter; if the time interval between the transmitted and received pulses is measured, the distance d between the source and the object is obtained from

$$2d = v_s \, t_f \tag{2-1}$$

where v_s is the speed of sound under given pressure conditions

t_f is the time of flight of the pulse

In order to avoid the loss of signal or any sort of signal attenuation in a practical system, it is not a single pulse but rather a set of pulses at different frequencies that is transmitted. However, ultrasonic ranging results in poor resolution image according to *Jarvis*' [22] paper in 1980, in which he described a variety of range techniques.

Ultrasonic systems are unsuitable for the range acquisition of complex and small scenes. Another drawback is that depending on the incidence angle of the pulse, it is possible that very little energy is reflected back, and the return pulse is lost in detector noise. *Brown* [39] introduced a method using three ultrasonic sensors to try to overcome this problem. It should be noted that due to the poor resolution images, ultrasound ranging technique is not suitable for small scenes inspection measurements such as SMT inspection.

2.2.1.2 Time of Flight: Light Optical Measurements

An optical time-of-flight rangefinder (also known as the serial structured light technique) typically consists of a transmitter that emits a collimated light beam, a scanning mechanism, and a receiver that detects the portion of reflected light on the target. The range is obtained from the time needed for the light to travel from the transmitter to the object and back. The time of flight can then be determined by two methods. First, one can use a pulsed laser and measure the time elapsed from emission to reception, rather like radar [25]. A laser pulse is transmitted through a semitransparent mirror towards the object as shown on Figure 2.1. An electronic sync pulse is also generated and fed to a coincidence analyser. The reflected pulse is collected by the same mirror and redirected towards a light-sensitive surface which then generates an arrival electronic pulse. The time interval between the sync and arrival pulses, measured by the coincidence electronics, is proportional to the range between the source and the scene. A complete range image is obtained by scanning the mirror over the scene. This requires accurate measurement of time; a sharp pulse

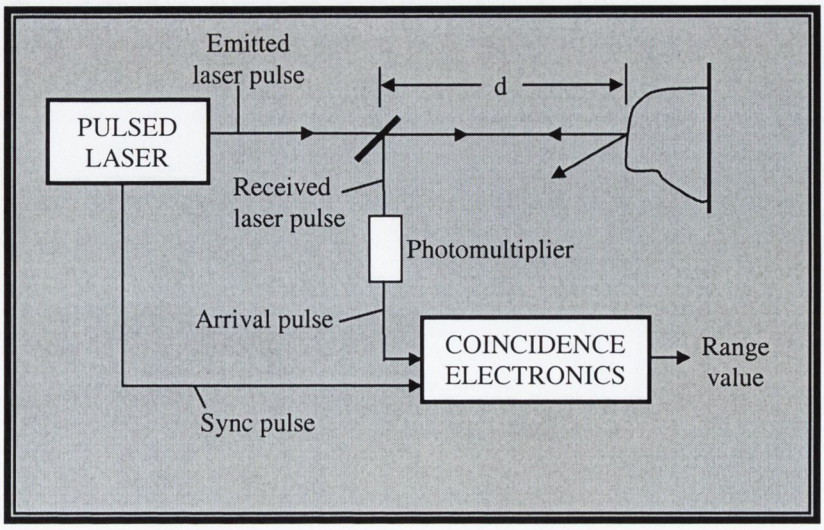

Figure 2.1: Time of flight – laser pulse rangefinder

may be deformed when it is reflected, and a difficult problem is how to determine the exact time at which the deformed pulse is received. A second method was proposed by *Nitzan et al* [26] in 1977. It involved modulating a laser beam in amplitude and measuring the phase shift of reflected light. The mechanism emits a laser beam that is amplitude modulated with a sinusoidal waveform. The beam is deflected by the mirror in the scanning unit. When the beam strikes an object, a portion of the light is reflected back to the scanning unit, and deflected into the photomultiplier of the receiver. The phase of the signal, relative to the reference phase, is proportional to the time of flight. The amplitude of the signal is proportional to the reflectance of the object. Thus, the system obtains both range and light intensity data. A typical laser rangefinder is illustrated in Figure 2.2.

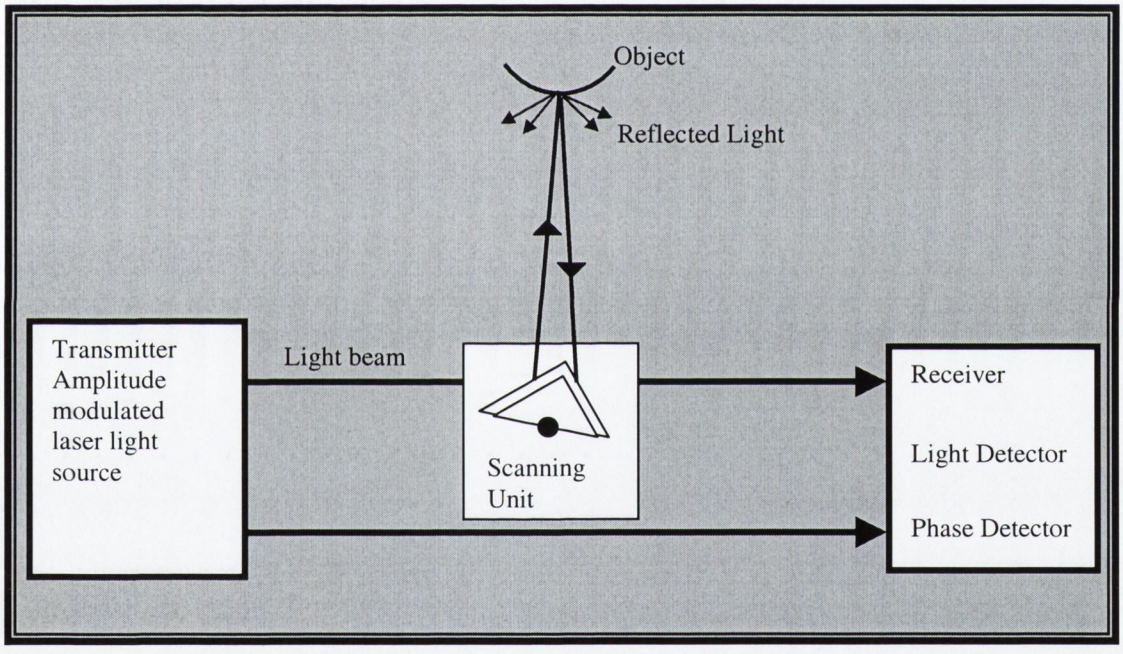

Figure 2.2: Time of flight - light ranging technique by phase detection

Laser time-of-flight systems give better resolution than that of the ultrasonic source since a laser beam is well focused compared to an ultrasonic beam. However, these laser-based systems lack the speed required to measure the characteristics of every solder paste deposit on a PCB in the manufacturing production line. Only a subset of the PCBs can be taken for sampling inspection. Despite their apparent simplicity of concept, these systems are not easy to design in practice and hence, they are more expensive. Moreover, like most depth extraction systems, laser based systems require a zero height reference plane to provide a starting base for solder paste depth measurements. Difficulties may occur in locating a suitable reference height for the

laser system, especially for systems with laser wavelengths near to infrared. With such systems, laser radiation may penetrate into the PCB materials before reflecting to a sensor, making it extremely complex to decide the actual reference plane, thus yielding an inaccurate measurement [40].

2.2.2 Triangulation Range Imaging

2.2.2.1 Passive Triangulation : Passive Stereopsis

'Stereopsis' [41,42] is the process of reconstructing a 3D representation of any object by combining a pair of 2D images captured from two different view points in order to establish the depth of the examined surface. Optical stereo depth extraction utilizes two or more cameras to identify features in a scene common to both cameras and uses the geometry co-ordinates between the cameras, which can be easily measured, to interpolate the distances of items or features in the scenes. This type of system processes the image data relatively fast and it is suitable for real-time operation. A prime example of passive stereopsis is the human visual system.

The principle of stereopsis is shown in Figure 2.3. Two cameras C_L and C_R separated by a distance of T from each other are used to capture a pair of 2D images of the point P. The corresponding points on the image plane are I_L and I_R. Employing simple Euclidean geometry, from similar triangles $\Delta C_L O_L I_L$ and $\Delta C_L Z_L P$ it is found that,

$$\frac{y_L}{f_L} = \frac{Y_L}{z + f_L} \tag{2-2}$$

and from triangles $\Delta C_R O_R I_R$ and $\Delta C_R Z_R P$ it is obtained

$$\frac{y_R}{f_R} = \frac{Y_R}{z + f_R} \tag{2-3}$$

where

y_L=distance from camera C_L's optical axis to the Image point I_L on the image plane

y_R=distance from camera C_R's optical axis to the Image point I_R on the image plane

f_L=focal distance of the camera C_L

f_R=focal distance of the camera C_R

z=distance of the point P from the image plane

Y_L=distance from camera C_L's optical axis to the 3-D point P

Y_R=distance from camera C_R's optical axis to the 3-D point P

T=the distance between the two cameras

Substituting equation (2-4)

$$Y_R = T - Y_L \tag{2-4}$$

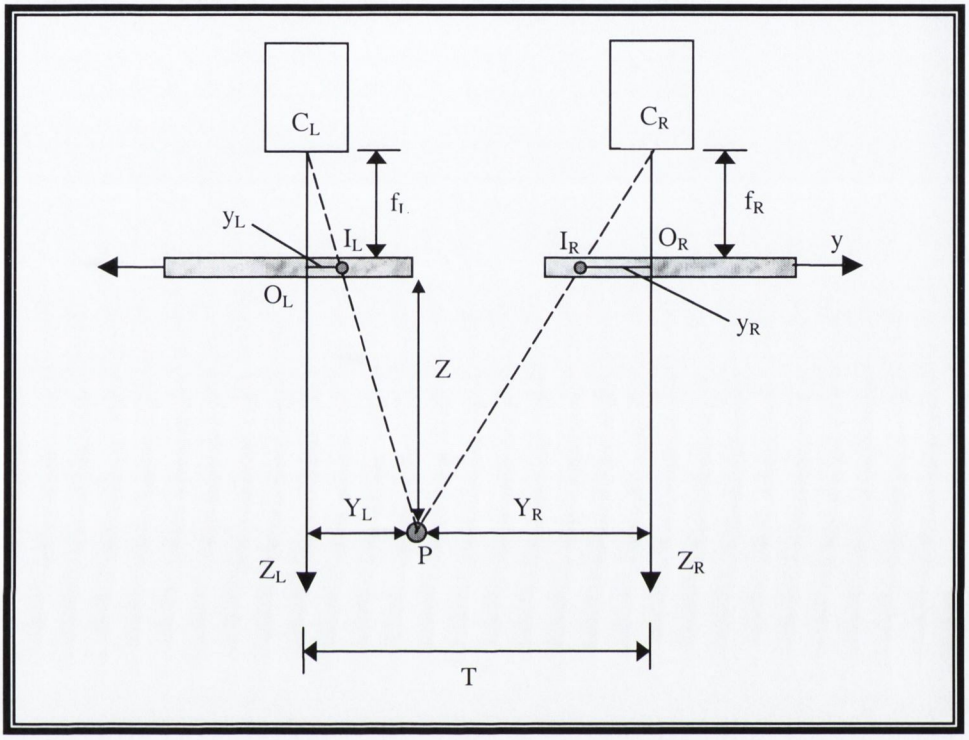

Figure 2.3: Geometry for Passive Stereopsis

into equation (2-3) to eliminate Y_R, the equation becomes

$$y_R(z + f_R) = (T - Y_L)f_R \tag{2-5}$$

Then rewriting equation (2-2),

$$y_L(z + f_L) = Y_L f_L \tag{2-6}$$

If the focal lengths of both cameras are the same, that is $f = f_L = f_R$, then by solving equations (2-5) and (2-6) simultaneously, Y_L can be eliminated and the range z of point P can therefore be calculated by:

$$z = \frac{f(T - y_L - y_R)}{y_L + y_R} \tag{2-7}$$

where

f = the focal length of the camera

The range accuracy is directly related to the stereo disparity between the images of the same point taken from two different locations and the separation between the cameras. Still, owing to its geometric simplicity, passive stereopsis is an attractive 3D ranging method.

Disadvantages relating to Stereopsis

Despite stereopsis' simple geometrical mathematical qualities, the requirement of capturing a pair of images is a cumbersome procedure:

1. Some part of the scene may appear in only one view of the stereo pair, due to occlusion (or shadow) effects. Occlusion diminishes when the distance between the cameras is reduced, but so then does the accuracy in range.
2. Since it is necessary to establish the correspondence between the two captured images, sometimes there may not be sufficient visual information at the points of interest to establish a unique pairing relationship, for instance, because of lack of intensity or colour identifiers.
3. Several candidate points may satisfy the matching operation with the resulting identification of false targets.

Many studies have focused on solving the correspondence problem. *Levine et al* [43] presented a method that employs the cross correlation between rectangular windows with hierarchical searches at coarse and fine resolutions. *Yakimovsky and Cunningham* [44] compute the cross correlation over cross or diamond-shaped areas with the search for a match being conditioned by a sufficient magnitude of the variance of the local masked region. The *Marr-Poggio-Grimson (MPG) approach* [45] and *Grimson* [46] tackled the problem by marking suitable points in object space, using specific illumination patterns such as grids or lines. By matching these points in image space and implementing them using the inverse perspective projection [25], the range in object space can be determined. Given such difficulties, in general, it is much more efficient if the range measuring application can be determined by employing only one image and thus, avoiding the correspondence problem.

2.2.3 Active Triangulation Range Imaging

2.2.3.1 Moiré Shadowing technique

Moiré Shadow Contouring was proposed by *Takasaki* [27] and *Meadows et al* [28] in 1970. A moiré topography is generated by observing two grating patterns, superimposing them on each other and analysing the interferograms between the demodulated grating shadow and the original reference-grating pattern in two dimensions. The resultant Moiré pattern produces a height contour map of the object.

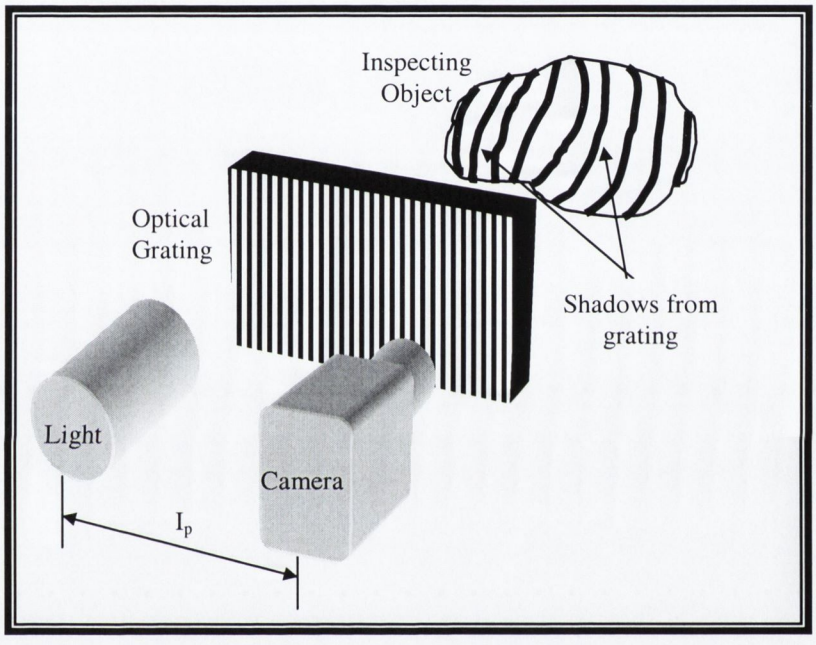

Figure 2.4: A typical Moiré Shadowing Set-up

The positions of these contours are then used to determine the shape of the surface. Figure 2.4 shows a typical Moiré Shadowing set-up. The range can be computed by considering the geometry in Figure 2.5. An optical grating of constant pitch x, illuminated by a linear light source, is projected onto the surface of the object P in the scene. A camera is positioned at a short distance Z_c before the grating. The camera captures the observed scene which consists of the distorted shadow lines (also known as fringes) and the regular reference fringe, the interference between them causing contour curves to appear as virtual images on the object's surface.

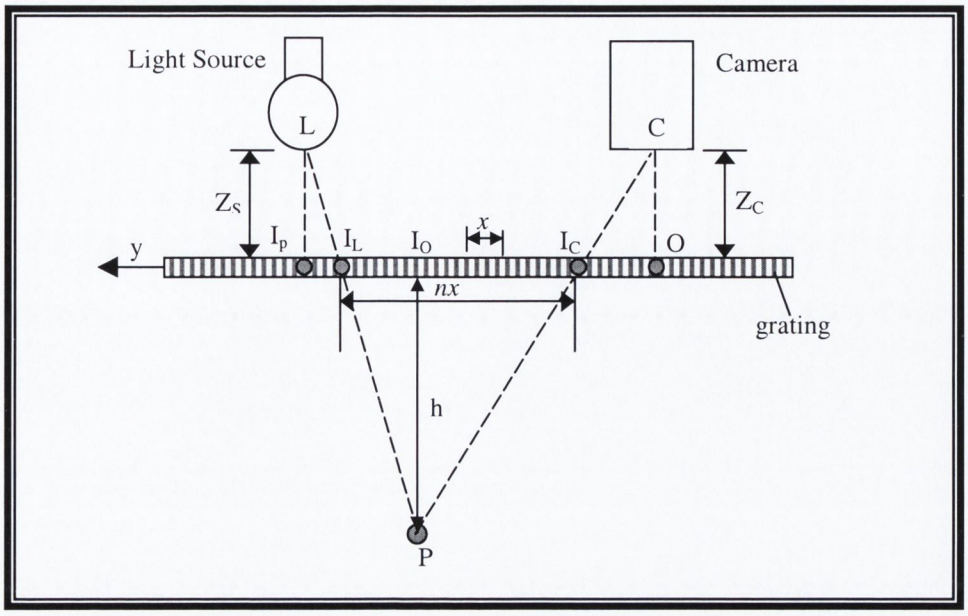

Figure 2.5: Geometry for Moiré Shadowing technique

The distance between the light source and the grating is denoted as Z_s and the distance between the camera and the grid is denoted as Z_c. From similar triangles ΔCOI_C and $\Delta I_O P I_C$

$$\frac{h}{Z_C} = \frac{I_O - I_C}{I_C} \tag{2-8}$$

where

h = the distance between the grating and the surface of the object

Z_C = the distance between the camera and the grating

Z_S = the distance between the light source and the grating

I_O = the distance of the object from the normal of the camera O

I_C = the distance of the object as seen by the camera from the normal of the camera O

I_P = the distance of the camera and the light source

From the other similar triangles $\Delta I_O P I_L$ and $\Delta I_P L I_L$, it is found

$$\frac{h}{Z_S} = \frac{I_L - I_O}{I_P - I_L} \tag{2-9}$$

The multiple fringe nx is determined by,

$$I_L - I_C = nx \tag{2-10}$$

where

n = (0,1,2…) = the fringe order as shown in Figure 2.5

Combining the above equations yields the range value h_n associated with the *nth* order fringe:

$$h_n = \frac{Z_S(nx - I_O + I_c) + Z_c(I_O - I_c)}{I_p - nx} \tag{2-11}$$

If the distance between the grating and the light source and the distance between the grating and the camera are equidistant, i.e. $Z_C = Z_L = Z$ then by replacing Z into equation (2-11) becomes

$$h_n = \frac{Z(nx)}{I_p - nx} = \frac{Zn}{\frac{I_p}{x} - n} \tag{2-12}$$

Hence, the range difference (h_n - h_{n-1}) between two adjacent fringes depends on the fringe order, it also depends on the distance between the grating and the camera and the light source. Different sets of quantized range values can be obtained by varying the grid pitch x. With the Moiré contouring strategy, ambiguities often arise in interrogating the fringe patterns and it is often not possible to determine whether a contour line is higher or lower than the adjacent contour line, the moiré fringe order [25]. There are various improved Moiré Shadowing techniques to overcome the slope ambiguity problem. A possible solution to the problem of fringe identification is to place a reference wire in front of the projection grid at a suitable location on the normal between the camera lens and the grid [47]. Shadow associated with the wire is projected on the surface of the scene and appears on the Moiré pattern. By measuring the distance between the image of the wire and its shadow on the Moiré photography, a particular fringe is identified and serves as a reference. *Duncan T. Moore and B. E. Traux* [29] presented a practical improvement by oscillating the phase of the Moiré pattern by a small amount so to distinguish the depression and elevation of the object. This is achieved by moving the grating in the observation system. The most significant problem is that the Moiré contouring technique was originally developed for fringe analysis by human observation and is therefore complex to implement on computers.

2.3 Structured Light

Structured light generation is a machine vision approach that takes advantage of the physics of ambient light and the image formation process. The technique acts as a kind of 'filter' by discarding irrelevant details, enhances the signal itself and increases the Signal Noise Ratio (SNR) where noise implies irrelevant background. *Shirai* [49] was one of the firsts to demonstrate structured light technique by constructing a very simple apparatus of a light beam through a vertical slit as the illumination source. Since then, structured light has been used extensively to obtain three-dimensional scene information for quick acquisition of range. It has proven to be the most popular and promising system for applications in which depth information is required. This non-contact optical technique makes use of texture gradients and utilises the projection of a regular light pattern. The projection must be done in such a way so that the position and orientation of the source of illumination, and the position of the camera are known. A Coupled Charged Device (CCD) camera grabs the images and the co-ordinates of the edges of the patterns can then be calculated. Progressively finer patterns are projected over this same area and greater depth detail results by the increase in edges displayed. By establishing the correspondence between the inspected object from the captured image and the light pattern in the scene, 3D surface geometric properties of the object can be extracted using *triangulation.*

Stripe based structured light pattern is a one dimensional pattern, and has the advantage of being able to provide a high sampling rate along the length of the stripes. Apart from the line stripe based patterns, patterns such as grids and spots [50] are also used as pattern projections in structured light. These pattern projections were not considered in this particular application since with a spot based projection system, low sampling rates are experienced in both x and y dimensions. Grid pattern projection systems are also two dimensional, but they are often more suitable if the shapes of the objects in question are quite curvy such as a human body, and depending on the direction of the projection of the light source, only one direction of the fringes would create fringe movement. Thus two grating patterns with horizontal and vertical fringes are required to be projected from two different directions if fringe movement is requested in both directions. Correspondence problems can then be solved at the grid intersections.

The principle underlying structured light is shown in Figure 2.6. An illumination system consists of a fibre-optic light source, a line grating, and an enlarger lens superimposes a well-defined pattern of light upon the object surface. A typical grating is a grating consisting of a sequence of equally spaced horizontal or vertical dark lines, (called "fringes" by analogy with Moiré contouring [27,28]), which are generated by the projection of a square wave grating, or Ronchi grating. The lighting/grating system is projected at an angle relative to the camera. This has the effect of compensating the error caused by non-perpendicular projection. When a grating pattern is projected onto an object's surface, the grating pattern is perturbed according to the topography of the object. A CCD camera is then used to record the perturbed grating pattern, which carries the 3D information of the object. From the camera's field of view, the pattern of light on the object appears curved and the amount of sideways displacement is related to the depth of the object at that point. No physical contact with the object is required, so the measurement process will not in itself deform it. The height and volume of the object can then be re-modelled with suitable profilometry.

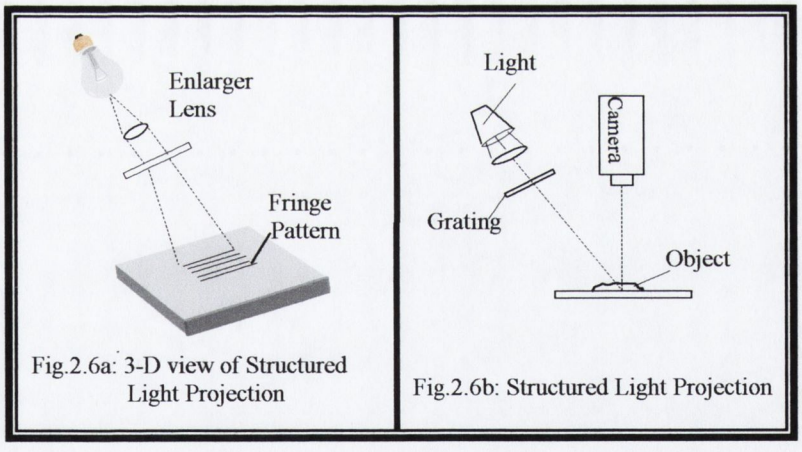

Fig.2.6a: 3-D view of Structured Light Projection

Fig.2.6b: Structured Light Projection

Figure 2.6: Structured Light Technique

2.4 Optical Geometry of Structured Light

Two different optical geometries used in Structured light have been investigated in this study; namely, the crossed-optical-axes geometry and the parallel-optical-axes geometry.

2.4.1 Crossed-Optical-Axes Geometry

A diagram of the principle behind the crossed-optical-axes geometry technique is shown in Figure 2.7. The crossed-optical-axes geometry technique consists of a camera, which is situated directly above the object being inspected; the optical axes of the camera are normal to the reference plane **R**, that serves as a reference from which object height distribution ***h(x,y)*** is measured. The grating ***G***, of period ***p***, (the spacing of the graticule) has its lines normal to the plane of the figure. A lighting projector, which is positioned at an angle relative to the camera, projects the fine grating pattern onto the plane **I** through its projector lens L_g. The camera captures the points projected on the reference plane **R** through the camera lens L_c. As the two optical axes are crossed at an acute angle to each other, the optical axes of the projector and the camera will intersect at a point **O**.

There are 3 cases, which must be taken into consideration.

Case 1: Telecentric Projection with *h(x,y)* = 0.

Consider the grating and the projector position at the infinite position, as indicated by L_∞ in Figure 2.7, where the projection rays are parallel. Also assume that the part of the inspected object is a flat surface coincident with plane **R**, with ***h(x,y) = 0***. The projection ray through L_∞ hits the reference plane **R** at point **B**, indicating that there is no deviation due to the lens of any kind since the projection are projecting at an infinite position. The periodic grating pattern may be expressed as a Fourier series. The exponential form of the Fourier series expansion is

$$a_\infty(x, y) = \sum_{n=-\infty}^{\infty} A_n e^{(j2\pi n f_o x)} \tag{2-13}$$

where

f_o is the fundamental frequency of the observed grating image
x is chosen as in the Figure 2.7
y axis is normal to the plane of the figure = $1/p_o = cos\theta/p$
A_n is the n^{th} fourier coefficient of the pattern
n is the multiple of the fundamental frequency, $n=1,2,3...$

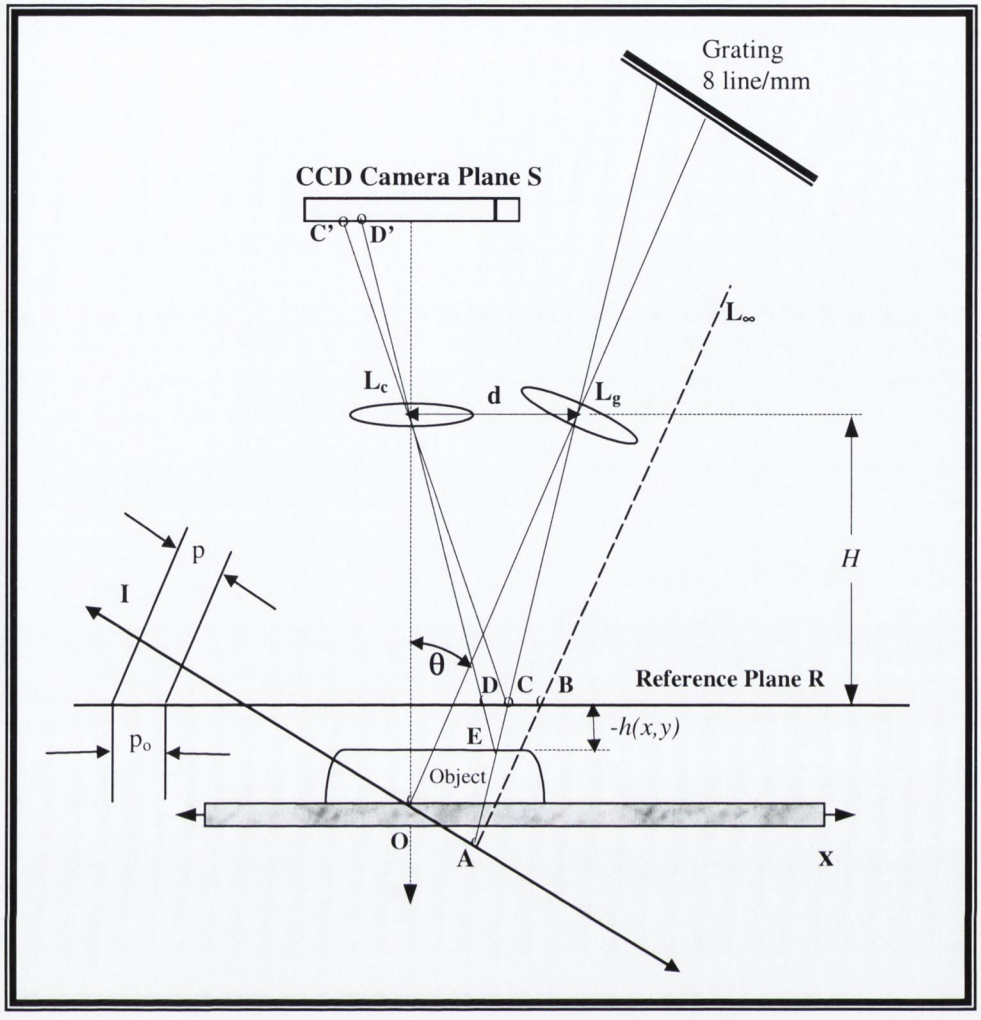

Figure 2.7: Crossed-optical-axes geometry

Case 2: Non-telecentric Projection with $h(x,y) = 0$.

In this case, the projection rays from the grating are projected at a finite distance L_g, where the projector rays are no longer parallel and the periodic grating image is deformed even in presence of a flat surface $h(x,y)$ as captured from the sensor plane **S**. By observing Figure 2.7, the differences between the telecentric projection and the non-telecentric projection can be distinguished. With respect to the telecentric projection, the principal ray through a conjugate image point **A** on plane **I** hits the reference plane **R** at point **B**, and for the non-telecentric projection, it hits the reference plane at point **C**, hence, there is a shift $s_o(x)$ from **B** to **C**. The deformed grating image for $h(x,y) = 0$ can be expressed as

$$a_o(x,y) = \sum_{n=-\infty}^{+\infty} A_n e^{j(2\pi n f_o [x + s_o(x)])} \tag{2-14}$$

where

$s_o(x) = \overline{BC}$ is a function of x
$\overline{BC}$ = the distance shift from B to C

By posing $\phi_O(x) = 2\pi f_o s_o(x)$, equation (2-14) can be rewritten as a phase-modulated signal.

$$\phi_o(x) = 2\pi f_o s_o(x) \tag{2-15}$$

$$a_o(x,y) = \sum_{n=-\infty}^{+\infty} A_n e^{j(2\pi n f_O x + n\phi_O(x))} \tag{2-16}$$

Equation (2-16) describes a sum of harmonics modulated in phase when the ray of projection is projected at a finite distance onto a flat surface. As a Fourier-series, $a_o(x,y)$ also denotes a superposition of phase-modulated sine and cosine terms.

Case 3: General Case non-telecentric projection where $h(x,y) \neq 0$.

Consider the general case where the object has a height of $\boldsymbol{h(x,y) \neq 0}$, the projection ray associated with the conjugate image point **A** hits the object at **E** and is reflected at point **D** on the reference plane **R** as seen through $\boldsymbol{L_c}$. Thus, from the camera viewpoint, point **A** shifts from point **B** to point **D**, and the viewed grating pattern can be written as

$$a(x,y) = r(x,y) \sum_{n=-\infty}^{+\infty} A_n e^{j2\pi n f_O(x + n s(x,y))} \tag{2-17}$$

where

$s(x,y) = \overline{BD}$, the shift from point B to point D
$r(x,y)$ represents the non-uniform reflectivity of object's surface

By re-writing equation (2-17) in terms of the phase-modulated summation.

$$\phi(x) = 2\pi f_o s(x,y) \tag{2-18}$$

$$a(x,y) = r(x,y) \sum_{n=-\infty}^{+\infty} A_n e^{j(2\pi n f_O x + n\phi(x,y))} \tag{2-19}$$

where

$\phi(x,y) = 2\pi f_o s(x,y) = 2\pi f_o \overline{BD}$
$r(x,y)$ represents the non-uniform reflectivity of object's surface

Equation (2-19) describes a sum of harmonics modulated in phase when the ray of projection is projected at a finite distance onto an object surface of certain height.

From the Figure 2.7, the distance $\overline{BD}$ is given by

$$\overline{BD} = \overline{BC} + \overline{CD}$$

Both relations in terms of phase are imposed; where in case 2, the relation $\phi_o(x) = 2\pi f_o s_o(x)$ gives rise to the phase-modulated signal when projection is projected at a finite distance for $\boldsymbol{h(x,y)} = 0$, and in the latter case, the relation $\phi(x,y) = 2\pi f_o s(x,y)$, the distance $\overline{CD}$ for the amount of phase deviation associated with the topography of the object can be easily derived.

Hence,

$$\overline{BD} = \overline{BC} + \overline{CD} \tag{2-20}$$

given that

$$\phi(x, y) = \phi_o(x) + \Delta\phi(x, y) \tag{2-21}$$

$$\Delta\phi(x, y) = 2\pi f_o \overline{CD} \tag{2-22}$$

where

$\Delta\phi(x, y)$ is the phase deviation associated with the shape of the objects.

Thus, extracting the amount of phase deviation caused by the shape of the object, the height can be determined as shown in Section 2.5.

2.4.2 Parallel-Optical-Axes Geometry

Parallel-optical-axes geometry consists of a camera and a grating projection system where their optical axes are in parallel to each other and are normal to the reference plane **R**. The conjugate image of the grating **G** is formed on plane **R**, and due to the positions of the camera and the projection system, the resulting image points of the telecentric projection, and the non-telecentric projection for $\boldsymbol{h(x,y) = 0}$ are reduced into one single image point. It can be seen that the three points **A**, **B** and **C** in Figure 2.7 have degenerated into one single point **C** in Figure 2.8.

So therefore, equation (2-15) from case 2 in the crossed-optical-axes geometry of Section (2.4.1) becomes

$$\phi_o(x) = 2\pi f_o s_o(x) = 2\pi f_o \overline{BC}$$

$$= 0 \tag{2-23}$$

That is when $\boldsymbol{h(x,y) = 0}$, the grating image projected on the plane **R** remains as a regular grating pattern regardless of the position of the projector.

And equation (2-18) becomes

$$\phi(x) = \Delta\phi(x) = 2\pi f_o s(x,y) = 2\pi f_o \overline{CD} \tag{2-24}$$

The main disadvantage of the parallel-optical-axes geometry is the optical set-up; because the two optical axes are in parallel, it requires a large distance from the reference plane in order to form its image within the field of view of the camera lens.

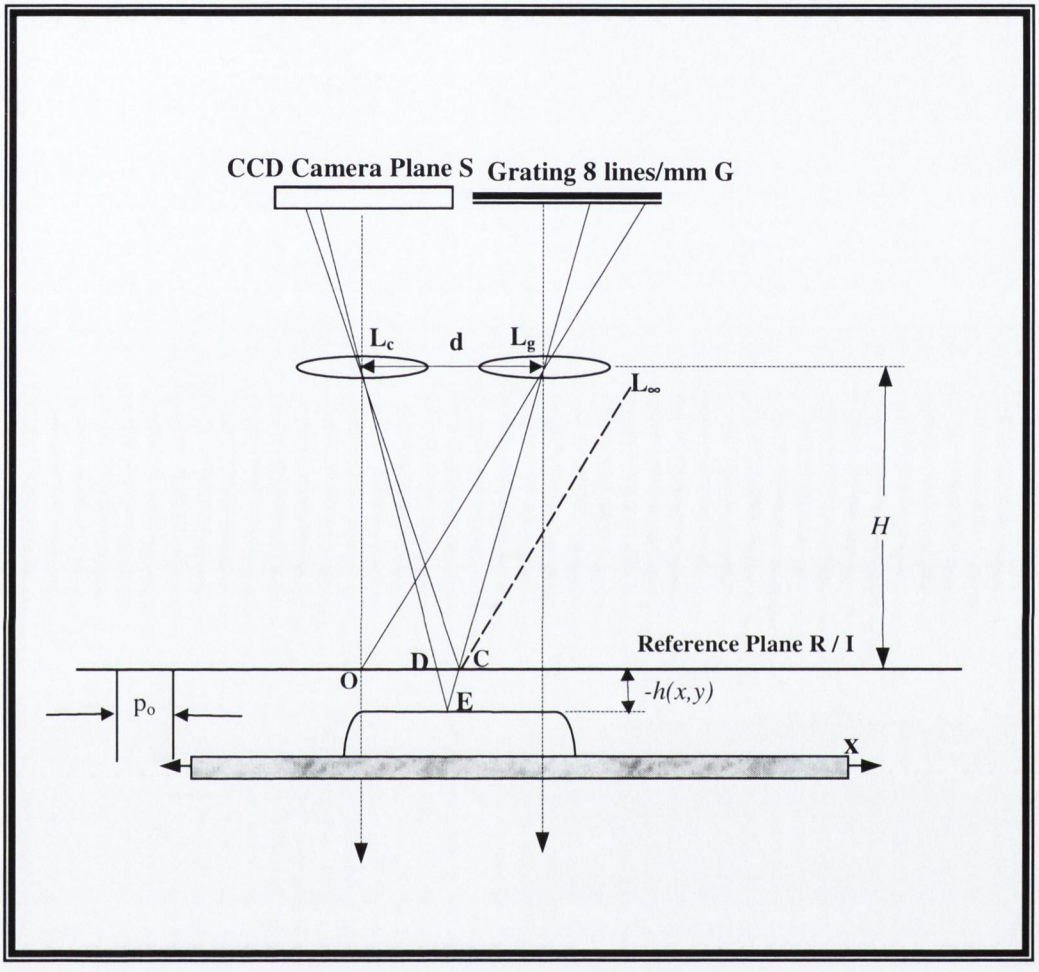

Figure 2.8: Parallel-optical-axes geometry

2.5 Triangulation - Phase to Height Relationship

In both geometries, the Crossed-Optical-Axes and the Parallel-Optical-Axes, a relationship between the phase deviation ***ϕ(x)*** and the height ***h(x,y)*** can be derived. Consider the $\Delta L_c HL_g$ and ΔDHC in Figure 2.7, by the principle of triangulation, the following can be written

$$\frac{\overline{CD}}{d} = \frac{-h(x,y)}{H - h(x,y)} \tag{2-25}$$

where

$h(x,y)$ is defined positive when measured upwards from the reference plane R.
$\overline{CD}$ is the distance displaced due to the object's topography.
d is the distance between the two lens

Since, from equation (2-22) and (2-24), the phase deviation $\Delta\phi(x)$ can be represented as

$$\phi(x) = \Delta\phi(x) = 2\pi f_o s(x,y) = 2\pi f_o \overline{CD}$$

$$\Rightarrow \qquad \overline{CD} = \frac{\Delta\phi(x)}{2\pi f_o}$$

by substituting $\overline{CD}$ into equation (2-25), an expression for the height distribution $h(x,y)$ as a function of the phase deviation $\Delta\phi(x,y)$ is derived:

$$h(x,y) = \frac{H\Delta\phi(x,y)}{\Delta\phi(x,y) - 2\pi f_o d} \tag{2-26}$$

2.6 Reasons for employing Structured Light technique

1. Unlike stereopsis, only one image pattern is sufficient in this approach for attaining 3D information of the inspected object. This keeps the computation time and memory storage to a minimum.
2. With an active sensing technique, the light and optics can be strictly control to the applications' advantage, simplifying any image post-processing and enabling greater accuracy.
3. The apparatus set-up is easy to construct relative to other depth extraction measurements.
4. Structured light techniques are suitable for real-time processing, hence it is a good choice for in-line use during manufacturing. It has the necessary speed and accuracy to inspect every board and identify quality problems immediately, permitting manufacturing personnel to fix defects before building large numbers of defective boards. This is in contrast to laser-based and X-ray systems which lack the speed required to measure the characteristics of every solder paste deposits, only sampling inspection can be done.

5. Structured light technique is less expensive to build and design than any laser based or X-ray system; the onus does not lie in the apparatus but on the profilometry to extract the depth measurements.
6. Given that the size of the objects under examination in this research are extraordinarily small, structured light would be most suitable for such inspection.

The crossed-optical-axes geometry of the Structured light approach was chosen for this research over the parallel-optical-axes geometry due to its simpler set-up. In the parallel-optical-axes geometry, the two optical axes are in parallel which require a large distance from the reference plane in order to form an image within the field of view of the camera lens. Also, since the two axes are in parallel, the amount of allowable deviation can be quite small, which is not favourable in this application since the volumetric measurements of solder paste pads are already very small. With the crossed-optical-axes geometry, the direction of the light source is projected at an angle. This allows greater control and variation, the bigger the angle, the larger the amount of fringes are shifted, making it clearer to identify. Moreover, the set-up is simpler to construct, and consequently, more commonly employed [32,57].

2.7 Conclusions

In this chapter, several range imaging techniques for general applications have been briefly examined. Among these range imaging techniques, the active triangulation Structured Light approach was found to be most suitable for our 3D solder paste measurements application. This is due to its easy construct apparatus set-up, and with the fact that only one image is required to reconstruct the 3D information, the correspondence problem would not arise. The importance of choosing the most adaptable set-up is a key factor to success.

Part I of the Thesis

Chapter 3

Phase Profilometry

3.1 Introduction

In Chapter 1, three phase extraction profilometry techniques were introduced. Namely, the fast-Fourier Transform Profilometry (FTP) proposed by *Takeda and Mutoh* [31,32], the Signal Domain Profilometry (SDP) proposed by *S.Tang and Y.Hung* [33], and the New Fast Phase Profilometry (NFP) proposed *by L.Di Stefano and F.Boland* [34,35].

In this Chapter, a complete description of these techniques is given with particular emphasis on the underlying theories. An image row of the grating image is selected for demonstrating the theoretical process, though in practice, all rows of the fringe image must be processed. In Section 3.3, it will be proved mathematically that by using a reference image map, the camera-grating misalignment problem arising from optical set-up can be compensated. The implementations and results of these techniques will be presented in the next Chapter.

3.2 Phase Profilometry

Phase Profilometry [52,53] is a technique for measuring the range based on the amount of phase modulation in the fringe image [from the principle of the structured light technique] due to the topography of the object. The example below demonstrates the basic idea of phase modulation in a fringe shifting image.

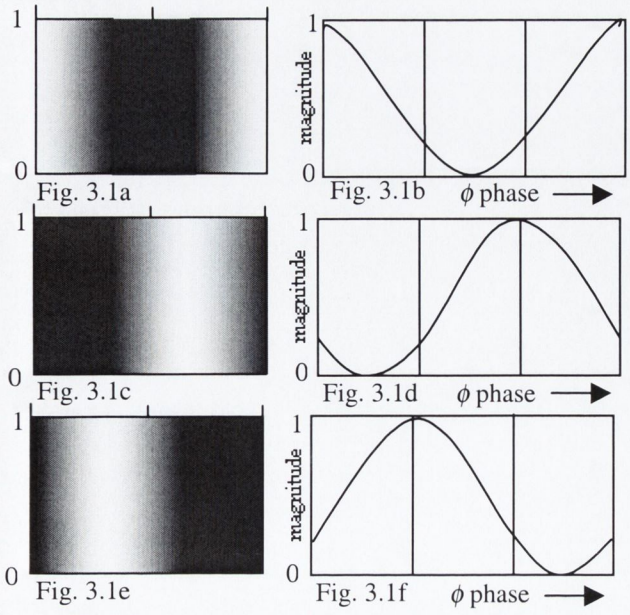

Fig.3.1: An example showing phase modulation

Figure 3.1a shows the initial fringe pattern, that is the pattern with no fringe shifting. The light intensity distribution of the fringe pattern can be described as a sinusoidal function as shown in Figure 3.1b.

Figure 3.1c and 3.1e illustrate the change of the fringe positions when the initial fringe pattern is shifted by an amount of 1/3 and 2/3 of the original pitch distances respectively. The phase is modulated by the same amount and is shown in Figure 3.1d and 3.1f respectively. Demodulation is the reverse process of modulation. It translates the same amount of fringe shift as in the distorted image/row to form the original image/row.

3.2.1 Fast-Fourier Transform Profilometry (FTP)

Takeda and *Mutoh* [31,32] proposed a Phase Profilometry technique known as the Fourier Transform Profilometry (FTP), based on the principle of Fourier Transform. Fourier Transform Profilometry is accomplished by suitably modifying the frequency spectrum of the grating image in order to extract the phase deviation arising from the 2-D image perturbed by the topography of the object.

The main advantage of transforming the fringe image pattern into the frequency domain is to facilitate extraction of the phase. In the frequency domain, the filtering of the harmonic which contains most of the relevant information can be readily executed by multiplying it with a window function in order to obtain the phase deviation caused by the object's height.

A deformed grating image $a(x,y)$ can be expressed as a sum of harmonics with spatial carrier frequencies nf_o modulated both in phase $\phi(x,y)$ and amplitude $r(x,y)$ as defined in Chapter 2, equation (2-19); for clarity, the equation is re-shown below.

$$a(x,y) = r(x,y)\sum_{n=-\infty}^{+\infty} A_n e^{j(2\pi n f_o x + n\phi(x,y))} \tag{2-19}$$

where

f_o is the fundamental frequency of the observed grating image
$\phi(x,y) = 2\pi f_o s(x,y)$ = is the phase deviation
$r(x,y)$ represents unwanted irradiance variations arising from the non-uniform light reflectivity or transmission of the object's surface

Equation (2-19) can be rewritten as follows:

$$g(x,y) = \sum_{n=-\infty}^{+\infty} q_n(x,y) e^{j2\pi n f_o x} \tag{3-1}$$

where

$$q_n(x,y) = A_n r(x,y) e^{jn\phi(x,y)}$$

By using Fourier Transform theory with y being fixed, the one-dimensional Fourier transform of the image row $y = \bar{y}$ with respect to x of q_n(x,y) can be computed.

$$G(f,\bar{y}) = \Im[g(x,\bar{y})] = \int_{-\infty}^{+\infty} g(x,\bar{y}) e^{-j2\pi fx} dx \tag{3-2}$$

$$= \sum_{n=-\infty}^{+\infty} Q_n(f - nf_o, \bar{y}) \tag{3-3}$$

where

$Q_n(f,\bar{y})$ is the 1-D Fourier transform with respect to x of $q_n(x,\bar{y})$

$G(f,\bar{y})$ is the 1-D Fourier transform with respect to x of $g(x,\bar{y})$

Note: y is treated as a fixed parameter, and in this case the row $\bar{y}$ is chosen.

Even though the original data consists of real identities, in general, $G(f,\bar{y})$ will be a complex quantity[i]. Provided that both r(x, $\bar{y}$) and ϕ(x, $\bar{y}$) vary slowly compared to the grating frequency, the overlap between the $Q_n(f,\bar{y})$ is small as they are separated from each other in the spectrum by the grating frequency $2f_o$. This is explained more thoroughly in the Section 4.4.2 on the Range of Measurements and grating frequency. The number of sampled pixels in the image and the number of fringes is usually known, and because the grating is of a square waveform, the pulse widths are therefore of the same length, as shown in Figure 3.2. The grating frequency f_o can be easily determined by dividing the number of grating fringes with the number of sampled pixels in the image. Alternatively, if the number of fringes is not known, the fundamental grating frequency f_o can be computed by selecting the first highest amplitude peak after the DC component and thus, the corresponding frequency is the fundamental grating frequency f_o.

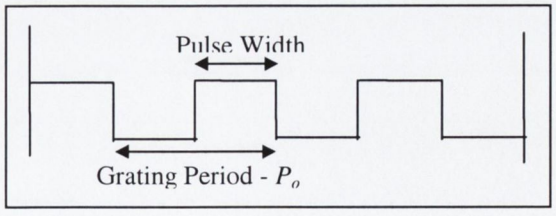

Fig.3.2: A diagram of a square wave form explaining the computation of the grating frequency

[i] Because of the presence of the 'j' in the exponential, the magnitude of phase becomes a significant element

$$No.of\ fringes = discrete\ fundamental\ grating\ frequency = \frac{line\ size}{grating\ period}$$

$$fundamental\ grating\ frequency = \frac{No.of\ fringes}{line\ size}$$

A choice on either of the two spectra, $Q_1(f - f_o, \bar{y})$ or $Q_1(f + f_o, \bar{y})$ centred on the fundamental frequency $\pm f_o$ can be selected as it consists of the identical information on the opposite sides of the origin. A narrow frequency domain filter centred on $+f_o$ is then used to extract one of these fundamental harmonics; $Q_1(f - f_o, \bar{y})$ was chosen intuitively. Figure 3.3 demonstrates the spectra of the deformed grating image.

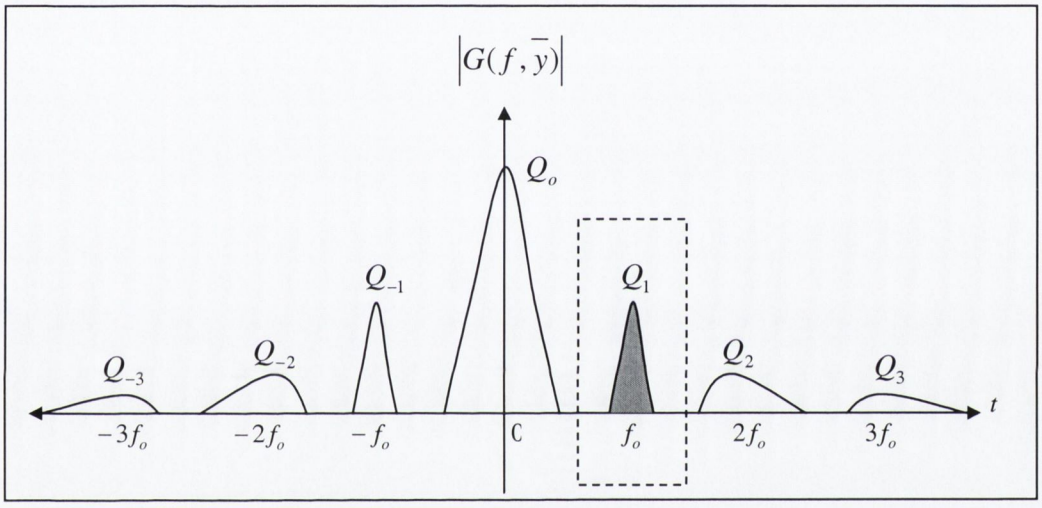

Fig. 3.3: Spatial frequency spectra of deformed grating image for a fixed y value. Notice Q_1 is selected for the filtering operation

The harmonic is then translated by f_o on the frequency axis towards the origin to obtain $Q_1(f, \bar{y})$. The inverse Fourier Transform is then performed on $Q_1(f, \bar{y})$, to obtain $g_1(x, \bar{y})$:

$$g_1(x, \bar{y}) = \Im^{-1}\left(Q_1(f, \bar{y})\right)$$

$$g_1(x, \bar{y}) = q_1(x, \bar{y})e^{j2\pi f_o x} = A_1 r(x, \bar{y})e^{j(2\pi f_o x + \phi(x, \bar{y}))} \qquad (3\text{-}4)$$

The same operations are performed on the image of the undistorted grating pattern, or the chosen reference row as given by equation (2-16),

$$g_o(x, y) = \sum_{n=-\infty}^{+\infty} A_o e^{j(2\pi n f_O x + n\phi_O(x))} \qquad (2\text{-}16)$$

$$\Rightarrow \quad g_o(x, \bar{y}) = A_1 e^{j(2\pi f_O x + \phi_O(x))} \qquad (3\text{-}5)$$

To evaluate the phase deviation, $\Delta\phi(x,\bar{y})$, the Fourier-series of $g_1(x,\bar{y})$ and the complex conjugate of $g_o(x,\bar{y})$ are multiplied together to cancel the original and first harmonic phase components.

$$g_o^{*}(x,\bar{y})g_1(x,\bar{y}) = |A_1|^2 r(x,y)e^{-j(2\pi f_O x+\phi_O(x))}e^{j(2\pi f_O x+\phi(x))} \tag{3-6}$$

By recalling equation (2-21), $\phi(x,y) = \phi_o(x,y) + \Delta\phi(x,y)$, equation (3-6) becomes

$$H(x,\bar{y}) = g_o^{*}(x,\bar{y})g_1(x,\bar{y}) = |A_1|^2 r(x,y)e^{j\Delta\phi(x,y)} \tag{3-7}$$

Strictly, the reflectivity *r(x,y)* only affects the magnitude of of $H(x,\bar{y})$, (i.e.) $|H(x,\bar{y})|$ whereas the phase deviation $\Delta\phi(x,\bar{y})$ caused by the distortion of the fringes is contained in the argument of $H(x,\bar{y})$, (i.e.) $\angle H(x,\bar{y})$. Thus, to separate the phase distribution $\Delta\phi(x,\bar{y})$ from the unwanted variation of reflectivity $r(x,y)$ in the real part of $H(x,\bar{y})$, the complex logarithm of equation (3-7) must be computed:

$$log[H(x,\bar{y})] = log\left[|A_1|^2 r(x,y)\right] + i\Delta\phi(x,y) \tag{3-8}$$

The phase deviation $\Delta\phi(x,\bar{y})$ is now completely separated from the unwanted variation of the reflectivity *r(x,y)*. Alternatively, the phase deviation can be found by computing the angle using the arctangent operation,

$$\Delta\phi(x,\bar{y}) = \tan^{-1}\frac{\mathrm{Im}(H(x,\bar{y}))}{\mathrm{Re}(H(x,\bar{y}))} \tag{3-9}$$

where

Im denotes as the imaginary part of the processed image row
Re denotes as the real part of the processed image row

The resulting phase deviation is indeterminate to a factor of 2π and, in most cases, the phase calculated by computer gives principal values ranging from $-\pi$ to π. These discontinuities can be corrected by a phase unwrapping algorithm, described in Section 3.4.

Once the unwrapped phase deviation is found, the actual height distribution can be evaluated using the relationship defined in equation (2-26).

3.2.2 Signal Domain Profilometry (SDP)

Tang and Hung in [33] presented a novel demodulation and convolution-based approach in the signal domain to replace the typical frequency domain approach for processing the grating image. Signal Domain Profilometry (SDP) provides a substantial reduction in computing time over FTP. For demodulation, the data is multiplied by sine and cosine terms, and the low frequency components are extracted by a low-pass FIR filter to yield the desired phase. The multiplication of the signal by these sine and cosine terms causes a shift of the whole frequency band by f_o. One of the main harmonics in the spectrum of the signal centred at the spatial carrier frequency f_o is shifted to zero frequency and is then extracted by a low-pass FIR filter.

For clarity, the crossed-optical-axes geometry of the Structured Light technique is again discussed here. Re-considering the telecentric case as discussed in Section 2.4.1 where the grating is situated at an infinite position and all the projection rays are in parallel, and the grating projected onto a perfect flat surface is a uniform grating pattern. If the initial undistorted grating pattern is extended to be a periodic even function, that is the Fourier series expansion consists of only cosine terms, the Fourier representation of the grating pattern captured through the camera is given by equation (3-10), similar to equation (2-19),

$$g_{\infty}(x,y) = r(x,y)\sum_{n=0}^{+\infty} A_n(x,y)\cos\left(\frac{2\pi n x}{p}\right) \tag{3-10}$$

where

p is the period of the grating on the reference plane.

For the non-telecentric case as discussed in Section 2.4.1 where the grating is now projected at a finite position onto a flat surface, the fringe pattern on the reference plane can be expressed as,

$$\begin{aligned} g_{nt}(x,y) &= r(x,y)\sum_{n=0}^{+\infty} A_n(x,y)\cos\left(\frac{2\pi n x}{p} + \frac{2\pi n r(x)}{p}\right) \\ &= r(x,y)\sum_{n=0}^{+\infty} A_n(x,y)\cos\left[\frac{2\pi n}{p}\left(x + r(x)\right)\right] \end{aligned} \tag{3-11}$$

And by substituting

$$\phi_{nt}(x) = \frac{2\pi r(x)}{p} \tag{3-12}$$

it can be rewritten as,

$$g_{nt}(x, y) = \sum_{n=0}^{+\infty} B_n(x, y)\cos\left[\frac{2\pi n x}{p} + n\phi_{nt}(x)\right] \tag{3-13}$$

where

$B_n(x, y) = r(x, y)A_n(x, y)$

$\phi_{nt}(x)$ is the phase shift due to a telecentric to a non-telecentric projection on the reference plane as shown in Figure (2.8).

For the general case where the grating is positioned at a finite distance from the object's surface, and the object has a height of $h(x,y) > 0$, the deformed grating pattern can be written as equation (3-14),

$$g(x, y) = r(x, y)\sum_{n=0}^{+\infty} A_n(x, y)\cos\left\{\frac{2\pi n}{p}\left[x + r(x) + s(x, y)\right]\right\} \tag{3-14}$$

or,

$$g(x, y) = \sum_{n=0}^{+\infty} C_n(x, y)\cos\left[\frac{2\pi n x}{p} + n\phi(x, y)\right] \tag{3-15}$$

where

$C_n(x, y) = r(x, y)A_n(x, y)$

$\phi(x,y)$ is the phase shift due to the topography of the object as shown in Figure (2.8).

And,

$$\phi(x, y) = \frac{2\pi}{p}\left[r(x) + s(x, y)\right] \tag{3-16}$$

The phase difference $\Delta\phi(x, y)$ between the reference plane and the object's surface can then be calculated as,

$$\begin{aligned}\Delta\phi(x, y) &= \phi(x, y) - \phi_{nt}(x) \\ &= \frac{2\pi}{p}\left[r(x) + s(x, y)\right] - \frac{2\pi r(x)}{p} \\ &= \frac{2\pi\, s(x, y)}{p}\end{aligned} \tag{3-17}$$

Signal Domain Profilometry involves a multiplication of the deformed grating pattern $g(x,y)$, by the cosine and sine terms to demodulate the signal. Equation (3-15) is first multiplied by $\cos\left(\frac{2\pi x}{p}\right)$ to give,

$$g(x,y)\cos\left(\frac{2\pi x}{p}\right)=\sum_{n=0}^{+\infty}C_n(x,y)\cos\left[\frac{2\pi nx}{p}+n\phi(x,y)\right]\cos\left(\frac{2\pi x}{p}\right) \tag{3-18}$$

Applying the Trigonometric identity, $2\cos A\cos B=\cos(A+B)+\cos(A-B)$ gives

$$\begin{aligned}
&g(x,y)\cos\left(\frac{2\pi x}{p}\right)= \\
&\sum_{n=0}^{+\infty}\frac{1}{2}C_n(x,y)\left\{\cos\left[\frac{2\pi(nx+x)}{p}+n\phi(x,y)\right]+\cos\left[\frac{2\pi(nx-x)}{p}+n\phi(x,y)\right]\right\} \\
&=a_0(x,y)\cos\left(\frac{2\pi x}{p}\right)+\frac{1}{2}a_1(x,y)\cos\left[\frac{4\pi x}{p}+\phi(x,y)\right]+\frac{1}{2}a_1(x,y)\cos[\varphi(x,y)] \\
&+\frac{1}{2}a_2(x,y)\cos\left[\frac{6\pi x}{p}+2\phi(x,y)\right]+\frac{1}{2}a_2(x,y)\cos\left[\frac{2\pi x}{p}+2\phi(x,y)\right] \\
&+\frac{1}{2}a_3(x,y)\cos\left[\frac{8\pi x}{p}+3\phi(x,y)\right]+\frac{1}{2}a_3(x,y)\cos\left[\frac{4\pi x}{p}+3\phi(x,y)\right]+\cdots
\end{aligned} \tag{3-19}$$

The low frequency term of equation (3-19) is $\frac{1}{2}a_1(x,y)\cos[\phi(x,y)]$. This low frequency term may be extracted by filtering $g(x,y)\cos\left(\frac{2\pi x}{p}\right)$ with a low pass filter. Let the filter input signal be *x(n)*,

$$x(n)=g(x,y)\cos\left(\frac{2\pi x}{p}\right)$$

and the length of the FIR filter be *M*, then the resulting signal after convolving the input signal with the filter impulse response is given by,

$$y_{real}(n)=\sum_{k=0}^{M-1}h(k)x(n-k) \tag{3-20}$$

$$=\frac{1}{2}a_1(x,y)\cos[\phi(x,y)] \tag{3-21}$$

where

$y_{real}(n)$ is the real term of the extracted low frequency signal.

To determine the phase $\phi(x,y)$, equation (3-15) must also multiplied by $\sin\left(\frac{2\pi x}{p}\right)$ to obtain the imaginary signal.

$$g(x,y)\sin\left(\frac{2\pi x}{p}\right)=\sum_{n=0}^{+\infty}C_n(x,y)\cos\left[\frac{2\pi nx}{p}+n\phi(x,y)\right]\sin\left(\frac{2\pi x}{p}\right) \qquad (3\text{-}22)$$

And again applying the Trigonometric identity, $2\cos A\sin B=\sin(A+B)-\sin(A-B)$ gives,

$$\begin{aligned}
&g(x,y)\sin\left(\frac{2\pi x}{p}\right)= \\
&\sum_{n=0}^{+\infty}\frac{1}{2}C_n(x,y)\left\{\sin\left[\frac{2\pi(nx+x)}{p}+n\phi(x,y)\right]-\sin\left[\frac{2\pi(nx-x)}{p}+n\phi(x,y)\right]\right\} \\
&=a_0(x,y)\sin\left(\frac{2\pi x}{p}\right)+\frac{1}{2}a_1(x,y)\sin\left[\frac{4\pi x}{p}+\phi(x,y)\right]-\frac{1}{2}a_1(x,y)\sin[\varphi(x,y)] \\
&+\frac{1}{2}a_2(x,y)\sin\left[\frac{6\pi x}{p}+2\phi(x,y)\right]-\frac{1}{2}a_2(x,y)\sin\left[\frac{2\pi x}{p}+2\phi(x,y)\right] \\
&+\frac{1}{2}a_3(x,y)\sin\left[\frac{8\pi x}{p}+3\phi(x,y)\right]-\frac{1}{2}a_3(x,y)\sin\left[\frac{4\pi x}{p}+3\phi(x,y)\right]+\cdots \qquad (3\text{-}23)
\end{aligned}$$

Similarly to the case of the low frequency extraction in the real signal, the low frequency term of the imaginary signal is $-\frac{1}{2}a_1(x,y)\sin[\phi(x,y)]$ and this low frequency term can be extracted by convolving $g(x,y)\sin\left(\frac{2\pi x}{p}\right)$ with the impulse response of the same low pass finite-duration impulse response (FIR) digital filter. Hence,

$$y_{imag}(n)=-\frac{1}{2}a_1(x,y)\sin[\phi(x,y)] \qquad (3\text{-}24)$$

where

$y_{imag}(n)$ is the imaginary term of the extracted low frequency signal.

In Tang and Hung's paper, the phase component due to non-telecentric and the object's height is found by processing the inverse tangent of equation (3-21) and (3-24).

$$\phi(x,y) = \tan^{-1}\left[\frac{-y_{imag}(n)}{y_{real}(n)}\right] = \frac{-\left(-\frac{1}{2}a_1(x,y)\sin[\phi(x,y)]\right)}{\frac{1}{2}a_1(x,y)\cos[\phi(x,y)]} \qquad (3\text{-}25)$$

In order to calculate the phase difference $\Delta\phi(x,y)$ between the reference plane and the object's surface, the same procedures must also performed on the reference grating pattern (i.e.) when the object's height is zero as given by equation (3-11). Then by using equation (2-21), subtracting the phase of the reference plane from the phase due in the distorted row, the phase difference $\Delta\phi(x,y)$ can be obtained.

3.2.3 New Fast Phase Profilometry (NFP)

A new profilometry technique known as the New Fast Phase Profilometry, was devised by *L. Di Luigi* and *F. Boland* [34,35]. This technique is similar to the Signal Domain Profilometry and uses two simple binary periodic functions to demodulate the image signal. The choice of these functions is based on the merit that by proper modification of the pixels' sign, the need for normal floating point multiplication of the signal with sine and cosine terms is eliminated, and hence the overall computational effort can be reduced dramatically. A suitable choice for the demodulation functions is a square wave function of unit amplitude between –1 and +1, and having the same fundamental frequency f_o as that of the grating. The phase extraction process is carried out using two types of filters, comb filters and moving averagers. Comb filters are exceptionally simple and useful for passing or eliminating specific frequencies and certain harmonics.

Assuming $c_1(x)$ and $c_2(x)$ represent the square waves function, they can be represented in a Fourier series form as

$$c_1(x) = \sum_{m=-\infty}^{+\infty} C_n e^{j2\pi n f_o x} \qquad (3\text{-}26)$$

where

$c_1(x)$ is a square wave function with fundamental grating frequency f_o

$$c_2(x) = c_1(x - p_o / 4) = \sum_{m=-\infty}^{+\infty} C_n e^{j2\pi m f_o x} e^{-jn\pi/2} = \sum_{m=-\infty}^{+\infty} \overline{C}_n e^{j2\pi m f_o x} \tag{3-27}$$

where

$\overline{C}_n = C_n e^{-jn\pi/2}$

p_o is the period of the grating period

$c_2(x)$ is the second square wave function with carrier frequency f_o and lags a quarter of the period from the first square wave function $c_1(x)$

The function $c_1(x)$ is the equivalent square wave equation of an even (cosine) function and the function $c_2(x)$, shifted by a quarter of a period, is the equivalent square wave equation of an odd (sine) function.

Considering a deformed grating image in its Fourier-series representation, again equation (2-19) is presented for clarity purposes,

$$a(x, y) = r(x, y) \sum_{n=-\infty}^{+\infty} A_n e^{j(2\pi n f_o x + n\phi(x,y))} \tag{2-19}$$

where

f_o is the fundamental frequency of the observed grating image

$\phi(x,y) = 2\pi f_o s(x,y)$ = is the phase deviation

$r(x,y)$ represents the non-uniform reflectivity of object's surface

A simple smoothing operator such as a moving averager is applied to each row of the image in order to attenuate the higher harmonics in the image row, $a(x,y)$. A 3-point moving averager can be defined as,

$$y(n) = \frac{1}{3}[x(n+1) + x(n) + x(n-1)] \tag{3-28}$$

Mean value subtraction is then applied to eliminate the DC component prior to the multiplication by the square waves.

An image row $y = \overline{y}$ of the grating image is selected for demonstrating the NFP process, though in practice, all rows of the fringe image must be processed.

$c_1(x)$ and $c_2(x)$ are multiplied by the selected grating image row $a(x, \overline{y})$,

$$g_{real}(x, \overline{y}) = a(x, \overline{y}) c_1(x) = r(x, \overline{y}) \left(\sum_{n=-\infty}^{+\infty} A_n e^{j(2\pi n f_o x + n\phi(x, \overline{y}))} \right) \left(\sum_{m=-\infty}^{+\infty} C_n e^{j2\pi m f_o x} \right) \tag{3-29}$$

$$g_{imag}(x, \overline{y}) = a(x, \overline{y}) c_2(x) = r(x, \overline{y}) \left(\sum_{n=-\infty}^{+\infty} A_n e^{j(2\pi n f_o x + n\phi(x, \overline{y}))} \right) \left(\sum_{m=-\infty}^{+\infty} \overline{C}_n e^{j2\pi m f_o x} \right) \tag{3-30}$$

If the mean value of c_1(x) and c_2(x) is zero, the low-frequency components of g_{real} and g_{imag}, which are denoted by $g_{real-low}$ and $g_{imag-low}$, can be generated from the products of the harmonics having the same order and the opposite sign. From the multiplication of these sums, special terms are obtained such as $A_{-1}C_1e^{j\phi(x)}$ *and* $A_1C_{-1}e^{-j\phi(x)}$, which contain only the phase information of $\phi(x)$ with no fundamental frequency f_o or multiples of the fundamental frequency nf_o component.

$$\begin{aligned} g_{real-low}(x,\bar{y}) &= r(x,\bar{y})(\ldots + A_{-1}C_1e^{j\phi(x)} + A_1C_{-1}e^{-j\phi(x)} + \ldots \\ &\quad A_1C_0e^{j(2\pi f_o x+\phi(x))} + A_1C_1e^{j(4\pi f_o x+\phi(x))} + \ldots) \qquad (3\text{-}31) \\ &= r(x,\bar{y})\left(\ldots + A_1^{*}C_1e^{j\phi(x)} + A_1C_{-1}^{*}e^{-j\phi(x)} + \ldots\right) \\ &= r(x,\bar{y})\sum_{n=-\infty}^{+\infty}\left(A_n^{*}C_ne^{j\phi(x)} + A_nC_n^{*}e^{-j\phi(x)}\right) \end{aligned}$$

$$g_{real-low}(x,\bar{y}) = r(x,\bar{y})\sum_{n=-\infty}^{+\infty}|A_n||C_n|\left(e^{\beta_n+j\phi(x)-\gamma_n} + e^{-(\beta_n+j\phi(x)-\gamma_n)}\right) \qquad (3\text{-}32)$$

where

β_n is the angle of the complex coefficient of A_n
γ_n is the angle of the complex coefficient of C_n

Using Euler's rule, equation (3-32) can be simplified further,

$$e^{jn\alpha} = \cos(n\alpha) + j\sin(n\alpha) \qquad (3\text{-}33)$$

$$e^{-jn\alpha} = \cos(n\alpha) - j\sin(n\alpha) \qquad (3\text{-}34)$$

By adding equation (3-33) and (3-34),

$$\left(e^{jn\alpha} + e^{-jn\alpha}\right) = 2\cos(n\alpha) \qquad (3\text{-}35)$$

By subtracting equation (3-33) and (3-34)

$$\left(e^{jn\alpha} - e^{-jn\alpha}\right) = 2j\sin(n\alpha) \qquad (3\text{-}36)$$

Hence, equation (3-32) can be rewritten in terms of its angle as follows,

$$g_{real-low}(x,\bar{y}) = 2r(x,\bar{y})\sum_{n=-\infty}^{+\infty}|A_n||C_n|\cos\left(\beta_n + n\phi(x) - \gamma_n\right) \qquad (3\text{-}37)$$

where

β_n is the angle of the complex coefficient of A_n

γ_n is the angle of the complex coefficient of C_n

The imaginary part, g_{imag} yields the same kind of result but with the sine angle,

$$g_{imag-low}(x,\bar{y}) = -2jr(x,\bar{y})\sum_{n=-\infty}^{+\infty}|A_n||C_n|\sin(\beta_n + n\phi(x) - \gamma_n) \tag{3-38}$$

In general, the only frequency of interest is the fundamental harmonic since most of the information about the phase deviation is contained in this frequency centred at f_o. Hence,

$$g_{1real}(x,\bar{y}) \approx 2r(x,\bar{y})|A_1||C_1|\cos(\beta_1 + \phi(x) - \gamma_1) \tag{3-39}$$

$$g_{1imag}(x,\bar{y}) \approx -2jr(x,\bar{y})|A_1||C_1|\sin(\beta_1 + \phi(x) - \gamma_1) \tag{3-40}$$

Thus, the angle of the combined demodulated image row containing the phase information is given as:

$$\begin{aligned} H_1(x,\bar{y}) &= g_{1real}(x,\bar{y}) - g_{1imag}(x,\bar{y}) \\ &= 2r(x,\bar{y})|A_1||C_1|\cos(\beta_1 + \phi(x) - \gamma_1) - \left(-2jr(x,\bar{y})|A_1||C_1|\sin(\beta_1 + \phi(x) - \gamma_1)\right) \\ &= 2r(x,\bar{y})|A_1||C_1|e^{j(\beta_1 + \phi(x) - \gamma_1)} \end{aligned} \tag{3-41}$$

The same demodulation operations are performed on the image of the undistorted grating pattern, or the chosen reference row as given by equation (2-16),

$$g_o(x,y) = \sum_{n=-\infty}^{+\infty} A_o e^{j(2\pi n f_o x + n\phi_o(x))} \tag{2-16}$$

The demodulated reference image becomes,

$$H_o(x,\bar{y}) = 2r(x,\bar{y})|A_1||C_1|e^{j(\beta_1 + \phi_o(x) - \gamma_1)} \tag{3-42}$$

After the phase components have been demodulated by the two square wave functions, the next step is the extraction of the phase information which is embedded in the low frequency spectrum. The main task is to reject and eliminate the unwanted portion of the spectra generated during the demodulation process. Comb filters are useful for the elimination of specific harmonics of the grating frequency; this is particularly effective since the unwanted spectral components are centred at these harmonics.

A comb filter [51] is a recursive filter that has a series of notches in its frequency response with the spacing of all the notches at multiples of the frequency of the lowest notch - they are all harmonically related. It takes its name from the shape of its magnitude response, which, with evenly spaced zeros, resembles a comb. Comb filters are useful for passing or eliminating specific frequencies and their harmonics. They have the disadvantage that there is not, in general, a large attenuation in the stopband. A sum comb filter is defined by

$$y_k = x_k + g x_{k-N} \tag{3-43}$$

The filter has ***N*** poles at the origin and ***N*** zeros on the unit circle at points

$$z = e^{j(2l+1)\pi / N} \tag{3-44}$$

where

$l = 0, 1 \ldots N - 1$

and the frequencies of the peaks in the magnitude response are calculated from

$$f_k = \frac{2l+1}{2N} f_s \tag{3-45}$$

where

$l = 0, 1 \ldots (N - 1)$

f_s is the sampling frequency

The transfer function of the filter is given by

$$H_{trans}(z) = \frac{z^N + 1}{z^N} \tag{3-46}$$

The frequency response is

$$H(jwT) = 2e^{(-j(N\omega T/2))} \cos(N\omega T/2) \tag{3-47}$$

The flow diagram for a sum comb filter is shown below.

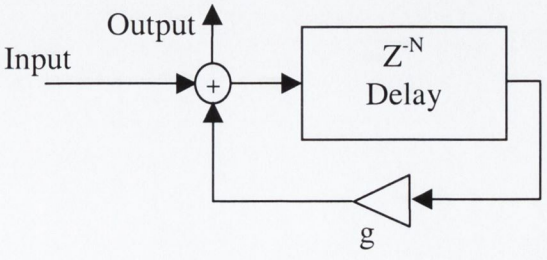

Fig.3.4: Flow diagram for a simple sum comb filter

In most real images, reflectivity is non-uniform and low frequency spectrum has relevant lateral bands that cannot be removed by mean value subtraction. Thus, a more complex comb filter must be designed to eliminate these harmonics. The modified comb filter is given by

$$y_k = x_k + x_{k-N} + x_{k-2N} + \ldots + x_{k-(r-1)N} \tag{3-48}$$

where

r is the number of taps of the filter, it determines the attenuation in the stopbands

The modified comb filter of the transfer function then becomes,

$$H_{trans}(z) = \sum_{i=1}^{r-1} \frac{1 - z^{-Nr}}{1 - z^{-N}}$$

$$\Rightarrow \qquad H_{trans}(z) = \frac{z^{Nr} - 1}{z^{N(r-1)}(z^{N} - 1)} \tag{3-49}$$

The filter has Nr zeros on the unit circles and Nr poles. There are N(r-1) poles at the origin and N poles on the unit circle where they cancel N of the zeros. The zeros are located at,

$$z_m = e^{j(2m\pi / Nr)} \tag{3-50}$$

and the frequencies where the zeros occur are given by,

$$f_m = \frac{m}{Nr} f_s \tag{3-51}$$

where

$m = 0,1\ldots(Nr-1)$

f_m is the frequency at which the zero occurs

f_s is the sampling frequency

and the cancelling poles are located at,

$$z_k = e^{j(2k\pi / N)} \tag{3-52}$$

$$f_k = \frac{k}{N} f_s \tag{3-53}$$

where

$k = 0,1\ldots(N-1)$

f_k is the frequency at which the pole occurs

To process a 16-fringe image the modified comb filter will be designed by the equation shown below

$$y_k = x_k + x_{k-2} + x_{k-4} + x_{k-6} + x_{k-8} + x_{k-10} + x_{k-12} + x_{k-14} \tag{3-54}$$

This is like a cascade of three simple sum comb filters with *N=2, N=4 and N=8.*

And the modified comb filter for a 32 fringe per line image can be processed by

$$y_k = x_k + x_{k-2} + x_{k-4} + x_{k-6} \tag{3-55}$$

which is like a cascade of two comb filters with *N=2* and *N=4.*

The flow diagram for a modified comb filter is shown below.

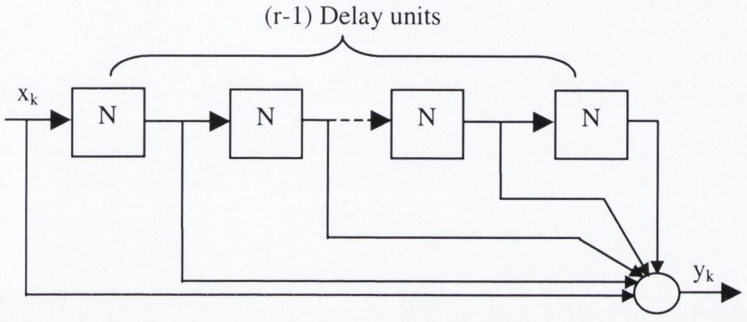

Fig.3.5: Flow chart of a modified comb filter with (r-1)N unit delays

Table 3.1 gives the frequency harmonics elimination by the delay of the comb filter for an image with a fringe frequency of *16* vertical fringes/image.

Delay (*N*) of comb filters	Frequency Elimination by particular delay of the comb filters							
	f_o	$2f_o$	$3f_o$	$4f_o$	$5f_o$	$6f_o$	$7f_o$	$8f_o$
	16	32	48	64	80	96	112	128
N = 2				*				
N = 4		*				*		
N = 8	*		*		*		*	

Table 3.1: Comb filters delay Frequency Elimination Table

Once the comb filters have removed the main noise components, a moving averager can be used to extract the remaining low frequency phase information of the signal. A moving averager requires an addition and a subtraction per point. It involves averaging the sequence of length *N* in successive sub-sequences of length *m*, $m < N$, $m = 2r + 1$, $r = 1, 2, 3, \ldots$.

To determine the phase deviation $\Delta\phi(x, \bar{y})$, the demodulated reference image $H_o(x, \bar{y})$ and the demodulated fundamental harmonic image row $H_1(x, \bar{y})$ are multiplied together in order to cancel the original and first harmonic phase components, as was also done in FTP and SDP. This multiplication procedure also has the effect of cancelling any errors caused by optical axes misalignments; this is

explained in detail in Section 3.3. Using the arctangent function, the desired phase deviation is then obtained by multiplying the complex conjugate of equation (3-42) and the respective part of equation (3-41),

$$\Delta\phi(x,y) = tan^{-1} \frac{H_{1imag}(x,\bar{y}) * H_{oimag}{}^{*}(x,\bar{y})}{H_{1real}(x,\bar{y}) * H_{oreal}{}^{*}(x,\bar{y})} \tag{3-56}$$

Flow charts of the three profilometries are shown at the end of this Chapter.

3.3 Misalignment of Camera and Grating

The three phase profilometry methods examined in the previous Section are all based on the principle of structured light. The grating pattern employed in the apparatus is assumed to be a typical grating consisting of a sequence of equally spaced horizontal or vertical dark fringes which are generated by the projection of a square wave grating known as the Rochi grating. In principle, these fringes should be perfectly parallel to the edge of the image depending on which direction the fringes are taken. A misalignment problem arises if the actual grating is not properly located in relation to the optical set-up so that the projected fringes are in an off-line position. In this Section, this problem is investigated and it is proven mathematically that by using a reference phase map allow one-dimensional techniques to cope effectively with camera-grating misalignment.

Given the rotational angle α between the grating and the image plane, with $\bar{\alpha} = \begin{bmatrix} \cos\alpha \\ -\sin\alpha \end{bmatrix}$ the unitary vector representing the direction of the grating in the image plane, equation (2-13) can be rewritten as,

$$a_{\infty}(x,y) = \sum_{n=-\infty}^{\infty} A_n e^{(j2\pi n f_O x)} \tag{2-13}$$

$$a_{\infty}(x,y) = \sum_{n=-\infty}^{\infty} A_n e^{j2\pi n f_o (x\cos\alpha - y\sin\alpha)}$$

$$=> \quad a_{\infty}(x,y) = \sum_{n=-\infty}^{\infty} A_n e^{j2\pi n \bar{\nu}\bar{r}} \tag{3-57}$$

where

$$\bar{r} = \begin{bmatrix} x \\ y \end{bmatrix}, \quad \bar{v} = \begin{bmatrix} u_o \\ v_o \end{bmatrix} = \begin{bmatrix} f_o \cos\alpha \\ -f_o \sin\alpha \end{bmatrix}$$

Hence, equation (2-16) and (2-19) in the structured light technique Section 2.4.1 can be re-written respectively as follows according to equation (3-57),

$$a_o(\bar{r}) = \sum_{n=-\infty}^{+\infty} A_n e^{j2\pi n\bar{v}(\bar{r}+\overline{s_o(r)})} \tag{3-58}$$

where

$$\left|\overline{s_o(r)}\right| = \overline{BC}$$

$$a(r) = r(x,y)\sum_{n=-\infty}^{+\infty} A_n e^{j2\pi n\bar{v}(\bar{r}+\overline{s(r)})} \tag{3-59}$$

where

$$\left|\overline{s(r)}\right| = \overline{BD}$$

Since $\bar{v}$, $\overline{s_o(r)}$ and $\overline{s(r)}$ are all oriented as $\bar{\alpha}$, from the principle of structured light technique, the previous two equations can be rewritten as

$$a_o(\bar{r}) = \sum_{n=-\infty}^{+\infty} A_n e^{j2\pi n\bar{v}\bar{r}} e^{jn\phi_o(\bar{r})} \tag{3-60}$$

where

$$\phi_o(\bar{r}) = 2\pi f_o \left|\overline{s_o}(\bar{r})\right| = 2\pi f_o \overline{BC}$$

$$a(\bar{r}) = \sum_{n=-\infty}^{+\infty} A_n e^{j2\pi n\bar{v}\bar{r}} e^{jn\phi(\bar{r})} \tag{3-61}$$

where

$$\phi(\bar{r}) = 2\pi f_o \left|\overline{s}(\bar{r})\right| = 2\pi f_o \overline{BD}$$

By substituting $\bar{r} = \begin{bmatrix} x \\ y \end{bmatrix}$, equation (3-61) can be expanded into its one-dimensional case for the selected image row $y = \bar{y}$, where the projection is finite and the object's height is greater than zero,

$$\begin{aligned} a(x,\bar{y}) &= \sum_{n=-\infty}^{+\infty} A_n e^{j2\pi n\bar{v}(x+y)} e^{jn\phi(x,\bar{y})} \\ &= \sum_{n=-\infty}^{+\infty} A_n e^{j2\pi n(u_o x + v_o \bar{y})} e^{jn\phi(x,\bar{y})} \\ &= \sum_{n=-\infty}^{+\infty} q_n(x,\bar{y}) e^{j2\pi n u_o x} \end{aligned} \tag{3-62}$$

where

$$q_n(x,\bar{y}) = A_n e^{j2\pi n v_o \bar{y}} e^{jn\phi(x,\bar{y})}$$

Equation (3-62) can then use any of the three profilometry methods discussed to extract the fundamental harmonic centered at frequency u_o to evaluate the phase deviation,

$$q_1(x,\bar{y}) = A_1 e^{j(2\pi v_o \bar{y} + \phi(x,\bar{y}))} \tag{3-63}$$

Hence, the complex signal containing the phase deviation due to the object's height is given in equation (3-63). The true phase deviation is offset by $2\pi v_o \bar{y}$, due to the rotation angle between the image plane and the grating. However, since the amount of phase offset is also introduced in the reference image,

$$q_o(x,\bar{y}) = A_1 e^{j(2\pi v_o \bar{y} + \phi_o(x,\bar{y}))} \tag{3-64}$$

The effect of misalignment is thus automatically cancelled by the multiplication of $q_1(x,\bar{y})q_o(x,\bar{y})^*$, since the phase offset of $2\pi v_o \bar{y}$ is subtracted from the conjugate's multiplication. Thus, when employing a reference image of undistorted projected fringes, the misalignment problem is avoided, since the computation is processed by comparing each row of the inspected image with the same row in the reference image. It is worth noticing that, while employing just one reference line saves processing time and storage space, in order to avoid the misalignment problem, a two-dimensional reference image is preferable.

3.4 Phase Unwrapping Technique

The three phase profilometry techniques discussed all require the operation of arctangent to determine the phase deviation $\Delta\phi(x,\bar{y})$ from the imaginary parts of the phase over the real parts of the phase. The arctangent formula is defined over a range between $-\pi$ to $+\pi$. This results in a discontinuous phase distribution, where $\pm 2\pi$ jumps occur when the phase deviation exceeds a certain value, (the approximate value is the relative height of the solder paste which is equivalent to one fringe pitch) and is then

wrapped into the range of the arctangent operation. In fact, the phase deviation should actually be written as

$$\Delta\phi(x,\bar{y}) = \tan^{-1}\frac{imag(H(x,\bar{y}))}{real(H(x,\bar{y}))} + m(x,y)2\pi \qquad (3\text{-}65)$$

where

$m(x,y)$ is unknown

An unwrapping technique [52] can correct the discontinuities caused by wrapping. It calculates the continuous phase distribution. This technique seeks those positions where the $\pm 2\pi$ jumps occur; each pixel of each row in an image is compared with its neighbouring pixel and corrected by adding an offset of $\pm 2\pi$ to the successive pixel points of the wrapped phase. Figure 3.6 shows the wrapped and unwrapped phase of a typical signal. Phase unwrapping is sensitive to noise. If the discontinuities are not properly detected due to noise, errors can propagate through the unwrapping of the dataset. There is no general solution to the unwrapping problem; the specific method depends on the actual details of the problem. Further details can be found in the reference paper [31,52] by *M.Takeda, H.Ina* and *S.Kobayashi.*

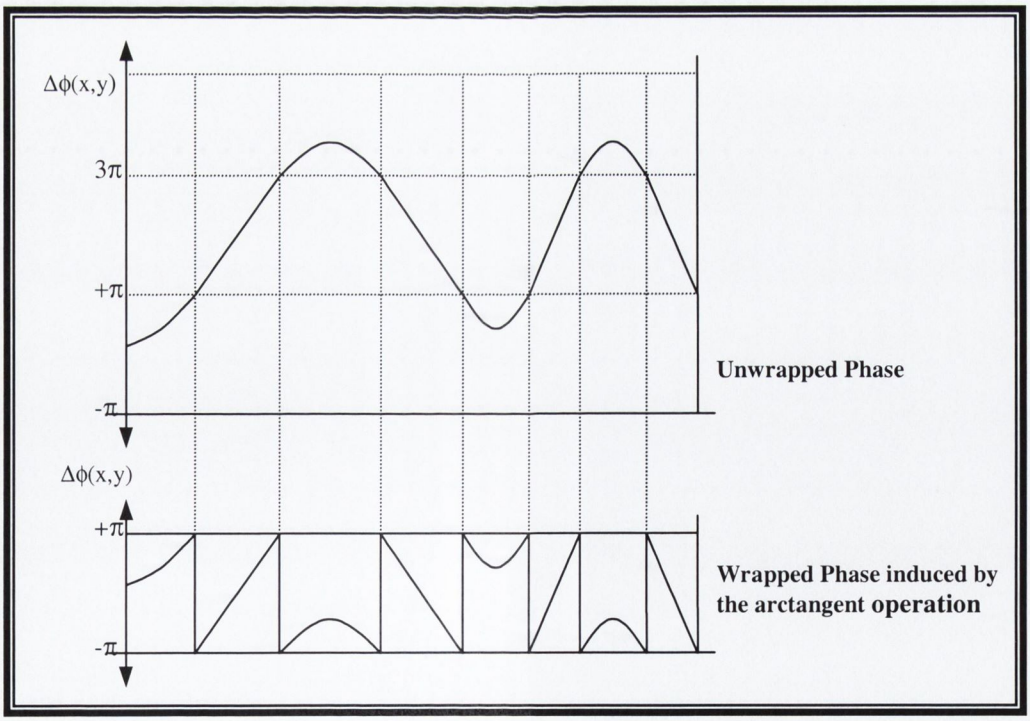

Figure 3.6: A diagram showing unwrapped-wrapped Phase

3.5 Conclusions

The underlying theories of the three phase profilometry techniques and their corresponding filters required to extract the information from the signal in the algorithm have been fully described in this chapter. The misalignment problem associated with the camera and grating set-up due to the structured light pattern was overcame by a 2D reference image, which was discovered and has been proved mathematically in Section 3.3. The phase unwrapping technique induced by the arctangent operation was also explained. The results from the implementations of the three phase profilometries and the factors associate with the accuracy and the overall effectiveness of these phase profilometry including phase unwrapping will be discussed in the next chapter.

Profilometry Flowcharts

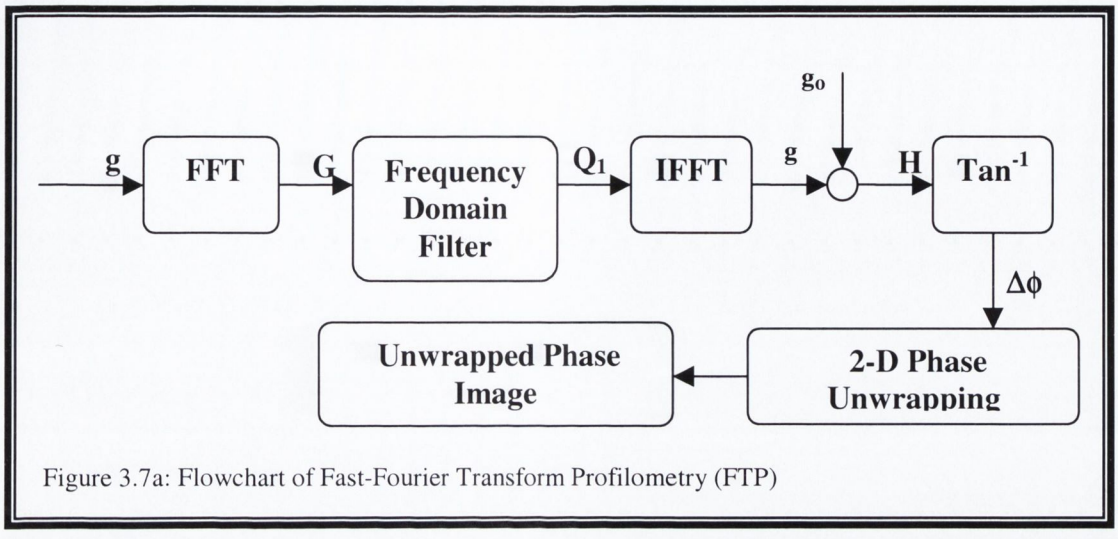

Figure 3.7a: Flowchart of Fast-Fourier Transform Profilometry (FTP)

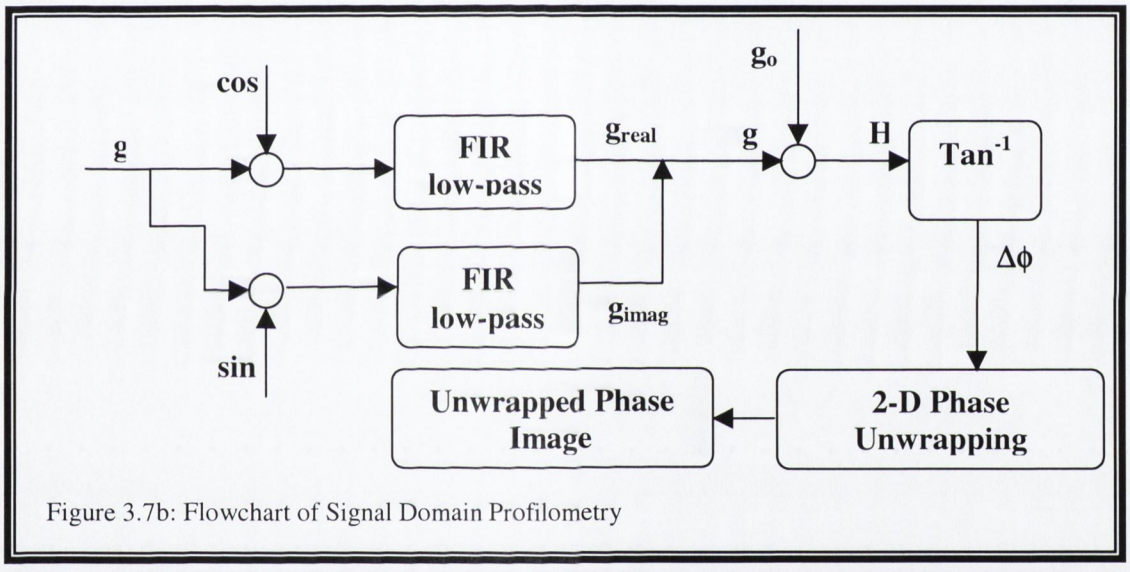

Figure 3.7b: Flowchart of Signal Domain Profilometry

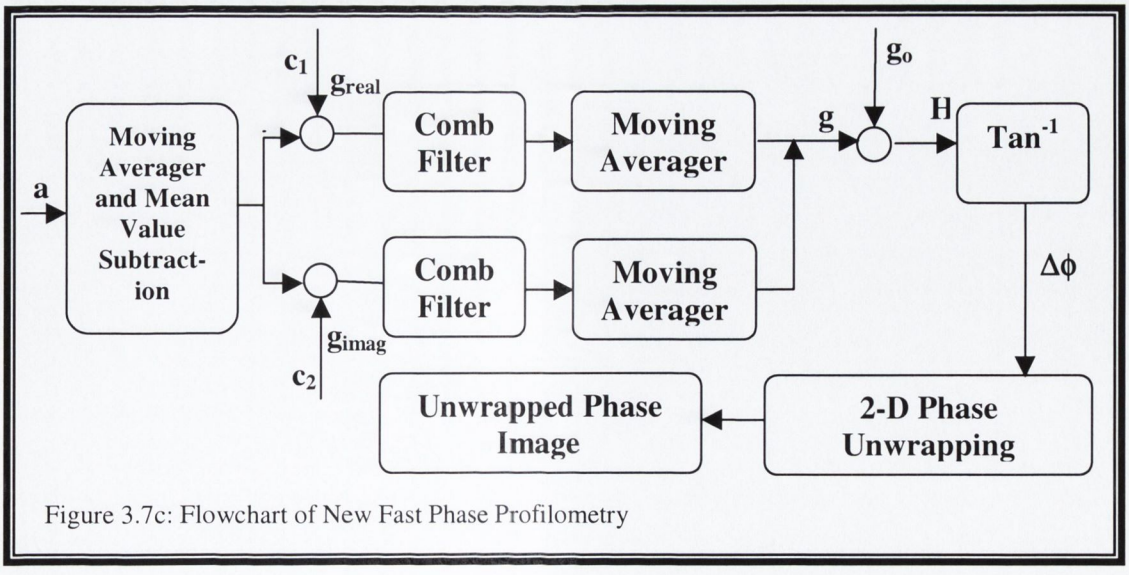

Figure 3.7c: Flowchart of New Fast Phase Profilometry

Chapter 4

Implementation of Phase Profilometry

4.1 Introduction

This Chapter illustrates the effectiveness of the phase profilometries for the application of solder paste inspection discussed in Chapter 3. For simplicity, all the implementations are shown in the frequency domain. In evaluating the results, one should note that PCB inspection systems strongly rely on the CAD layout with accurate knowledge of pad positions being available. Due to the unavailability of suitable high-accuracy metrology equipment, the height measures of solder paste on pads to be used as references could not be acquired, and thus, the assessment of the accuracy in the reconstruction of the 3D shape of solder paste can only be done on an approximate basis. However, since the analysis is aimed at comparing different phase extraction techniques, in such a context comparisons can be addressed from errors using synthetic images associated with these techniques. Real images captured by the structured light technique as described in Section 2.3 are used to demonstrate the step by step computations for both the Fourier Transform Profilometry (FTP) and New Fast Phase Profilometry (NFP) to give a more comprehensive and practical perspective on the results. But synthetic images produced by computer programs are used to assess the accuracy of each profilometry. The hardware specification can be found in Appendix A. The computations for Signal Domain Profilometry (SDP) are not shown since all the steps before the FIR filtering operation are similar to FTP. However, the FIR design and the results of the filtering process using low and high grating frequencies for SDP will be shown and discussed in detail. And in Section 4.4.3, the adaptiveness of each phase extraction techniques to different grating frequencies is addressed. Lastly, a complete comparative discussion of each profilometry is made.

4.2 Experimental Set-up for Phase Profilometry

An optical apparatus based on the crossed-optical-axes geometry as described in Section 2.4.1 was set-up to analyse phase profilometry techniques on a set of PCB samples provided by Motorola. A projector which contains a (*150W*) fibre-optic light source, a collimating lens, a Ronchi-type grating and an enlarger lens were employed for fringe acquisition. The fibre-optic light source is illuminated at an angle relative to the plane of the inspected PCB samples, and this is followed by the collimating lens, which is arranged on the same optical path to direct the light source as a parallel projection. Gratings of *8 lines/mm*, illuminated by the parallel projection rays, produce well-defined fringe patterns of constant pitch onto the surface of the inspected solder paste. The enlarger lens allows the fringe pattern to be properly focused onto the object's surface. The image pattern is then viewed by a CCD camera equipped with a telecentric lens.

There are several important factors, which must be considered in order to obtain sharp fringe images:

1. The telecentric lens of the CCD camera is used to ensure parallel projection occurs in the imaging process, thus, maintaining a linear relationship between the phase and the height.
2. The projector set-up establishes the grating frequency (number of fringes per line) at the object plane, this being the main parameter for determining the accuracy and the height range, thus, the image acquisition system must be carefully adjusted to obtain sharp fringe images; This implies proper distance adjustment is required between the projector elements for the object plane and regulation of the object-camera distance and camera magnification for the image plane. These two tasks are independent. The image acquisition system can be made automatic by suitable use of motors.
3. Camera adjustment at the image plane affects the field of view, and smaller field of view contains fewer fringes, hence, the number of fringes in the image at the image plane depends on the camera set-up. A small camera-object distance, (thus a small field of view) is usually preferable since it increases the light transmission from the object to the camera.

4. Fringe quality is also influenced by the grating period, coarse gratings allow a greater amount of light to be transmitted from the source onto the surface of the object. However, with finer fringe grating, a more accurate measurement of the relative height can be allowed. This is demonstrated in more detail in Section 4.4.3.

The experimental set-up is based on *8lines/mm* Rochi grating and the fringe frequency is set to either *16* or *32* per *256x256 pixels* image depends on the projector's focal length. The viewing area was approximately $36mm^2$ and the image size was *256x256* pixels.

4.3 Implementation of Phase Profilometry

Several images of the PCB board were captured for analysis. Figure 4.1 shows a typical image of solder paste deposits with *16* vertical fringes superimposed on them, the red line in the image indicated the chosen reference row. The defined black and white fringe pattern is projected at an angle onto the surface of the PCB. The captured image from the camera shows that where the area contains no solder paste, no distortion appears on the pitch of the fringes, whereas the area with solder paste demonstrates a sideways displacement that shifts at the pitch of the fringe. The approximate solder paste height range in the PCB given by Motorola is in the range of $200\mu m - 300\mu m$.

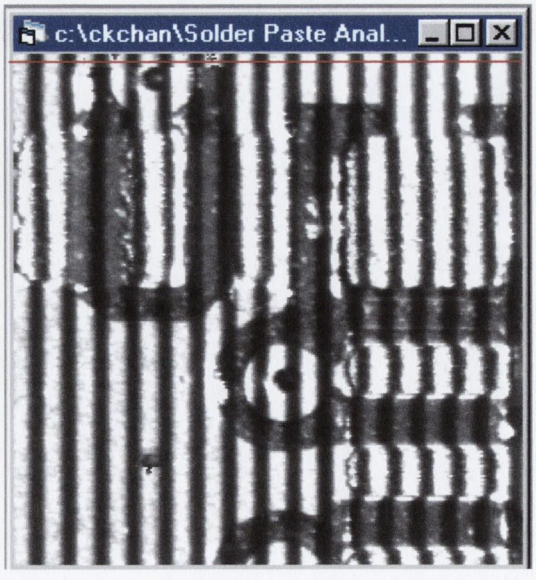

Fig 4.1: Sample Solder paste with 16 vertical fringes

The fundamental grating frequency and the discrete fundamental grating frequency are calculated as,

$$fundamental\ grating\ frequency = \frac{No.of\ fringes}{line\ size}$$

$$= \frac{16}{256} = 0.0625\ fringe / pixel$$

$$discrete\ fundamental\ grating\ frequency = \frac{line\ size}{grating\ period}$$

$$= \frac{256}{16} = 16$$

4.3.1 Fast Fourier Transform Profilometry Implementation

Figure 4.2 shows the *FFT* of the reference row, the main harmonics are clearly located at the discrete frequency ± 16, and other multiple harmonics are also shown. The reference row serves as a reference plane from which object height distribution is measured. A reference row is a row in the image which is captured on a part of the PCB where there is no solder paste, holes, or tracks or any SMD components. It is an image row of only the grating pattern on the board itself. For the purpose of this experiment, only one row was selected to use as a reference, but in practice it is desirable to use a whole reference image as it eliminates misalignments that might arise from optical set-up, as already explained in Section 3.3. When capturing a separate reference image for the corresponding solder paste fringe image, the focal length of the projection system must be set the same for both the distorted image and

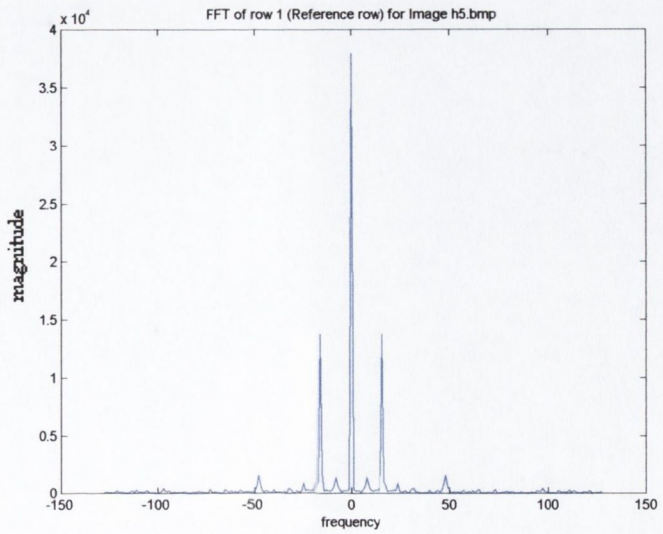

Fig 4.2: FFT spectrum of the select reference row in Fig 4.1

the reference image, otherwise the width of the grating fringes of one image might differ from that of the other, resulting in an incorrect phase shift measurement. The line size of the image is *256* pixels, and the fringe frequency is *0.0625 fringe/pixels (16 fringes)*.

Figure 4.3 shows the *FFT* of an image row which is modulated by the object's height. As shown, the modulated image row has the same signal form as the reference row, except the peaks are less distinctive and the spectrum contains more noise due to reflections and surface differences. The main peak centred at the discrete frequency $f = 0$ results from the DC component. The information of the phase deviation is centred at the discrete fundamental frequency $f_o = \pm 16$.

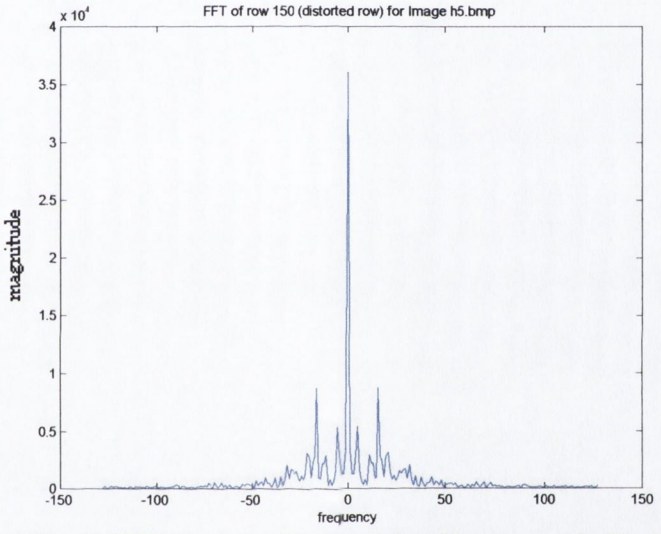

Fig 4.3: FFT spectrum of the modulated image row in Fig 4.1

The next step following the *FFT* algorithm is the filtering operation. A suitable filter must be selected in order to extract accurate phase information from the Fourier transform of the modulated grating image. In an ideal case of constant reflectivity and linear projection of a sinusoidal pattern, the bandwidth available for the phase signal would be f_o - the discrete fundamental grating frequency. However, actual implementations rely on narrow filters, which are designed to separate the modulated first harmonic from the low-frequency spectrum associated with object reflectivity and from higher modulated harmonics. The discrete fundamental grating frequency f_o has been calculated to be *16* from the acquisition of the image and with this knowledge a suitable filter centred on the discrete fundamental grating frequency can be used to extract the first harmonic of the modulated signal. Fig. 4.4 shows a one-

dimensional view of the filter. The result of the filtering operation is shown in Fig.4.5.

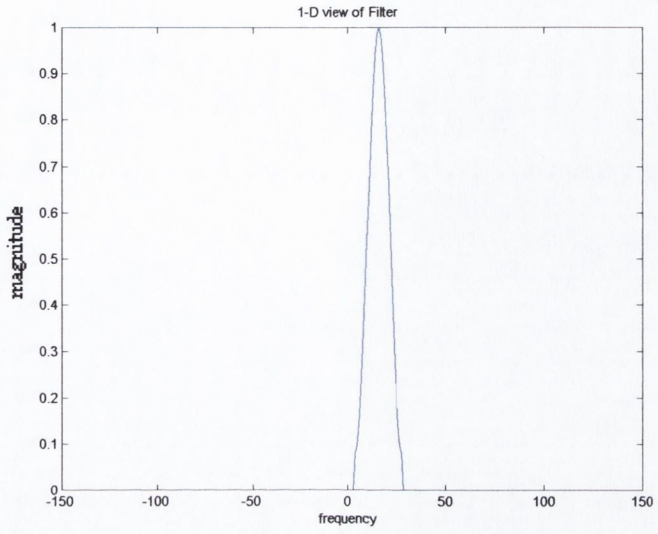

Fig 4.4: 1-D view of filter

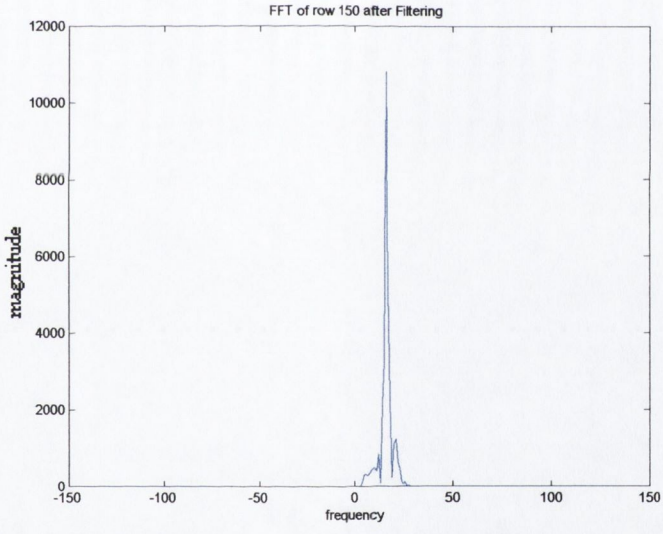

Fig 4.5: The modulated signal after filtering.

All previous procedures must also be performed on the reference signal in order to find the phase deviation of the modulated signal as developed in Section 3.2.1. Demodulation is done by multiplying the Fourier-series of $g_1(x, \bar{y})$ and the complex conjugate of $g_0(x, \bar{y})$; this cancels the original and first harmonic phase components as defined in equation (3-7), leaving only the phase deviation components $\Delta\phi(x, y)$. Figure 4.6 shows the result $H(x, \bar{y})$ containing only the phase deviation information.

The inverse Fourier Transform is then applied to the resulting signal containing the phase deviation. The *IFFT* can be applied to the signal and the complex conjugate of the reference signal separately before the multiplication or alternatively, the *IFFT* can be performed after the multiplication of the conjugate reference signal and the modulated signal; both operations yield the same result.

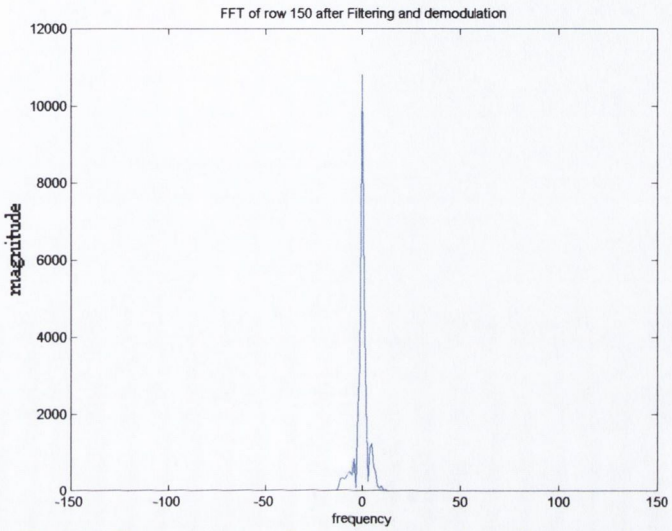

Fig 4.6: The extraction of phase information after demodulation

The arctangent and phase unwrapping operation are then performed on each row. Figure 4.7 shows the resulting phase deviation of the demodulated image in 3-dimensional view. The shapes of the solder paste pads correspond to the original image as shown in Figure 4.1. Note that there is a blob of area which is not part of the paste, this is due to a hole in the PCB. This ambiguity could be overcome with the

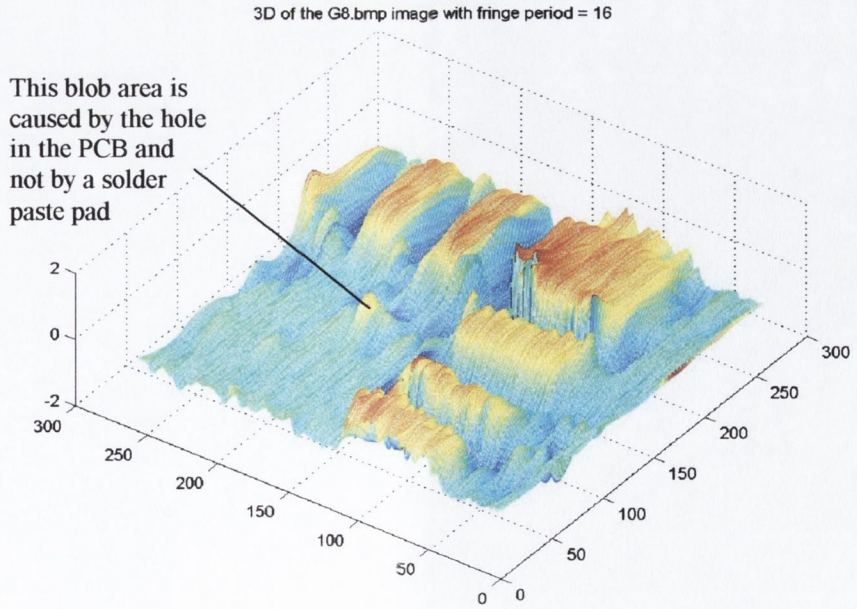

Fig 4.7: The 3D view showing the phase deviation of the PCB image in Fig 4.1

knowledge of pad positions from the PCB CAD layout, so that only the image data of the pad areas are examined in conjunction with the image of undisturbed fringes. This is a standard procedure in all AOI systems for electronics manufacturing. The 3D inspection is done before the solder paste reflowing stage when the paste is still dull and the reflectance is low, however, some reflectance from the solder paste is still unavoidable when white light is projected directly on top of the PCB. A suitable despeckle filter may be applied to the image prior to the phase profilometry procedure to remove unwanted noises. For completeness, an implementation of an image with a grating frequency of *32* is shown in Appendix B.1.

4.3.2 New Fast Phase Profilometry (NFP) Implementation

The New Fast Phase Profilometry algorithm described in Section 3.2.3 is applied using the same solder paste image used in the previous section and again a fringe frequency of *0.0625 fringe/pixels (16 fringes image)* is employed. Figure 4.8 shows the *FFT* of an image row. To aid comprehensible explanations, each step is shown explicitly in the frequency domain even though the actual profilometry is performed in the signal domain.

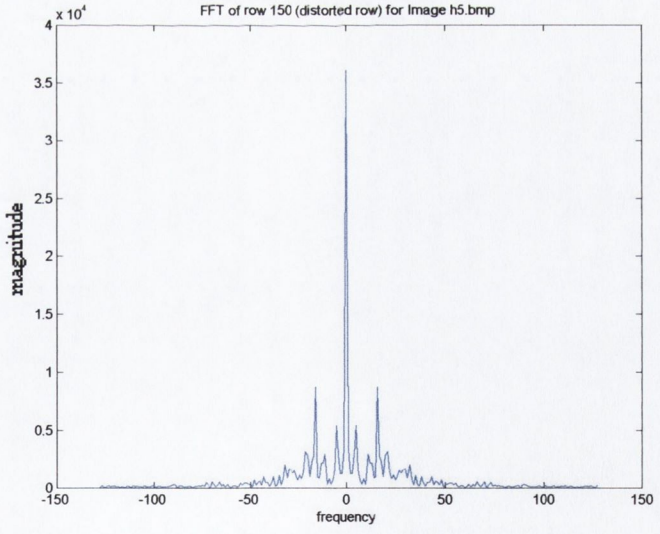

Fig 4.8: FFT spectrum of the modulated image row in Fig 4.1

Mean value subtraction is applied to eliminate the DC component at $f = 0$. Figure 4.9 shows the *FFT* spectrum after the mean-value subtraction, note the DC component has been reduced but not completely eliminated due to non-uniform reflectivity in the image as described in Section 3.2.3. Since there are no major higher harmonics

spectra in the image signal spectrum, no moving averager is applied to the image prior to the multiplications by the square waves.

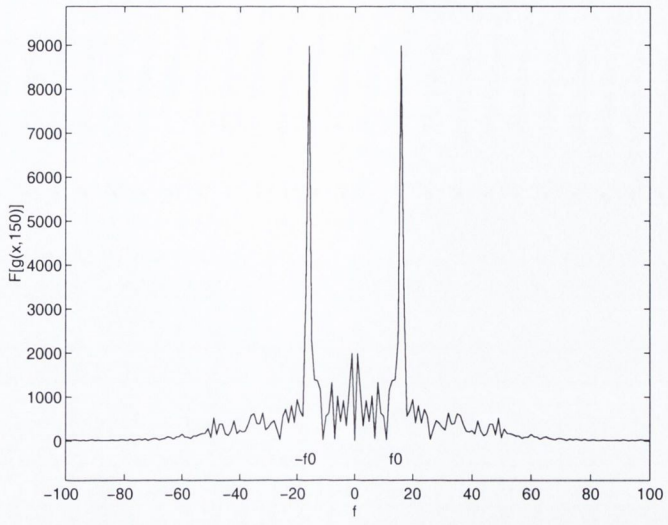

Fig 4.9: FFT of the image row after Mean Value Subtraction

The next step shown in the NFP flowchart on page 56 is the demodulation process. By multiplying the signal by odd and even square waves, both having the same fundamental frequency as the grating, the real and imaginary parts of the image signal can be extracted. In fact, by proper modification of pixels' sign, the demodulation process can be done without executing any multiplication. Thus, computational effort can be reduced dramatically. The whole frequency band is shifted by f_o, so the first harmonic, which contains the information of the phase deviation, is now moved to the D.C. point. Figure 4.10 shows the *FFT* spectrum of a row of the image after the demodulation process. Unfortunately, the demodulation

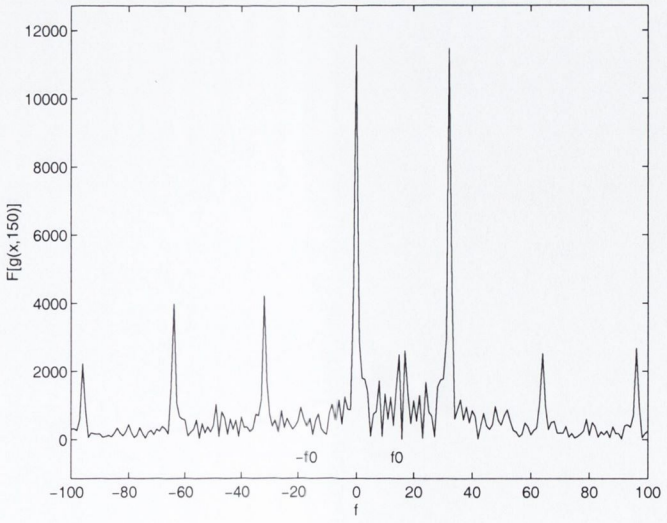

Fig 4.10: FFT of the image signal after demodulation using NFP

process with square waves generates unwanted components at certain harmonic frequencies, with suitable comb filters, these unwanted harmonics can be eliminated.

Uniform reflectivity can be assumed when dealing with synthetic images and a sum comb filter with $N=2$ is all that is required to eliminate the main harmonics of a *32* fringe high grating frequency. For a lower grating frequency synthetic image with a *16* fringe frequency, two sum comb filters with $N=2$ and $N=4$ are easily used to eliminate the harmonics at $\pm 4f_o$, $\pm 2f_o$ and $\pm 6f_o$ respectively. However, in the case of actual images, the reflectivity is significantly non-uniform and the low frequency spectrum has relevant lateral bands that cannot be removed by mean value subtraction as shown in Figure 4.9. This would introduce errors with every phase extraction technique, since the low frequency spectrum may overlap with the spectral components of interest. Effective pre-elaboration procedures, based on the acquisition and averaging of several images taken under different lighting conditions can be used to obtain normalised images in which the reflectivity function can be considered almost uniform. Some details on such normalisation techniques can be found in Appendix C and references [59,60,61]. However, normalisation of images is not suitable for on-line inspection applications that are characterised by tight speed constraints since it takes a few seconds to complete and would slow the entire production process. With Fourier Transform Profilometry, the potential overlap between the low-frequency spectrum due to reflectivity and the fundamental harmonic spectrum at f_o can be readily avoided by reducing the size of the frequency domain filter. But for the New Fast Phase Profilometry, the simple mean value subtraction which is applied before the demodulation process does not provide effective attenuation of the spectra centred at odd harmonics as shown in Figure 4.9. In order to correctly extract the low-frequency spectrum of the image, a more complex comb filter must be designed for the image shown in Figure 4.1 which has a discrete central frequency $f_o = 16$. Recall that the odd harmonics are generated by the multiplication of the low-frequency spectrum of the image with the (odd) harmonics of the square wave, and the even harmonics are due to the primary spectral components at f_o, $-f_o$. Thus, by designing a slightly more complex comb filter with the addition of one sum comb filter with $N=8$ to the original two comb filters with $N=2$ and $N=4$ used for a synthetic image of *16* fringe grating frequency, the non-

uniform reflectivity can be corrected and the odd harmonics are eliminated completely. The general formula for a simple sum comb filter is given by,

$$y_k = x_k + x_{k-N}$$

With delay $N = 2$ the harmonics at $\pm 4f_o$ is suppressed

$$y_k = x_k + x_{k-2} \tag{4-1}$$

Figure 4.11 shows the Fourier transform of the image row after suppressing the spectral harmonics at $\pm 4f_o$ with a sum comb filter of $N=2$.

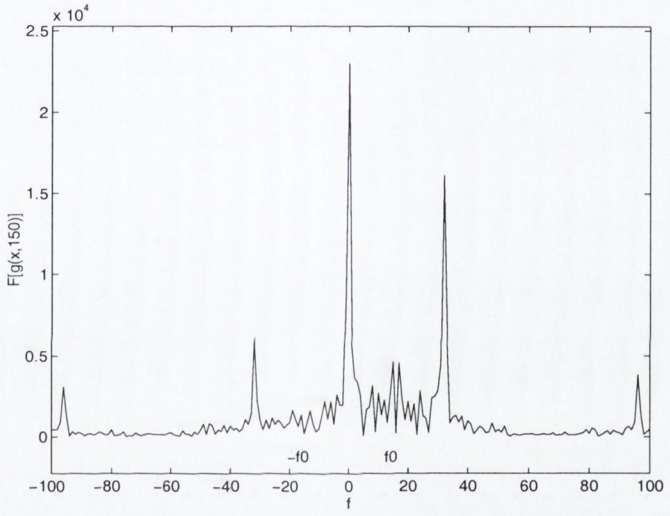

Fig 4.11: FFT of the image signal after comb filtering with delay $N=2$

With delay $N = 4$, the harmonics at $\pm 2f_o$ and $\pm 6f_o$ are greatly suppressed. Figure 4.12 shows the Fourier transform of the image row after suppressing the spectral harmonics at $\pm 2f_o$ and $\pm 6f_o$ using equation (4-2).

$$y_k = x_k + x_{k-4} \tag{4-2}$$

The equation of the modified comb filter can be derived from the general modified comb filter equation (3-48).

$$y_k = x_k + x_{k-N} + x_{k-2N} + \ldots + x_{k-(r-1)N}$$

The cascade of the two comb filters is shown in equation (4-3),

$$y_k = x_k + x_{k-2} + x_{k-4} + x_{k-6} \tag{4-3}$$

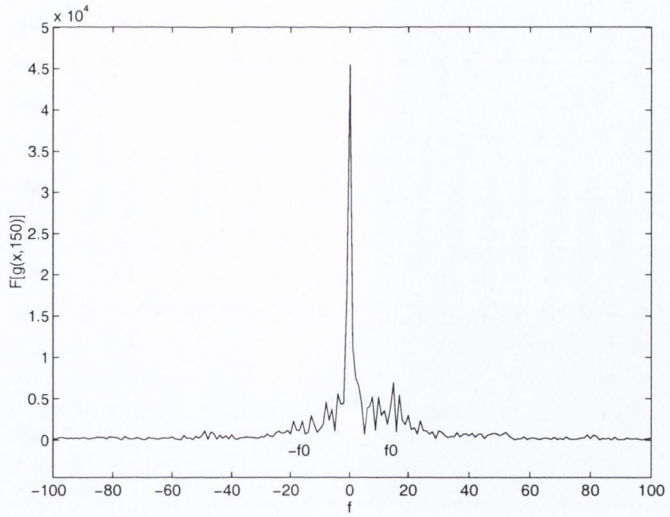

Fig 4.12: FFT of the image signal after comb filtering with delay *N=4*

With delay $N = 8$, the odd harmonics at $\pm f_o$ are finally eliminated. Figure 4.13 shows the Fourier transform of the image row after suppressing the spectral harmonics at $\pm f_o$, using equation (4-4).

$$y_k = x_k + x_{k-8} \tag{4-4}$$

This comb filter can be cascaded with the previous two comb filters generating an equation shown in equation (4-3),

$$y_k = x_k + x_{k-2} + x_{k-4} + x_{k-6} + x_{k-8} + x_{k-10} + x_{k-12} + x_{k-14} \tag{4-5}$$

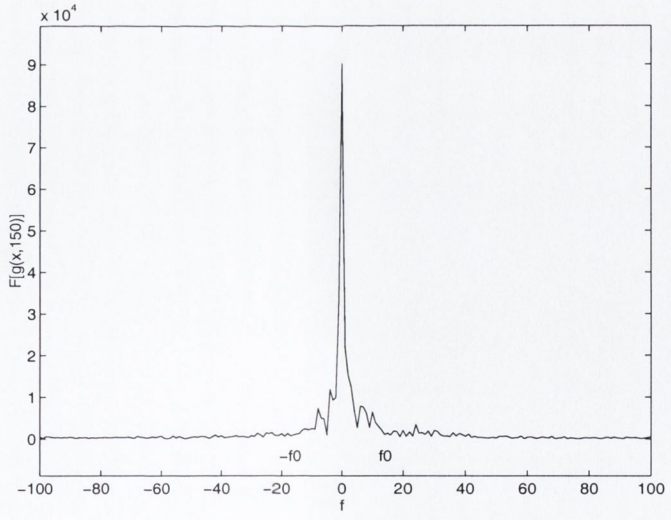

Fig 4.13: FFT of the image signal after comb filter with delay *N=8*

The frequency response of the filter is shown in Figure 4.14.

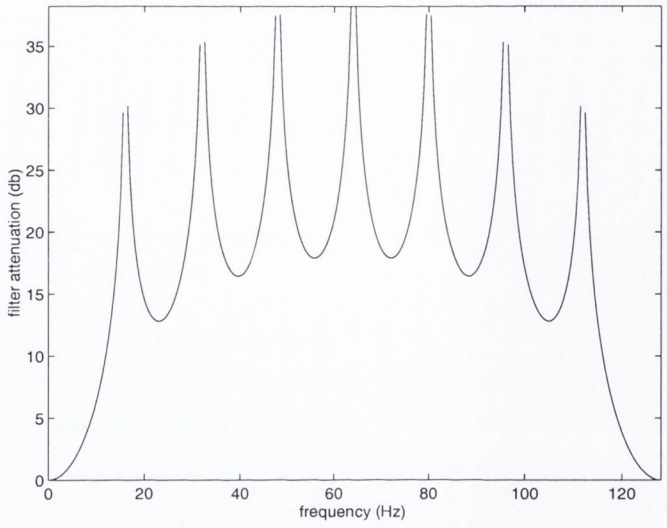

Fig 4.14: The frequency response of the modified comb filter for 16 fringe non-uniform image

Infinite attenuation is achieved in correspondence to all of the specified harmonics, with the exception of $8f_o$. A 9-point moving averager is implemented to attenuate the frequency spectrum centred at $8f_o$; this low-pass filter is sufficient to extract the remaining low frequency component. Figure 4.15 shows *FFT* spectrum of the image signal at the final stage of the NFP algorithm.

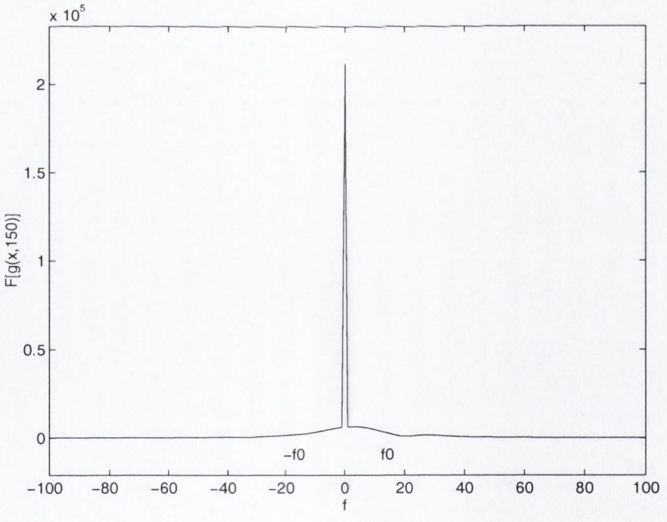

Fig 4.15: FFT of the image signal after 9points moving averager

The phase map extracted from the image in Figure 4.1 is shown in Figure 4.16, where the phase deviation is mapped into grey-levels and brighter points representing higher phase deviation (i.e. the relative height). The 3D model of the extracted phase looks similar to Figure 4.7. Notice the first 18 columns of the phase map are blank due to the 9-point moving averager.

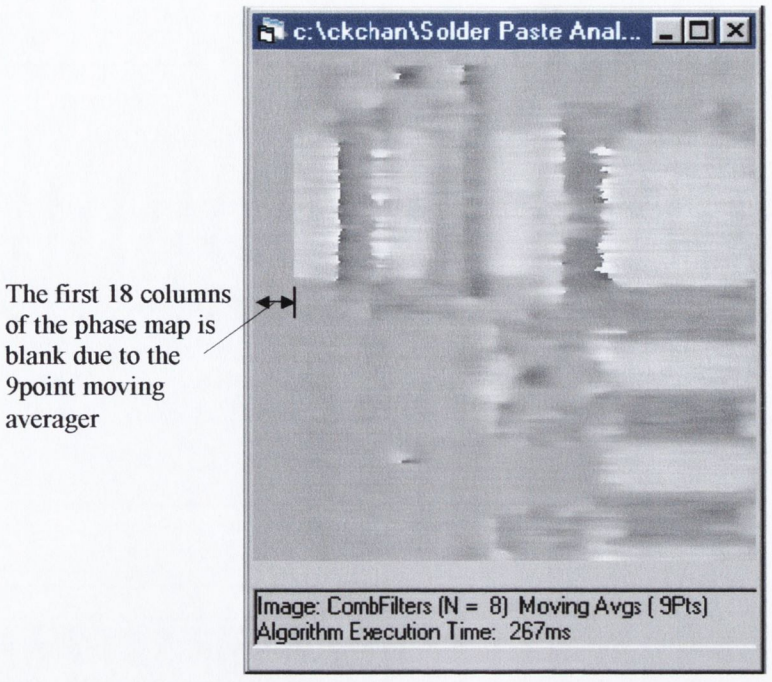

Fig 4.16: The Phase map of the inspected PCB

4.3.2.1 Choice of the Filters

Several filters are employed in New Fast Phase Profilometry. In order to choose the best filter parameters and combinations, a program was generated to investigate the effect of each individual filter by switching them on and off, and adjusting their filter length.

A synthetic fringe image, with an object in the shape of a rectangular box having *16* vertical fringes and a line size of *256* is used as a sample image shown in Figure 4.17a. Figure 4.17(b–g) show the cross profiles of the rectangular box calculated with different filter combinations. The criterion for determining the best filter combination is based on the average absolute error.

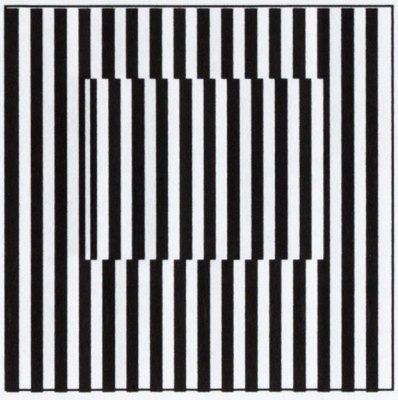

Fig. 4.17a: A synthetic fringe image with an object in the shape of a rectangular box having 16 vertical fringes

For the NFP approach, the window size of the moving averager was varied from 5 to 9 points. Versions of the algorithm with or without mean value subtraction have also been tested. The comb filters have different delays with $N = 2$, $N = 4$, $N = 8$ in order to eliminate or suppress different harmonics. Table 4.1 shows the filter combinations. From Figure 4.17b, all profiles consist of steep slope, which does not strictly correspond to the actual image profile. This is caused by the lack of information about the vertical edges of the rectangular box, which are parallel to the projected light pattern. Only edges that are perpendicular to the fringes can be detected properly, this is because stripe based structured light technique is only a one-dimensional technique as described in Section 2.4. In Section 4.6, an improved technique known as the Dual Projection structured light technique will be demonstrated; this technique compensates the slope error arising from the lack of edge information.

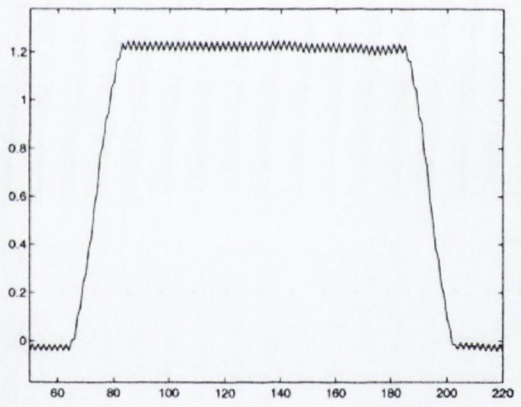

Fig 4.17b: Filters Combination 1 - C1

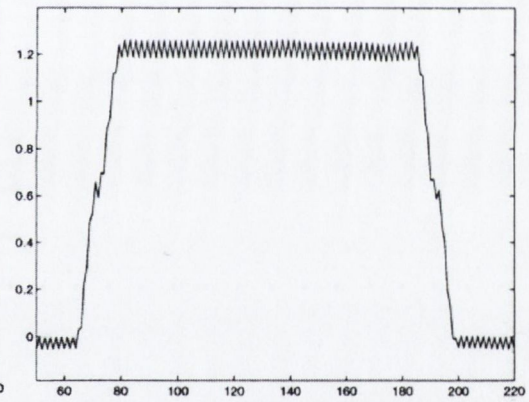

Fig 4.17c: Filters Combination 2 - C2

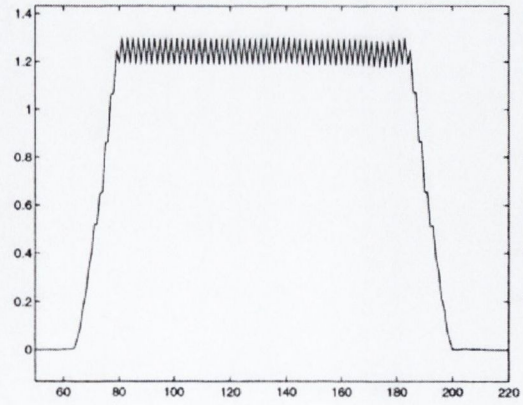

Fig 4.17d: Filters Combination 5 - C5

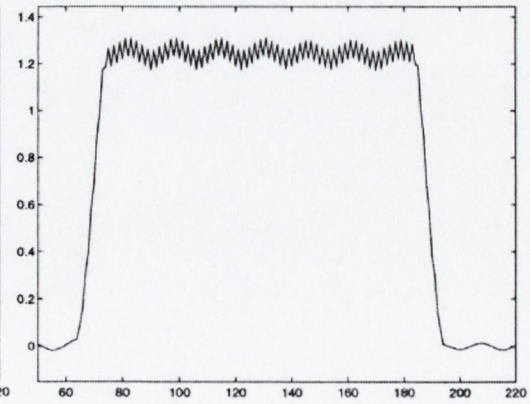

Fig 4.17e: Filters Combination 6 - C6

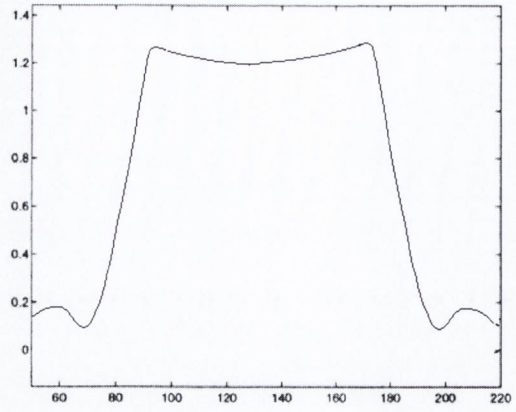

Fig 4.17f: Profile using Fourier Transfrom Profilometry

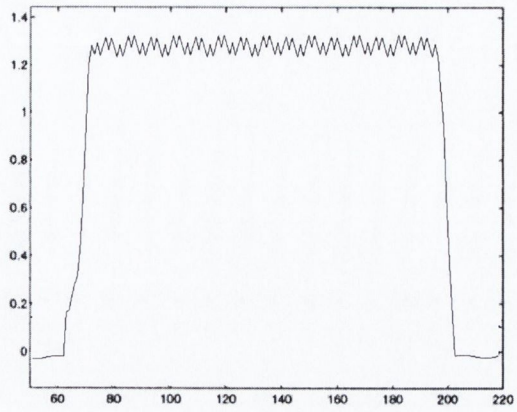

Fig 4.17g: Profile using Signal Domain Profilometry

The best filter combination with NFP for a *16* fringe image is when a mean value subtraction is applied, a modified comb filter with delays $N = 2,4,8$, and a 9-point moving averager are used to eliminate the harmonics arising from the demodulation stage. The results were found to be less accurate if the mean value subtraction is not applied.

	sqr (error)	Mean Val. Sub	AV	Comb Filter		
				N = 2	N = 4	N = 8
C1	0.0703	ON	9	ON	ON	ON
C2	0.1463	ON	5	ON	ON	ON
C3	0.5765	OFF	5	ON	ON	ON
C4	0.2898	OFF	7	ON	ON	ON
C5	0.1731	OFF	9	ON	ON	ON
C6	0.6421	ON	5	ON	ON	OFF
Fourier	0.0515	-	-	-	-	-
SDP	0.2031	-	-	-	-	-

Table 4.1: Filters Combination Table

4.4 Monitor factors associated with the grating frequency

4.4.1 Distances of Spectral components and Grating Frequency

A basic trade-off between the resolution and the range/height of the measurement is associated with the choice of the grating frequency, f_o. It was shown previously a given height variation produces an image shift would result in a phase deviation that is dependent on the grating frequency, ($\Delta\phi(x,y) = 2\pi\Delta s(x,y)f_o$). The grating

frequency also determines the bandwidth of the allowable profile variations, so that the higher the frequency, the higher the spatial resolution of the measurement. Moreover, if the grating frequency is high, the bandwidth between the main harmonic and the DC, and the other higher harmonics, is wide so the filtering operation becomes relatively easier for phase extraction. Thus, employing a higher grating frequency allows a wider separation between spectral components. This is demonstrated in Figure 4.18 (a-b) and 4.19 (a-b).

Figure 4.18 shows a *FFT* spectrum with a rather wide separation between spectral components spreading over a range of frequencies. The fringe width is *4 pixels* wide and the period of the grating is *8 pixels*. The grating frequency is therefore *256/8 pixels/fringes = 32 pixels/fringes*, hence, the main harmonic can be found at the discrete fundamental grating frequency of *32* as shown.

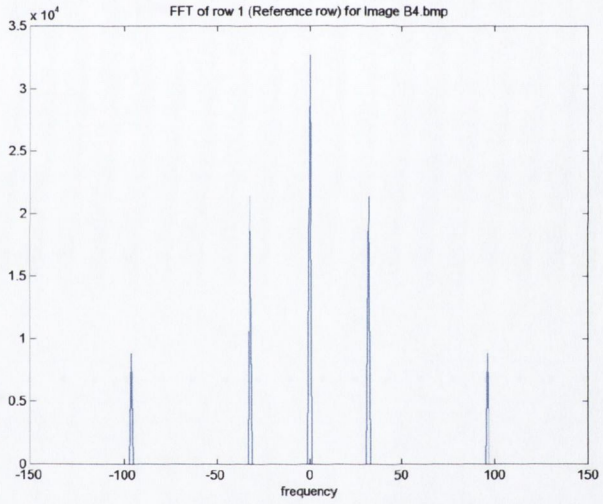

Fig.4.18a: FFT spectrum of 32 fringes grating frequency as in figure 4.18b

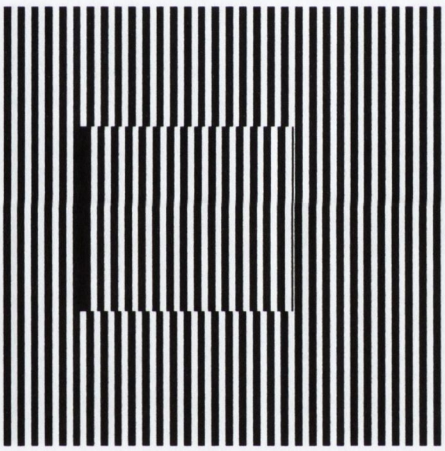

Fig 4.18b: A synthetic image with 32 fringe grating frequency

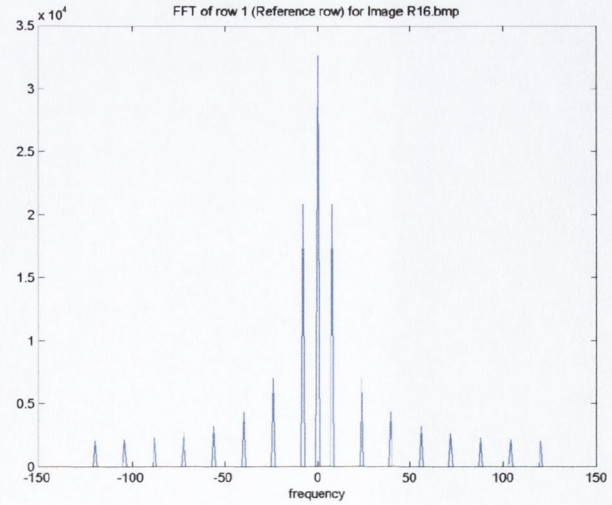

Fig.4.19a: FFT spectrum consists of a 8 fringes grating frequency as in figure 4.19b

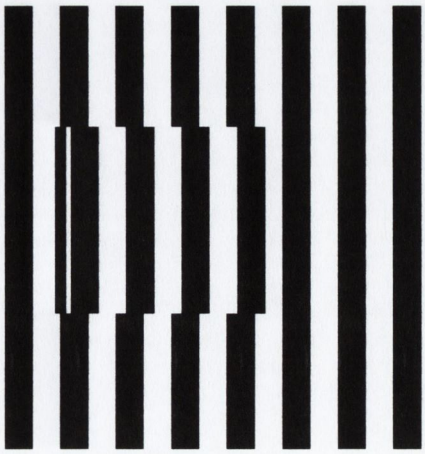

Fig 4.19b: A synthetic image with 8 fringe grating frequency

In contrast, Figure 4.19b shows a synthetic image with a rather low grating frequency *256/32 pixels/fringes = 8 pixels/fringes*. An image of such a low grating frequency generates a much narrower separation between spectral components, as explained, and this narrow separation is less suitable for filtering as it is more difficult to pinpoint the desired harmonic exactly.

For completeness, it is worth mentioning that the grating used is a binary black and white grating, which is equivalent to an image of a square waveform. And that a square wave is represented only by the odd harmonics of the fundamental grating frequency when transformed in the frequency domain. Thus, with no even harmonics of the fundamental frequency, the distance between any two consecutive frequency components is equal to twice the grating frequency - $2f_o$. Therefore, the Fourier transform of the square wave allows a more precise filtering operation of the selective frequency spectrum for phase extraction in the frequency domain.

4.4.2 Range of Measurements and Grating Frequency

As explained previously, the extraction of phase information from the modulated grating image relies on a filtering operation, which can be carried out in the Fourier or in the signal domain. The spectrum centred on the first harmonic should be separated from the low-frequency and higher harmonic components for accurate extraction of phase information. [An upper limit must be fixed on the maximum height of the object allowable for inspection as this affects the amount of overlapping at the frequency spectrum]. To define this upper limit, the mathematical representation of FFT and SDP are investigated as shown below.

4.4.2.1 Fourier Transform Profilometry

The mathematical representation in equation (2-19) defines the modulated image row due to height distribution by the object for Fourier Transform Profilometry.

$$a(x,y) = r(x,y)\sum_{n=-\infty}^{+\infty} A_n e^{j(2\pi n f_o x + n\phi(x,y))} \tag{2-19}$$

where

f_o is the fundamental frequency of the observed grating image

$\phi(x,y) = 2\pi f_o s(x,y)$ = is the phase deviation

$r(x,y)$ represents unwanted irradiance variations arising from the non-uniform light reflectivity or transmission of the object's surface

In equation (2-19) the exponential terms contain the carrier frequency and phase modulated elements. This can be use to define the local spatial frequency function as the instantaneous frequency of the n^{th} order of the spectrum component in equation (4-6).

$$f_n = \frac{1}{2\pi}\left\{\frac{\partial}{\partial x}\left[2\pi n f_o x + n\phi(x,y)\right]\right\}$$

$$= nf_o + \frac{n}{2\pi} \times \frac{\partial \phi(x,y)}{\partial x} \tag{4-6}$$

From Figure 4.20, it is clearly shown that the maximum frequency of the spectral band of interest must be smaller than the minimum frequency of the next successive harmonic spectral band, and the minimum frequency of the fundamental frequency spectral component be larger than the maximum frequency spread of the DC centred low-frequency component in order to avoid overlapping. Hence,

$$(f_1)_{\max} < (f_n)_{\min} \tag{4-7}$$

where

n =2, 3, ...

$$f_b < (f_1)_{\min} \tag{4-8}$$

where

$f_b, (f_n)_{\min}, (f_n)_{\max}$ are shown in Figure 4.20

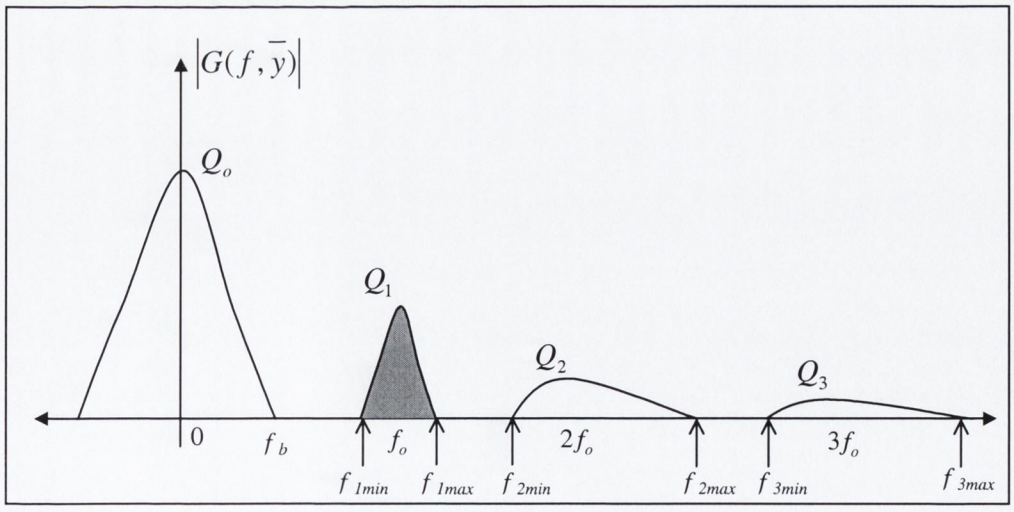

Fig. 4.20: Spatial frequency spectra of deformed grating image demonstrating the limitations of overlapping

By substituting eqn.(4-6) into eqn.(4-7), it becomes,

$$f_o + \frac{1}{2\pi} \times \left(\frac{\partial \phi}{\partial x} \right)_{\max} < n f_o + \frac{n}{2\pi} \times \left(\frac{\partial \phi}{\partial x} \right)_{\min} \tag{4-9}$$

and eqn. (4-6) into eqn. (4-8),

$$f_b < f_o + \frac{1}{2\pi} \times \left(\frac{\partial \phi}{\partial x} \right)_{\min} \tag{4-10}$$

From equation (4-9), it can be shown that if the rate of change in the phase along the direction normal to the line of the grating is small, then the bandwidth of the spectrum is narrow. Hence, if

$$\frac{\partial \phi}{\partial x} \approx 0 \tag{4-11}$$

Equation (4-9) becomes

$$f_o < n f_o \tag{4-12}$$

for n =2, 3, ...

Equation (4-11) shows that if the rate of change in the phase along the direction normal to the line of the grating is equal to zero, then the bandwidth of the spectral component at the fundamental grating frequency f_o would spread over f_o - that is it will only exist at one point. This can be seen in Figure 4.18a and 4.19a – the *FFT* of an undistorted image row in a synthetic image. It follows that if the phase $\phi(x, \bar{y})$ varies slowly compared to the grating frequency, the overlap between the $Q_n(f, \bar{y})$ terms of the spectrum is small and are separated from each other by the grating frequency $2f_o$ for a binary grating.

The above conditions can be rewritten for extra security to avoid any overlapping by changing the sign of bounded frequency. Equation (4-6) becomes

$$f_o + \frac{1}{2\pi} \times \left(\frac{\partial \phi}{\partial x} \right)_{\max} < n f_o - \frac{n}{2\pi} \times \left| \frac{\partial \phi}{\partial x} \right|_{\max} \tag{4-13}$$

and equation (4-7) becomes

$$f_b < f_o - \frac{1}{2\pi} \times \left| \frac{\partial \phi}{\partial x} \right|_{\max} \tag{4-14}$$

where

$\left|\frac{\partial\phi}{\partial x}\right|_{\max}$ denotes the maximum absolute value which is a larger value of $\left(\frac{\partial\phi}{dx}\right)_{\max}$ and $\left(\frac{\partial\phi}{dx}\right)_{\min}$.

Eqn. (4-13) and eqn. (4-14) give

$$\left|\frac{\partial\phi}{\partial x}\right|_{\max} < \left(\frac{n-1}{n+1}\right)2\pi f_o \tag{4-15}$$

$$\left|\frac{\partial\phi}{\partial x}\right|_{\max} < 2\pi\left(f_o - f_b\right) \tag{4-16}$$

There would be no overlapping between the spectral components if equations (4-15) and (4-16) are fulfilled. In general, equation (4-15) is usually satisfied since $\left(\frac{n-1}{n+1}\right)$ increases monotonically with n, for all values of n = *2,3...* . For equation (4-16), f_b is always much smaller than $f_o/2$, so the condition also holds true. By placing n =2, equation (4-15) becomes

$$\left|\frac{\partial\phi}{\partial x}\right|_{\max} < \frac{2\pi f_o}{3} \tag{4-17}$$

When discussing the maximum range of measurement, it can be assumed that $\phi(x,y)$ is much larger than $\phi_o(x)$. Thus, from the phase deviation equation in (2-21)

$$\phi(x,y) = \phi_o(x,y) + \Delta\phi(x,y) \tag{2-21}$$
$$\phi(x,y) \approx \Delta\phi(x,y)$$

And from equation (2-26) the height distribution $h(x,y)$ as a function of the phase deviation $\Delta\phi(x,y)$ can be rewritten from

$$h(x,y) = \frac{H\Delta\phi(x,y)}{\Delta\phi(x,y) - 2\pi f_o d} \tag{2-26}$$

where

$h(x,y)$ is defined positive when measured upwards from the reference plane R.
d is the distance between the two lens
H is the distance from the reference plane to the lens

To give

$$\phi(x,y) \approx \Delta\phi(x,y) \approx -\frac{2\pi f_o d}{H} \cdot h(x,y) \tag{4-18}$$

assuming that $H >> h(x,y)$. Substituting eqn. (4-17) into (4-18), equation (4-19) is finally obtained

$$\left|\frac{\partial h(x,y)}{\partial x}\right|_{\max} < \frac{1}{3} \cdot \left(\frac{H}{d}\right) \tag{4-19}$$

This condition states that the maximum range of measurement is not limited by the height distribution $h(x,y)$ but by its derivative in the direction normal to the line of the grating and the geometric setup of a measurement system. The maximum range of measurement can be extended by employing a geometry in which H/d is large in order to prevent the phase from being overmodulated.

4.4.2.2 Signal Domain Profilometry

In SDP the phase information is extracted in the signal domain by a low pass FIR filter. Similar to FTP, the desired low frequency term in any one of the demodulated signals must be separated out. The demodulation is achieved by multiplying the signal by cosine and sine terms. Below shows the mathematical representation of the modulated image row due to the object height distribution after demodulation as described in Chapter 3, Section 3.2.2.

$$g(x,y)\cos\left(\frac{2\pi x}{p}\right) = \sum_{n=0}^{+\infty} C_n(x,y)\cos\left[\frac{2\pi n x}{p} + n\phi(x,y)\right]\cos\left(\frac{2\pi x}{p}\right) \tag{4-20}$$

$$\begin{aligned} &= a_0(x,y)\cos\left(\frac{2\pi x}{p}\right) + \frac{1}{2}a_1(x,y)\cos\left[\frac{4\pi x}{p} + \phi(x,y)\right] + \frac{1}{2}a_1(x,y)\cos[\varphi(x,y)] \\ &+ \frac{1}{2}a_2(x,y)\cos\left[\frac{6\pi x}{p} + 2\phi(x,y)\right] + \frac{1}{2}a_2(x,y)\cos\left[\frac{2\pi x}{p} + 2\phi(x,y)\right] \\ &+ \frac{1}{2}a_3(x,y)\cos\left[\frac{8\pi x}{p} + 3\phi(x,y)\right] + \frac{1}{2}a_3(x,y)\cos\left[\frac{4\pi x}{p} + 3\phi(x,y)\right] + \cdots \end{aligned} \tag{4-21}$$

$$g(x,y)\sin\left(\frac{2\pi x}{p}\right) = \sum_{n=0}^{+\infty} C_n(x,y)\cos\left[\frac{2\pi n x}{p} + n\phi(x,y)\right]\sin\left(\frac{2\pi x}{p}\right) \tag{4-22}$$

$$= a_0(x,y)\sin\left(\frac{2\pi x}{p}\right) + \frac{1}{2}a_1(x,y)\sin\left[\frac{4\pi x}{p} + \phi(x,y)\right] - \frac{1}{2}a_1(x,y)\sin[\varphi(x,y)]$$
$$+ \frac{1}{2}a_2(x,y)\sin\left[\frac{6\pi x}{p} + 2\phi(x,y)\right] - \frac{1}{2}a_2(x,y)\sin\left[\frac{2\pi x}{p} + 2\phi(x,y)\right]$$
$$+ \frac{1}{2}a_3(x,y)\sin\left[\frac{8\pi x}{p} + 3\phi(x,y)\right] - \frac{1}{2}a_3(x,y)\sin\left[\frac{4\pi x}{p} + 3\phi(x,y)\right] + \cdots \qquad (4\text{-}23)$$

The $\frac{1}{2}a_1(x,y)\cos[\phi(x,y)]$ and $-\frac{1}{2}a_1(x,y)\sin[\phi(x,y)]$ are the low frequency terms which should be extracted by the FIR filter for phase information. Since $a_n(x,y)$ varies very slowly and the next successive harmonics are $\frac{1}{2}a_2(x,y)\cos\left[\frac{2\pi x}{p} + 2\phi(x,y)\right]$ and $-\frac{1}{2}a_2(x,y)\sin\left[\frac{2\pi x}{p} + 2\phi(x,y)\right]$ for the real and imaginary parts, the rate of change in phase of the low harmonic component to the next successive harmonic component is,

$$\left|\frac{\partial\phi(x,y)}{\partial x}\right|_{\max} < \frac{\partial}{\partial x}\left|\frac{2\pi x}{p} + 2\phi(x,y)\right|_{\min} \qquad (4\text{-}24)$$

Again for conservative purposes, equation (4-24) can be rewritten as,

$$\left|\frac{\partial\phi(x,y)}{\partial x}\right|_{\max} < \frac{\partial}{\partial x}\left|\frac{2\pi x}{p} - 2\phi(x,y)\right|_{\min}$$
$$\left|\frac{\partial\phi(x,y)}{\partial x}\right|_{\max} < \frac{2\pi}{p} - 2\left|\frac{\partial\phi(x,y)}{\partial x}\right|_{\max} \qquad (4\text{-}25)$$

which yields,

$$\left|\frac{\partial\phi(x,y)}{\partial x}\right|_{\max} < \frac{2\pi}{3p} \qquad (4\text{-}26)$$

Equation (4-26) illustrates that using a high frequency grating carrier is desirable so as to increase the measurement range. Again, by substituting the phase to height equation (2-26) into equation (4-26),

$$h(x,y) = \frac{H\Delta\phi(x,y)}{\Delta\phi(x,y) - 2\pi f_o d} \qquad (2\text{-}26)$$

the previous bound in eqn.(4-19) for the FTP case is found again,

$$\left|\frac{\partial h(x,y)}{\partial x}\right|_{\max} < \frac{1}{3}\cdot\left(\frac{H}{d}\right) \tag{4-27}$$

4.4.3 Resolution and Grating Frequency

The effects of various grating frequencies for each profilometry are investigated and the resolutions of the results are compared. The relationship between the grating frequency and the resolution is demonstrated using the Fourier Transform Profilometry by simulating a synthetic fringe image with an object in the shape of a rectangular box, similar to Figure 4.18b. It will be shown that high-frequency gratings allow accurate measurement of height steps, while with low-frequency gratings, large errors are detected in the transition regions. For example, if the filter cut off frequency is set to $f_o/2$, the actual spatial resolution of an N pixels phase profile is $p_o = 1/f_o$ pixels, since it can be reconstructed by sampling with period p_o and interpolating the resulting by N/p_o phase samples. The simulation results relative to the measurement by FTP of a rectangular profile (solid line) using a high-frequency (dotted line) and a low-frequency (dashed line) gratings are plotted in Figure 4.21. The line size is 256 pixels, the two grating frequencies are *0.125 pixels^{-1} (32 fringes per line)* and *0.03125 pixels^{-1} (8 fringes per line)* respectively.

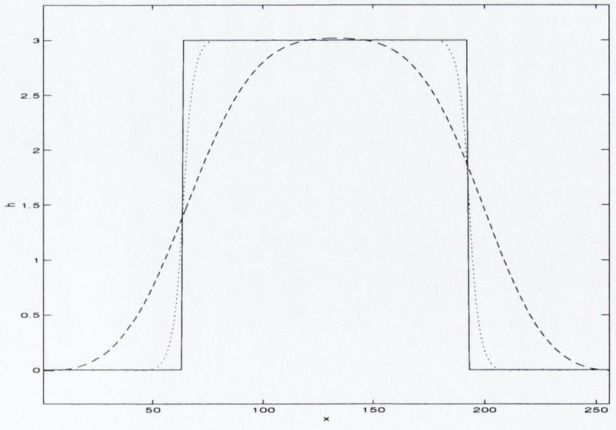

Fig 4.21: Demonstrating low and high fringe frequency of a rectangular phase profile

As mentioned already, low fringe grating frequency patterns are effective only for measuring coarse surface variations with large errors detected in the transition regions, while fine grating frequency patterns are suited to measuring fine surface details. This is only true depending on the profilometry method employed; not all profilometries are capable of low frequency grating phase extraction as in the case of Signal Domain Profilometry. Fortunately, the solder paste inspection application is more adaptable with high frequency grating. The abilities of each technique in relation to various grating frequencies will be demonstrated next.

There are a number of issues concerning the implementations of the three phase profilometry techniques. These issues include the varying grating frequency and the filter design which can greatly affect the resolution of the result. To evaluate the performance of the different techniques using various grating frequencies, a rectangular linear shift profile with a 3-pixels step is used for the simulation and the synthetic shift profile may be translated into height profile based on the actual optical configuration as shown in Chapter 2.

4.4.3.1 High Frequency Fringe Pattern ~ f_o=0.125 $pixel^{-1}$

The simulation analysis of high-frequency grating pattern is first considered. A *32* fringes per line *(f_o=0.125 fringe/pixel)* grating is used.

FTP : In the FTP algorithm a rectangular filter was initially employed as the frequency domain filter for the frequency extraction. However, the rectangular window yields significant ripple in the object and background regions. These ripples as shown in Figure 4.22 associated with the amplitude of the side lobes in the frequency response can be substantially reduced if a weighting window such as the Hanning window is used instead of the rectangular window.

The mathematical definition of a Hanning window [54,55,69,70] is shown below:

$$w[n] = 0.5 + 0.5\cos[n\pi/(m+1)] \tag{4-27}$$

where

n are values between $-m$ and $+m$, giving $2m+1$ sample points in total

The occurrence of the ripple is due to frequency domain multiplication by a window centred on the grating frequency which is equivalent to signal domain convolution with the corresponding complex unit sample response. The result with the Hanning

window is very effective as it allows almost flat reconstruction. Figure 4.22 shows the reconstruction of a rectangular phase profile using a rectangular and a hanning window. The solid line indicates the hanning window and the dash line with ripple marks the rectangular filter.

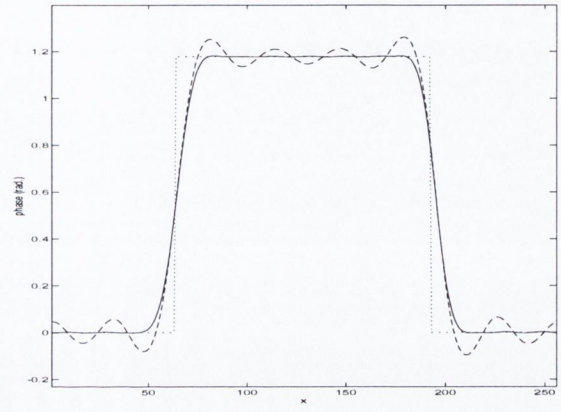

Fig 4.22: The FTP simulation of a rectangular profile using rectangular and hanning window with $f_o=0.125\ pixel^{-1}$

SDP : For Signal Domain Profilometry implementations, an FIR filter designed by the Parks-Mc Clellan algorithm [48] was used. In order to design the FIR filter required by SDP, the Fourier Transform of the image spectrum after the demodulation process is analysed. This is plotted in Figure 4.23.

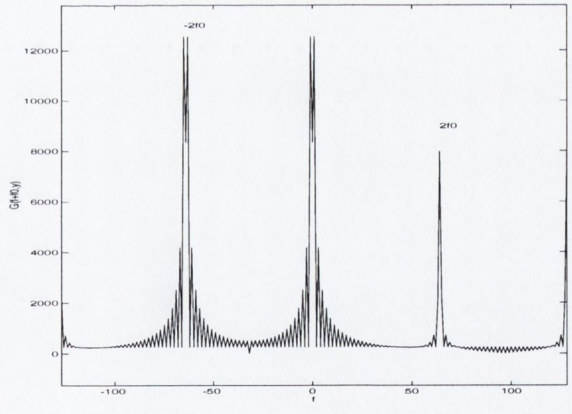

Fig. 4.23: SDP - 32 fringes pattern after demodulation in frequency domain

There are no even harmonics in the *FFT* of the square wave (black and white grating) and the fundamental grating frequency is quite high. Thus, the distance separation between the low-frequency spectrum and the $2f_o$ and $-2f_o$ frequency spectrum are quite large with a discrete frequency of $2f_o= 64$, the filter transition from passband to stopband can be smooth. The magnitude of the normalized frequency response for the designed filter is shown in Figure 4.24. The attenuation at $2f_o=0.5$ and $4f_o=1$ is –

55.4db and *–28.5db* respectively. The unwanted spectral components are adequately rejected and accurate profile measurement is expected. Figures 4.27 and 4.28 show the reconstruction of the rectangular profile by FTP and SDP with a 32 fringes per line grating pattern. Due to the non-ideal stopband rejection of the FIR filter, the SDP profile is slightly sharper and noisier. The mean value of the absolute shift error is *0.0393* for FTP and *0.0642* for SDP.

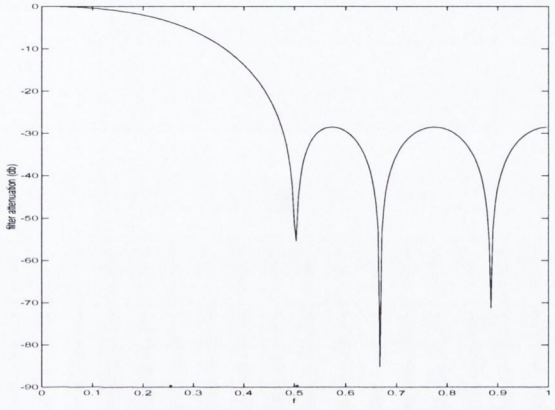

Fig 4.24: SDP – Magnitude of a normalised FIR filter frequency response for 32 fringe grating pattern

NFP : The performance of the New Fast Phase profilometry approach is demonstrated using the same shift profile of fundamental grating frequency $f_o=0.125$ $pixel^{-1}$, as used for the simulation in the FTP and SDP. As previously described in Section 4.3.3, the image row is firstly smoothed by a moving averager to attenuate higher harmonics, and for this a 3-point moving averager was used. Since the reflectivity is constant, mean value subtraction is used to subtract the DC component. The next step is the demodulation process which is carried out by proper manipulation of pixel signs. The *FFT* of the distorted image row after demodulation is shown in Figure 4.25. Since the main interfering spectral component is localised at frequency $\pm 2f_o=64$, a sum comb filter capable of eliminating this frequency must be designed. A suitable filter with $N=2$ is used which is defined by equation (4-28). The frequency response of the filter is shown in Figure 4.26.

$$y_k = x_k + x_{k-2} \tag{4-28}$$

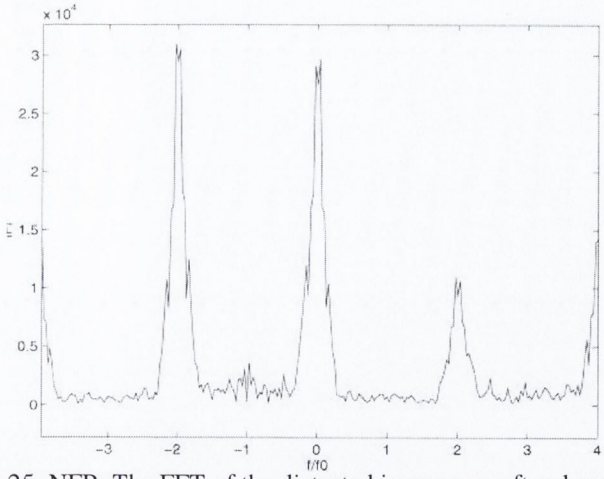

Fig. 4.25: NFP- The FFT of the distorted image row after demodulation

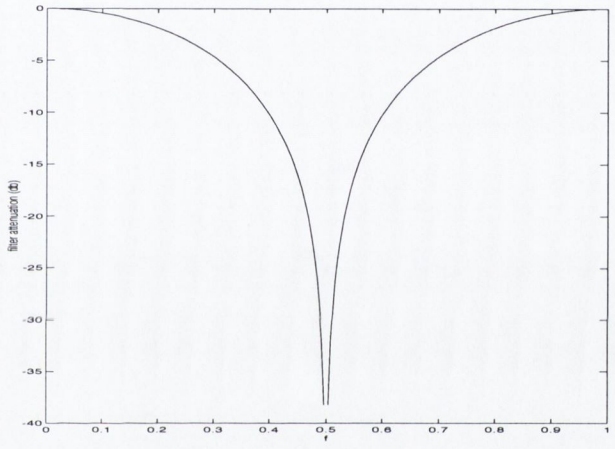

Fig 4.26: The frequency response of the normalised modified comb filter for a 32 fringe uniform image

Finally, a 9-point moving average filter is used to extract the low-frequency signal. The absolute shift error for NFP is *0.0571*. The extracted phase profile for a *32* fringe grating pattern is shown in Figure 4.29.

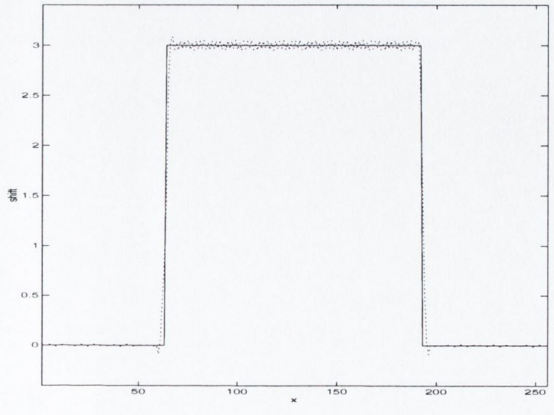

Fig 4.27: SDP - Phase profile simulation with a 32 fringes grating frequency

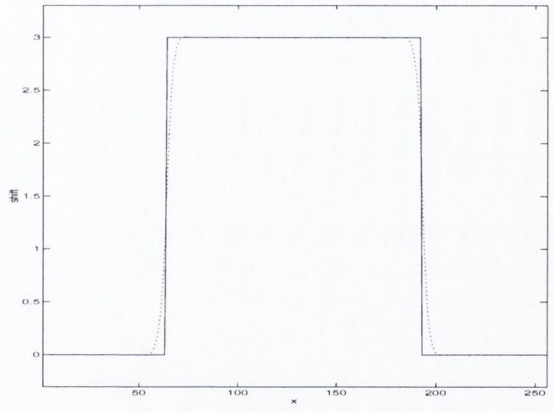

Fig 4.28: FTP - Phase profile simulation with a 32 fringes grating frequency

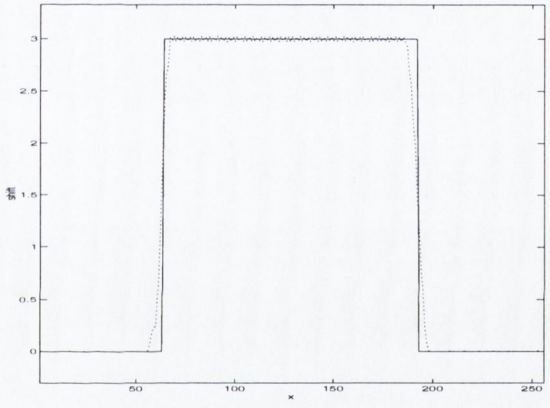

Fig 4.29: NFP - Phase profile simulation with a 32 fringes grating frequency

The three techniques all yield a pretty good approximation of the target profile when a high frequency fringe pattern is used.

4.4.3.2 Low Frequency Fringe Pattern ~ f_o=0.0625 $pixel^{-1}$

The simulation analysis of a low-frequency grating pattern is now considered. A *16* fringes per line *(f_o=0.0625 fringe/pixel)* grating is used.

FTP : Consider now the coarse fringe grating pattern. For Fourier Transform Phase Profilometry, only small changes are required to adapt it to the new frequency. The length of the Hanning window must be halved for the extraction of the phase information and must be centred on the fundamental grating frequency. Unfortunately, since the computation time is largely dominated by the *FFT-IFFT* pair, this complexity is independent of the grating pattern frequency. Figure 4.30 shows the phase profile of a 3 step shift. The absolute shift error is *0.0755*.

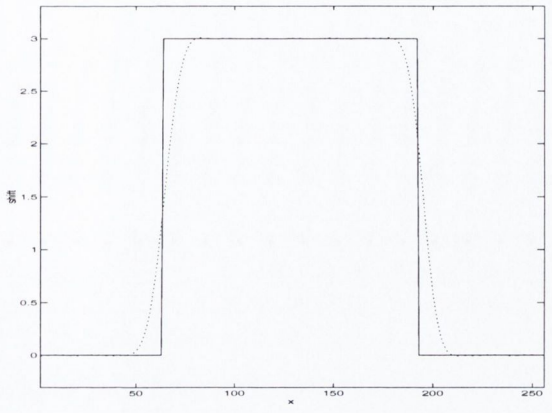

Fig 4.30: FTP - Phase profile simulation with a 16 fringes grating frequency

SDP : For Signal Domain Profilometry, the FIR filter must be designed from scratch to adjust its response to the new fringe frequency. The plot of the image spectrum after demodulation using the cosine and sine functions in Figure 4.31, and shows clearly how a sharper transition band is required to separate the low-frequency spectrum as the main unwanted spectra centred at $2f_o=32$, $-2f_o=-32$ are located rather close to DC. Moreover, substantial stopband attenuation is needed to reject the higher unwanted spectra. Unfortunately, given the small number of taps for the filter, these two design requirements cannot be optimised simultaneously, and great care must be taken in establishing a trade-off between them. This makes the design of the low-pass filter for a low fringe pattern extremely problematic. By way of a compromise, a 9-tap FIR filter was used. The magnitude of the normalised frequency response is shown in Figure 4.32.

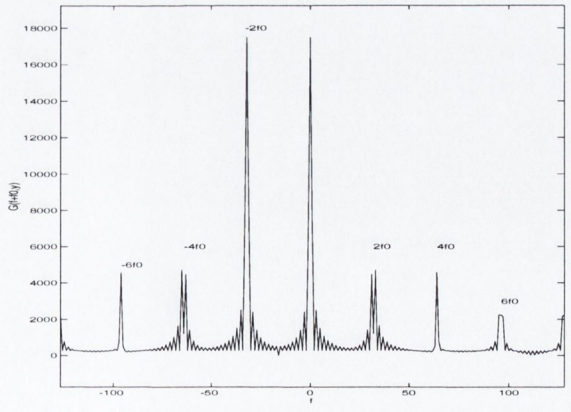

Fig. 4.31: SDP - 16 fringes pattern after demodulation in frequency domain

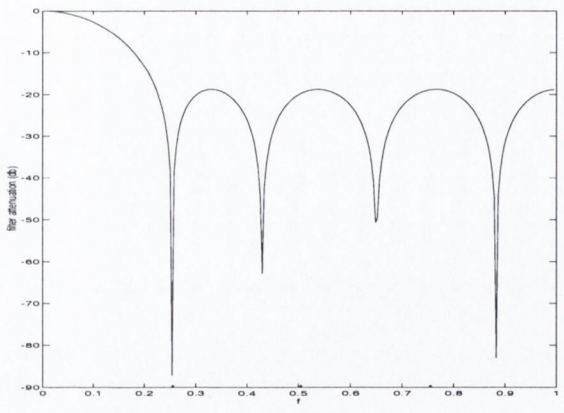

Fig. 4.32: SDP – Normalised Frequency Response of the FIR filter for 16 fringes grating pattern

The reconstructed rectangular profile by SDP with a low frequency fringe of *16* is shown in Figure 4.33. There is a strong variation in the height profile compared to the original profile, the absolute mean error is *0.2231*. This is because the higher spectra *($4f_o$, $6f_o$)* have not been attenuated by the filter effectively. These higher spectra can only be reduced by sharpening the transition from passband to stopband. This would allow the higher spectral components to be reduced. However, the main unwanted spectral components at $\pm 2f_o$ would not be eliminated since they are in the main lobe of the filter. This would however result in an even higher shift error due to the fundamental unwanted spectrum at $\pm 2f_o$.

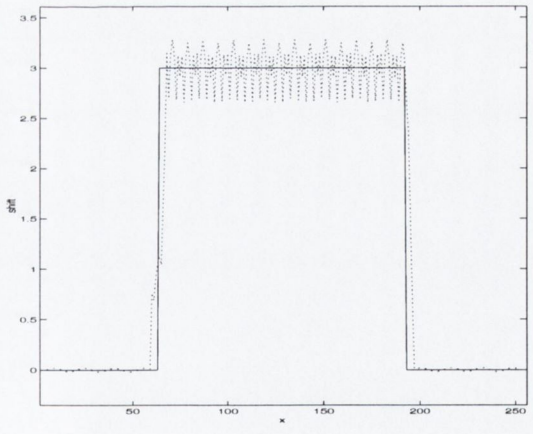

Fig 4.33: SDP - Phase profile simulation with a 16 fringes grating frequency

NFP : For New Fast Phase Profilometry technique, due to uniform reflectivity, only two comb-filters with *N=2* and *N=4* are required to eliminate the unwanted harmonics. These two comb filters are cascaded together according to equation (4-3). The computation for a normal sum comb filter requires one addition per point, and with the modified comb filter shown in equation (4-3), only one extra subtraction per

point is required since it can be split into two independent filters, running on even and odd pixels, computed through the recursive relation shown below:

$$y_k = y_{k-2} + x_k - x_{k-8} \tag{4-29}$$

The frequency response of the modified comb filter for a *16* fringe grating frequency is shown in Figure 4.34. The resulting phase profile is shown in Figure 4.35. The absolute shift error is *0.0823*.

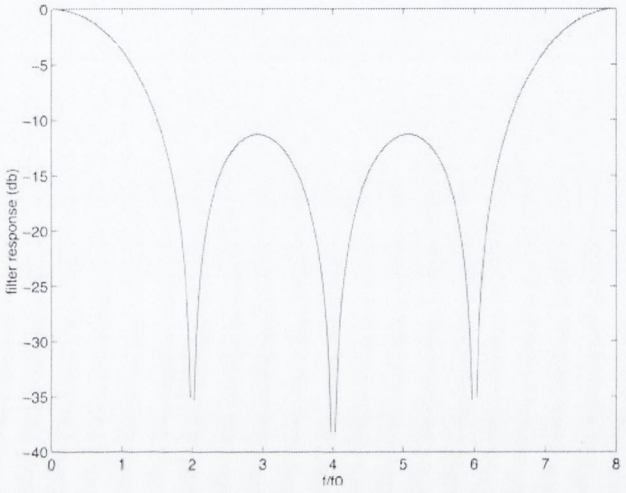

Fig. 4.34: The frequency response of the modified comb filter normalised to the fundamental frequency for a 16 fringe grating frequency

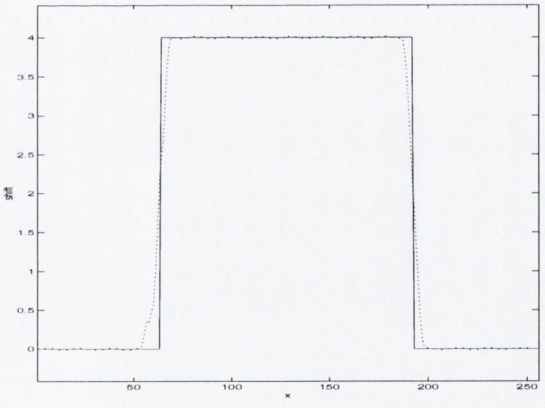

Fig 4.35: NFP - Phase profile simulation with a 16 fringes grating frequency

Thus, with both FTP and NFP, one can easily modify the procedure to adapt to a different fringe frequency pattern. No practical variation in the computational complexity is associated with the frequency change, and the accuracy with a low fringe frequency pattern remains rather good compared to that of the high fringe frequency pattern case. Conversely, adapting SDP implies the carrying out of a FIR

filter design process which turns out to be very problematic in the case of a coarse pattern. If the order of the FIR filter is low, SDP is significantly less accurate than if a high frequency fringe pattern is employed, in addition to being less accurate than the other two techniques. The only way to improve SDP accuracy with a low frequency fringe pattern is to increase the order of the filter. The improved accuracy is achieved at the expense of a substantial increase on the computational load.

4.4.4 Computational Speed

The computational load associated with profilometry techniques is estimated on the basis of the number of floating-point multiplication operations. Addition and subtraction operations may be neglected as they are not as time consuming. From the computational point of view, the Fourier phase extraction technique turns out to be most expensive of the 3 methods since it requires calculation of an *FFT-IFFT* pair for each image row. The time it takes to compute an *FFT* varies greatly depending upon the sequence length. The *FFT* of sequences whose lengths have many prime factors is computed quickly; the *FFT* of those that have a few is not. Sequences whose lengths are prime numbers are reduced to the raw (and slower) discrete Fourier transform (DFT) algorithm. For this reason it is generally better to stay with power-of-two *FFTs* unless other circumstances dictate that this cannot be done. That is why an image of *256 x 256* is usually taken. The estimated number of floating points is *5700* for an image of 256 x 256 pixels. The number of real multiplications per line for FTP is given by *4NlogN* where *N* is the number of pixels in a line and a standard Radix-2 *FFT* algorithm with *(N/2)logN* complex multiplications has been used for the *FFT* and *IFFT*. When the sequence length is a power of two, a high-speed radix-2 Fast Fourier transform algorithm is employed. The radix-2 *FFT* routine is optimised to perform a real *FFT* if the input sequence is purely real, otherwise it computes the complex *FFT*. This causes a real power-of-two *FFT* to be about 40% faster than a complex *FFT* of the same length. When the sequence length is not an exact power of two, an alternate algorithm finds the prime factor of the sequence length and computes the mixed-radix discrete Fourier transforms of the shorter sequences.

The Signal Domain Profilometry method proposed by Tang and Hung processes the demodulated image directly in the signal domain instead of frequency domain. This has the advantage of reducing the computation time substantially in comparison

to FTP. SDP requires $2N+N(M+1)$ operations, where $M = 9$ is the order of the FIR filter for a high or low fringe frequency. The speed ratio determines how fast SDP is in relation to FTP and can be calculated by

$$SpeedRatio = \frac{4N\log N}{2N + N(M+1)} = \frac{4\log N}{M+3} \tag{4-29}$$

Equation (4-29) indicates that if the order of the FIR filter is low, SDP is considerably faster than FTP. As shown in the previous section, SDP is not suitable for low frequency fringe pattern as it produces inaccurate results. The inaccuracy can only be compensated with the expense of a high order FIR filter which demerits the objective of finding a faster algorithm as it substantially increases the computational load.

The New Fast Phase Profilometry is very fast since only fast filters such as moving averagers and comb or modified comb filters are used, thus the demodulation cost is practically negligible. A moving averager requires an addition and a subtraction per point, while a comb filter requires just a new addition per point, and a modified comb filter can be implemented as a set of moving averagers, so that the amount of computation time is the same as that of the moving averager. This technique allows phase deviation to be extracted with only integer additions and subtractions. The computational complexity is also independent of the fringe frequency. The speed remains practically the same for high frequency as for low frequency patterns.

4.5 Problems and discussions

According to the simulation-based comparative analysis, the New Fast Phase technique proposed by *F.Boland* and *Luigi* [34,35] yields a better approximation to the profile than the SDP technique. Nevertheless, FTP is still the most accurate phase technique for reconstructing solder paste profiles as can be seen in Table 4.2 below.

	Abs. Shift Error 32 frequency	Abs. Shift Error 16 frequency	Computational Time (*ms*) for a 256x 256 image
FTP	0.0393	0.0755	530
SDP	0.0642	0.2231	340
NFP	0.0571	0.0823	263

Table 4.2: The Abs. mean shift error of the Phase Profilometry

Several limitations and problems were discovered when implementing the profilometries. The only disadvantage with the FTP system is the computation load associated with the calculation of FFT-IFFT. Signal Domain Profilometry on the other hand provides a faster degree of computation, but it is not suitable when utilised in conjunction with a low-frequency fringe pattern because the absolute shift error is large and the FIR filter has to be re-designed. The New Fast Phase Profilometry technique, although providing sufficient speed irrespective of a high or low frequency grating pattern, relies on too many filters. In order to reduce the computational effort, the demodulation scheme is carried out by multiplication of the image signal with two square wave functions having the same spatial frequency. However, errors of unwanted spectral components at certain spatial frequencies are generated, and these unwanted harmonics must be eliminated by suitable comb filters. This additional filtering procedure is an inconsequential step of NFP. The design of comb filters requires accurate knowledge of which frequencies are to be eliminated, hence, the quality of the NFP approach strongly relies on a precise projection system. Furthermore, comb filters can only be tuned to eliminate the exact central frequency of the main noise spectrum if the ratio of the sampling frequency and the grating frequency is an integer number, $f_s/2f_o$. This is demonstrated by designing a modified comb filter with a basic delay equal to 3 and 4 taps for a synthetic image with *30* black and white fringes as the grating pattern. Equation (4-30) shows the modified comb filter in mathematical form.

$$y_k = x_k + x_{k-3} + x_{k-6} + x_{k-9} \tag{4-30}$$

Figure 4.36 shows the magnitude frequency response of the modified comb filter.

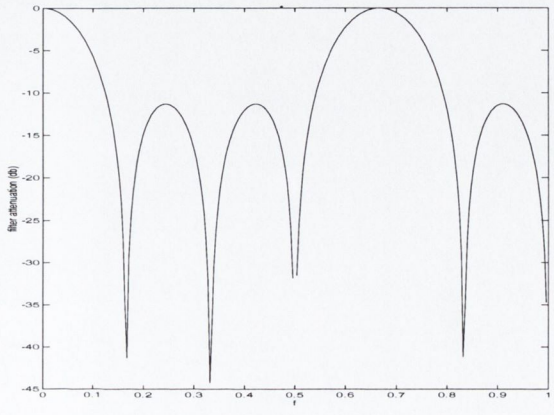

Fig. 4.36: The magnitude normalised frequency response of the modified Comb filter designed for 30 fringes image

Following the steps of NFP, the final profile of the *30 fringes* grating pattern image is reconstructed and is shown in Figure 4.37. The profile presented is quite inaccurate and has an absolute mean error of *0.4215*. In contrast, the FTP and SDP can process an arbitrary value of grating frequency.

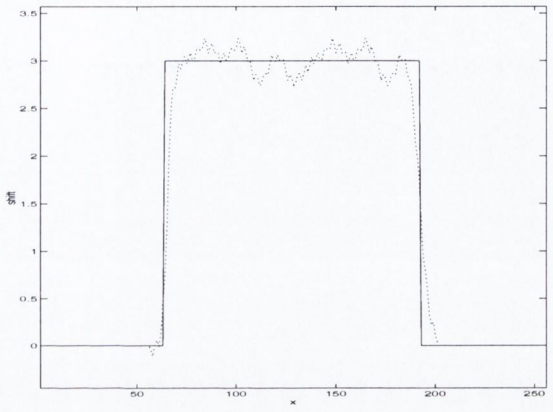

Fig. 4.37: NFP - Phase profile simulation with a 30 fringes grating frequency

Another disadvantage of NFP is the low-pass behaviour of the fast moving-averager filter. It is used to extract the remaining low frequency component of the signal. A moving averager requires an addition and a subtraction per point. It involves averaging the sequence of length N in successive sub-sequences of length m, $m < N$, $m = 2r + 1$, $r = 1, 2, 3,\ldots$ Unfortunately, using a moving averager results in the loss of $2r$ data due to transient effects, which affects the final phase-map. For example, the first eighteen columns of the phase map are lost when using a 5-step moving averager. Figure 4.38 shows the loss in information on the phase map.

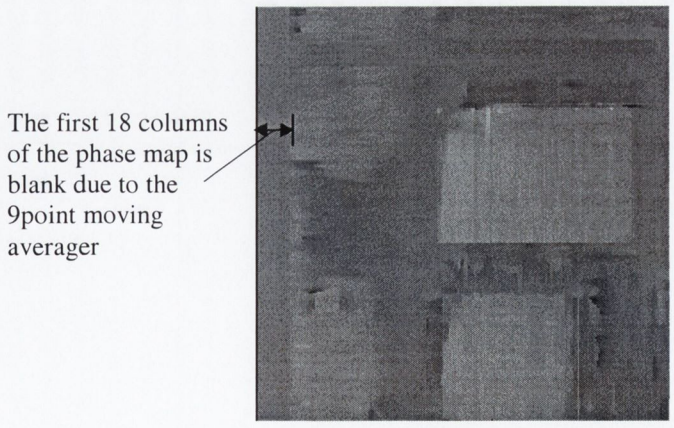

Fig.4.38: NFP – The Phase map showing the loss of information due to moving averager

In general, phase profilometry techniques for range imaging measurements have a much higher sensitivity than the conventional Moiré contouring technique. They have

the capability of a fully automatic distinction between a depression and an elevation on the object surface. There is also no requirement for assigning fringe orders and interpolating data in the regions between contour fringes, while with the Moiré contouring strategy, ambiguities often arise in interrogating the fringe patterns; it is often not possible to determine whether a contour line is higher or lower then the adjacent contour line (i.e.) the moiré fringe order. This phenomenon can be explained by substituting the period of the fringe $f_o = \frac{1}{p_o}$ into equation (2-26).

$$h(x,y) = \frac{H\Delta\phi(x,y)}{\Delta\phi(x,y) - \frac{2\pi}{p_o}d}$$

Dividing by 2π, it becomes

$$h(x,y) = \frac{H\Delta\phi(x,y)/2\pi}{\Delta\phi(x,y)/2\pi - d/p_o}$$

Note that the fraction $\frac{\Delta\phi(x,y)}{2\pi}$ in the above equation is equivalent to the number N of the fringe order in Moiré topography technique [27]. In fact, the equation is exactly the same as the formula of Moiré technique with one single difference. In Moiré technique, when a fringe order N is employed, the height distribution information is given only along a discrete set of N contour lines, whereas with the phase profilometry techniques, height information at all picture elements, regardless of whether $\frac{\Delta\phi(x,y)}{2\pi}$ is an integer or not, are defined. For this reason phase profilometry requires no fringe interpolation. These problems are related to the basic design of Moiré contouring technique; it was originally developed for fringe analysis by human observation and therefore is difficult to implement as an automated technique on a computer.

The biggest problem associated with all phase profilometry techniques is the arctangent operation which is required for the computation of the desired phase deviation. The problem lies in the fact that the arctangent formula is defined over a range from $-\pi$ to $+\pi$. This results in a discontinuous phase distribution, where $\pm 2\pi$ jumps occur when the phase deviation exceeds a phase value of π that are then wrapped into the range of the arctangent operation. Figure 4.39 shows a binary pattern

and the relationship between the phase wrapped by the arctangent operation according to the amount of fringe shift due to the topography of the object.

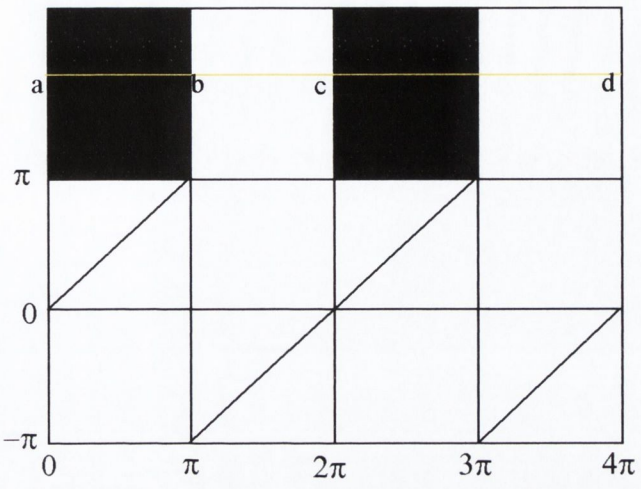

Figure 4.39: shows a binary pattern and the relationship between the phase wrapped by the arctangent operation according to the amount of fringe shift due to the topography of the object.

From point *a* to point *b*, (i.e) within a pulse width, the phase is wrapped between *0* to π, and from point *b* to point *c*, the values of the phase wrapped are between $-\pi$ to *0*. Of course, in reality, no height values are negative, thus, the wrapped values must be *unwrapped* to find the true value. This can be done by using an unwrapping algorithm. An unwrapping algorithm can correct the discontinuities caused by wrapping. This algorithm seeks those positions where the $\pm 2\pi$ jumps occur and then adds an offset of $\pm 2\pi$ to the successive pixel points of the wrapped phase, resulting in a continuous phase distribution. However, during this research, it was discovered that the unwrapping algorithm can only work on certain situations; if the solder paste contains sharp edges or if its height caused the fringes to shift more than one pulse width, then the algorithm would fail to work. This is shown by the example in Figure 4.40. The fringes are shifted by 1½ times of the pulse width, and according to Figure 4.39, the amount of phase wrapped should be approximately $-\frac{1}{2}\pi$. Since the unwrapping algorithm only seeks those positions where the $\pm 2\pi$ jumps occur between two consecutive pixel points, and the example does not consist of any two consecutive points which have phase jumps greater than $\pm 2\pi$ or even $\pm\pi$, the image phase could then not be unwrapped properly. The resultant 2D height profile is shown in Figure 4.41.

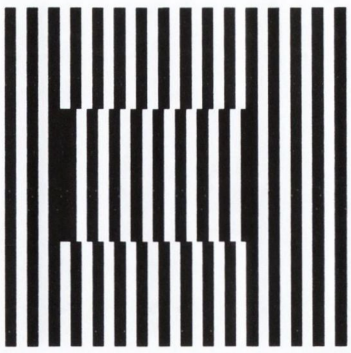

Fig. 4.40: A synthetic image with an object containing sharp sudden edges

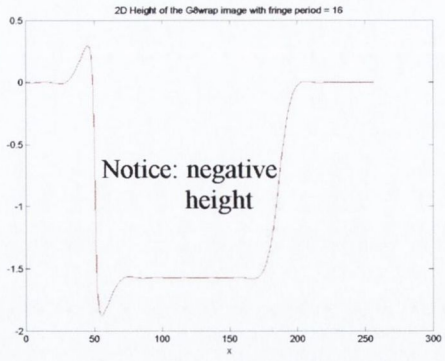

Fig. 4.41: The resultant 2D height with an object containing sharp sudden edges

Fortunately, most solder paste pads usually contain gradually steeped edges. This is shown in an example in Figure 4.42 and the resultant 2D height is shown in Figure 4.43.

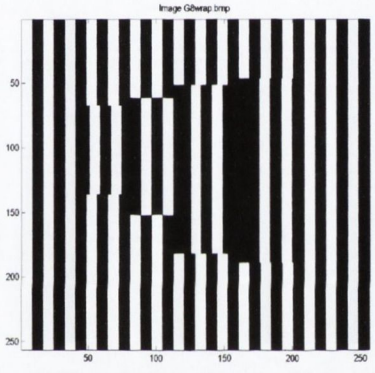

Fig. 4.42: A synthetic image with an object containing gradually steeped edges

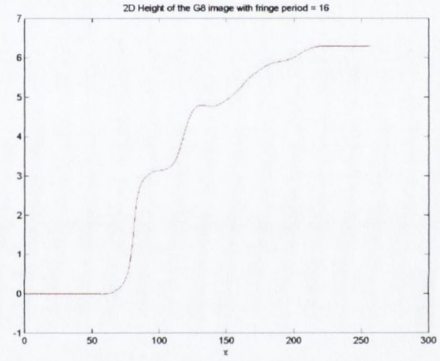

Fig. 4.43: The resultant 2D height with an object containing gradually steeped edges

Since the grating pattern is represented by sine and cosine terms in the Fourier series which repeat periodically every 2π, the maximum lateral deviation of the object's height is therefore limited by one fringe grating period, which is equal to 2π in terms of the phase. From Figure 4.39, the amount of wrapped phase is indistinguishable between point *a* to point *c* and point *c* to point *d*, even though the relative height at point *d* should be twice as high as point *c*. This makes it impossible to employ a higher frequency grating, even though the higher the fringe frequency the better the resolution. In the next part of the research, methods to overcome this drawback are proposed.

Figure 4.44 shows the problem associated with object consist of higher height. It can be seen from the black part of the phase-map in Figure 4.44 that when the object consists of a relative height higher than two fringe pitches, the highest part of the object wrapped itself as if the object consists of a low attitude. The 3-D view of the

object after being processed by phase profilometry is also shown. Appendix B.2 shows a window layout of the software developed.

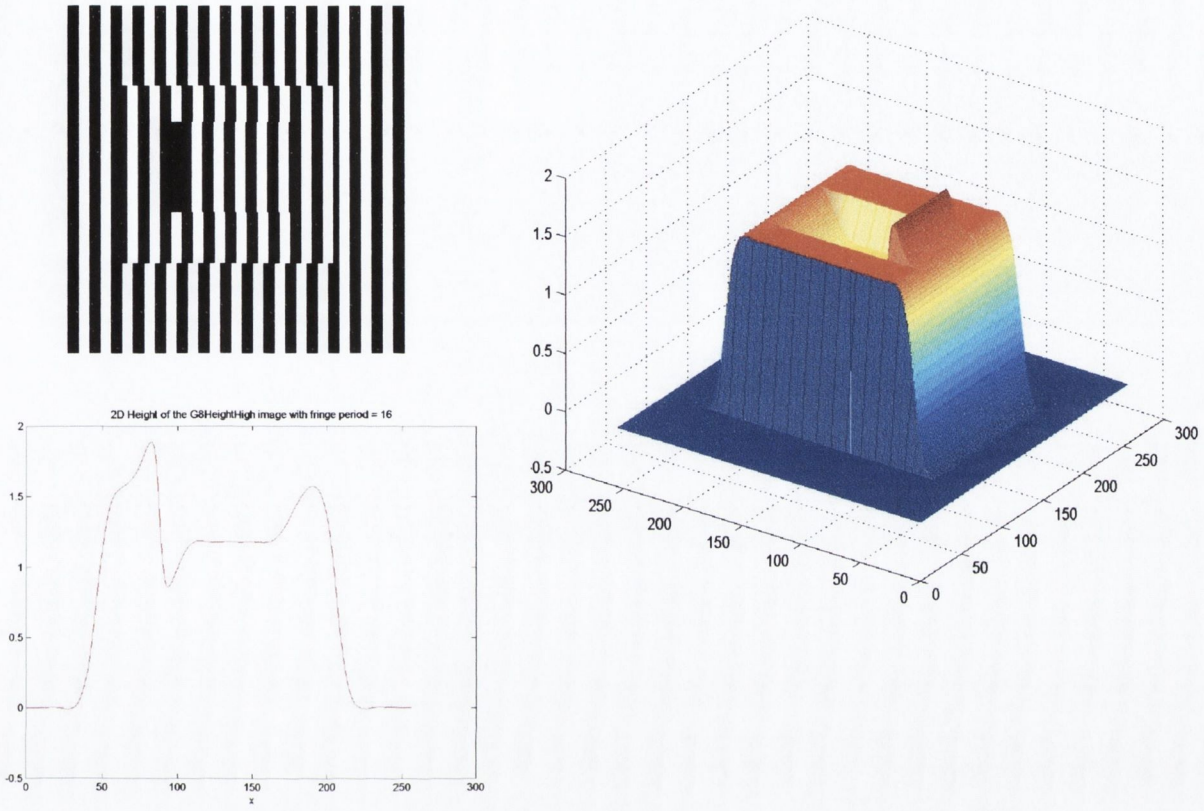

Fig. 4.44: The problem associated with object consists of a relative height higher than two fringe pitches.

4.6 Dual Projection Structured Light System

In Section 4.3.3.1, it was noticed that when one set of fringe patterns is projected onto the PCB surface from a particular direction, information may be lost from the edges of the solder paste pad. The representation of the perturbed image only gives an approximate area at the edges parallel to the fringes if the edge of the solder paste lies within a black fringe. The formation of this edge inaccuracy is explained in Figure 4.45.

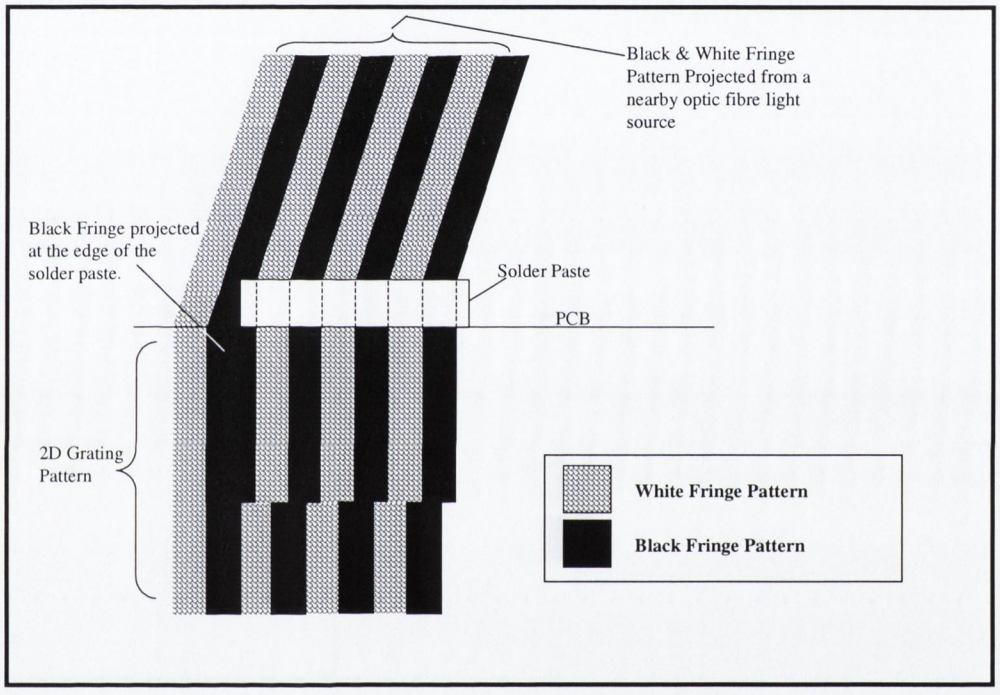

Fig 4.45: Edge of Solder Paste lies within a black fringe

The bottom part of Figure 4.45 shows the captured 2-D image. It shows that when a black fringe is projected onto the edge of the solder paste, the edge consists of a thicker black fringe, this black fringe hides the edge information of the solder paste, thus providing an inaccurate phase deviation.

4.6.1 Dual Projection Structured Light Technique

In this Section, an alternative approach is implemented to demonstrate how this edge inaccuracy can be overcome. Instead of acquiring only one set of imaged patterns with well-defined fringes projected onto the PCB surface at a particular direction, a second projection system is also mounted at an orthogonal angular offset

from the first system. After the first set of grating images is taken, the second grating is switched into position, allowing the second set of image patterns with horizontal fringes relative to the first to be captured, the two grating patterns are not superimposed on each other. With the support of a second projection system, it is possible to compensate the data inaccuracies that arise from the edges of the solder paste pad. The projection angles for the two systems have to be the same, otherwise the phase deviation will differ and, hence will directly affect the 3-D profile of the solder paste.

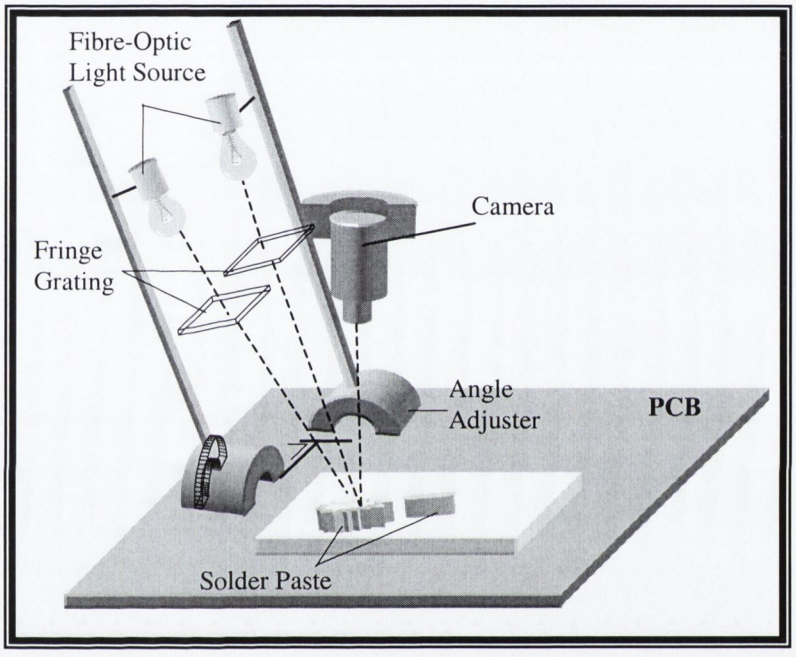

Fig. 4.46: Dual Projection Structured Light System

The dual structured light system is similar to stereopsis, in which the two images are captured to gain extra information by matching the corresponding coordinates of the two images together. But unlike stereopsis, dual projection is a much more straightforward system where the main difficulty of the former lies in the correspondence problem in which two images are acquired at different positions in the scene (i.e. a stereo pair), while for the latter, the perspective view remains exactly the same, i.e. no correspondence problem occurs. Instead, the difficulty of the dual projection system lies in the mechanism of the apparatus for which stability is the key issue. The amount of vibration movement caused by the projected position of one fringe grating to the other perpendicular position at any one time must be restricted. Even a small amount of fluttering may cause changes to the field of view, resulting in thicker or thinner fringes, or ultimately misalignments and de-focusing the view. It

should be noted that the system shown in Figure 4.46 is only a prototype; the second projection grating is not required if the first projection grating system has an alternative mechanism to switch from a vertical patterned fringes to a horizontal pattern using a source such as a liquid crystal to project the stripes.

4.6.2 Combining Algorithm

The two captured images are formed into one single integrated image by combining them in such a way as to determine the optimum accuracy according to the CAD layout of the PCB, permitting relevant solder paste deposits being measured.

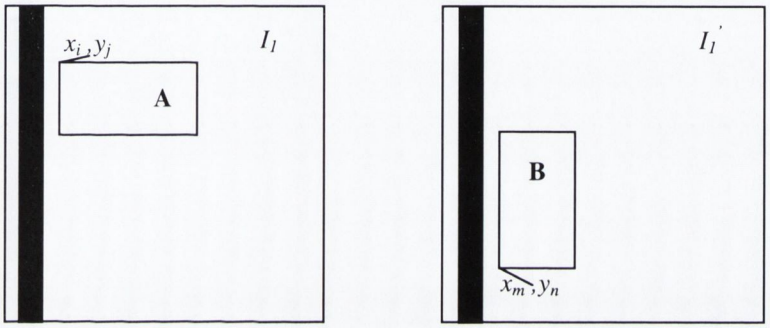

Fig. 4.47: A layout of the vertical and horizontal fringes images

Consider the two *256 x 256* pixels images, I_1 and I_1' representing the vertical fringes image and the horizontal fringes image respectively. Note: solder paste pads A and B are the same solder paste pad.

The two images are combined according to the formula below equation (4-31). If the function (4-31) is greater than or equal to zero at any pixel point, then the combined image I_c at that pixel is

$$I_c(x_i, y_j) = \begin{cases} I_1(x_i, y_j) & I_1(x_i, y_j) \geq I_1'(x_m, y_n) \\ I_1'(x_m, y_n) & otherwise \end{cases} \quad \text{for all} \quad \begin{matrix} i, j \in A \\ m, n \in B \end{matrix} \tag{4-31}$$

where

I_1 = grey level data of the vertical image

I_1' = grey level data of the horizontal image

I_c = grey level data of the combined image

A denotes the area of the solder paste pad in image I_1

B denotes the area of the solder paste pad in image I_1'

x_i is the pixel element in the x direction in I_1

y_i is the pixel element in the y direction in I_1

x_m is the pixel element in the x direction in I_1'

y_n is the pixel element in the y direction in I_1'

The combining function measures the difference between the grey-level data of a pixel coordinate of the vertical image I_1 and the grey-level data of a pixel coordinate of the corresponding horizontal image I_1'. It produces a grey-level value at that pixel coordinate in the resultant image I_c that is determined by the higher value between the two grey-levels. Note: the corresponding pixels are compared to each other in the two images according to the CAD layout.

As noted, when a black fringe lies parallel to the edge of the solder paste, the captured image would consist of a dark patch around the edge causing inaccuracies to the final height distribution. With a second projection system, the errors are compensated. Since the fringes are projected at 90 degree to the first projection system, the black fringe which was parallel to the edge of the solder paste is now perpendicular to it, and thus, by choosing the correct edges of the solder paste pad from the two captured images, the optimum combined image is determined.

4.6.3 Experimental Results

Following the explanation of the dual projection system, two synthetic fringe images were implemented to serve as sample images, (Figures 4.48a & 4.48b), with an object in the shape of a rectangular box having 16 vertical and horizontal fringes respectively. The two images are processed using the New Fast Phase Profilometry to obtain the phase-maps shown in Figure 4.48c & 4.48d.

The phase-maps clearly indicate the inaccuracy of using a single projection system. The implementation of the image with vertical fringes only gives an approximate area at the edges parallel to the fringes, hence the blurry effect in the phase map. The same problem arises with the horizontal fringe image.

This problem can be solved using the algorithm above, which combines the two phase-maps in such a way that the area containing the solder paste deposit (i.e. the rectangular box), is maximised, whereas, the area outside the solder paste deposits is minimised, as shown in Figure 4.48e. The phase-map is mapped into grey levels with darker points representing higher phase deviations. The algorithm permits areas containing relevant solder paste deposits to be measured as positioned in the CAD

layout of the PCB, which has the advantage of providing a more precise indication of the volume of solder paste pads on the phase-map.

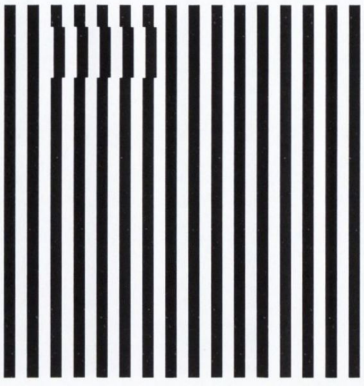

Fig. 4.48a: Synthetic image with 16 vertical fringes

Fig. 4.48b: Synthetic image with 16 horizontal fringes

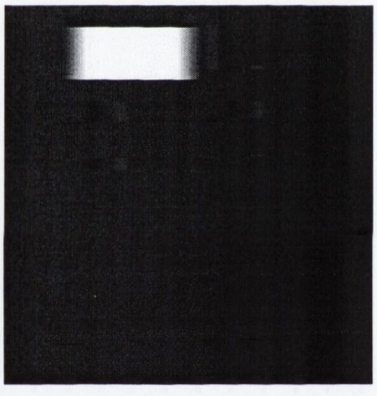

Fig. 4.48c: Phase-map of the synthetic image with vertical fringes

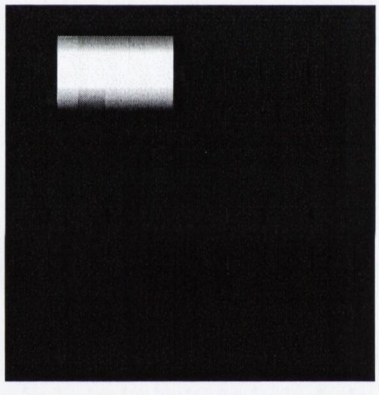

Fig. 4.48d: Phase-map of the synthetic image with horizontal fringes

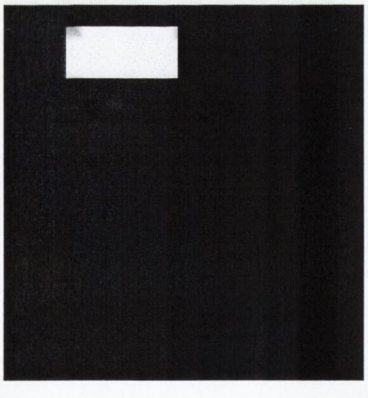

Fig. 4.48e: The resulting Phase-map of the synthetic image.

Figures 4.49a and 4.49b show a typical solder paste deposit of a sample PCB under the Dual Projection Structured Light System. The resulting phase-map and the 3-D representation calculated from the phase deviation are shown in Figure 4.49c and

4.49d. Appendix B.3 shows a window interface for the Dual Projection System generated by Visual Basic.

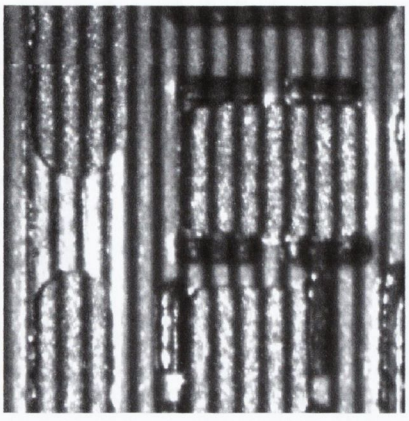

Fig. 4.49a: Solder paste deposits with vertical fringes superimposed on them

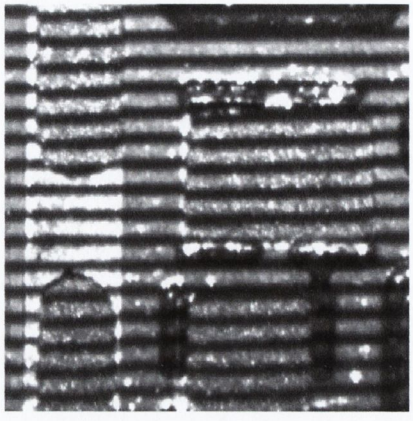

Fig. 4.49b: Solder paste deposits with horizontal fringes superimposed on them

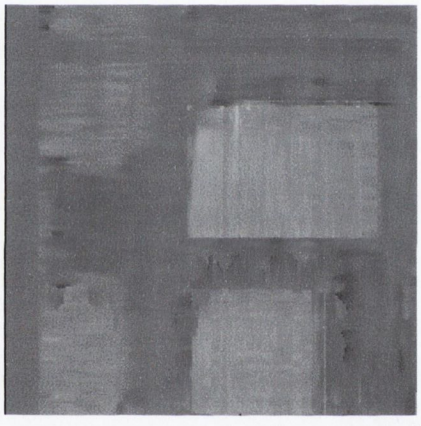

Fig.4.49c: Combined Phase-map of the sample solder paste deposits

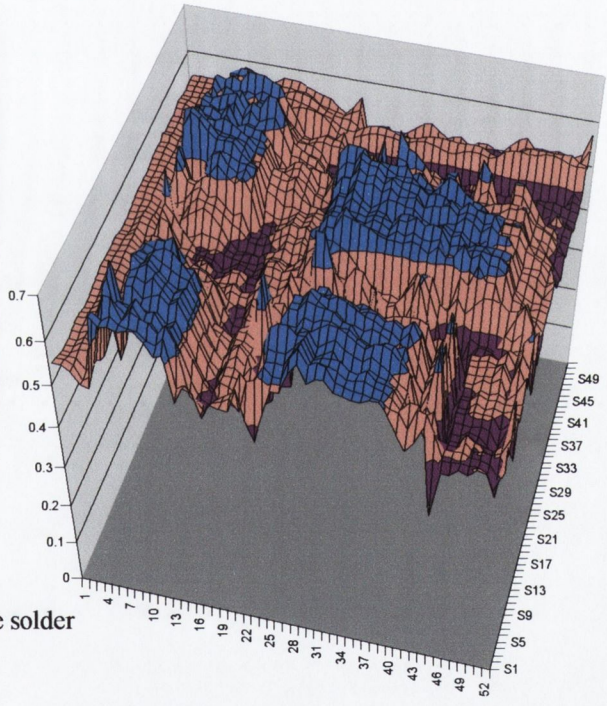

Fig. 4.49d: 3-D Representation of the solder paste deposits from a sample PCB

The dual projection technique improves the final accuracy, which allows the areas surrounding the edges parallel to the fringe pattern to be more accurately detected. It permits only areas containing relevant solder paste deposits being measured as positioned in the CAD layout of the PCB. The dual projection system has one major drawback - the processing time. Since two images are captured and processed each time, the computation time is increased by two. A suggestion is to employ a parallel processing approach to reduce the time required for the two images to be processed. Another future development would be the use of Liquid Crystal Display shutter

(LCD) for the projection of fringe patterns, this would make it possible to change from one orthogonal fringe pattern to the next with no grating movement.

4.7 Conclusions

Using the synthetic images as simulation comparative analysis, the effectiveness of each of the three phase profilometries has been fully investigated. Several limitations and problems were discovered when implementing the profilometries. It was found that FTP yields the most accurate result for reconstructing the 3D solder paste profile. The only disadvantage with the FTP system is the computational load. Signal Domain Profilometry on the other hand provides a faster degree of computation, but it is not suitable when utilised in conjunction with a low-frequency fringe pattern. The New Fast Phase Profilometry techniques provides sufficient speed irrespective of high or low frequency grating pattern, but the filtering process is elaborate and produced unwanted spectral components. The problem associated with the phase unwrapping has been shown and discussed, in the next chapter, a novel approach is taken to avoid the phase unwrapping problem.

Part II of the Thesis

Chapter 5

Geometric Profilometry with Colour Encoded Structured Light Pattern Recognition

5.1 Introduction

In this part of the research, a novel approach is developed for measuring the height and volume of solder paste in real time. This is performed by employing colour encoded structured light (CESL) strips and using computer vision and image processing methods to extract the appropriate colours and to filter out the unwanted data. The implementation of such system has not been investigated previously for volumetric inspection of solder paste or similar size inspection. The main objective of this approach is to avoid the phase unwrapping problem due to the arctangent operation and other drawbacks associated with Phase Profilometry techniques as discussed in Section 4.5. Above all, the aim is to improve the lateral accuracy, which was previously limited by the maximum spatial frequency of the light-stripe pattern.

The operation of the system relies on the principle of structured light technique that has a well-defined pattern of light projected onto the object's surface. This perturbed pattern of light brings about the forthcoming strategy. It uses simple geometric theory to determine the actual height of the inspecting object, and instead of applying a typical Rochi grating with equally spaced vertical dark lines, a special tailor made colour grating is used concurrently with the system. The use of the colour grating was inspired by Boyer and Kak [36], who first published the idea on colour encoded structured light in 1987. The study demonstrated that a pattern consisting of fringes of the six primary and secondary colours projected onto a set of smooth white platonic solids could be decoded in the camera image. All processing was performed on a raster scan basis in the anticipation of a future hardware implementation. A simple edge detection technique was used to locate the positions of the fringes and a crystal growing algorithm was employed for matching a detected stripe with its position in the projection grid, the term *indexing* was given for this fringe matching process. With binary encoded grating, ambiguity arises when identifying the reference fringe with the fringe caused by surface steps due to the fact only black and white colours were used, but with the colour fringes, this ambiguity was solved with no

supplementary processing. Unfortunately, Boyer and Kak's system was dealing with much larger objects and scenes. They employed about 100 stripes to cover a scene of about 2 feet square (*185806 mm*^{2}) while the SMT application would require a system capable of measuring objects and scenes of less than *36 mm*^{2} using a 32 high frequency fringes. And such small volumetric measurement is the key difficulty for which this project must address. Thus, the fringe detection algorithm presented by Boyer and Kak would therefore be entirely unsuitable for our application and a much-more sophisticated algorithm is needed.

Our system adopts the colour-encoded stripes to circumvent the fringe identification problem and to improve the lateral deviation of the grating frequency range, but proposes a new algorithm for the extraction of fringes and the indexing process. The implementation is a combination of various image processing techniques. Unlike the previous phase profilometries discussed, which tackled the 2D image data as a signal or phase, this method does not employ 1-D digital signal processing techniques. Instead the algorithm is implemented using computer vision and image processing methods to extract the appropriate colours and to filter the unwanted data in order to compute the relative pixel shift due to the topography of the object. A computer graphics program using C++ and OpenGL is also developed to represent a 3D rotate-able model. The complete methodology, including the manufacturing process of suitable colour grating will be discussed in this Chapter. The implementations and results will be presented in the next Chapter.

5.2 Geometric Profilometry

The central concept used in conjunction with structured light lies within the simple geometric theory outlined in this Section. Figure 5.1 shows a diagram of the optical arrangement. A grating *G* is projecting a set of fringe patterns onto an area of the printed circuit board at a given angle α. The optical axes of the camera and the grating meet at point C. At point *O*, the grating pattern is on the reference plane, *R*, where no holes or solder paste are disturbing the fringe pattern. Similar to the phase profilometry techniques, it also requires the use of a reference plane in its algorithm. The reference plane should therefore be carefully selected from the CAD layout; fringes can be 'lost' temporarily in holes on the printed circuit board, causing inaccuracies on the algorithm.

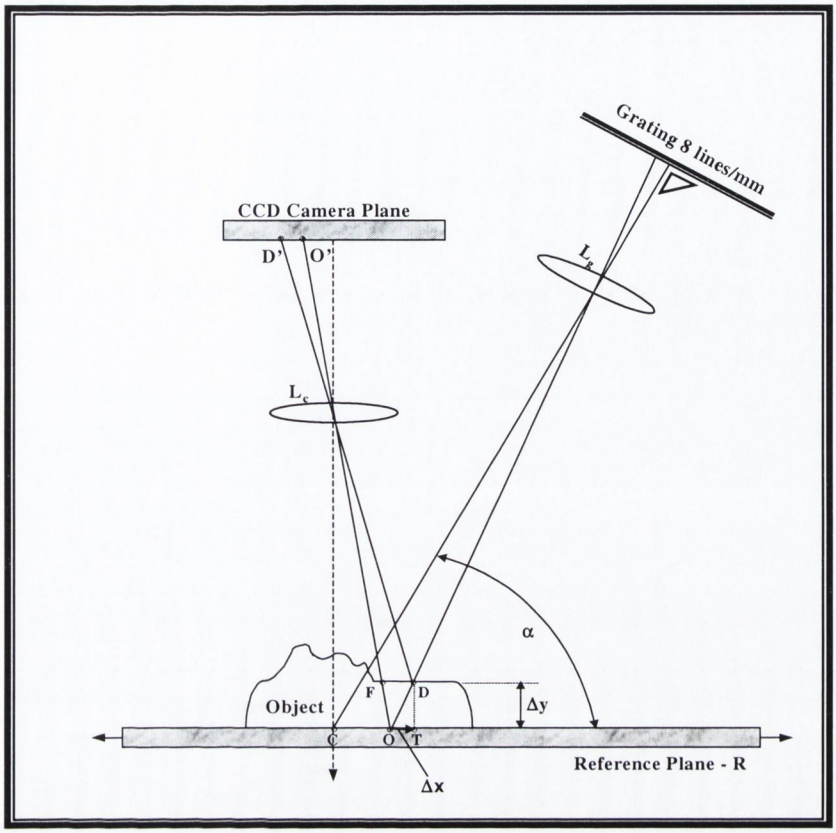

Fig. 5.1: Schematic Diagram of the Optical Geometry for Geometric Profilometry with CESL

From the viewpoint of the camera, the light beam reflects from the reference plane at point *O*, and lands at point *O'* on the camera plane through the camera lens L_c. However, the same fringe projecting onto the object (solder paste) will cause a deviation Δx at point *D* due to its height, while the camera captures the reflected beam at point *D'*.

In practice, the actual inspection system would only be considering a very small area on the PCB at any one time, less than *6mm x 6mm*. The pattern on the grating is very small, about *8 ~ 20* lines per mm. All light beams through the enlarger lens are practically parallel to the grating fringes. Thus, it is safe to assume that all light beams projected onto the PCB surface are projected from the same angle α.

Hence,

$$\angle L_g CO \quad \cong \quad \alpha$$

Thus from the above assumption, it can be assumed,

$$\angle DOT \quad \cong \quad \angle L_g CO$$

$$\Rightarrow \qquad \angle DOT \quad \cong \quad \alpha$$

To obtain the true displacement in real world co-ordinates, the pixel shift is multiplied by the depth of view ratio, IO_{ratio}. This is the ratio of the size of the image relative to the true size of the object. Thus, the

$$IO_{ratio} = \frac{Width_{object}}{Width_{image}} \tag{5-1}$$

$$\Delta x_{world}(x, y) = IO_{ratio} \times \Delta x(x, y) \tag{5-2}$$

where

$\Delta x(x,y)$ is the relative pixel shift due to the object at any point (x,y) in the image

$\Delta x_{world}(x,y)$ is the actual shift due to the object at the point (x,y)

Consider the right angle triangle $\triangle DOT$. The height of the object, Δy, at the point D can be determined by using the simple trigonometric function,

$$\tan \alpha = \frac{\Delta y(x,y)}{\Delta x_{world}(x,y)}$$

$$\Rightarrow \quad \Delta y(x,y) = \tan \alpha * \Delta x_{world}(x,y) \tag{5-3}$$

where

$\Delta y(x,y)$ is the actual height of the object at coordinate (x,y)

Thus, by using equation (5-3), the height of any object at any pixel point on the captured image is calculated. The amount of fringe shift Δx is calculated using the colour recognition program, which will be discussed, in the Section 5.4.

5.3 Colour Encoded Grating Pattern

This application requires a highly dense fringe colour pattern from the grating. Such high grating frequency colour diffraction gratings are not yet available from optical manufacturers, so fabricating appropriate slides to suit such an application is therefore obligatory. A program using C programming language was written to automatically calculate the number of colour fringes on the slide image and generate the slide. Figure 5.2 shows the window interface of the program. This program allows us to input the number of colours in the grating pattern, the width of the fringes in pixels, the r,g,b component values of each fringe and the size of the slide image.

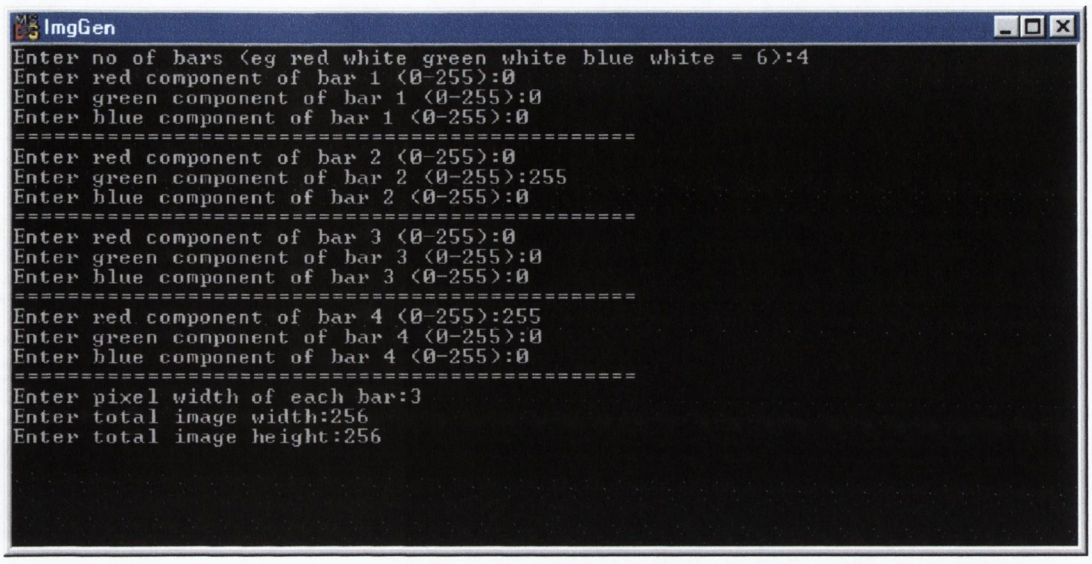

Fig. 5.2: ImgGen Program

Due to the number of fringes required on the slide grating ~ (approx. *8lines/mm – 20lines/mm*) being very fine, a number of uncertainties arose during the development of a suitable colour grating. Initially, the complementary white colour (whose presence is inferred by the simultaneous occurrence of red, green and blue in nearly equal intensities), was used in between each of the three primary colours, red, green and blue for the fringe pattern, producing a Red-White-Green-White-Blue-White fringe pattern. However, when this grating pattern is projected onto the PCB surface using a fibre optic light source, the white colour emits brighter fringes than the other colour fringes, creating a diffusion around the edges of the white fringes, resulting in imprecision in the captured image. A Red-White-Blue-White colour fringe pattern is shown in Figure 5.3b. Black colour fringes were then used to replace the white colour fringes, since black absorbs light. The strategy was somehow effective but another issue arises. When projecting the colour grating onto the surface of the PCB, the black and blue colour fringes becomes very similar in shade. It was laborious to separate these fringes even with automated thresholding methods, hence, causing inaccuracy in the deviation. Finally, a colour pattern consists of Red-Black- Green-Black is used. This is shown in Figure 5.3a.

Since all colours are made up of different intensities of the primary colours, (for simplicity sake), the three primary colours along with the complementary colour were chosen initially. In principle, there is no limit to the number of colours which can be used in the system, but the system must be able to project and detect the colours without error in the given work environment. In this case, this freedom of the number

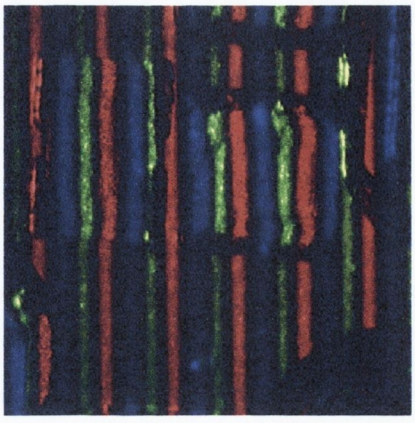

Fig 5.3a: Red-Black-Green-Black-Blue-Black Pattern Slide Grating

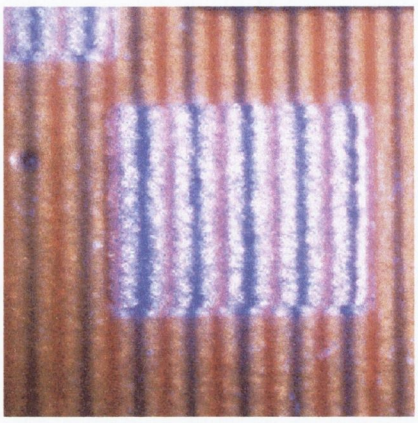

Figure 5.3b: Red-White-Blue White Pattern Slide Grating

of colours used in the grating pattern is limited by the size of the application. One potentially difficult problem associated with the use of colour is accommodating objects which themselves are of some deeply saturated colour. Reflections from these objects will alter the colour balance of the light from that which was projected and could serve to make colour pattern identification difficult. Nonetheless, this should not present a major problem since it is possible in many instances to control the colour content from the camera's visual environment. In fact, the dominant hues in a typical manufacturing environment tend to neutral shades of grey, dull metallic surfaces, and the like.

Although only two of the primary colours and black were used in our colour encoded grating pattern, it has appeared that our system did not fully exploit the advantages of CESL, with only 2 fringe widths for the improvement of lateral resolution more than the original monochrome stripe system. The limitations of not employing more colours were due to the colour of the boards and other factors discussed above. Nevertheless, there are many conditions which have not yet been explored, such as the use of secondary colours. It should also be noted that since our application involves only very small height, using only two colour fringes should be quite sufficient for the measurements.

5.4 Colour Encoded Recognition Algorithm

All captured images are originally captured in 16 million colours (*24 bits per pixel*). They are then formatted into *256* Colour Bitmap Image (*8 bits per pixel*) to diminish complexity [64,65]. An image's less common colours can be eliminated

when the colour depth is reduced. These uncommon colours are often not crucial. Therefore, their elimination by a colour reduction algorithm would not damage any part of the image's composition. A palette for each red, green and blue channel is generated to store the colour information for each pixel in the image containing *256* levels of colours. The level of red, green and blue in each pixel can be separated into 3 different images for colour thresholding and extraction, allowing easy pixel manipulations. Figure 5.4a show the original captured image; Figure 5.4b and 5.4c show the split Red and Green channels of the captured image.

Fig. 5.4a: Solder Paste deposit with colour grating pattern.

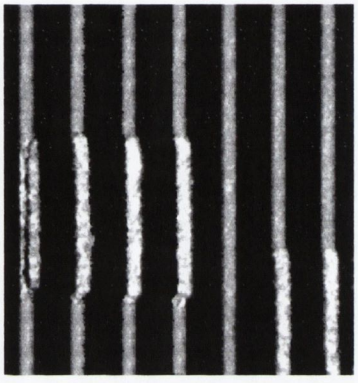

Fig. 5.4b: Solder Paste deposit of the Red Channel Image.

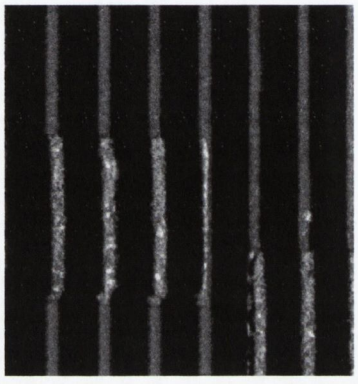

Fig. 5.4c: Solder Paste deposit of the Green Channel Image.

The Colour Encoded Recognition Algorithm comprises of 6 major stages, namely,

- De-Speckling Technique.
- Colour Extraction with the laws of relative equality technique.
- Black Colour Threshold using Segmentation – (T_{Bseg}).
- Image Channel Subtraction.
- Colour Encoded Comparison Technique

5.4.1 De-Speckling Technique

De-Speckling [9,37,64,65] is a neighbourhood operation for removing noise from an image. It can get rid of the diffuse colour at the edge of the fringes to give a slightly clearer cutting edge. It is based on the observation that pixels are small and many are required to make up significant objects in an image. De-speckling does not require pixels to be critically connected, i.e. pixels which are part of an object may still be deleted or split. Figure 5.5 demonstrates a pixel, which is critically connected.

If pixel '**C**' is deleted, the object is no longer *critically connected*, and the object is split into 2 sets of objects.

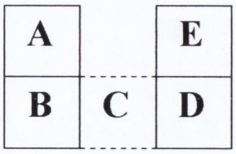

Fig. 5.5: Critically Connected object

Pixels that have less than an arbitrary number of the same colour pixels as neighbours are turned off. The required number of neighbouring pixels is called the dependency level. A dependency level is set initially. Each line is then scanned pixel by pixel to ensure the dependency level is reached, otherwise, the pixel is eroded.

Consider the *2x2* matrix structure below, the dependency level is set to be *2*. Each box consists of a colour pixel, depending on which channel is being analysed, which can either be red pixel or black pixel, or alternatively green pixel or black pixel. Pixel *[i,j]* consists of a colour pixel (a non-black colour). In order for pixel *[i,j]* not to be eroded, two of its neighbouring pixels must also be coloured (a non-black pixel). Therefore, as long as one of the 4 possibilities is satisfied, the pixel remains the same colour as before, that is the pixel *[i,j]* is eliminated from erosion.

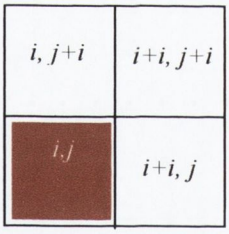

Fig 5.6a: 2x2 matrix

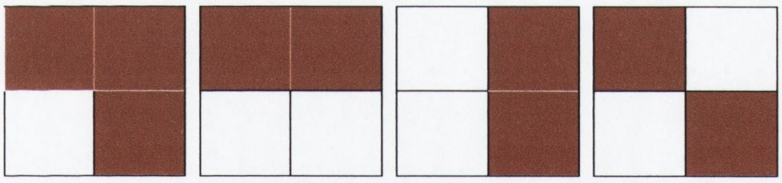

Figure 5.6b: 4 Possibilities with dependency level of 2

Equation (5-4) represents the mathematical function of de-speckling technique for a 2x2 neighbourhood ,

$$\left(\sum_{m=0}^{1} \sum_{n=0}^{1} C(i-m, j-n) \right) \geq Dependency\ \ Level \qquad (5\text{-}4)$$

where

C indicates a non-black colour for the red and green channels,

if $C(i\text{-}m,j\text{-}n)$ contains a non-black colour, a value of 1 is assigned to it.

m is the index in the i-axis

n is the index in the j-axis

If the left hand side of equation (5-4) is greater than or equal to the dependency level set, then the pixel *[i,j]* remains the same.

The higher the dependency level, the smoother the image, however it must be ensured that the smoothing function does not distort the image excessively.

Figure 5.7 shows a part example of an image subjected to the de-speckling technique.

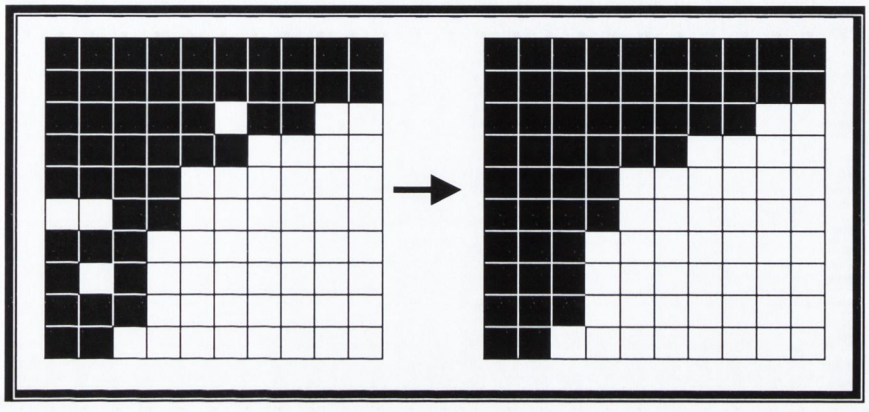

Figure 5.7: De-Speckling Technique with a dependency level of 5

5.4.2 Colour Extraction with the laws of relative equality technique

Thresholding [9,37,64,65] is a commonly used technique to determine which pixels represent foreground (solder paste and objects), and which pixels represent the background (colour-grating pattern of the image). In any realistic colour image, there are many varying levels of RGB colours, with many varying levels of hue, luminance and saturation. Any one surface may vary in its shade of colour depending on its orientation to nearby light sources, shadowing and texture. To threshold an image a threshold level for each red, green and blue channel must first be decided. Image histograms, entropy and other image statistics are all customary methods for calculating the threshold level. This level is the level of colour that divides the image into two sets of pixels, namely, the brightest of the RGB colour for its corresponding RGB channel or black whose presence is inferred by the simultaneous occurrence of red, green and blue in zero intensities. The set of pixels darker than the threshold level constitutes one important entity, the dark fringes, while the set of pixels brighter than the level constitutes the colour fringes in the image.

In a more general sense, a threshold operation is an operation involving some function T of the grey level at a pixel point $g(x,y)$, and/or some local property of the

pixel point *N(x,y)*, and/or the position of the point in the image *(x,y)*. Thus, the function is given by,

$$T = T(x, y, N(x, y), g(x, y)) \tag{5-5}$$

where

x is the pixel co-ordinate in the x-axis

y is the pixel co-ordinate in the y-axis

g indicates the grey-level element

N indicates the Neighbourhood property

In this system, all these three classes of thresholding (global, local and dynamic) are employed in different part of the algorithm. Their operations are displayed beside the respective thresholding classes below.

Properties & Classes of Thresholding functions	***Description of each functions***	***Listings of the related Image Processing Operations in our system***
$T = T(g(x, y))$	Global thresholding: the test is dependent only on the grey-level of the point.	• Photometric Decalibration using Background Subtraction • Colour Extraction with the laws of relative equality • Image Channel Subtraction
$T = T(N(x, y), g(x, y))$	Local thresholding: the test is dependent on a neighbourhood property of the point and on the grey-level of the point.	• De-speckling Technique
$T = T(x, y, N(x, y), g(x, y))$	Dynamic thresholding: the test is dependent on the point co-ordinates, neighbourhood property of the point, and on the grey-level of the point.	• Black Colour Threshold using simple Segmentation • Colour Encoded Comparison Algorithm

Table 5.1: Three Classes of thresholding

Since the projected grating consists only of Red-Black-Green-Black pattern, the law of relative equality can be employed to make assumptions for those pixels which consist of higher intensity colour components in one channel palette than the other two channel palettes. The number of colours and the colour components of the image are stored in a *palette*. Instead of dealing with each pixel of the image individually

where some pixels would consist of the same colour components, the palette is used so as to minimise the repetition of the isolation of such pixels.

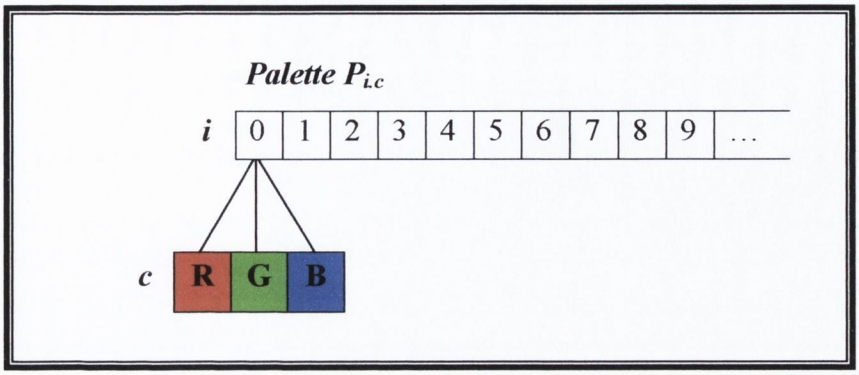

Fig. 5.8: The structure of a Palette

The palette can then be extracted and thresholded according to the equation below.

$$Q_{i,c} = \begin{cases} 255 & P_{i,c} = \max\{P_{i,R}, P_{i,G}, P_{i,B}\} \\ 0 & otherwise \end{cases} \quad \forall\, i \qquad (5\text{-}6)$$

where

c is a variable corresponding to the respective colour channel

i is the index number of the palette

P is the palette of the known image

Q is the palette of the thresholded / resultant image

The function (5-6) states that given the original palette P, the value for the colour channel, c, of the index, i, for the resultant palette Q is equal to the value of *255*, where c corresponds to the channel holding the highest value between the red, green and blue channel of the same index i in the palette P. And the colour values of the two remaining lower channels are then replaced by *zero*.

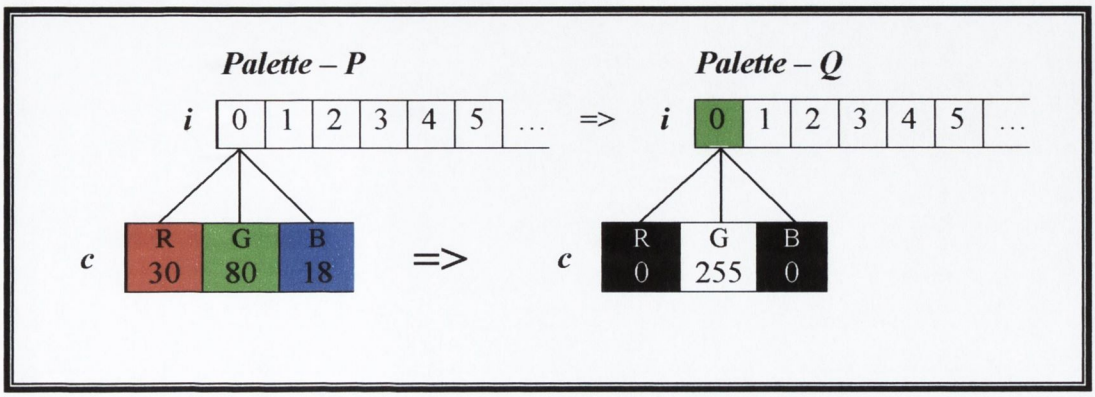

Fig. 5.9: Example demonstrating the relative equality thresholding

It follows then that any pixel, which has a higher green component relative to its red and blue component is assumed to be green. An example of this operation is shown in Figure 5.9. Since blue is not used as the projected fringes, and as mentioned before that black and blue were very similar in shade when the fringes are projected, it was therefore assumed that any pixel with a higher blue component relative to their red and green components, is black. Finally, if values of the green and blue components are relatively low compared to the red pixel value, the pixel is assigned to red. Hence, if equation (5-6) is satisfied, the colour for all those pixels corresponding to the particular index i in the palette can be detected.

5.4.3 Black Colour Threshold using Segmentation – (T_{Bseg})

In addition to the above assumptions, there is one other case which must also be included in the algorithm. The colour black is made up of red, green and blue in zero intensity. The assumption outlined in the previous section has only considered the occurrence of high intensity blue components which appear as black under intense lighting but it has disregarded the low level of all three colour components, which could also appear to be black. The appropriate threshold level must first be determined by examining the histogram of the data, so any pixels whose red, green and blue intensity components are lower than the threshold level can be immediately set to black. The threshold is computed from its original RGB image, by segmenting [6,27] the image and calculating its appropriate mean value. It should be noted that this threshold is a once-off calculation.

In theory, approximately 50% of the original image should be comprised of black pixels projected by the black fringes of the grating. These black areas must be identified and segmented from the rest of the image before calculating the threshold. In partial segmentation, the inspected image is divided into separate regions that are homogeneous with respect to a chosen property such as brightness, colour, reflectivity, context, etc. All pixels in a region are connected. Once the image is segmented, both the colour of the regions and the shape of the regions can be used to extract the particular features of interest.

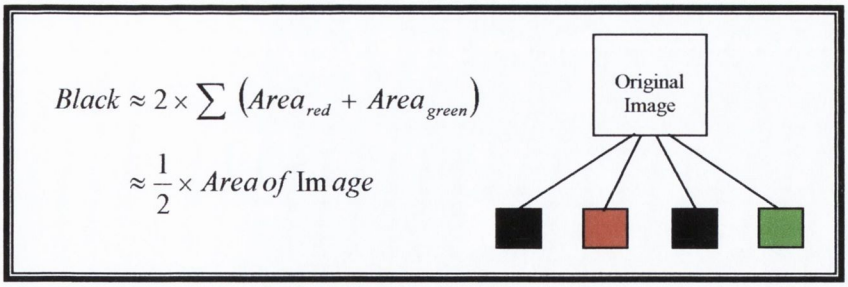

Fig. 5.10: Illustration on how the area of the image is split.

The partial segmentation technique is accomplished by selecting one single reference row across the x-axis of the original image and segmenting where the black fringes are located by simply defining the plot profile of the image as shown in Figure 5.11, comprising those pixels (regions) that are close to black in colour.

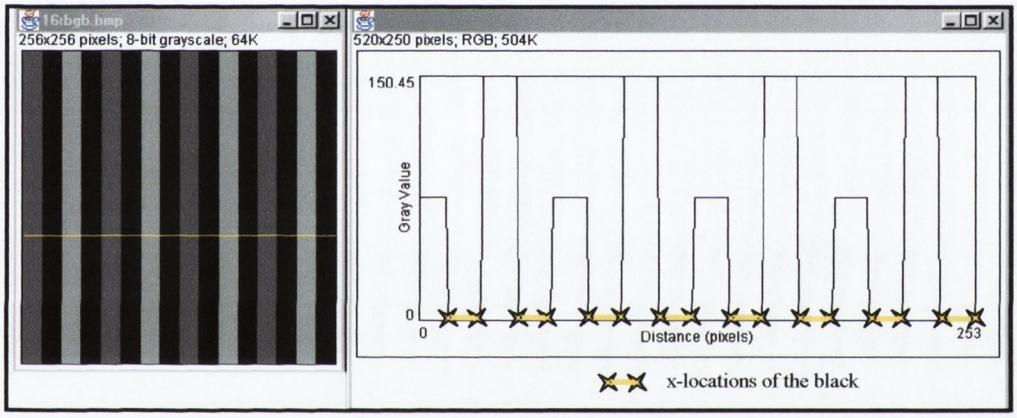

Fig. 5.11: The luminance representation of the synthetic RGB image (L) and its plot profile (R)

The plot profile in Figure 5.11 displays a two-dimensional graph of the intensities of pixels along a line within the image. The x-axis represents distance along the line and the y-axis is the pixel intensity. The plot profile of the image is computed by first removing the colours from the image and replacing each colour with a grey value matching its luminance value. The luminance value Y, is measured as

$$Y = 0.30R + 0.59G + 0.11B \tag{5-7}$$

where

Y – the luminance value of the pixel

R – red component of the pixel

G – green component of the pixel

B – blue component of the pixel

Luminance represents the brightness that corresponds best to human perception and the weightings 0.30, 0.59 and 0.11 most closely match the sensitivity of the human eye to the colours red, green and blue. Note that green is most sensitive to human eyes

[66], hence, the luminance grey values correspond to the green fringes have the highest weighting values. From Figure 5.11, the x-axis locations of the black fringes are indicated by a yellow 'X-X ' in the plot profile. Once the approximate x-locations of the black pixels are found, the entire segmentation region can be located with little difficulty. Figure 5.12 shows the segmented image, the regions are indicated by the black lines with yellow hatching.

The threshold for any pixels, which have a low red, green and blue intensity component, is then calculated by finding the mean value between the three colour channels in the selected regions.

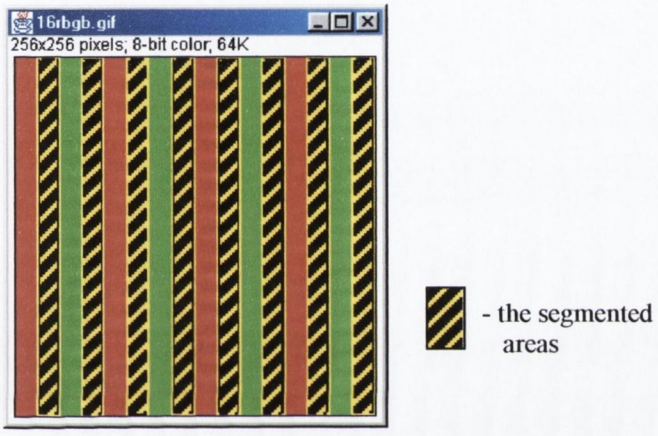

Fig.5.12:The segmented image indicating the segmented areas with yellow strips

The total segmented regions R of the image, contains a finite set of regions $R_1,\ldots, R_t$

$$R = \bigcup_{i=1}^{t} R_i \qquad R_i \bigcap R_j = 0 \quad for\ i \neq j \tag{5-8}$$

The *Integrated Optical Density* (*IOD*) is calculated in each channel for each segmented regions from $R_1,\ldots, R_t$ by summing all the grey values by using their appropriate histograms.

$$IOD = \sum_{R_i=1}^{R_t} \left(\sum_{k\min}^{k\max} kH_R(k) + \sum_{m\min}^{m\max} mH_G(m) + \sum_{n\min}^{n\max} nH_B(n) \right) \tag{5-9}$$

where

$H_R(k)$ – the grey level histogram of the red channel for the selected segmented area

k_{max} – the maximum grey level value of the red channel within the selected segmented area

k_{min} – the minimum grey level value of the red channel within the selected segmented area

$H_G(m)$ – the grey level histogram of the green channel for the selected segmented area

m_{max} – the maximum grey level value of the green channel within the selected segmented area

m_{min} – the minimum grey level value of the green channel within the selected segmented area

$H_B(n)$ – the grey level histogram of the blue channel for the selected segmented area

n_{max} – the maximum grey level value of the blue channel within the selected segmented area

n_{min} – the minimum grey level value of the blue channel within the selected segmented area

t – total number of segmented regions

The Mean grey level is therefore,

$$Mean\,Grey\,Level = \frac{Integrated\,Optical\,Density}{Total\,no.of\ pixels\,in\,segmented\,areas} \tag{5-10}$$

We used this mean grey level as the threshold value and named it as the black segmented threshold value T_{Bseg} for clarity sake so as to distinguish it from the previous threshold value.

$$T_{Bseg} = \frac{\sum_{k_{min}}^{k_{max}} kH_R(k) + \sum_{m_{min}}^{m_{max}} mH_G(m) + \sum_{n_{min}}^{n_{max}} nH_B(n)}{\left[\left(\sum_{k_{min}}^{k_{max}} H_R(k)\right)\times 3\right]\times t} \tag{5-11}$$

This threshold can then be used to extract the black pixels.

$$P_{i.R,G,B} = 0 \quad if\ B_{i.R,G,B} \le T_{Bseg} \quad \forall i \tag{5-12}$$

i.e. $if\ B_{i.R} \le T_{Bseg}\ \&\&$

$if\ B_{i.G} \le T_{Bseg}\ \&\&$

$if\ B_{i.B} \le T_{Bseg}$

where

T_{Bseg} – Black segmented threshold value

$B_{i.R,G,B}$ – Palette of the original RGB image

$P_{i.R,G,B}$ – the resultant Palette after thresholding using T_{Bseg}

i – the index of the Palette

The equation (5-12) states that if each red, green and blue components of a particular index i, in the palette B is lower than the black segmented threshold value T_{Bseg}, then the result of that particular index element of the Palette $P_{i.R,G,B}$ from the segmented image is a pixel element of the projected black fringes.

5.4.4 Image Channel Subtraction

The assumptions of relative equality are sufficiently effective so that the fringes can be extracted without difficulty when encountering synthetic images. However, for actual PCB images, the green fringes may become yellowish green, which is caused by the luminance brightness projected by the optical-fibre source onto the green fringe grating. Since yellow is a secondary colour, made up of green and red, it is therefore possible for a pixel to possess a high value of green but with an even higher

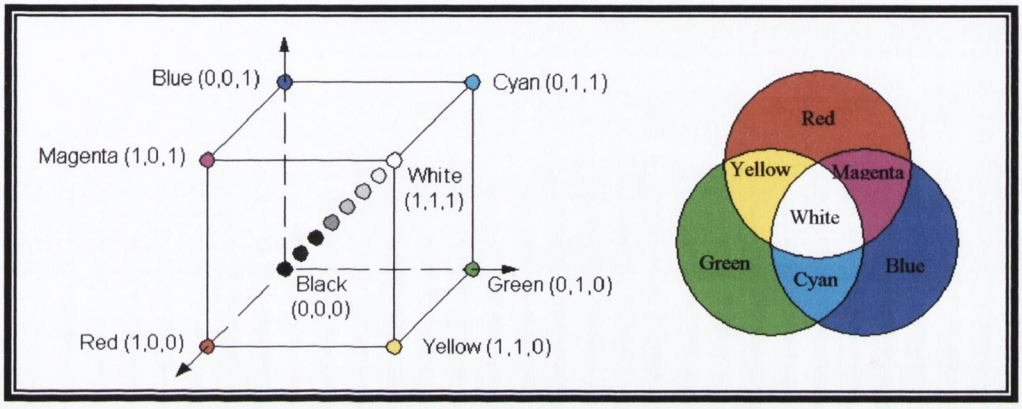

Fig. 5.13: RGB Colour Space represents in a cube and circle

value of red component. Thus, causing the principle of relative equality condition to be violated. Figure 5.13 shows a RGB Colour Space represented in a cube and circle. The grey-level of the red channel image in Figure 5.14 shows these high red component values embedded in the green fringes after splitting the channels of the image. It contains red fringes while also containing a faint medium intensity of the green fringes. In order to eliminate the violation error, these pixels must be eliminated in the red channel. This must be corrected so that even the red components do exceed the green components in a pixel of the green fringe, the algorithm would recognise that the error is due to the projection of bright light.

The threshold, T_{Bseg}, which accounts for determining black pixels induced by the low level of all three-colour components is firstly calculated as described in the segmentation algorithm Section 5.4.3 and the respective black pixels in the image are therefore identified. The green channel provides a rather good indication of the grey-level constituents of where the green fringes are located and, thus, the channel can be extracted effortlessly as shown in Figure 5.14c. In the red channel, the red components from the red fringes have much higher values compared to their red

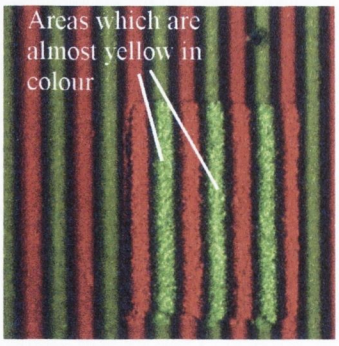

Fig.5.14a: Solder Paste deposit with colour grating pattern.

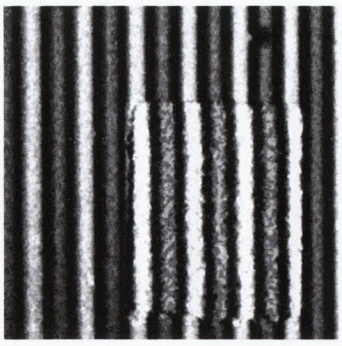

Fig.5.14b: Solder Paste deposit of the Red Channel Image.

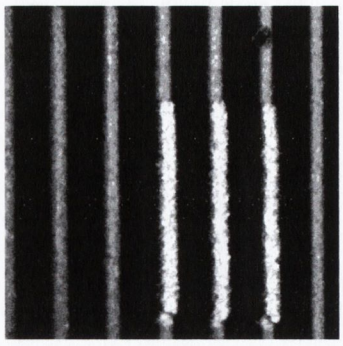

Fig.5.14c: Solder Paste deposit of the Green Channel Image.

components in the green fringes, and also the difference between the red component in the green fringes and its corresponding green component in the green fringes of any individual pixel is very small. Then by subtracting the green channel from the red channel, those pixels, which lie on the green fringes in the red channel, that have high value of green but even higher value of red, can easily be extracted and the correct components in the red channel can be deduced. The values of the new channels are recorded in the new palette L according to equation (5-13)

$$\begin{aligned} L_{i\cdot R} &= \begin{cases} \left| P_{i\cdot R} - P_{i\cdot G} \right| & P_{i\cdot R} - P_{i\cdot G} > 0 \\ P_{i\cdot R} & \textit{otherwise} \end{cases} \\ L_{i\cdot G} &= P_{i\cdot G} \qquad \forall i \\ L_{i\cdot B} &= 0 \end{aligned} \tag{5-13}$$

where

i is the index number of the palette

P is the palette of the known image

L is the palette of the subtracted image

Those pixels, which have a greater red component than green component caused by the bright projection as described earlier, and not by its high red component intensity projected by the red fringes, now have much lower red component values and are stored in the new palette $L_{i\cdot R}$. Note also that as the blue components of the Palette L are not important, they are set to zero for simplicity.

By using the Colour Extraction with the laws of relative equality assumptions as described in Section 5.4.2, the red channel of the palette L is compared with the green and blue channels of the original palette P as shown in equation (5-14). Most of the

pixels of the green fringes in the green channel image can be identified, and all the grey-level values occurring from the green fringe in the red channel are eliminated to zero. The channel images now consists of only 0 and 255 grey-level intensities. This is shown more clearly in an example in Chapter 6 page 132.

$$Q_{i\cdot c} = \begin{cases} 255 & P_{i\cdot c} = \max\{L_{i\cdot R}, L_{i\cdot G}, L_{i\cdot B}\} \\ 0 & otherwise \end{cases} \tag{5-14}$$

where

c is a variable corresponding to the respective colour channel

i is the index number of the palette

P is the palette of the known image

L is the palette of the subtracted image

Q is the palette of the thresholded / resultant image

5.4.5 Colour Encoded Comparison Technique

The colour encoded comparison technique employs a similar measure to the local template matching. A reference row, which represents the local template, is first carefully selected. This row must not be disturbed by holes, solder paste or any other components. It must be a row of expected colour pattern. The width of each fringe from the undistorted reference row is then calculated by comparing each pixel to its neighbouring pixel. The pixels marking the start of each fringe and the end of each fringe are first recorded. The image from each of the Red and Green channels is then scanned line by line to match the original colour sequence of the reference row in order to reconstruct line dropouts.

Consider a perturbed grating image, $S(i,j)$, where the reference row is given by $R(i,j)$, and the pixels marking the start of each fringe of each row is denoted by i. Equation (5-15) below represents all the starting pixels of a fringe in the image $S(i,j)$.

$$Marking\ the\ starting\ pixels\ of\ all\ the\ fringes = \sum_{j=0}^{\substack{image \\ height}} \left(\sum_{i} S(i, j) \right) \tag{5-15}$$

where

i = the pixels marking the start of each fringe for row j

$S(i,j)$ = the perturbed grating image

The similarity measure between the local template $R(i,j)$ and the grating image $S(i,j)$ can be defined by the mathematical function below for the pixel point at $[i,j]$,

$$\sum_{m=0}^{fringe\ width} |R(i,j) - S(i+m,j)| = D(i,j) \qquad \forall\, i,j \qquad (5\text{-}16)$$

where

i = the pixels marking the start of each fringe for row j

j = the row of the image

m = the index marking the start of the fringe to the end of the fringe (each fringe width)

$S(i,j)$ = the perturbed grating image

$R(i,j)$ = reference row, the local template

$D(i,j)$ = the deviation at $[i,j]$ due to the surface

Note: the Reference pixel $R(i,j)$ does not need to be translated since it has the same value all along the fringe width.

This mathematical function involves translating the grating image $S(i,j)$ to a position $[m,j]$ along the x-axis in the grating image, and evaluating the similarity measure with the reference row $R(i,j)$ at that point. Thus, the starting pixel of each fringe is effectively moved along its x-axis to match the template $R(i,j)$ at each position. And the number of pixels deviated at each position is recorded as $D(i,j)$. $D(i,j)$ is equivalent to Δx in Figure 5.1, so by using equation (5-3), the height distribution of the object can be determined.

With a black and white grating, only a relative height of less than two fringe pulse widths can be measured. This undesired consequence is induced by the arctangent and unwrapping operations as discussed in Section 4.5. Yet with the Colour Encoded Comparison algorithm, an object height with a relative pixel shift of up to 4 times the fringe pulse width can be measured, i.e. the fringe deviation can deviate until the next equivalent colour fringe of the reference row appears. This also has the advantage of employing a higher frequency colour grating, thus improving the final accuracy. The algorithm should be used in conjunction with the CAD layout of the PCB to measure the areas where the solder paste pads are positioned and to avoid holes. Otherwise it will give inaccurate result. Figure 5.15a and 5.15b shows the maximum deviation.

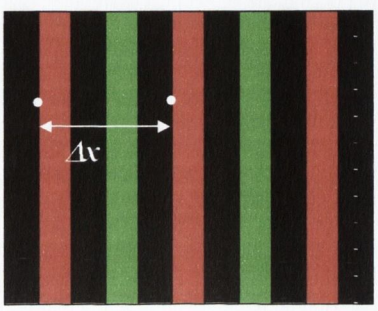

Fig. 5.15a: Max Deviation on a Colour grating

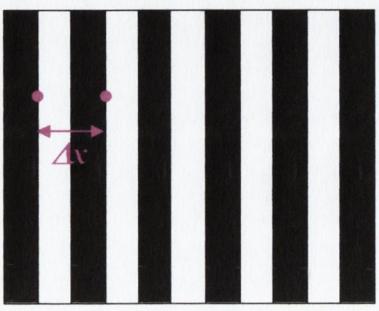

Fig. 5.15b: Max Deviation on a B&W grating

5.5 Reference Line or Image

The Section illustrating the Structured light technique in Chapter 2 describes in detail how the object's height distribution phase-modulates the grating image and that at each image point the height with respect to the reference plane is a known function of the phase deviation. The importance of properly selecting a reference plane is therefore mandatory, as the reference plane provides the information for the baseline of the PCB.

A reference image is an image which captures the part of the PCB where there is no solder paste, holes, or tracks or any SMD components, but an image of only the grating pattern on the board itself. The captured image consists only of lines projected from the grating, and there is no fringe deviation as the area of interest is a flat surface coincident with the reference plane, i.e. $h(x,y) = 0$, there is no differential in height. Although the reference image is only required to be processed once for the inspection, a precise reference image is however desirable.

5.5.1 Misalignment errors from Reference plane

It is usually desirable to employ a reference image since a reference image can compensate the misalignment problem due to optical set-up. This problem arises if the actual grating is not properly located in relation to the optical set-up, so that the projected fringes are not precisely in parallel to the vertical edges of the image, creating misalignment errors. This misalignment problem does not arise when employing a reference image of undistorted projected fringes as discussed in Chapter 3, Section 3.3), since the computation may be processed by comparing each row of the inspected image with the same row in the reference image.

If the misalignment was adjusted prior to the processing, the reference image could be reduced to a reference line and the effort of reading and storing the whole reference image is abolished during processing. This has the advantage of reducing computational time dramatically.

The basic process involves firstly capturing a reference image and then the amount of misalignment in the reference image is calculated. An adjustment in the actual system will then instantly correct the grating's misalignment. Figure 5.16

shows a synthetic image with fringes which are not parallel to the vertical edges of the image.

A line is drawn vertically indicating the pixel at the top of the image - (row 0) to the pixel at the bottom of the image - (row j), *j* being the height of the image.

The pixel misalignment, ε is calculated by counting the total number of pixels displaced horizontally from X_n to X_0 which is clearly shown in the figure opposite.

The pixel misalignment displacement ε is given by

$$X_n - X_0 = \varepsilon \qquad (5\text{-}17)$$

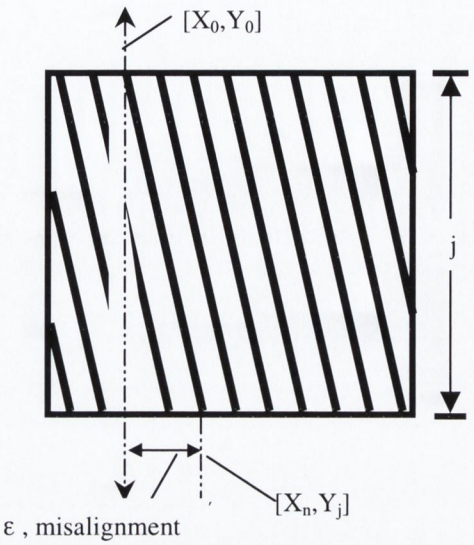

Fig. 5.16: A synthetic grating showing the misalignment problem due to optical setup

To obtain the true displacement in world co-ordinates, the pixel misalignment is multiplied by the depth of view ratio, IO_{ratio}. This is the ratio of the size of the image relative to the true size of the object.

For example, if an object of *50mm x 50mm* is under inspection by the camera, the captured image is *256pixels x 256pixels* and the pixel misalignment ε is *30 pixels*. Since only the horizontal misalignment is of concern here, the IO_{ratio},

$$IO_{ratio} = \frac{Width_{object}}{Width_{image}} \qquad (5\text{-}18)$$

$$= \frac{50mm}{256\,pixel} = 0.1953mm/pixel$$

The true displacement is

$$\textbf{\textit{True Displacement}} = IO_{ratio} \times \varepsilon \qquad (5\text{-}19)$$

$$= 0.1953mm/pixel \times 30pixel$$

$$= 5.859mm.$$

Hence, to compensate the misalignment errors, a horizontal adjustment of *5.859mm* is needed for the correction. This automatic adjustment is done before any computation

processing, and the operations should be set to repeat every short period of time in the case of camera shock or other vibrations.

5.5.2 Vertical Projection for the reduction of edge noise in a Reference Image

The projection of the grating pattern onto the PCB surface using a fibre optic light source does not give 100% sharp edge fringe images. And even after several steps of filtering [the reference image is processed the same way as the distorted image containing solder paste], the sides of the fringes may still indicate the presence of noise. This may be due to many miscellaneous factors including apparatus set-up, white light dispersion and poor equipment. Figure 5.17 shows how imprecise a reference plane may appear. As indicated in Figure 5.17c, the rows are not identical, and the choice of taking any line as the reference may not be the most ideal solution. The noise at the fringe edges can be eliminated if the Signal to Noise Ratio (SNR) is not too high.

Fig. 5.17a: shows the original reference image before any steps of image filtering.

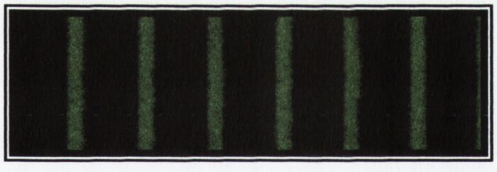

Fig. 5.17b: shows the green channel image after channel splitting and basic thresholding.

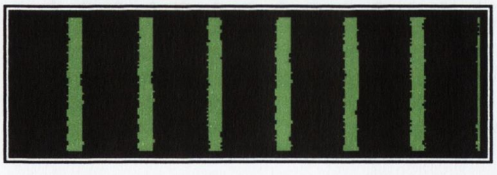

Fig. 5.17c: shows the green channel image after thresholded by the Colour recognition algorithm. Note the edge of the fringes is not perfectly straight, indicating some levels of noise.

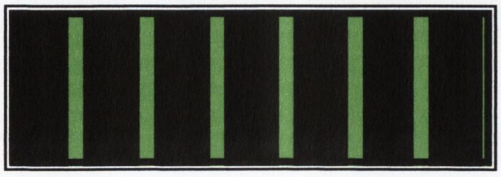

Fig. 5.17d: shows the green channel image after the vertical projection is performed.

A new algorithm has been generated to determine a more accurate reference plane. This algorithm combines some inspirations from a basic concept of binary image processing known as ***vertical projection*** and some fundamental image filtering.

Projections are compact representations of images, and much useful information is retained in the projection. The vertical projection of a binary image onto a line can be obtained by partitioning the line into bins and then finding the number of black pixels in the vertical directions that are on lines perpendicular to each bin. A simple example is shown in Figure 5.18.

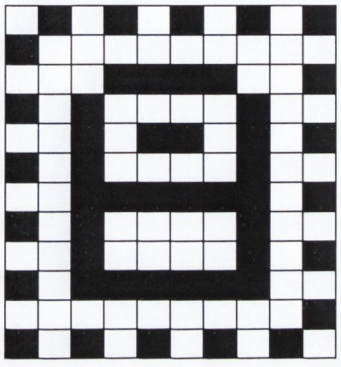

Fig. 5.18a: A 10x12 pixels image

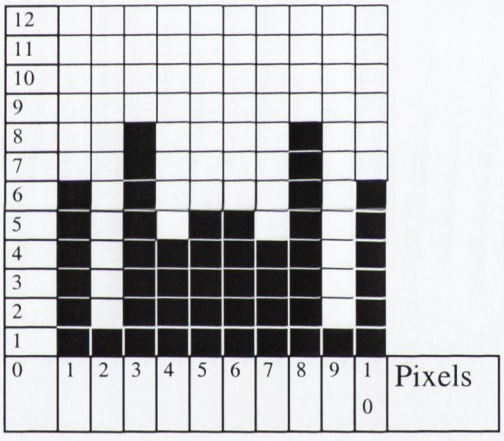

Fig. 5.18b: The resulting histogram illustrating the vertical projection of the 10x12 image

The projection $V[j]$ along the columns of any binary image is given by equation (5-20):

$$V[j] = \sum_{i=1}^{m} I[i, j] \qquad (5\text{-}20)$$

where

$V[j]$ is the resulting vertical projection

m is the total number of rows

i, j is the image's co-ordinate pixel pair

$I[i,j]$ indicates a black pixel at $[i,j]$

The horizontal projection can be determined the same way, by taking the pixels along the rows.

A *10x12* pixels image is employed to demonstrate how the vertical projection technique is performed. According to equation (5-20), the vertical projection of any column *[j]* is calculated by summing the total number of occupied black *(I[i,j])* pixels along the column in the binary image. Figure 5.18b shows the resulting vertical projection in histogram format.

With the concept of vertical projection, comparisons can now be made. Considering an image with only a green channel, as long as the height of the image is known, the decision of whether a column is black or green can be resolved, hence, providing the colour of the pixel for the reference line.

$$\left(V_{green}[j] = \sum_{i=1}^{m} I_{green}[i, j] \right) \qquad (5\text{-}21)$$

$$V_{black}[j] = \sum_{i=1}^{m} (I_{green}[i, j] \not\subset V_{green}[j]) \qquad (5\text{-}22)$$

If the total number of green pixels of the j-column exceeds the total number of unoccupied pixels,

$$V_{green}[j] > V_{black}[j] \tag{5-23}$$

for a given j

then the colour of the pixel for that particular j-column is green.

$$I_{green}[i, j] = 255$$

If the total number of green pixels of the j-column is less than the total number of unoccupied pixels,

$$V_{green}[j] < V_{black}[j] \tag{5-24}$$

for a given j

then the colour of the pixel for that particular j-column is black i.e. unoccupied.

$$I_{green}[i, j] = 0$$

Figure 5.17d shows the result of the vertical projection on the reference image. It should be noted that the vertical projection alogrithm should only be performed after ensuring there is no misalignment of the grating.

If a reference image is not available for the RGB processing, the alternative solution is to select several reference lines with no holes or tracks or any distortions from the image or the CAD layout and then employ the vertical projection program to determine the most appropriate reference row. A flowchart of the Colour Encoded Pattern Recognition algorithm is shown in Figure 5.19.

5.6 Conclusions

Geometric Profilometry with CESL pattern recognition has been fully explained. We utilise simple image processing methods and show how by combining these methods, the desired 3D information of the solder paste image can be easily reconstructed. More importantly, the use of CESL pattern avoids the phase unwrapping problem due to the arctangent operation. It improves the lateral accuracy of the frequency pattern which was previously limited by the maximum spatial frequency of the binary encoded light-stripe pattern. The effectiveness of the technique will be demonstrated in the next chapter.

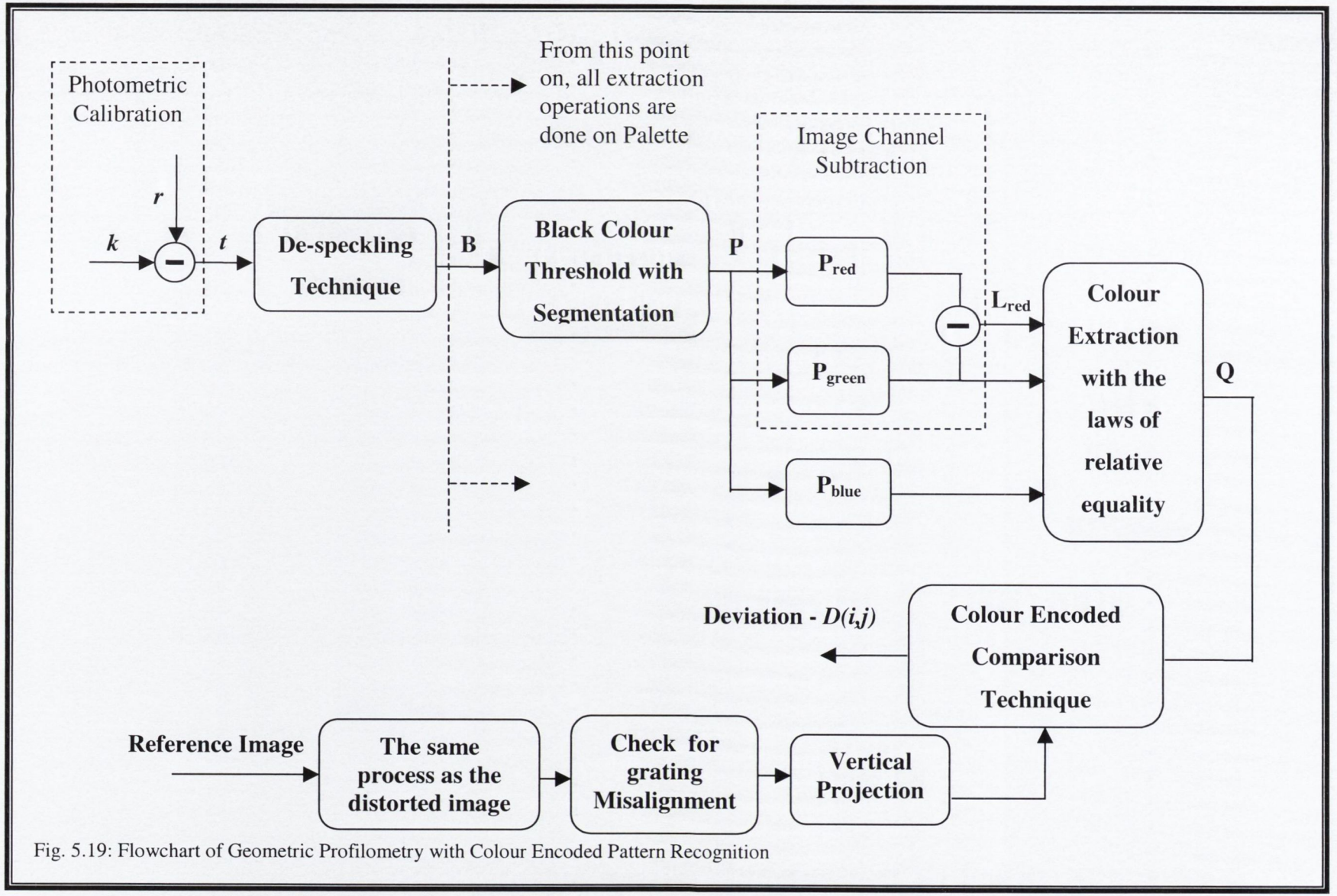

Fig. 5.19: Flowchart of Geometric Profilometry with Colour Encoded Pattern Recognition

Part III of the Thesis

Chapter 6

Implementation of Geometric Profilometry with CESL Pattern Recognition

6.1 Introduction

Following the theory of geometric profilometry with colour encoded recognition structured light technique in the previous Chapter, a prototype model has been implemented for on-line inspection of solder paste pads, permitting reconstruction of 3D shape in real time. The work was motivated by the need to obtain a profilometry that is free from the phase unwrapping problem and to also have the capability of employing a higher fringe frequency so as to improve the resolution.

6.2 Results

The adopted optical configuration used to demonstrate the result is based on a *6 lines/mm* colour grating, this is a very low fringe frequency grating. It is possible to employ much higher fringe frequency grating, so to deduce a more accurate result. The pattern used in our implementation of Colour Encoded Structured Light (CESL) consists of strips of red and green coloured light separated by black spaces, so that peaks in the resulting intensity modulation can be used as the features from which the position information can be generated. The captured image size is *768x512 pixels* with a colour fringe frequency of *0.0547 fringe per pixel.* Due to the fact that this is only a prototype, and that examining the entire captured image each time might require a significant amount of processing time, it was therefore decided that only part of the captured image is examined each time, a *256x256 pixels* image with approximately *14* colour fringes, and the corresponding area viewed under the CCD camera is approximately $36mm^2$. The contours traced by the light stripes on the surface are detected and tracked in the camera image, and the colour sequence of the stripes is used to uniquely identify each contour, while allowing an increase in displacement present by the objects' height. Given the identity of such a stripe and additional calibration information, the image of the stripe from the camera focal plane can be projected back through the focal point of the camera, and the 3D intersection

line between this and the corresponding projected stripe can be found, thereby allowing reconstruction of range data.

The first step of the profilometry was to reduce some of the salt and pepper noise that appears in the image before extracting the information embedded in the colour fringes. This step is known as the de-speckling technique and is similar to erosion. De-speckling has the effect of smoothing and blurring the image, but since detailed information of the circuit board is not of prime concern here, this effect has no bearing on the results. The two histograms of the red channel image before and after being de-speckled were compared as shown in Figures 6.1 and 6.2 and it clearly indicated that some of the noise has been eliminated by the operation as shown by the yellow oval line on the histogram.

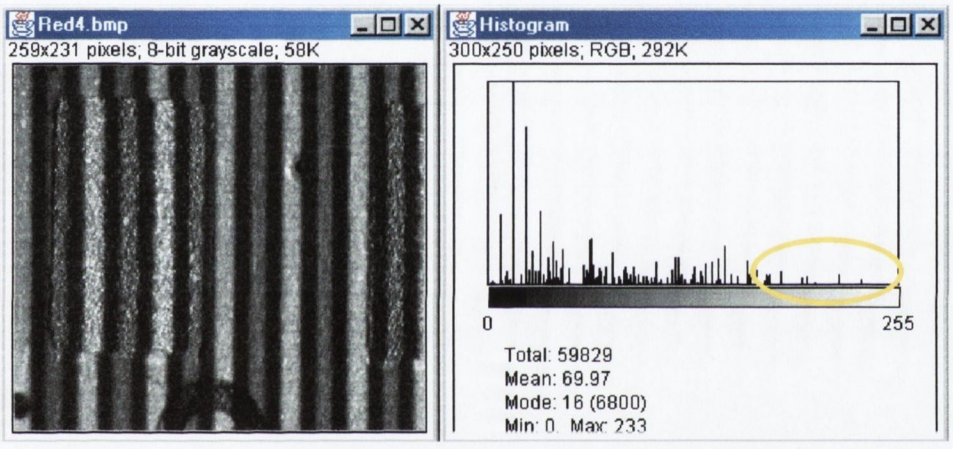

Fig. 6.1: The red channel of an image consists of solder paste (L) and its histogram (R)

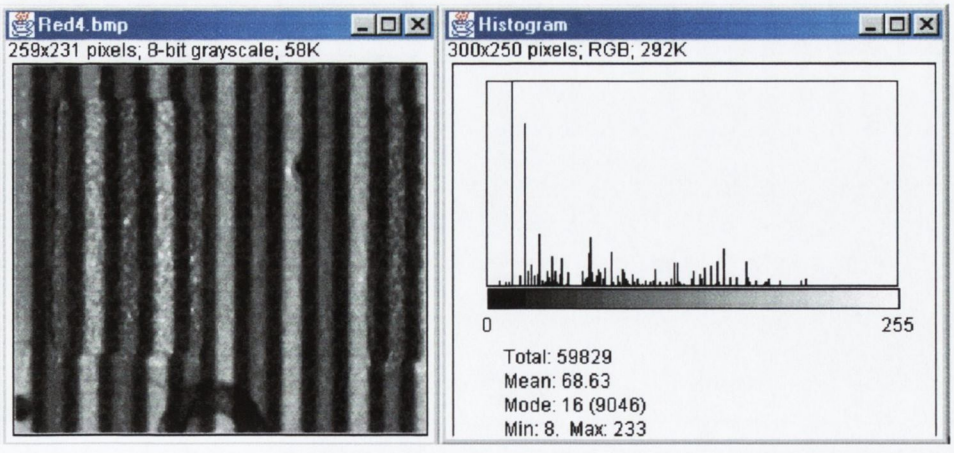

Fig.6.2: The red channel image in fig 6.1 after despeckling (L) and its histogram (R)

After the de-speckling technique is applied to each channel, each of the red, black and green colour fringes are ready to be extracted. In order to decrease computation time, all the image processing operations for colour fringes extraction are executed

with the colour palette of the image, rather than processing them pixel by pixel. Figure 6.3 shows a *256x256 pixels* image of a PCB after the operations of despeckling have been processed. The black segmented threshold T_{Bseg} is calculated from the reference image or the part of the image which is suitable to be taken as the reference.

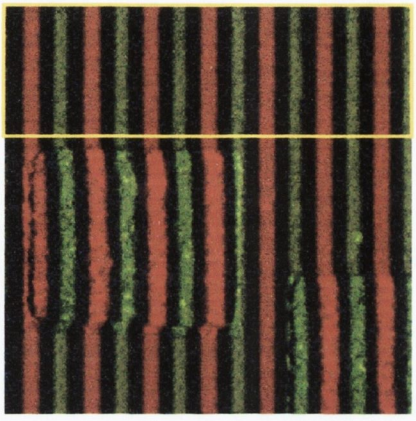

Fig. 6.3: A *256x256* image consists of solder paste. The noise in the image has been de-speckled

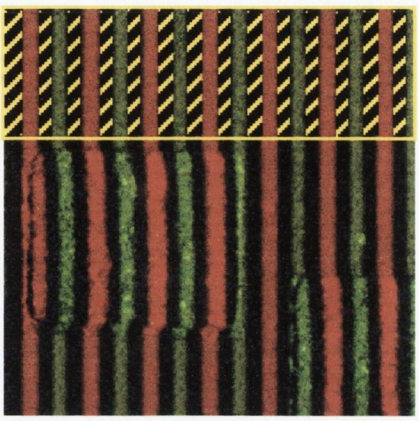

Fig. 6.4: Image showing the segmented regions of Figure 6.3

For our analysis, the procedures were simplified by taking the top part of Figure 6.3 as the reference image, where there are no holes or solder paste; however, a more accurate reference image/plane can be selected by the method described in Section 5.5. From the segmented regions in Figure 6.4, the value of the black segmented threshold T_{Bseg} is determined as *42*; this value is a reasonable approximation. For any pixels whose red, green and blue intensity components are lower than this threshold value, the pixel is considered as black as defined by equation (5-11).

After the black pixels from the black fringes have been extracted, the green and red fringes are now ready to be extracted using the assumptions discussed in Section 5.4.4. It is important to firstly account for those pixels in the green fringes which consist of high value of green but with an even higher value of red intensity components due to luminance brightness projected by the lighting conditions, else ambiguities may arise in the proceeding step due to the violation of the laws of relative equalities. Figure (6.5a-c) shows the red, green and blue channels of the image. By using the Image Channel Subtraction technique as discussed in Section 5.4.4, the removal of the inappropriate red components in the red channel can be easily achieved. This is carried out by subtracting the values of the green palette from the values of its red palette as according to equation (5-13), and so computing a new palette for the red channel. Figure 6.6 demonstrates how the technique operates. Two

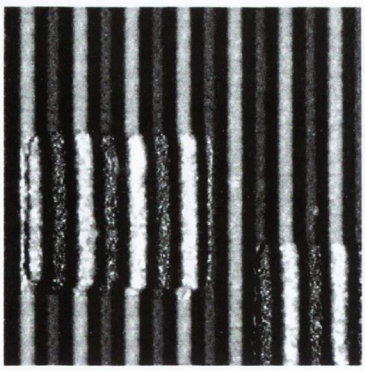

Fig. 6.5a: Red Channel of a solder paste image.

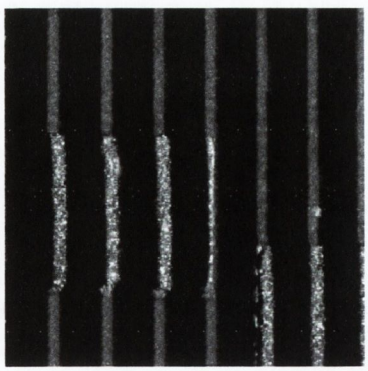

Fig. 6.5b: Green Channel of a solder paste image

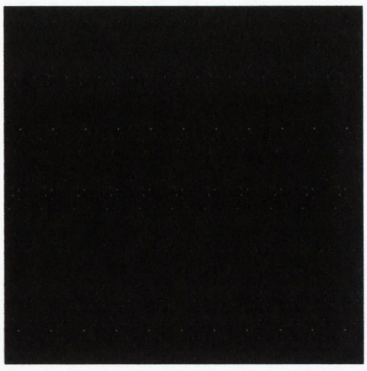

Fig. 6.5c: Blue Channel of a solder paste image

pixels were selected, one pixel lies within the red fringe and the other pixel lies within the green fringe and has a higher red component than its green component. The essence lies on the basis that the red components from the red fringes in the red channel have much higher values compared to their red components in the green fringes of the red channel. After the subtraction of the palette, the values of the resultant red components in the new palette of the red fringes are still much greater than its corresponding green component in the original palette. But, the value of red component in the new palette of the green fringe has a much smaller value than the green component in the original palette.

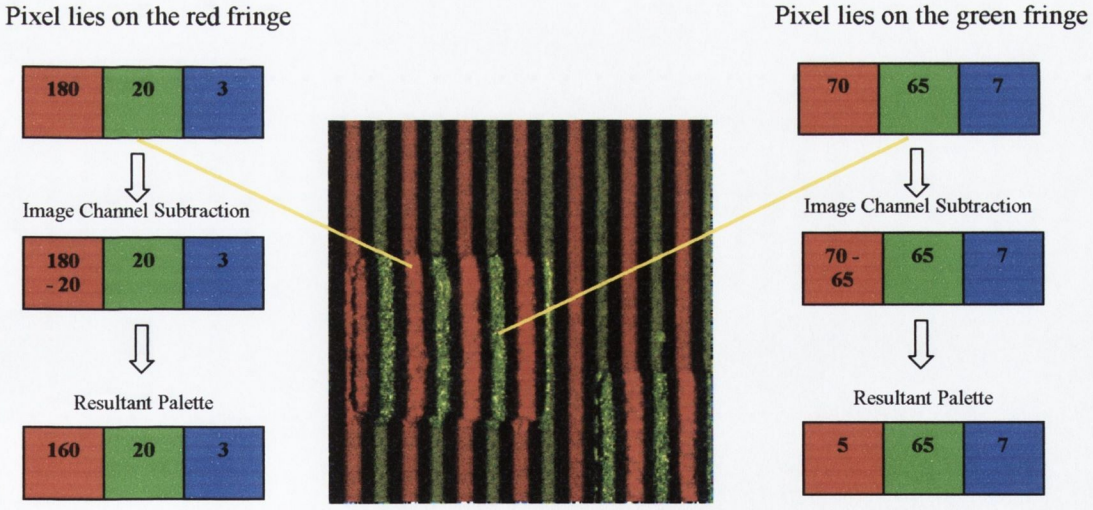

Fig. 6.6: Two different pixels on different colour fringes are split into their channels to demonstrate how the Image Channel Subtraction is performed.

As shown in Fig. 6.7a, the high intensity red components which were embedded in the green fringes shown in the red channel have either been eliminated or consist of a much lower red intensity value. By using the assumptions of relative equality as given in equation (5-14), all pixels can now be properly extracted as shown in Fig. 6.7b.

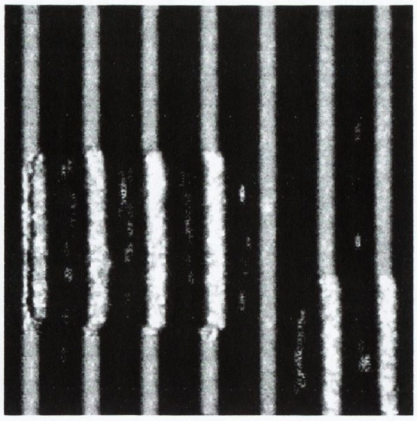

Fig. 6.7a: Red Channel of the solder paste image after image channel Subtraction

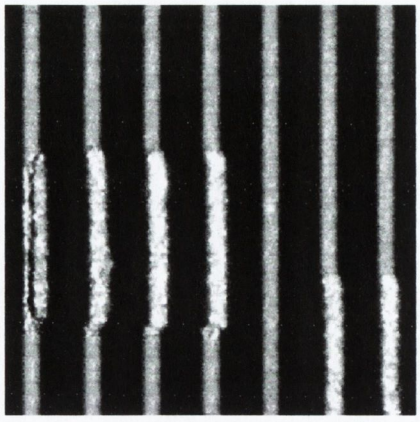

Fig. 6.7b: Red Channel of the solder paste image after all colour extractions using the laws of equality

The final step as shown on the flowchart at the end of Chapter 5, is the Colour Comparison technique. It determines the actual sideways displacement caused by the height of the solder paste by comparing each row of the image with its appropriate reference plane as explained in Section 5.4.6. Figure 6.9 shows the result of the 3D rotate-able surface representation of the solder paste pad as shown in Figure 6.8. The 3D representation was generated using C++ and OpenGL computer graphics languages.

Fig. 6.8: The original image with colour pattern of the solder paste in the PCB

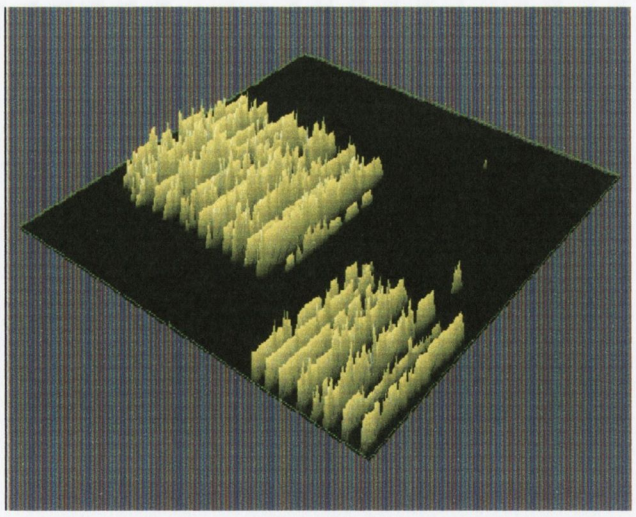

Fig. 6.9: 3D re-model of the solder paste in Figure 6.8.

The total execution time for the Geometric profilometry with Colour Encoded Structured Light pattern recognition to complete on a 200*Mz Pentium* PC, running on *Windows 95* is approximately *180ms* for a *256x256* pixel image. It is reasonably fast as it does not require any complicated calculations of multiplication, division or phase unwrapping operations unlike the phase profilometries. The height of this rectangular

solder paste profile was calculated using the trigonometric formula in equation (5-3), where the angle α, was projected at an angle of 60 degrees to the reference plane. The average height was calculated to be approximately $265\mu m$. The exact height of the solder paste pads on the PCB supplied by Motorola are not available, but can be expected to be of an approximate range between $200\mu m$ - $300\mu m$, the calculated height value is in the range accuracy. A comparative test will be presented in the next Section. Due to the unavailability of any height reference solder paste pads, the assessment of the accuracy in the reconstruction of the 3D shape of solder paste can only be done on an approximate basis.

6.3 Problems and Discussions

Unlike the phase profilometries investigated, a totally different approach was taken for this work, shifting from pure digital signal/image processing to a more computer vision based approach. In digital signal processing, the 2D image was tackled in terms of signal, frequency or phase elements that required many filters to eliminate the unwanted harmonics in order to extract the phase information from the image. An alternative to these ideas has been shown with the CESL algorithm, by analysing the image in terms of its colour and pixel elements, and processing it with a combination of computer image processing techniques.

The main objective for the development of this work was to obtain a more accurate system that would avoid the unwrapping problem due to the arctangent operation and other drawbacks associated with Phase Profilometry techniques, that would also be capable of employing a higher fringe frequency so as to improve the lateral displacement, which was limited by the maximum spatial frequency of the fringe pattern if phase profilometry techniques were used. The sequence of the stripes were unambiguously identified if the deviation (i.e. the relative lateral displacement caused by the objects' height) is greater than the grating period, (i.e. if the fringe distorted more than two fringe pulse widths). This in turn caused inaccurate computation for the phase unwrapping operation, which is used to correct the discontinuities of the wrapped signal (arctangent operation) to determine the desired phase deviation. From such behaviour, it is therefore difficult to employ a high fringe frequency grating as it imposes a very narrow restriction on the height of the object being inspected, even though in theory, the higher the fringe frequency, the more

accurate the result. The restriction was overcome by the utilisation of Colour Encoded Structured Light (CESL), for which this work is based on. The introduction of colour stripes allows precise idenfication of each stripe and a possible measure of object height with lateral displacement until the next equivalent colour fringe as demonstrated in Figure 5.15a and 5.15b, which implies the use of higher fringe grating. In our application, only two colours were employed in the grating. This allows the CESL method to measure twice the amount of the lateral displacement at the same grating frequency of the phase profilometry techniques. As the amount of colours increase in the employment of the grating, the lateral displacement increases by the same fold, thus allowing even greater accuracy.

Another major advantage of this colour profilometry over the phase profilometries is that it is not required to operate at a certain grating frequency. As has already been discussed in Section 4.4, Signal Domain Profilometry is not suitable when utilised in conjunction with low-frequency fringe pattern, and the FIR filter must be re-designed to filter any subsequent different fringe frequency as shown in the simulation in Section 4.4.3. With the New Fast Phase Profilometry, the comb filters which were applied for the elimination of unwanted harmonics can only be tuned to eliminate the exact central frequency of the main noise spectrum if the ratio of the sampling frequency and the grating frequency is an integer number, $f_s/2f_o$. And the Fourier Transform Profilometry requires a known grating frequency for the design of the filter's bandwidth. However, for FTP, the grating frequency is much easier to determine and can be done by computer automation as described in Section 3.2.1.

Unfortunately, similar to Moiré contouring, the colour encoded pattern recognition technique can only provide height distribution information along a discrete set of contour lines. As shown by the 3D reconstruction model in Figure 6.9, only the pixels which lies at the edges of the fringes are computed. One should also note that PCB inspection systems strongly rely on the CAD layout with accurate knowledge of the pad positions. This would allow neglecting holes and dark areas, which the comparison algorithm does not take into account. Another drawback of the comparison algorithm is that the matching is executed by counting the number of pixels which must be converted back into real practical measurement terms using IO_{ratio} for meaningful results. The image to object conversion ratio (IO_{ratio}), although only requires as a once-off calculation, may be difficult to approximate precisely.

With only one set of fringe patterns projected onto the reference surface at a particular direction, the results of the perturbed image would only give an approximate area at the objects' edges that are parallel to the fringes if these edges lies within a black fringe. This kind of inaccuracy can only be avoided if a second projection system is used. However, by using higher frequency colour grating, the resolution can be increased significantly.

The whole set of procedures was repeated many times in different parts of many different boards to test the speed and uniformity of the system. A repetition test was also performed by first capturing a solder paste pad in one direction as shown in Figure 6.10 and then capturing the same solder paste pad in a direction perpendicular to it as shown in Figure 6.11. In Figure 6.10, the bottom left hand corner of the image consists of a darker shade, which was affected by non-uniform lighting conditions.

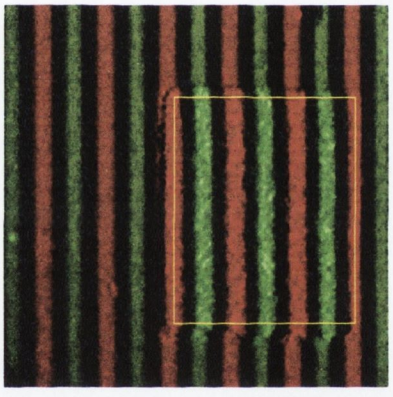

Fig. 6.10: Rectangular Solder Paste Deposit with Colour Projection

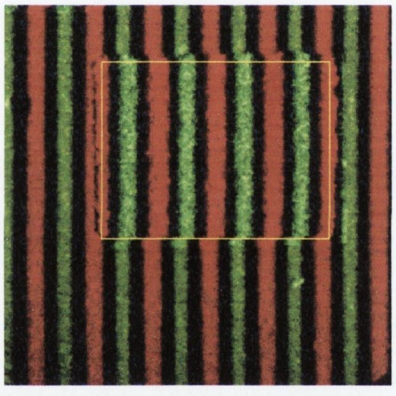

Fig. 6.11: Repetition test of the identical Rectangular Solder Paste with Colour Grating Pattern.

But since that part of the image does not consist of any solder paste pad, and for the purpose of showing how non-uniform lighting may affect the final outcome of the 3D model and also to minimise processing time, photometric decalibration was not performed on the image (See Appendix C.1 for information on photometric decalibration). The same rectangular solder paste pad was then re-captured in a different position *90* degrees from the original image to fulfil the repetition test. The first image has grating fringes vertically projected onto it, while the grating fringes are projected horizontally on the PCB in the second image. The 3D re-models of the solder paste pad are shown in Figure 6.12 and 6.13 respectively. When carrying out the repetition test, it is impossible to pinpoint and compare one single pixel on the solder paste pad in both images. Since the number of fringes projected is different, the

pixel which lies on the edge of a fringe in one image might not necessarily lie on the edge of a fringe in the other image. And as mentioned earlier in this Section, it is not possible to measure the height on the pixels between the fringes. The solution was to determine an average height on the main area of the solder paste pad that according to the CAD layout, lies within the yellow box[i]. The whole procedure was repeated 3 times before an average height was computed to check the consistency of the operation. Unlike the phase profilometry techniques, synthetic images produced by computer programs can not be used to assess the accuracy, since this technique calculates the topography of the object by counting and matching the number of pixels shift by the fringes, thus, 100% accuracy would be achieved if synthetic images are used for the accuracy assessment. Although, no reference height solder paste pad is available to compare the computed result, the approximate solder paste height in the PCB given by Motorola should be in the range of $200\mu m - 300\mu m$. Both images seem to yield a constant result in the test.

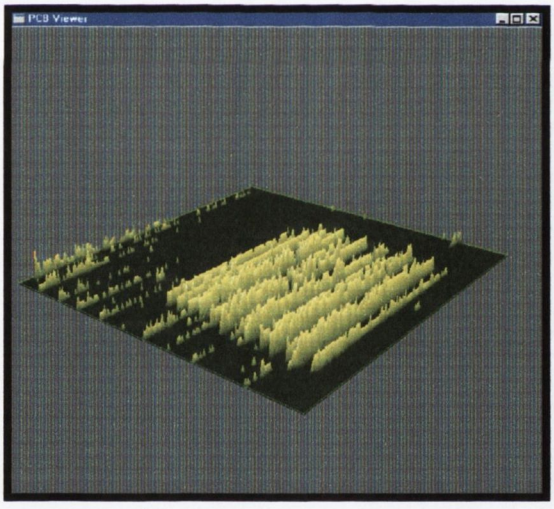

Fig. 6.12: 3D Re-model of the Rectangular Solder Paste. Note: the bottom left-hand corner – the errors are due to unclear dark image as shown in Figure 6.10.

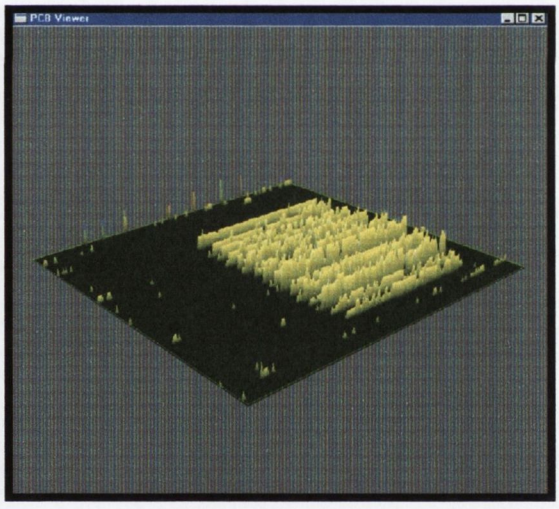

Fig. 6.13: 3D Re-model of the Rectangular Solder Paste from the Repetition Test.

Image	*Height 1*	*Height 2*	*Height 3*	*Average Height*
Vertical Image	$280\mu m$	$272\mu m$	$295\mu m$	$282\mu m$
Horizontal Image	$265\mu m$	$280\mu m$	$312\mu m$	$285\mu m$

Table 6.1: Table showing the average height in the repetition test using the geometric profilometry with CESL pattern recognition

[i] Note: 5 pixels width was subtracted on each edge since the edges usually consist of less paste.

6.4 Conclusions

The use of colour encoded structured light pattern for this application is an attractive way of improving the grating frequency particularly the size of the object in question is small. In the next part of the thesis a new approach which combines some of the advantageous algorithms of the phase profilometry and the colour encoded structured light technique is presented.

Chapter 7

Rectangular Pulse Phase Profilometry and Colour Encoded Structured light Pattern Recognition

7.1 Introduction

In this part of the thesis, a novel approach which combines some of the advantages of phase profilometry algorithms with those of the colour encoded structured light technique is presented. An explanation of the reasons why and how this technique comes about, and what merits this technique provide over the previous techniques is firstly discussed. The mathematical digital signal theory of the algorithm is then derived. Finally, the step by step simulations and implementations of the technique are illustrated and the effectiveness of the results is assessed.

7.2 Objectives

In Chapter 4, Section 4.4, the factors associated with the grating frequency were investigated. It was proved and shown diagrammatically that the higher the grating frequency, that is the more fringes in a sampled image, the better the resolution of the recovered phase profile. In addition, the extraction of the phase information can be performed more accurately with a high grating frequency since the bandwidth of the Fourier spectrum is wide and thus, there is little overlap between the harmonics. The fundamental harmonic can then be extracted in a relatively easy manner using simple filtering operations. However, the maximum spatial grating frequency is limited by the lateral movement of the projected fringes due to the object's height. If the object being inspected is of a certain height and the relative lateral deviation is greater than the maximum spatial grating frequency, then, the phase deviation would deviate more than the fringe period, resulting in an unresolveable phase shift. This drawback was overcome by introducing the colour encoded structured light pattern in Part II of the thesis. With the colour RGB image, the image can be separated into 3 channels containing its corresponding colour constituents. Thus, the frequency of the fringe grating can be increased up to a factor related to the number of different colour fringes used, and the lateral deviation from the range of measurements should then be

sufficient without surpassing the maximum limit imposed by the spatial grating frequency. The grating frequency is directly related to the accuracy of the phase extraction and must be compromised with the object's height itself. Normal black and white square wave gratings [62,63] with a set of different fringe frequencies ranging from low to high frequency gratings can be used to replace the colour pattern projection. However, this will result in more captured images of the same scene, which is totally inefficient in terms of computational speed and memory space.

The main deficiency of the Geometric Profilometry with Colour Encoded Structured Light pattern technique is the Colour Encoded Comparison algorithm. It uses a template matching approach to derive the actual sideways displacement arising from the height of the solder paste by comparing each row of the image with its appropriate reference plane. The main problem is that it does not provide any height computation within the fringes, only the pixels which lie at the edges of the fringes are computed. This is similar to Moiré topography where the height distribution information is given only along a discrete set of contour lines as explained in Section 4.5. Also the comparison of the template is executed by counting the number of pixels from the fringe movement which must be converted back into actual realistic displacements for meaningful results. The image to object conversion ratio (IO_{ratio}), although required only as a once-off calculation, may be difficult to acquire and approximate accurately. In an attempt to avoid this possible error, the Colour Encoded Comparison algorithm is replaced by one of the digital signal phase profilometry methods discussed in Part I of the thesis. By investigating the problems and drawbacks from the study of all the profilometries that have been examined so far and combining the competent algorithms of the two parts of this thesis, it is possible to devise a solder paste inspection system which would provide accurate, low-cost and real time measurements.

7.3 Rectangular Pulse Phase Profilometry and CESL

The concept of the colour encoded structured light pattern projection technique (before applying the phase profilometry) is precisely identical to a normal square wave Rochi grating structured light technique as defined in Section 2.4.1. The only exception is that when the colour structured light image pattern is separated into its RGB channels, the displacement spectrum is of a rectangular pulse wave rather than a

square wave. The image must be split into the 3 colour RGB channels before implementing the phase extraction algorithm. Among the three phase extraction profilometries previously studied, the Fourier Tranform Profilometry (FTP) was chosen for use in conjunction with the colour encoded structured light pattern. FTP provides the most accurate results and can be readily employed for the extraction of phase information in the frequency domain. The other two techniques produce too many unnecessary complications as discussed in Section 4.5. The main disadvantage of FTP is its computation load associated with the calculation of *FFT-IFFT*, but with the ever-increasing speed of today's computers, it has the potential for an on-line solder paste inspection.

The principle of the Structured light technique is once again employed. A periodic colour fringe pattern is projected onto the object and imaged by a camera from an offset position. The fabrication process of the colour fringe pattern is the same as for the Geometric Profilometry with CESL pattern described in Chapter 5.

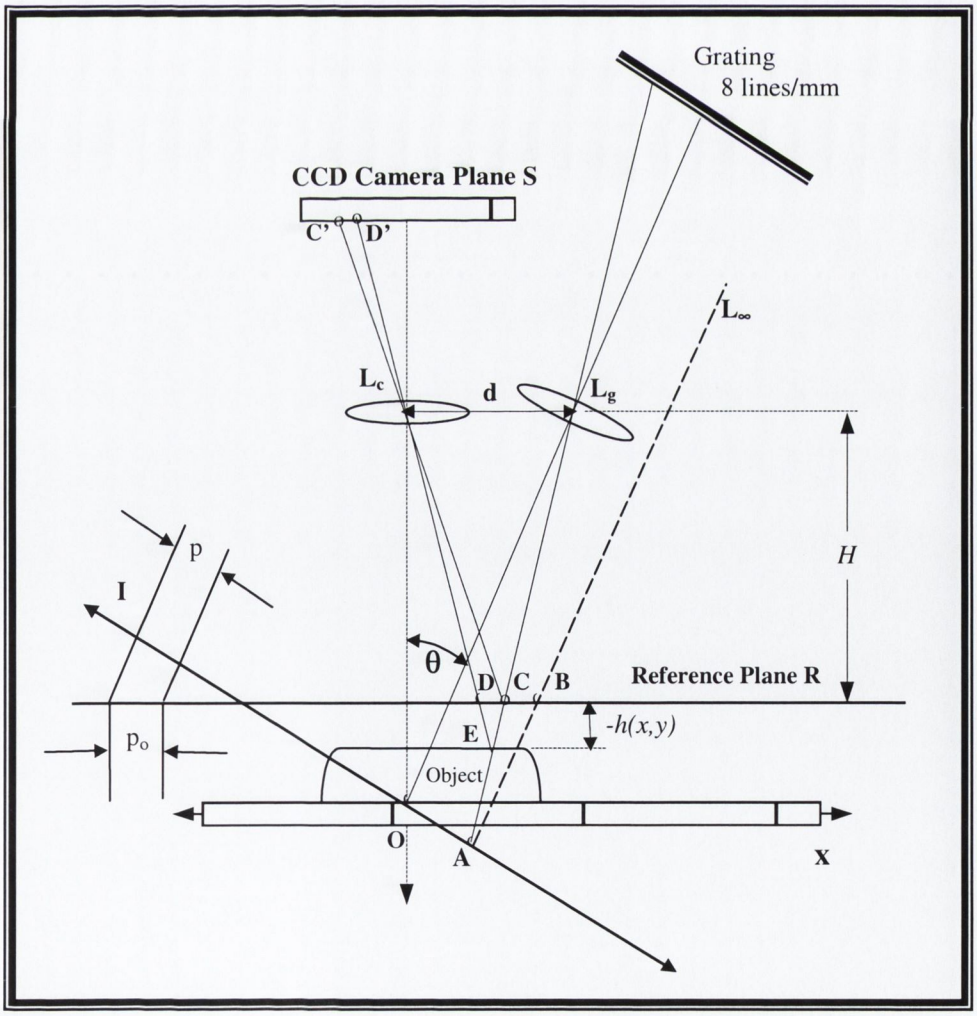

Figure 7.1: Crossed-optical-axes geometry for Rectangular Pulse Phase Profilometry and CESL Pattern Recognition

Recall the optical geometry of the Crossed Optical Axes Structured Light technique in which there are 3 cases to consider. The first is the telecentric projection case, where the projector is situated at an infinity point and the projector rays can be assumed to be in parallel. If the object is a flat surface, the grating pattern viewed by the camera is periodic and can be expressed as,

$$a(x, y) = \sum_{n=-\infty}^{+\infty} A_n e^{j(2\pi n f_o x)} \tag{2-13}$$

where

f_o is the fundamental frequency of the observed grating image
x is chosen as in the figure (8.1)
y axis is normal to the plane of the figure = $1/p_o = cos\theta/p$

The second case is when the projection rays from the grating are projected at a finite distance, and the projector rays are no longer parallel. This causes the periodic grating image to deform or shift from the original position B to C as shown in Figure (7.1), even in the presence of a flat surface as captured from the sensor plane. The imaged pattern is given by,

$$a_o(x, y) = \sum_{n=-\infty}^{+\infty} A_n e^{j(2\pi n f_o [x + s_o(x)])} \tag{2-14}$$

where

$s_o(x) = \overline{BC}$ is a function of x as in the figure (7.1)
$\overline{BC}$ = the distance shift from B to C due to the non-telecentric projection

To present the series in terms of its phase-modulated harmonics, the distance shift can be represented in terms of phase shift as follows:

$$\phi_o(x) = 2\pi f_o s_o(x) \tag{2-15}$$

$$a_o(x, y) = \sum_{n=-\infty}^{+\infty} A_n e^{j(2\pi n f_o x + n\phi_o(x))} \tag{2-16}$$

Consider the general case where the object has a height greater than zero. The periodic grating image is now further deformed from the original position B to D due to the height of the object as shown in Figure (7.1). The viewed pattern can be written as

$$a(x, y) = r(x, y) \sum_{n=-\infty}^{+\infty} A_n e^{j2\pi n f_o (x + s(x,y))} \tag{2-17}$$

where

$s(x,y) = \overline{BD}$, the shift from point B to point D
$r(x,y)$ represents the non-uniform reflectivity of object's surface

By re-writing equation (2-17) in terms of the phase-modulated summation,

$$\phi(x) = 2\pi f_o s(x,y) \tag{2-18}$$

$$a(x,y) = r(x,y)\sum_{n=-\infty}^{+\infty} A_n e^{j(2\pi n f_o x + n\phi(x,y))} \tag{2-19}$$

where

$\phi(x,y) = 2\pi f_o s(x,y) = 2\pi f_o \overline{BD}$

$r(x,y)$ represents the non-uniform reflectivity of object's surface

Equation (2-19) represents the deformed grating colour pattern image expressed as a sum of harmonics with spatial carrier frequencies nf_o modulated both in phase $\phi(x,y)$ and amplitude $r(x,y)$. The deviation of the deformed colour pattern caused by the height of object is shown in Figure 7.2. The frequency f_o is defined by the period P_o as shown in Figure 7.2.

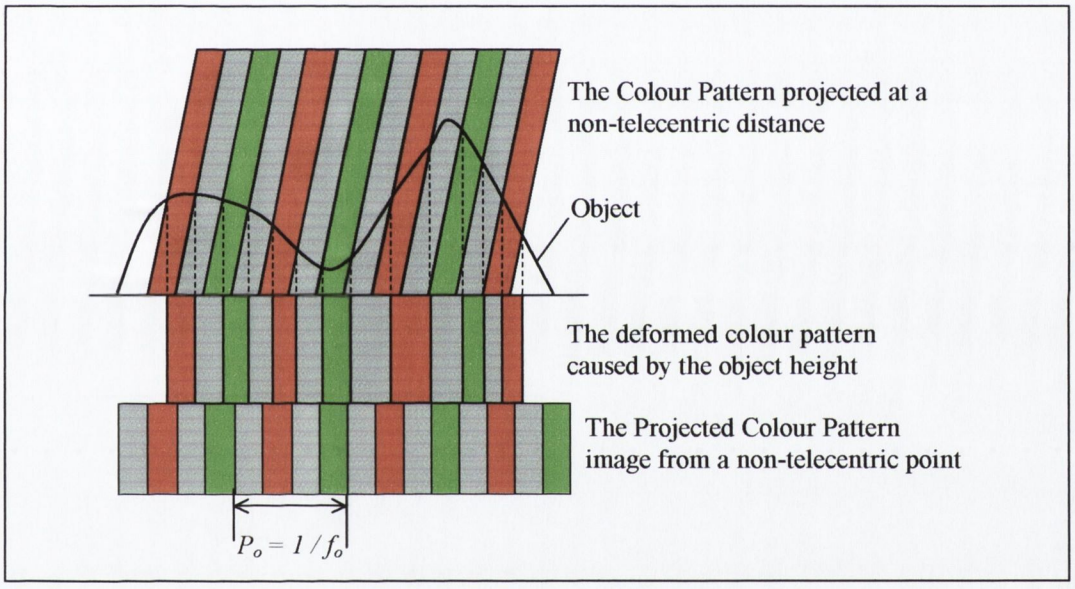

Fig. 7.2: The deformed colour pattern caused by an object

With the use of colours, the image pattern must be separated into their appropriate channels by thresholding and then converted into a 256 greyscale image before computing the phase. Before phase extraction, each gray scale image is processed using the first four stages of the Colour Encoded Recognition Algorithm,

- De-Speckling Technique.
- Colour Extraction with the laws of relative equality technique.
- Black Colour Threshold using Segmentation – (T_{Bseg}).
- Image Channel Subtraction.
- Fourier Transform Phase Profilometry.

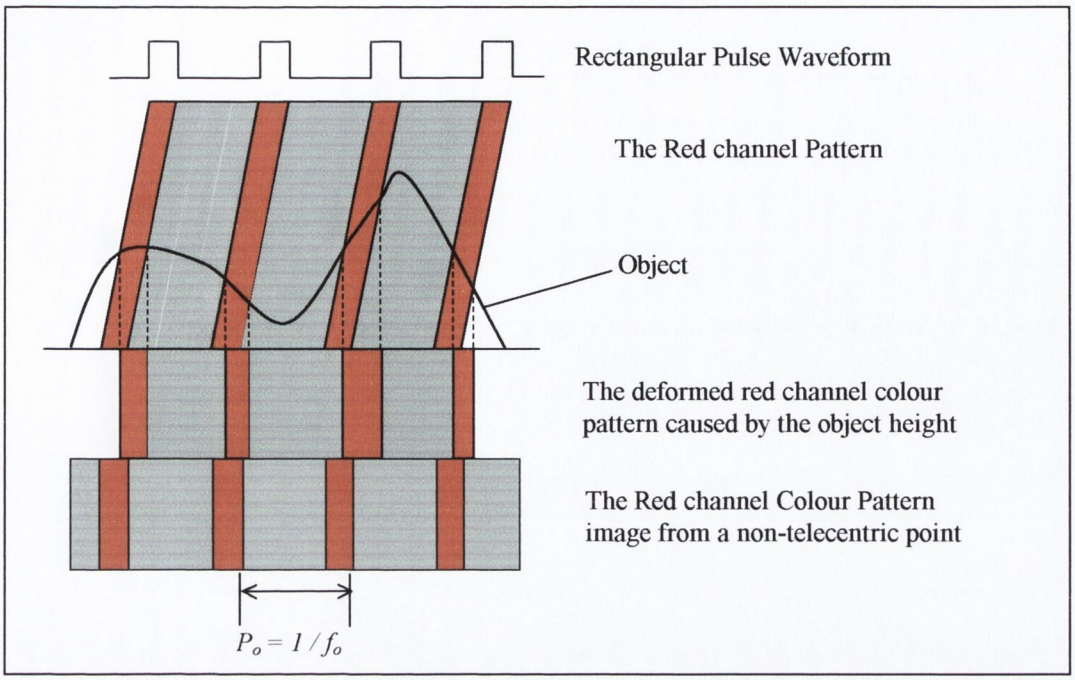

Fig. 7.3: The Red Channel of the deformed colour pattern caused by an object

Figure 7.3 shows the red channel of the original deformed colour image of Figure 7.2. The deformed grating colour pattern image expressed as a sum of harmonics with spatial carrier frequencies nf_o modulated both in phase $\phi(x,y)$ and amplitude $r(x,y)$, as represented in equation (2-19), has became a deformed rectangular pulse wave image that repeats periodically with the period P_o. After the colour pattern image is separated into its RGB channels, the Fourier Transform phase profilometry algorithm is executed on each of the channels to extract the phase information.

Fourier Transform Profilometry is accomplished by suitably modifying the frequency spectrum of the grating image in order to extract the phase deviation arising from the 2-D perturbed image due to the topography of the object.

Equation (2-19) can be rewritten as a representation of the Fourier Transform as follows:

$$g_{red}(x,y) = \sum_{n=-\infty}^{+\infty} q_n(x,y) e^{j2\pi n f_o x} \tag{7-1}$$

$$q_n(x,y) = A_n r(x,y) e^{jn\phi_{red}(x,y)}$$

where

$g_{red}(x,y)$ is the Fourier series representation of the red channel grating image

By using Fourier Transform theorem with y being fixed, the one-dimensional Fourier transform of image row $y = \bar{y}$ with respect to x of $q_n(x,y)$ can be computed as

$$G_{red}(f,\bar{y}) = \Im\left[g(x,\bar{y})\right] = \int_{-\infty}^{+\infty} g(x,\bar{y}) e^{-j2\pi fx}\, dx \tag{7-2}$$

$$= \sum_{n=-\infty}^{+\infty} Q_n(f - nf_o, \bar{y}) \tag{7-3}$$

where

$Q_n(f,\bar{y})$ is the 1-D Fourier transform with respect to x of $q_n(x,\bar{y})$

$G_{red}(f,\bar{y})$ is the 1-D Fourier transform with respect to x of $g_{red}(x,\bar{y})$

Note: y is treated as a fixed parameter, and in this case the row $\bar{y}$ is chosen.

Either of the two spectra, $Q_1(f - f_o, \bar{y})$ or $Q_1(f + f_o, \bar{y})$ centred on the carrier frequency $\pm f_o$ can be selected as they consist of the identical information. A narrow frequency domain filter centred on $+f_o$ is then used to extract one of these fundamental harmonics; $Q_1(f - f_o, \bar{y})$ was chosen. The harmonic is then translated by f_o on the frequency axis towards the origin to obtain $Q_1(f,\bar{y})$. The inverse Fourier Transform is then performed on $Q_1(f - f_o, \bar{y})$, to obtain $g_1(x,\bar{y})$:

$$g_{red1}(x,\bar{y}) = \Im^{-1}\left(Q_1(f,\bar{y})\right)$$

$$g_{red1}(x,\bar{y}) = q_1(x,\bar{y}) e^{j2\pi f_o x} = A_1 r(x,\bar{y}) e^{j(2\pi f_o x + \phi_{red}(x,\bar{y}))} \tag{7-4}$$

The same operations are performed on the image of the undistorted red channel grating pattern, or the chosen reference row as given by equation (2-16),

$$g_{red\,o}(x,y) = \sum_{n=-\infty}^{+\infty} A_o e^{j(2\pi n f_o x + n\phi_{red\,o}(x))} \tag{2-16}$$

$$\Rightarrow \quad g_{red\,o}(x,\bar{y}) = A_1 e^{j(2\pi f_o x + \phi_{red}(x))} \tag{7-5}$$

To evaluate the phase deviation, $\Delta\phi_{red}(x,\bar{y})$, the Fourier-series of $g_{red1}(x,\bar{y})$ and the complex conjugate of $g_{red\,o}(x,\bar{y})$ can be multiplied together so as to cancel the original and first harmonic phase components.

$$g_{red\,o}^{*}(x,\bar{y}) g_{red1}(x,\bar{y}) = |A_1|^2 r(x,y) e^{-j(2\pi f_o x + \phi_{red\,o}(x))} e^{j(2\pi f_o x + \phi_{red}(x))} \tag{7-6}$$

From the principle of structured light and phase profilometry, the phase deviation is calculated by taking the phase change of the original reference grating pattern from the phase change of the deformed grating pattern due to the topography of the object,

$$\Delta\phi_{red}(x, y) = \phi_{red}(x, y) - \phi_{red\,o}(x, y) \tag{7-7}$$

This is calculated by multiplying the Fourier-series of $g_{red}(x, \bar{y})$ and the complex conjugate of $g_{red_o}(x, \bar{y})$ as shown in equation (7-8),

$$H_{red}(x, \bar{y}) = g_{red\,o}{}^{*}(x, \bar{y}) g_{red\,1}(x, \bar{y}) = |A_1|^2 r(x, y) e^{j\Delta\phi_{red}(x,y)} \tag{7-8}$$

The amplitude modulation caused by the reflectivity is hidden in the real part of $H_{red}(x, \bar{y})$, whereas the phase deviation $\Delta\phi_{red}(x, \bar{y})$ caused by the distortion of the fringes can be extracted from the imaginary part. The phase distribution $\Delta\phi_{red}(x, \bar{y})$ must be separated from the unwanted variation of reflectivity *r(x,y)* in the real part of $H_{red}(x, \bar{y})$. By computing the complex logarithm of equation (7-8), the real and imaginary parts are separated:

$$\log[H_{red}(x, \bar{y})] = \log\left[|A_1|^2 r(x, y)\right] + i\Delta\phi_{red}(x, y) \tag{7-9}$$

The phase deviation $\Delta\phi_{red}(x, \bar{y})$ is now completely separated from the unwanted variation of the reflectivity *r(x,y)*. Alternatively, the phase deviation can be found by computing the angle using the arctangent operation

$$\Delta\phi_{red}(x, \bar{y}) = \tan^{-1} \frac{\mathrm{Im}(H_{red}(x, \bar{y}))}{\mathrm{Re}(H_{red}(x, \bar{y}))} \tag{7-10}$$

where

Im denotes as the imaginary part of the processed image row
Re denotes as the real part of the processed image row

Once the amount of phase deviation $\Delta\phi_{red}(x, \bar{y})$ associated with the topography of the object for the red channel grating image is derived, the actual height of the part of the object that is embedded in the red channel can be calculated using the expression below,

$$\Delta\phi_{red}(x, y) = 2\pi f_o \overline{CD} \tag{7-11}$$

$$\overline{CD} = \frac{\Delta\phi_{red}(x, y)}{2\pi f_o}$$

where

$\Delta\phi_{red}(x, \bar{y})$ is the phase deviation associated with the shape of the object in the red channel image.

$\overline{CD}$ is the distance shifted due to the shape of the object.

An expression for the height distribution $h_{red}(x,y)$ as a function of the phase deviation $\Delta\phi_{red}(x, \bar{y})$ is derived using the same theory as in section 2.5:

$$h_{red}(x,y) = \frac{H\Delta\phi_{red}(x,y)}{\Delta\phi_{red}(x,y) - 2\pi f_o d} \tag{7-12}$$

Similarly, the phase deviations and the resultant heights of the green channel are extracted using the same procedure given above. The two image channels are then combined together to form a full height map of the object according to the pixel positions of each colour fringe in the thresholded image. The height distribution information of the non-colour fringes can be determined by approximating to the nearest colour fringe or, alternatively, interpolation of height values from one of the channels can be used since there should be little difference between the height values of both the red and green channels.

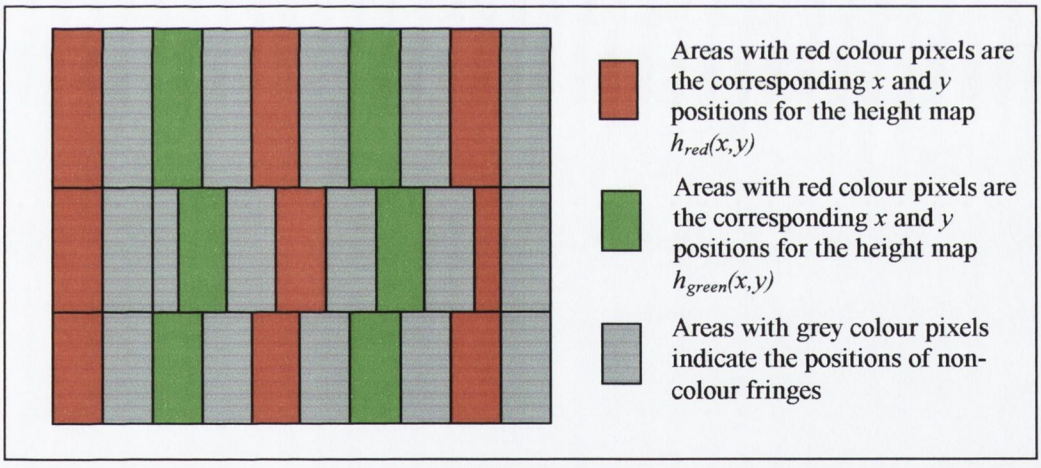

Fig. 7.4: The height positions for the combined image

7.4 Square Wave Vs Rectangular Pulse

A deformed square wave grating image which can be expressed as a sum of harmonics with spatial carrier frequencies nf_o modulated both in phase $\phi(x,y)$ and amplitude $r(x,y)$ as defined in Chapter 2 equation (2-19) is firstly considered. For clarity purposes, the equation is re-shown.

$$a(x,y) = r(x,y)\sum_{n=-\infty}^{+\infty} A_n e^{j(2\pi n f_o x + n\phi(x,y))} \tag{2-19}$$

$$a(x,y) = r(x,y)\sum_{n=-\infty}^{+\infty} A_n e^{j(2\pi n f_o x + n\phi(x,y))} \tag{2-19}$$

where

f_o is the fundamental frequency of the observed grating image

$\phi(x,y) = 2\pi f_o s(x,y)$ = is the phase deviation

$r(x,y)$ represents unwanted irradiance variations arising from the non-uniform light reflectivity or transmission of the object's surface

The phase carries information about the 3D shape of the object in question, and to obtain this phase deviation $\phi(x, \bar{y})$, it must be separated from the unwanted amplitude variation $r(x, \bar{y})$ caused by non-uniform reflectivity on the object surface. The maximum phase deviation, [that is the maximum amount of distance shift caused by the topography of the object limited by the grating frequency] for a normal black and white square wave grating is one grating period which when expressed in Fourier series is indicated by 2π. The operation can be accomplished by filtering a single selective spectral component of the fundamental frequency.

Similarly, a deformed rectangular pulse wave image that repeats periodically should also be expressable as a sum of harmonics and should also be of the same form as equation (2-19). The maximum phase deviation for a rectangular pulse wave is also 2π when expressed in Fourier series, even though the pulse width is different. In order to interpret the difference between the two waves, their Fourier series are computed and analysed.

The general form of the Fourier Series [67] is given by,

$$f(x) = a_o + \sum_{n=1}^{\infty}\left(a_n \cos\left(\frac{n\pi}{L}x\right) + b_n \sin\left(\frac{n\pi}{L}x\right)\right) \tag{7-13}$$

and their coefficients are calculated from the below equations:

$$a_o = \frac{1}{2L}\int_{-L}^{L} f(x)\, dx \tag{7-13a}$$

$$a_n = \frac{1}{L}\int_{-L}^{L} f(x)\cos\left(\frac{n\pi}{L}x\right) dx \tag{7-13b}$$

$$b_n = \frac{1}{L}\int_{-L}^{L} f(x)\sin\left(\frac{n\pi}{L}x\right) dx \tag{7-13c}$$

$$L = \frac{T}{2} \qquad , n = 1,2,3,.... \tag{7-13d}$$

For a square wave :

The square wave shown opposite has a period of T, the function $f(x)$ is given as,

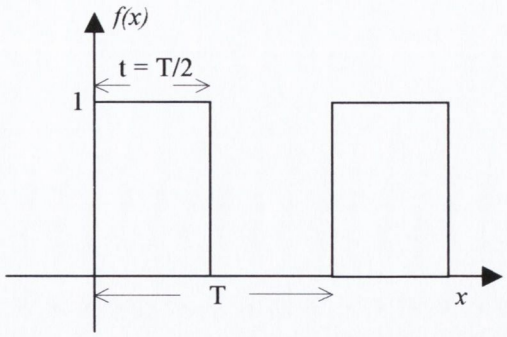

$$f(x) = \begin{cases} 1 & 0 < x < T/2 \\ 0 & T/2 < x < T \end{cases}$$

Using the above equations, the Fourier series of the square wave pattern can be expressed as

$$f(x) = \frac{1}{2} + \frac{2}{\pi}\sin\left(\frac{2\pi}{T}x\right) + \frac{2}{3\pi}\sin\left(\frac{6\pi}{T}x\right) + \ldots \qquad (7\text{-}14)$$

for n = 1,3,... (odd values)

$$f(x) = \frac{1}{2} + \frac{2}{\pi}\sin\left(\frac{2\pi}{T}x\right) \quad for\ n = 1$$

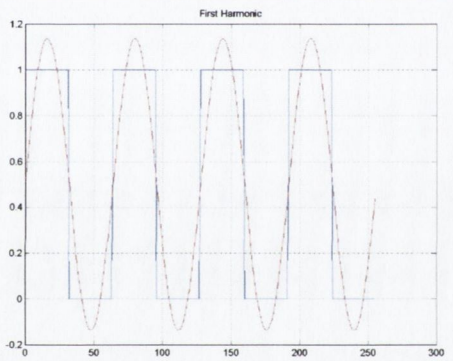

Fig. 7.5a: The first harmonic of a square wave

$$f(x) = \frac{1}{2} + \frac{2}{\pi}\sin\left(\frac{2\pi}{T}x\right) + \frac{2}{3\pi}\sin\left(\frac{6\pi}{T}x\right) + \ldots$$

$for \quad n = 1, 3$

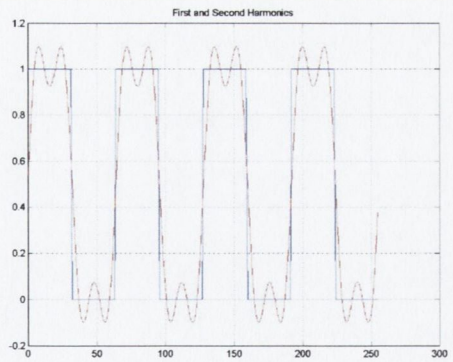

Fig. 7.5b: The first and third harmonics of a square wave

$$f(x) = \frac{1}{2} + \frac{2}{\pi}\sin\left(\frac{2\pi}{T}x\right) + \frac{2}{3\pi}\sin\left(\frac{6\pi}{T}x\right) + \frac{2}{5\pi}\sin\left(\frac{10\pi}{T}x\right) + \ldots$$

$for \quad n = 1, 3, 5$

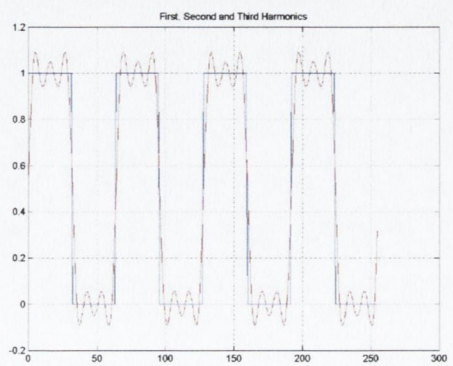

Fig. 7.5c: The first, third and fifth harmonics of a square wave

Hence, the square wave is represented only by the odd harmonics of the fundamental grating frequency. With no even harmonics of the fundamental frequency, the overlap between the frequency component terms of the spectrum is small as they are separated from each other by the grating frequency $2f_o$ and not just f_o as shown in Figure 7.6. Thus, the Fourier transform of the square wave allows a more precise filtering operation of the selective frequency spectral component for phase extraction in the frequency domain. The fundamental grating frequency f_o of the below square wave shown in Figure 7.6 is *16*, there are *16* fringes in the image, the line size of the image is *256*, and the pulse width is *8* pixels wide.

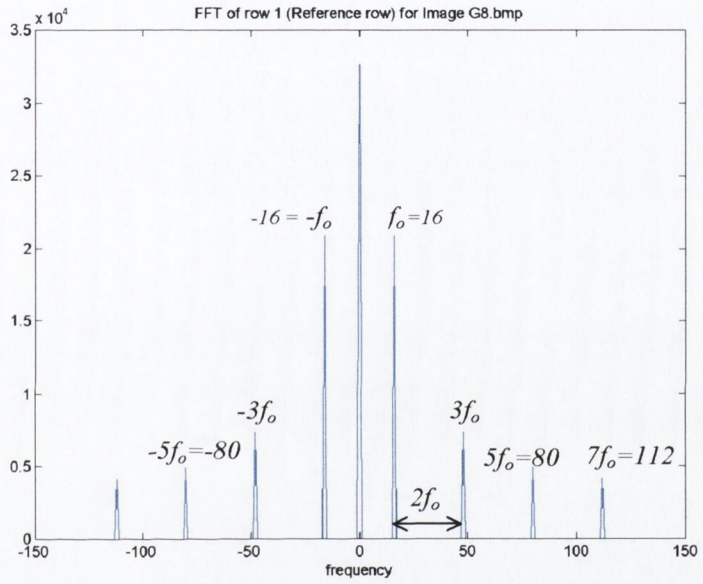

Fig. 7.6: The Fourier Transform of a square wave with 16 pixel/fringe

For a rectangular pulse wave :

The rectangular pulse wave shown opposite has the same period T as the square wave in the previous example, and the function $f(x)$ is given by,

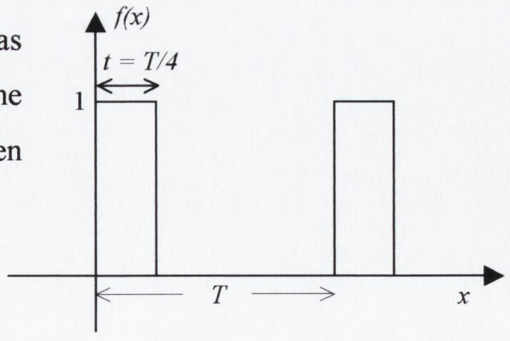

$$f(x) = \begin{cases} 1 & 0 < x < T/4 \\ 0 & T/4 < x < T \end{cases}$$

Using equation (7-1) again, the Fourier coefficients are calculated as follows:

$$a_o = \frac{1}{2\left(T/2\right)} \int_0^{T/4} dx = \frac{1}{T}(x)_0^{T/4} = \frac{1}{4}$$

$$a_n = \frac{1}{T/2}\int_0^{T/4} \cos\left(\frac{2n\pi}{T}x\right) dx = \frac{2T}{2Tn\pi}\sin\left(\frac{2n\pi}{T}x\right)_0^{T/4} = \frac{1}{n\pi}\sin\left(\frac{2n\pi}{T}x\right)_0^{T/4}$$

$$\begin{aligned} a_n &= \frac{1}{n\pi}\left\{\sin\left(\frac{2n\pi}{T}\left(\frac{T}{4}\right)\right) - \sin\left(\frac{2n\pi}{T}(0)\right)\right\} \\ &= \frac{1}{n\pi}\sin\left(\frac{n\pi}{2}\right) \end{aligned} \tag{7-15}$$

$$\begin{aligned} a_n &= 0 && \textit{for all } n = \textit{even} = 2,4,... \\ a_n &= \frac{1}{\pi} - \frac{1}{3\pi} + \frac{1}{5\pi} - \frac{1}{7\pi} + ... && \textit{for all } n = \textit{odd} = 1,3,5,7,... \end{aligned} \tag{7-16}$$

$$b_n = \frac{1}{T/2}\int_0^{T/4} \sin\left(\frac{2n\pi}{T}x\right) dx = \frac{2T}{2Tn\pi}\left[-\cos\left(\frac{2n\pi}{T}x\right)_0^{T/4}\right] = \frac{1}{n\pi}\left[-\cos\left(\frac{2n\pi}{T}x\right)_0^{T/4}\right]$$

$$\begin{aligned} b_n &= \frac{1}{n\pi}\left\{-\cos\left(\frac{2n\pi}{T}\left(\frac{T}{4}\right)\right) + \cos\left(\frac{2n\pi}{T}(0)\right)\right\} \\ &= \frac{1}{n\pi}\left[-\cos\left(\frac{n\pi}{2}\right) + 1\right] \end{aligned} \tag{7-17}$$

$$\begin{aligned} b_n &= 0 && \textit{for all } n = 0,4,8,... \\ b_n &= \frac{2}{2\pi} + \frac{2}{6\pi} + \frac{2}{10\pi} + ... && \textit{for all } n = 2,6,10,... \\ b_n &= \frac{1}{\pi} + \frac{1}{3\pi} + \frac{1}{5\pi} + ... && \textit{for all } n = \textit{odd} = 1,3,5,... \end{aligned} \tag{7-18}$$

The Fourier Series of the rectangular pulse wave is expressed as

$$\begin{aligned} f(x) = \frac{1}{4} + \frac{1}{\pi}\cos\left(\frac{2\pi}{T}x\right) - \frac{1}{3\pi}\cos\left(\frac{6\pi}{T}x\right) + \frac{1}{\pi}\sin\left(\frac{2\pi}{T}x\right) + \\ \frac{1}{\pi}\sin\left(\frac{4\pi}{T}x\right) + \frac{1}{3\pi}\sin\left(\frac{6\pi}{T}x\right) + ... \qquad \textit{for } n = 1,2,3,... \end{aligned} \tag{7-19}$$

$$f(x) = \frac{1}{4} + \frac{1}{\pi}\cos\left(\frac{2\pi}{T}x\right) + \frac{1}{\pi}\sin\left(\frac{2\pi}{T}x\right)..$$

for $n = 1$

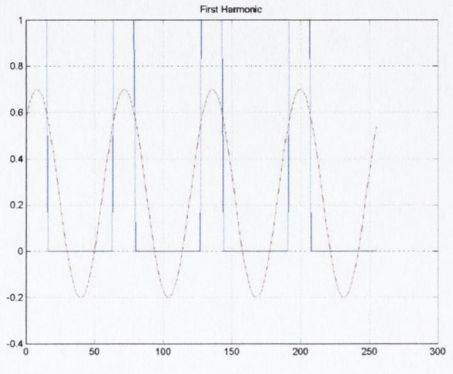

Fig. 7.7a: The first harmonic of a rectangular pulse wave

$$f(x)=\frac{1}{4}+\frac{1}{\pi}\cos\left(\frac{2\pi}{T}x\right)+\frac{1}{\pi}\sin\left(\frac{2\pi}{T}x\right)+\frac{1}{\pi}\sin\left(\frac{4\pi}{T}x\right) \qquad for\ n=1,2$$

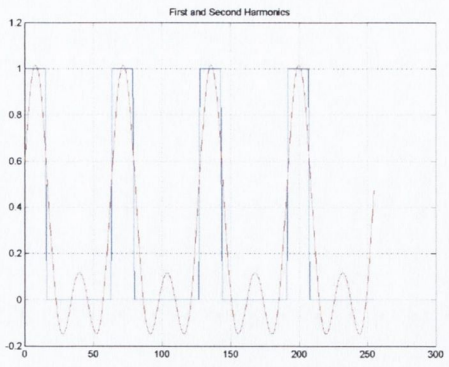

Fig. 7.7b: The first and second harmonics of a rectangular pulse wave

$$f(x)=\frac{1}{4}+\frac{1}{\pi}\cos\left(\frac{2\pi}{T}x\right)-\frac{1}{3\pi}\cos\left(\frac{6\pi}{T}x\right)+\frac{1}{\pi}\sin\left(\frac{2\pi}{T}x\right)+\frac{1}{\pi}\sin\left(\frac{4\pi}{T}x\right)+\frac{1}{3\pi}\sin\left(\frac{6\pi}{T}x\right) \qquad for\ n=1,2,3$$

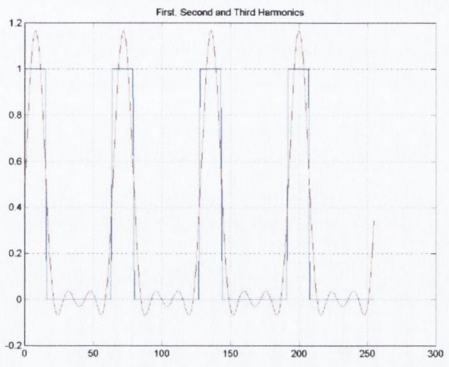

Fig. 7.7c: The first, second and third harmonics of a rectangular pulse wave

By comparing the Fourier series of the square wave in equation (7-14) and the rectangular pulse wave in equation (7-19), the difference is prominent. For the particular example above, apart from the amplitude range of the above series being half that of a regular square wave having the same period, some additional even harmonics and odd harmonics are introduced in order to represent the rectangular pulse wave. This phenomenon is caused by the frequency of the pulse width.

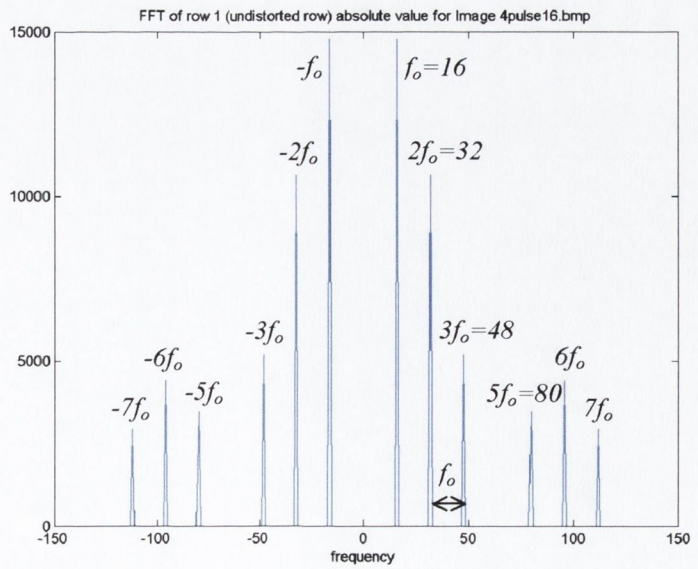

The fundamental discrete grating frequency f_o of the Fourier Transform of the rectangular wave is shown at *16* with a line size of *256 pixels*, the pulse width is *4 pixels* wide. Note: at $4f_o$, $-4f_o$ the components are zero.

Fig. 7.8: The Fourier Transform of a rectangular pulse wave with 4 pixel/fringe

Unlike the Fourier transform of the square wave, the frequency components in the spectrum of the rectangular pulse wave are separated from each other only by f_o as shown in Figure 7.8. This is important since it affects how accurate the filter can perform in the phase extraction process.

From Section 4.4.2 on the subject of the Range of Measurements and the Grating frequency, it was shown that the maximum range of measurements was limited by the rate of change in the height distribution *h(x,y)* in the direction normal to the line of the grating. It was also proved that, if the rate of change in the phase along the same direction is small, then the bandwidth of the spectrum is quite narrow, and thus the overlap between the $Q_n(f,\bar{y})$ terms of the spectrum is small and are separated from each other by the grating frequency f_o.

Apart from the distance separation between the harmonics spectrum which might affect the performance of the phase extraction process, the phase $\phi(x,\bar{y})$ and the amplitude $r(x,\bar{y})$ also play a role. It was mentioned in Chapter 3 that, provided that both $\phi(x,\bar{y})$ and $r(x,\bar{y})$ vary slowly compared to the grating frequency, the overlap between the $Q_n(f,\bar{y})$ terms of the spectrum is small and are separated from each other by the grating frequency f_o. This is illustrated in the diagram below.

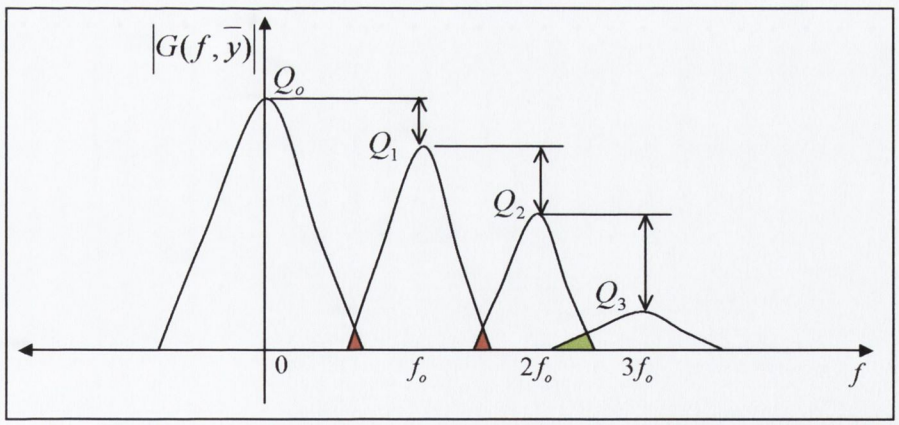

Fig. 7.9: The spectral components demonstrating the overlapping relationship between the amplitude and grating frequency

As shown in Figure 7.9, the differences between the amplitudes of $Q_o(f,\bar{y})$, $Q_1(f,\bar{y})$ and $Q_2(f,\bar{y})$ are quite small, thus the overlapping [indicated by the red coloured area] within the spectrum is less significant in proportion to the size of the spectrum. In contrast, the relative change between the amplitudes of $Q_2(f,\bar{y})$ and $Q_3(f,\bar{y})$ is much larger, causing a significant amount of overlapping [indicated by the green coloured

area] between them since the proportion in $Q_3(f,\bar{y})$ is more significant compare to the size of its spectrum. This overlapping may cause the filter to over extract the phase during the phase extraction process. In order to avoid a significant amount of overlapping during the filtering process, it is favourable to select a spectrum of the fundamental frequency which has the smallest amount of difference between the amplitudes of its spectral components and their neighbouring components. There is one exception however, that is if the amplitude spectrum of the harmonics is zero, the differences between that particular spectral component and its adjacent component would be large. This is demonstrated in Figure 7.10. The amplitude differences between $Q_3(f,\bar{y})$ and $Q_4(f,\bar{y})$ is d_4, which is greater than d_1, d_2 and d_3. By the condition described above, the frequency spectral component at $3f_o$ should not be selected for phase extraction, but because the amplitude spectrum at $4f_o$ is zero, there would be no overlapping on that side of $Q_3(f,\bar{y})$. It is obviously desirable to select a frequency spectrum with no overlapping on one side of its frequency spectrum, but for the optimum phase extraction, the amount of overlapping on both sides of the harmonic chosen must be balanced in order to determine the 3D object accurately. This is demonstrated experimentally at the end of the next Section.

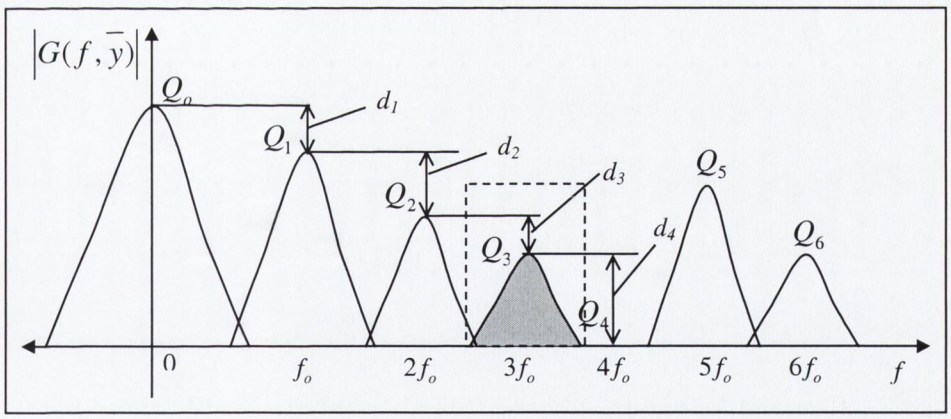

Fig. 7.10: The spectral components with minimum harmonics spectrum overlapping

7.5 Simulation of the Rectangular Pulse Phase Profilometry

In this Section, the feasibility of the Rectangular Pulse Phase Profilometry is demonstrated and the implementations of its processing steps are described in detail. Due to the unavailability of a 3D reference solder paste pad, a synthetic fringe image

with an object in the shape of a rectangular box has been developed for the simulation of the Rectangular Pulse Phase Profilometry. Thus, the assessment of its accuracy in the reconstruction of the 3D shape of solder paste can be tested rigorously. The simulated profile is a rectangular linear shift profile with a *4-pixels* step, the translation of the shift profile into the height profile is based on the actual optical configuration and can be calculated through equation (7-12) with $\overline{CD}$ = *4 pixels*. A demodulated fringe row is selected as the reference line $g_o(x,\bar{y})$. The phase deviation $\Delta\phi_{red}(x,\bar{y})$, $\Delta\phi_{green}(x,\bar{y})$ and $\Delta\phi_{blue}(x,\bar{y})$ for each channel can be calculated using equation (7-11). Using a line size of *256 pixels*, a grating period of *16 pixels* wide, and a pulse width of *4 pixels* wide, the fundamental grating frequency f_o is calculated as *16/256 = 0.0625 pixel*$^{-1}$ or the discrete fundamental grating frequency is *16 pixels/fringe*. Assuming uniform reflectivity, the phase deviation of the proposed rectangular linear shift profile is,

$$\Delta\phi(x,y) = 2\pi f_o \overline{CD} \qquad (7\text{-}11)$$

$$= 2\pi(0.0625)(4)$$

$$= 1.57$$

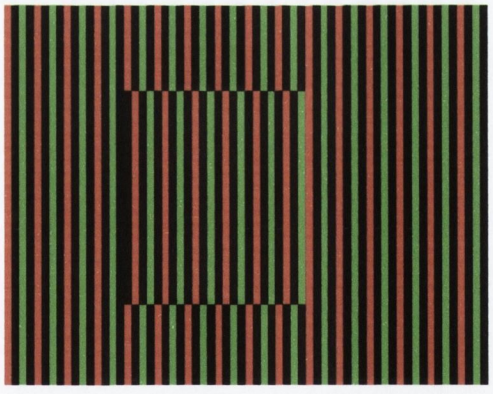

Fig.7.11a: A synthetic image with red and green colour fringe pattern, the grating frequency is *0.0625 pixel*$^{-1}$

Figure 7.11a shows the synthetic fringe image of red and green fringe patterns with an object in the shape of a rectangular box. The image processing of the Colour Encoded Recognition Algorithm is not required for this particular image, since the synthetic image pattern is of very well-defined colours with *(R=0,G=255,B=0)* for green values and *(R=255,G=0,B=0)* for red values. This is specially employed to present the feasibility of Rectangular Phase Profilometry rather than to show the difficulty of colour extraction. Three dimensional views of some real solder paste pads images will be demonstrated at a later stage to give a more comprehensive and practical perspective on the results as these images would require the use of the Colour Encoded Recognition Algorithm.

The red and green colour pattern image in Figure 7.11a is split into its respective channels for the phase extraction process and are shown in Figure 7.11b and Figure 7.11c.

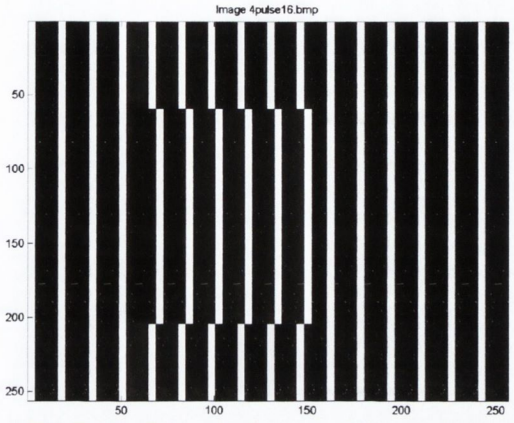

Fig.7.11b: The red channel of the synthetic image with grating frequency $0.0625\ pixel^{-1}$

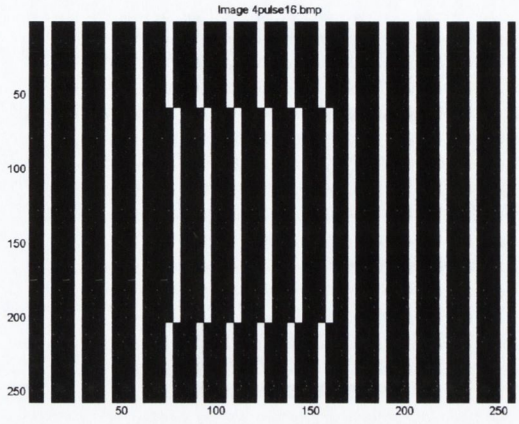

Fig.7.11c: The green channel of the synthetic image with grating frequency $0.0625\ pixel^{-1}$

The Fourier transform is then performed on the split channel images. The Fourier transform of the reference plane and the distorted row for both the red and green channel images are identical even though the shift has one fringe period difference. This is because the magnitude of the Fourier transform is shift invariant. Thus to avoid duplication, only the Fourier transform of the chosen reference plane and the distorted row of the red channel image are shown in Figure 7.12a and 7.12b. As shown in both figures, the main harmonics can be found centred at the discrete frequency $f_o = \pm 16$

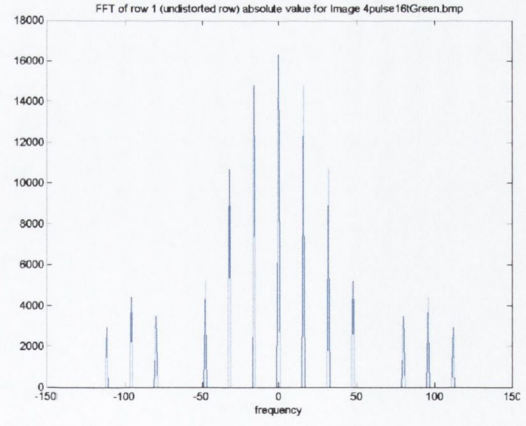

Fig.7.12a: The Fourier Transform of the reference row chosen in Figure 7.11b

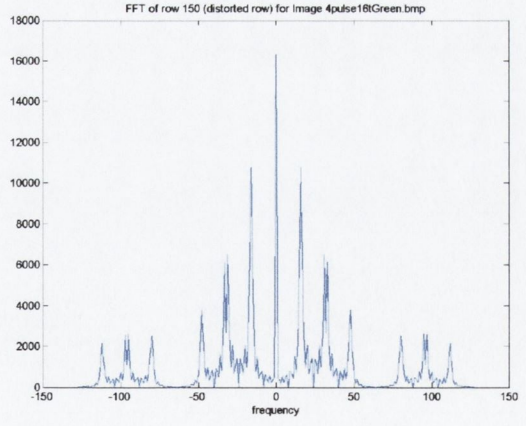

Fig.7.12b: The Fourier Transform of the distorted row in Figure 7.11b

and the other harmonics are centred at nf_o.

After transforming into the frequency domain, the phase information embedded in the fundamental harmonic can be easily extracted by multiplying the spectrum with a window function. By applying a window function, the desired frequency spectrum can be readily extracted. Several fixed shape window functions (Rectangular, Hanning, Hamming and Blackman) [54,55,69,70] were examined and their results were noted and compared. Figure 7.13 shows the various window functions centered at the discrete grating frequency *16* of the modulated frequency spectrum from the red channel image

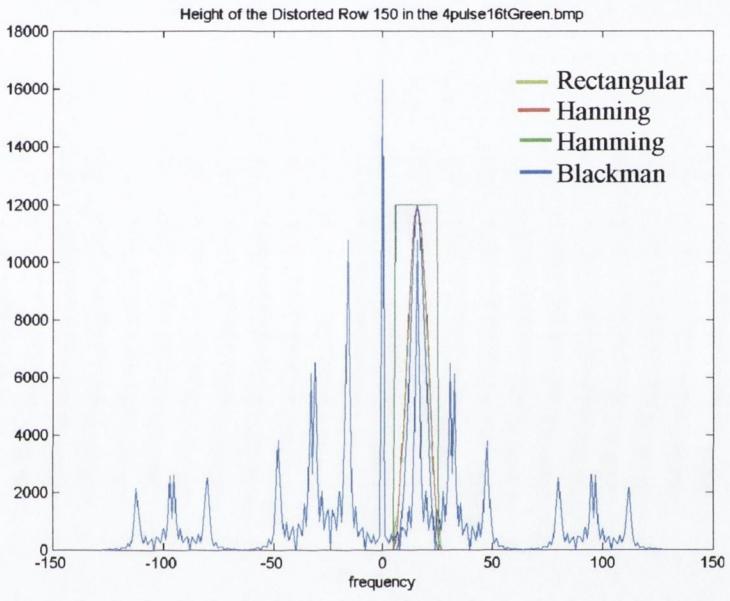

Fig.7.13a: Various Window Functions centered at the discrete frequency = 16 of the distorted frequency spectrum

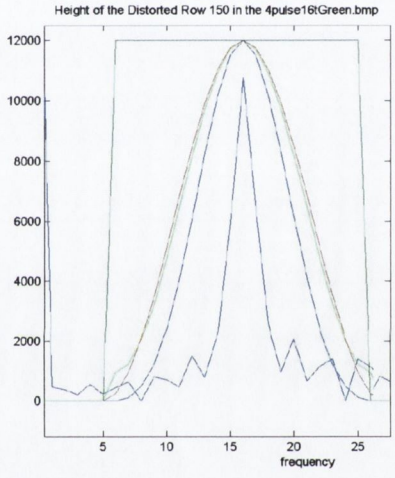

Fig.7.13b: Zoom in picture of Figure 7.13a

A rectangular window was initially applied to the Fourier transform of the distorted signal. The rectangular window gives maximum sharpness in frequency resolution providing a precise extraction when multiplied by the Fourier transform of the distorted signal. However, due to the abrupt rising and falling edges of the rectangular window, large ripples may arise in the resulting phase deviation when transforming the extracted frequency spectrum into the signal domain. This is shown by the Fourier transform pairs of the rectangular window between the frequency domain and time domain in Table 7.1. These ripples are caused by the waveform *sin(x)/x* which is the inverse transform of a rectangular window. As shown in the frequency response plot in Figure 7.14b, the side lobes of the rectangular window are rather large. In order to reduce these large side lobes, the sharp rising and falling edges of the rectangular window must be smoothed. Tapered data window functions such as Hanning,

Hamming and Blackman, given in Table 7.2, have a much smoother edges, they are symmetrical about the centre line and have a maximum value of 1. As shown in Table 7.1, the inverse Fourier transform of the Hanning window has very few ripples in comparison to the rectangular window. The shapes of these tapered windows are very similar especially with the Hamming and Hanning window as shown by the plots in Figure 7.14a, except that the Hamming window has the characteristic that its endpoints do not quite reach zero. The window functions and their frequency responses are plotted in Figure 7.14.

Frequency Domain	*Fourier Transform Pairs*	*Time Domain*
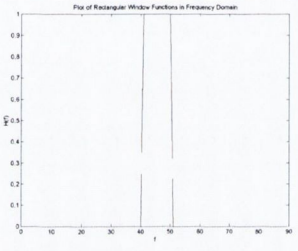	$H(f) = A \quad \lvert f \rvert < f_o$ $= \frac{A}{2} \quad \lvert f \rvert = f_o \Leftrightarrow h(t) = 2Af_o \frac{\sin(2\pi f_o t)}{2\pi f_o t}$ $= 0 \quad \lvert f \rvert > f_o$ **Rectangular**	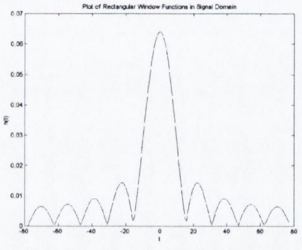
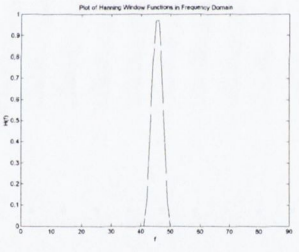	$H(f) = \frac{A}{2} + \frac{A}{2}\cos\left(\frac{\pi f}{f_c}\right) \Leftrightarrow h(t) = \frac{Af_c}{2} q(t) +$ $\lvert f \rvert \le f_c \qquad \frac{Af_c}{4} q\left(t + \frac{1}{2f_c}\right) +$ $\lvert f \rvert > f_c \qquad \frac{Af_c}{4} q\left(t - \frac{1}{2f_c}\right) = 0$ $q(t) = \frac{\sin(2\pi f_c t)}{2\pi f_c t}$ **Hanning**	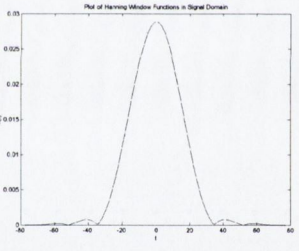

Table 7.1: The Transform Pairs of a Rectangular and Tapered Data Window in Frequency and time domain

Window Type	*w(n)*
Rectangular	1
Hanning	$w(n) = 0.5 + 0.5\cos[n\pi/(m+1)]$
Hamming	$w(n) = 0.54 + 0.46\cos(n\pi/m)$
Blackman	$w(n) = 0.42 + 0.5\cos(n\pi/m) + 0.08\cos(2n\pi/m)$
n are values between $-m$ and $+m$, giving $2m+1$ sample points in total	

Table 7.2: The mathematical Equations for window functions

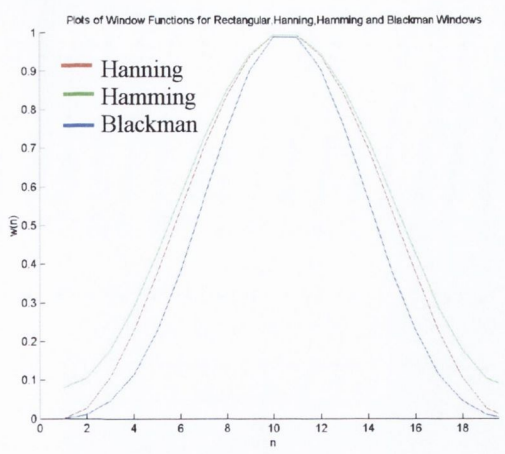

Fig.7.14a: Window Functions of Rectangular, Hanning and Hamming windows

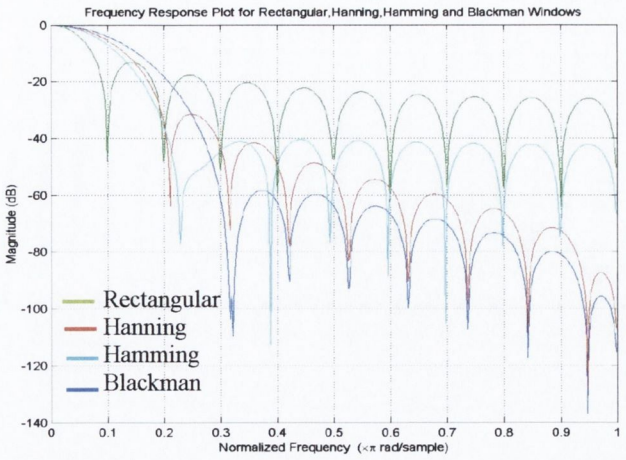

Fig.7.14b: Normalised Frequency Response of the Rectangular, Hanning and Hamming fn.

The frequency responses shown in Figure 7.14b have been normalised so the main-lobe for each curve starts at *0dB*. The rectangular window yields the narrowest main lobe, providing the best frequency resolution for spectral analysis. Unfortunately, the first side lobe for the rectangular window drops only by *13dB* below the peak of the main lobe; this may result in an inaccurate phase extraction with large ripples as indicated in Figure 7.15. The Blackman window has the lowest level of side lobes among the four window functions, but the width of its main lobe in the frequency response is over three times as wide as the main lobe of the rectangular window. These wider main lobes may cause degradation in frequency resolution. The Hamming window has quite a low level on its first side lobe and is only twice as wide as the main lobe of the rectangular window, but after its first side lobe, its remaining side lobes decay relatively slowly to those of the Hanning window. These slow decays may be favourable for data signals near to the signal's centre frequency but for data signals further away, it may not perform as accurately. This kind of decay is known as equiripple. The Hanning window seems to be the best trade-off between the four chosen windows. The average absolute errors for each of the window functions are calculated against the known phase deviation value *1.57* computed earlier using a common form of the Gaussian distribution equation [68] as shown in equation (7-20).

$$\overline{X} = \frac{\sum_{i=N} |X_i - X|}{N} \tag{7-20}$$

where

N is the line size

X is the known value of the phase deviation.

All previous procedures must also be performed on the reference signal as explained in Section 7.3. After the filtering process, the modulated signal must be demodulated by multiplying the Fourier-series of $g_{red}(x,\bar{y})$ and the complex conjugate of $g_{red\,o}(x,\bar{y})$ together as defined in equation (7-8). The result of the demodulation is presented in $H(x,\bar{y})$. The inverse Fourier Transform is then applied to the resulting signal containing the phase deviation. To compute the phase deviation, the arctangent and phase unwrapping operation must also be performed on each row. Figure 7.15 shows the resulting phase deviation of the modulated image in 2-dimensional view.

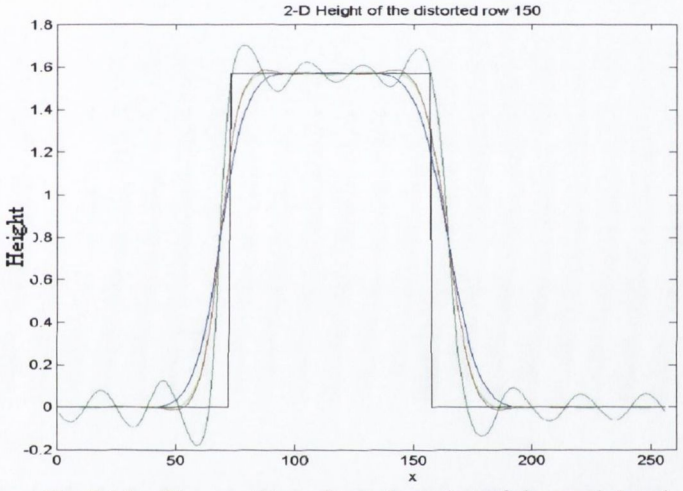

Fig.7.15a: The resulting phase deviation of the modulated row 150 as in figure 7.11c using various window functions for the filtering process

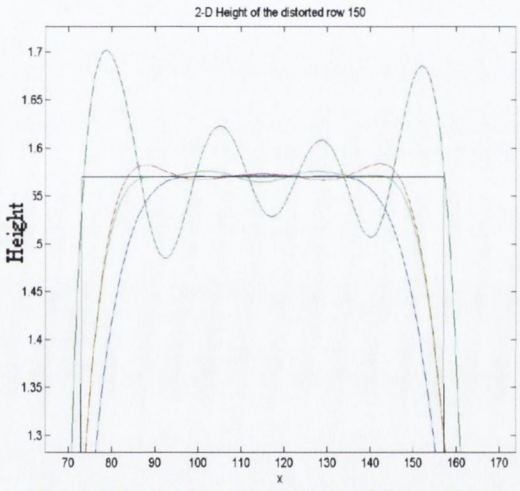

Fig.7.15b: A zoom in picture of figure 7.15a showing the top part of the phase

Window Type	*Absolute Mean Error*
Rectangular	*0.1199*
Hanning	*0.0896*
Hamming	*0.0903*
Blackman	*0.1093*

Table 7.3: Table showing the Absolute Mean Error of the chosen Window

Table 7.3 shows the absolute mean errors for the four window filters examined. The filter length *m* for these filters is based on a width of *10* pixels. Out of the *4* windows, the Hanning window has proven to be the most accurate since it gives the smallest absolute mean error of *0.0896*. In order to choose the best filter parameters for the Hanning window, different *m* values for the filter length centred on the first discrete frequency $f_o = 16$ were analysed for the optimum result.

m values	*Number of sampled points*	*Colour Curves in fig 8.16*	*Abs. Mean Error*
6	13	Black	0.1283
8	17	Green	0.1258
10	21	Red	0.0896
12	25	Cyan	0.0810
14	29	Magenta	0.0757
			0.0719

Table 7.4: Table showing the absolute mean errors for Hanning window with different lengths of filter based on a discrete frequency of *16*

With filter length *6* and *8*, the absolute mean errors are *0.1283* and *0.1258* respectively. Although these errors are very small, they are more than 30% less accurate than the wider filters. This indicates the phase information extracted might be insufficient since the filters are too narrow. The absolute mean errors for the 14 and 16 point filters, although suggesting a minimal level of errors, but since each harmonic of the spectrum is separated by $f_o = 16$, the total number of sampled points could overlap to the next spectrum, causing over extraction of the neighbouring spectral component. The *25* sampled points with $m = 12$ Hanning filter was therefore chosen.

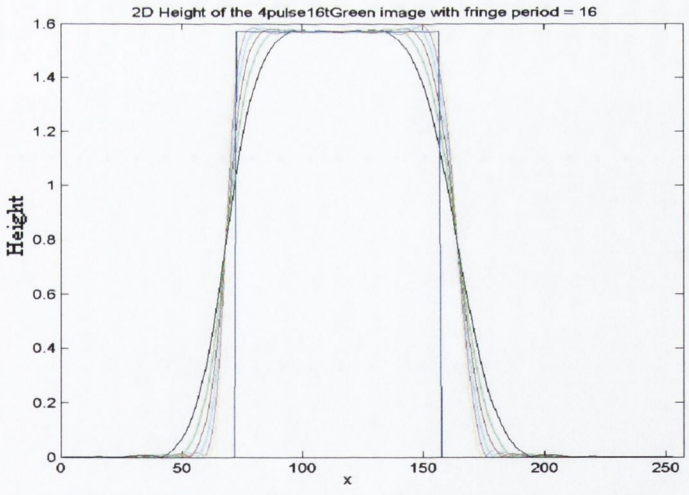

Fig.7.16a: The resulting phase deviation of the modulated row 150 as in figure 8.11c extracted by Hanning window with various filter lengths

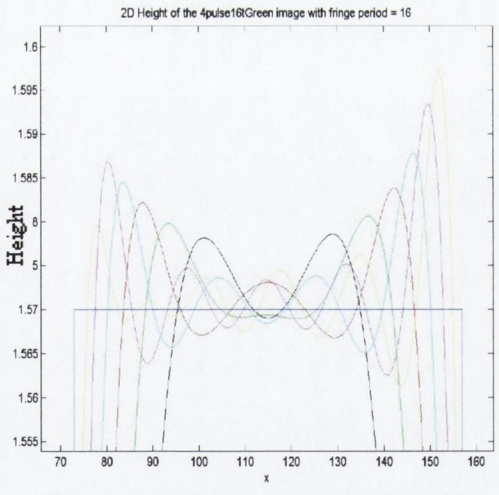

Fig.7.16b: A zoom in picture of figure 7.16a showing the top part of the phase

Figure 7.17 shows the resulting phase deviation for the red channel and green channel of the image in figure 7.11a. The two channels are separated from each other by one period and thus explain why the red curve and green curve differ in position on the graph. The two curves are then combined according to their known fringe colour positions and the final combined phase deviation is shown in Figure 7.18.

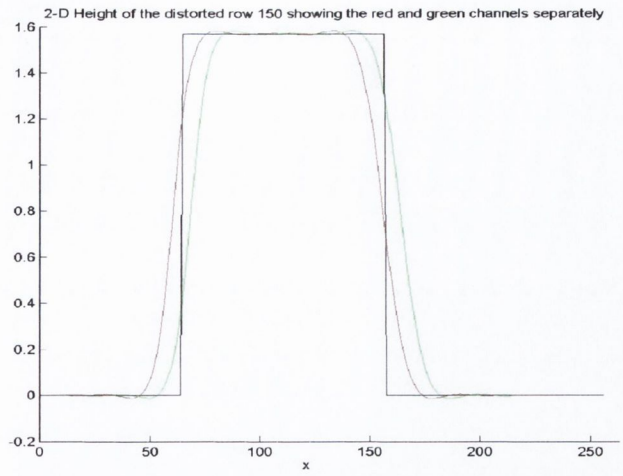

Fig.7.17: Graph showing the resulting phase deviation for the red and green channel of the image in figure 8.11a

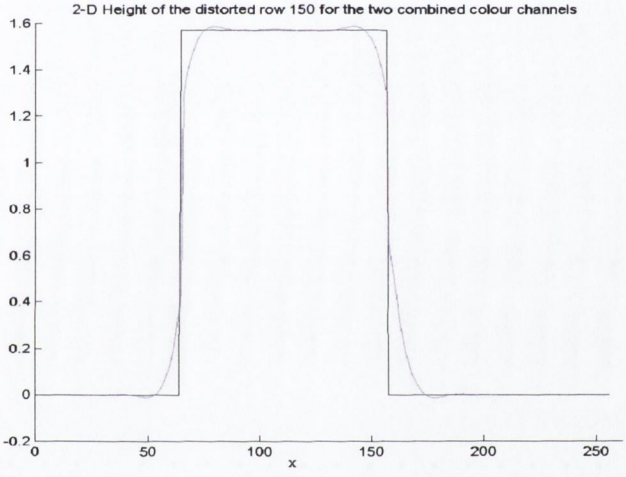

Fig.7.18: Graph showing the combined red and green channel phase deviation of the image in figure 8.11a

The absolute mean error of the combined curve is *0.0366* which is two times more accurate than each of the single channels. It is correct to interpret that for a rectangular linear shift profile with a *4-pixels* step as used in the above simulation, the same accuracy can be achieved by using a normal binary pattern [62] that has the same number of fringes as the red and green channels together. That is, a *32* black and white fringes image of a pulse width of *4 pixels* and a line size of *256 pixels* wide, with a grating frequency of $32/256 = 0.125\ pixel^{-1}$. However, if the rectangular linear shift profile is of a relative height of 8-pixels step or more, the algorithm would misinterpret the binary pattern resulting in an incorrect phase shift as the lateral deviation of the object's range is limited by the maximum spatial grating frequency. In contrast, the colour encoded pattern allows a greater shift profile, which is the main advantage of employing colour encoded pattern for this application particularly when the volume of the object being analysed is very small.

Recall the discussion on the overlapping of frequency spectral components in Section 7.4 - Square wave versus Rectangular Pulse wave. It was illustrated that the amplitude of the spectral components must vary slowly compared to the grating frequency to avoid a significant amount of overlapping during the filtering process, in particular on the Fourier transform of the Rectangular pulse wave where the distance separation between each consecutive harmonic spectrum is only separated by the fundamental grating frequency f_o. To achieve this, it is advantageous to select a

harmonic spectrum that has the smallest amount of difference between the amplitudes of its spectral components. However, the statement was invalidated by one exception, where the amplitude of a harmonic is zero; the differences between that particular spectrum and its adjacent spectrum may be large, but it might also be desirable to select that frequency spectrum since there would indicate no overlapping on that side of the frequency spectrum.

The argument is put to test by simulating a rectangular linear shift profile with a *2-pixels* step. Again a line-size of *256* is generated with a pulse width of *4*, and a grating period of *16*. The relative phase deviation of this shift profile is computed to be *0.7853*. Figure 7.19 shows the modulated row due to the rectangular shift profile. Two Hanning filters are used to extract the first harmonic component centred at a discrete frequency of *16* and the third harmonic spectrum centred at a discrete frequency of *48* as shown. The phase profiles of the extracted frequency components are shown in Figure 7.20. The curve indicated by the colour magenta is the extracted phase profile of the first harmonics component, its average value is approximately *0.7853*. The curve indicated by the colour red is the extracted phase profile of the third harmonic component and its average value is *2.356*. This is expected as it is a multiple of the fundamental harmonic (nf_o where $n=3$) and produces a value of phase deviation that is about three times the value for the first harmonic.

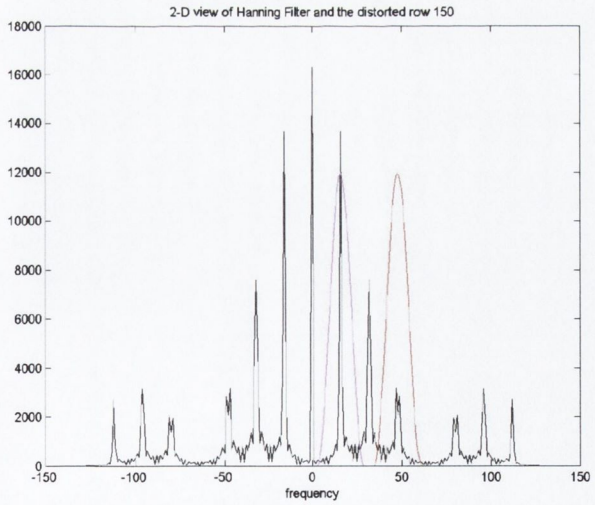

Fig.7.19: Hanning window filters at the 1st Harmonics and 3rd Harmonics spectrum of the modulated row

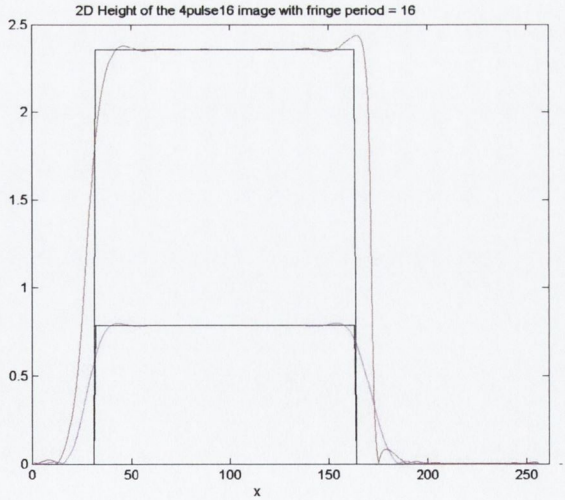

Fig.7.20: The Phase Profile of the 1st and 3rd Harmonics of the rectangular shift profile with 2-pixels step

The phase profile by the filter extraction of the 3^{rd} harmonic component shows some inaccuracies especially at the edge near to the *160 pixels* column. This is caused by the

imbalance of overlap on both sides of the harmonic component. The average absolute error in the object region is found to be *0.1629*. And the average absolute error for the 1^{st} harmonic component is *0.0726*. From this simulation, it is seen that for the optimum phase extraction, the amount of overlap on both sides of a harmonic component chosen must not only be small but also be balanced in order to determine the 3D profile of the object accurately.

7.6 Implementations of the Profilometry using Real PCB Images

All captured images were formatted into *256* Colour Bitmap Image (*8 bits per pixel*) to diminish complexity. The colour fringe pattern is made up of a Red-Black-Green-Black pattern. Figure 7.21 shows a real image of solder paste pads from a printed circuit board with the colour fringes projected onto it. The photometric decalibration using background subtraction in the Colour Encoded Recognition Algorithm was not performed for the capturing of this image. The image size is *256 pixels x 256 pixels*. The total number of fringes in the image is *13.5*. The pulse width is calculated as

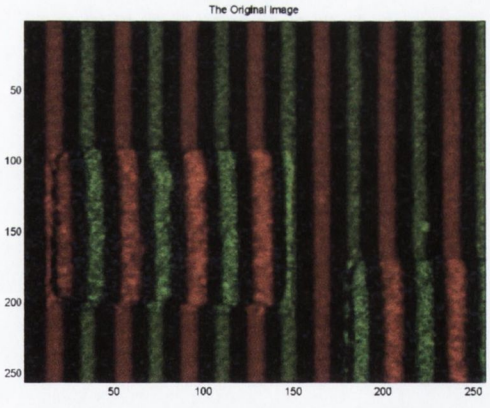

Fig.7.21: A solder paste pad of a PCB with colour fringes projection

$$Pulse\ Width = \frac{\text{Im}age\ Width}{no.\ of\ fringes\ (incl.\ black\ lines)}$$

$$= \frac{256}{(13.5)x2} = 9.48\,pixels$$

$$Grating\ Period = Pulse\ Width\ x\ 4$$

$$= 9.48\,pixels\ x\ 4$$

$$= 37.92\,pixels$$

$$Discrete\ grating\ frequency = \frac{\text{Im}age\ Width}{Grating\ Period}$$

$$= \frac{256}{37.92} = 6.7 \approx 7$$

The first fundamental of the harmonic spectral component is expected to be centred around a discrete frequency of *7*. The colour image is then separated into its RGB channels; the red and green channels are shown in Figure 7.22a and 7.22b respectively. The blue channel is insignificant in this case since it mainly comprises of dark and black pixels.

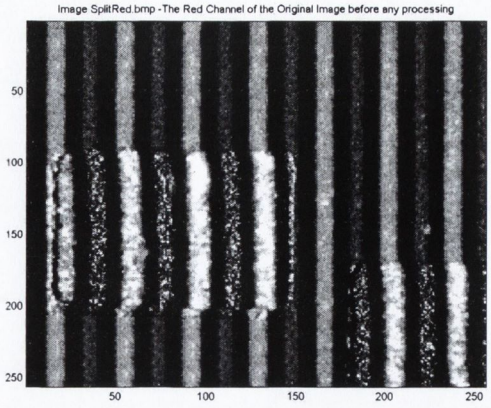

Fig.7.22a: The red channel of Figure 7.21

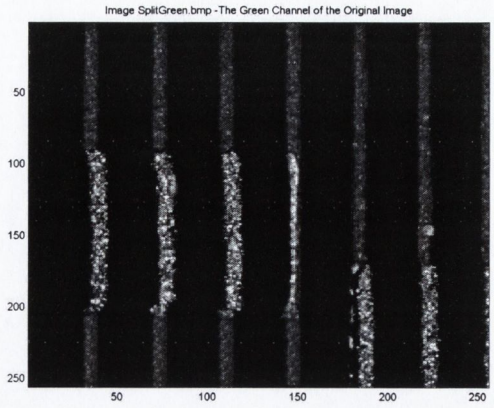

Fig.7.22b: The green channel of Figure 7.21

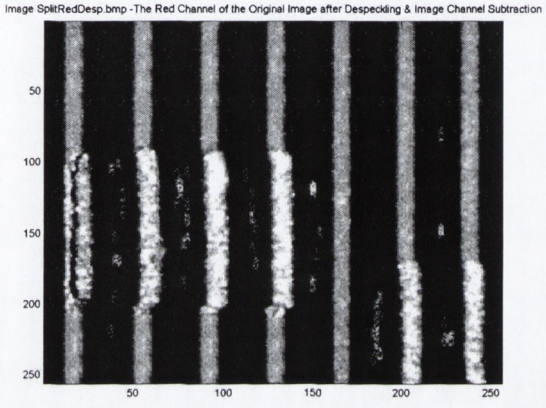

Fig.7.23: The red channel image after despeckling and subtracting the green channel.

The two channel images are then de-speckled to remove some of the noise and the black colour threshold value (T_{Bseg}) is calculated. The Image channel Subtraction is then executed on the red channel and the result is shown in Figure 7.23.

Finally, the Colour Extraction with the laws of relative equality technique and the extraction using the black colour threshold are performed. The final thresholded channel images are shown in Fig. 7.24.

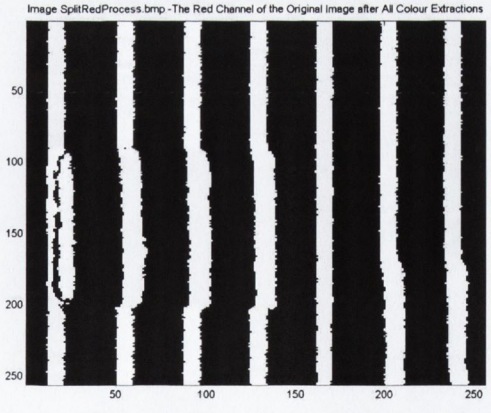

Fig.7.24a: The red channel image after all colour extraction in the Colour Encoded Recognition algorithm.

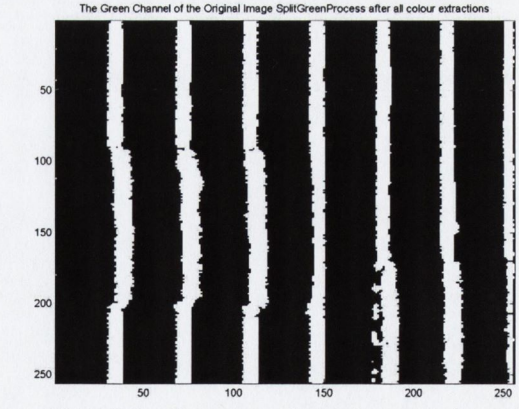

Fig.7.24b: The green channel image after all colour extraction in the Colour Encoded Recognition algorithm.

The *FFT* of a modulated row (row 190 in the image) containing part of the solder paste pad for both red and green channels in Figure 7.21 are shown in Figure 7.25a & 7.25b. A Hanning filter with a filter length of 9 sampled points is used to extract the first harmonic spectrum.

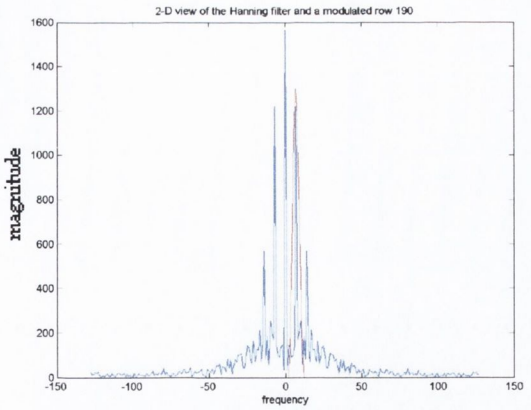

Fig.7.25a: Hanning Window Function centered at the discrete frequency = 7 of the distorted frequency spectrum for the red channel.

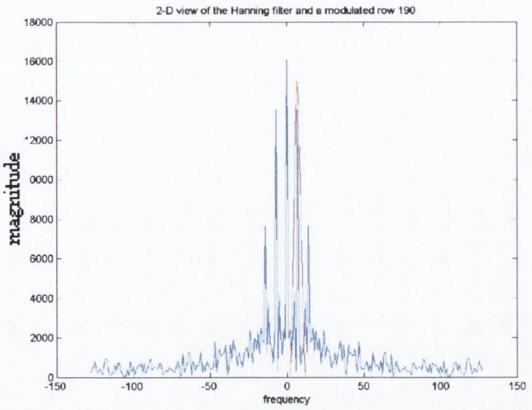

Fig.7.25b: Hanning Window Function centered at the discrete frequency = 7 of the distorted frequency spectrum for the green channel.

The 3D view for both the red and green channel images are shown in Figure 7.26a and 7.26b respectively.

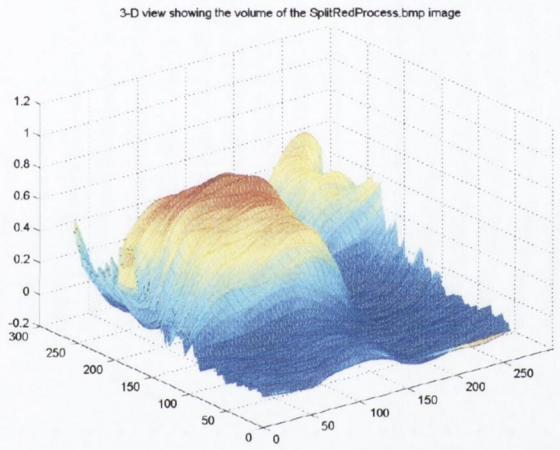

Fig.7.26a: 3D view of the solder paste pad in red channel

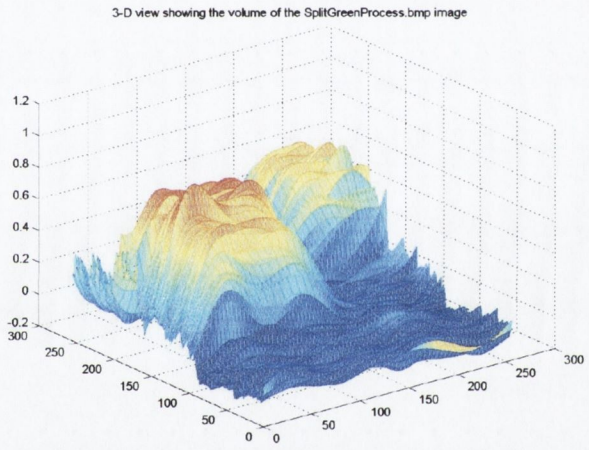

Fig.7.26b: 3D view of the solder paste pad in green channel

The combined volume of the red and green channels is shown in Figure 7.27.

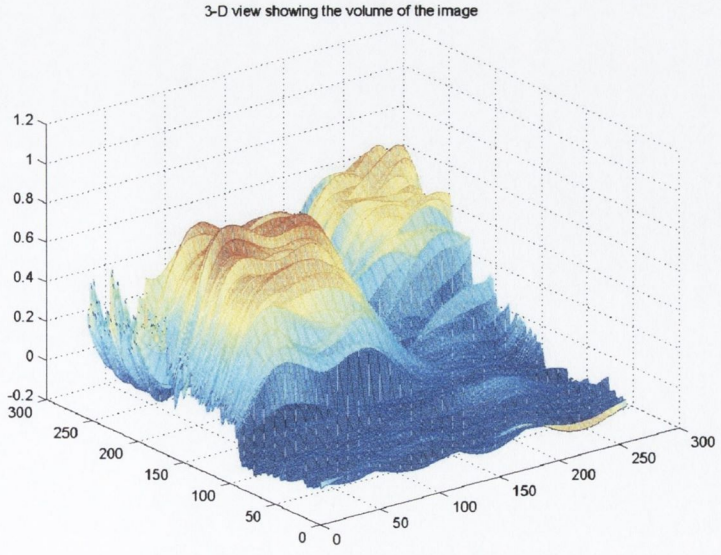

Fig.7.27: The final combined 3D volume of the solder paste pads

In order to reduce computation time, it is not always necessary to extract and threshold the channel images all the way into binary images using the Colour Extraction with the laws of relative equality technique, since FTP allows the phase extraction directly from 8-bit grey level images. For example, the images after the Image Channel subtraction step in Figure 7.21 and 7.20b should be sufficient to obtain accurate results. But if the fringes in the images are very badly defined and do not contain much noise, the Colour Extraction with the laws of relative equality technique is recommended.

7.7 Conclusions

The Rectangular Pulse Phase Profilometry with Colour Encoded Structured Light technique has been presented. The simulations have shown that the algorithm can yield a much better approximation than a normal square wave with Fourier Transform Profilometry by using a colour fringe pattern to increase the maximum spatial grating frequency. This is important since with more fringes projected in a sample image means the higher the grating frequency with a corresponding improvement in the resolution of the recovered phase profile.

The Rectangular Pulse Phase Profilometry with CESL has been demonstrated reliably. The only weakness of the profilometry is its computational speed. The computational load of the Colour Recognition Algorithm is practically negligible since there are only additions and subtractions which are not as time consuming. The complex multiplication operations required for the calculation of the *FFT* and *IFFT* are perhaps the biggest drawback of the algorithm, but with the increasing speed of today's processors, this drawback can be compensated.

Chapter 8

Overall Discussions and Suggestions for future work

This thesis reports on a study of 3D inspection of solder paste pads as used in Surface Mount technology in electronics manufacturing. Unlike many PhD researches which usually specialise in a narrow area on a particular subject, this research consists of a wider area on the entire volumetric measurements of 3D solder paste inspection as a whole. It aimed at comparing and studying different DSP and image processing techniques in order to discover the most suitable algorithms for a system which might have the potential to provide accurate, low cost and real time volumetric measurements.

This work began by continuing further investigations on the study of phase profilometry with structured light that had previously been developed by former colleagues *Luigi and Boland* [34,35] at Trinity College Dublin. The work was then expanded by looking at several range-imaging techniques for general applications and also other Automated Optical Inspection systems. It was, however, found that structured light technique with phase profilometry is a more effective alternative compared to laser sampling, and other techniques such as X-ray laminography especially if it is to satisfy the criterions of a low cost and real time solder paste inspection system as described in Section 2.6. Thus, structured light was chosen as the basis of the research.

It was mentioned several times in the thesis that PCB inspection systems strongly relies on CAD layout for accurate knowledge of the pad position. This is an important requirement as the fringe grating projected onto holes and dark areas of the PCB would cause the fringes to be temporarily lost or result in an image with disturbed fringes and dark areas which may not be accounted for. Images with a lot of dark areas or holes would cause problems for any methods of height extraction. Figure 8.1 shows a fringe image of a PCB with dark areas and holes. This can be overcome with the knowledge of pad positions from the CAD layout, so that only the image data of the pad areas are examined in conjunction with the image of undisturbed fringes. The total execution time is also reduced since the size of the image area is smaller. In addition, the reference plane can be properly selected from the CAD layout. As well

as the height distribution, the volume of the solder paste in question is also of interest, the CAD layout provides the accurate pad areas for volumetric measurements.

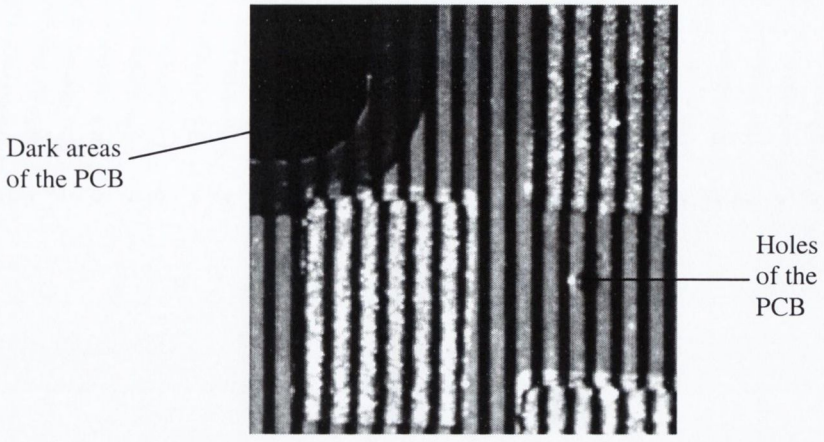

Fig. 8.1: Fringe image of the PCB indicating dark areas and holes

For this research, the supply of the Motorola PCB CAD layout was not available, but the nature of the research is to find effective algorithms for the inspection system and the assessment of the accuracy can be addressed using synthetic images produced by computer programs. Thus by avoiding holes and dark areas on the PCB when capturing test images, the PCB CAD layout was not required. However, it should be noted for all AOI systems within the electronics manufacturing, PCB CAD layout are standard requirement.

Apart from the unavailability of the CAD layout, the actual height measurements of the solder paste pads on the inspected PCB were also not available due to the lack of high accuracy metrology measurement equipment. The height measurements of the solder paste pads were only given in an approximate range of $200\mu m - 300\mu m$. For *FTP, SDP, NFP* and *the Rectangular Pulse Phase Profilometry*, comparisons and accuracy tests were done using synthetic images but for the Geometric Profilometry with CESL pattern recognition, accuracy tests cannot be done in the similar manner as the technique is based on processing the relative pixel shift. Thus, using synthetic images to assess the accuracy of the Geometric Profilometry would give a misleading accuracy of *100%*. The only alternative was to compare the volumetric measurements resulted in the Geometric Profilometry to the given approximate height range. The research on the Geometric Profilometry using Colour Encoded Structured Light Pattern as described in Part II is probably more appropriate for inspecting or measuring heights of slightly larger objects rather than solder paste pads since it is based on a pixel by pixel image manipulation. Although pixel is a very small quantity

representation, the method adopted in the last step (the colour encoded comparison technique) which includes counting the number of pixels shift from the edge of the fringes is not suitable for such small objects as solder paste pads. This is especially true as it does not measure solder paste at every pixel point in the 2-D image; it calculates the pixels marking the start of each fringe and the end of each fringe, providing height distribution information only along a discrete set of contour lines. Although this problem is not substantially big, since by using higher frequency grating, the problem can be reduced slightly; it would however be ideal to develop this profilometry further to precision so the algorithm can measure at every pixel point in the image especially if small objects such as solder paste pads are to be considered.

From the implementation of the Phase Profilometry, it was clearly shown that the Fourier Transform Profilometry was by far the most accurate phase extraction technique among the three profilometry studied. It is also the least complex to construct, with little or no other dependent components as discussed in Section 4.5. Unfortunately, from the computational point of view, the Fourier phase extraction technique turns out to be quite time-consuming, as it requires calculation of FFT-IFFT pair for each image row. In order to improve the computational speed, it is recommended to set the sequence length so it is a factor of the power of two as discussed in Section 4.4.4, Thus the time and the system can then be reduced and optimised. A look-up-table for the arctangent values can also be predetermined to facilitate the arctangent calculation process. This would reduce the amount of time required to complete the phase extraction. To further increase the speed, the FFT-IFFT operations can be made into a hardware component, and with the ever-increasing speed of today's computer, the computational load associated with the calculation of FFT-IFFT can surely be minimised. Some of the factors and problems which influence the accuracy and the overall effectiveness of the phase profilometries were also investigated for further improvements. Among these factors was the grating frequency associated with object height. This problem was overcome by using colour encoded structured light (CESL) strips in the second and third parts of the research.

CESL is a promising method in enhancing 2D image for volumetric inspection of PCB as it has shown its compatibility for measuring the height of solder paste. In our algorithm, only two of the primary colours and black in the RGB space were

employed in the grating. This allowed the CESL method to measure twice the amount of the lateral displacement at the same grating frequency as of the original monochrome strips system. As the number of colours increase in the employment of the grating, the lateral displacement increases by the same fold, thus allowing even greater accuracy. In principle, there is no limit to the number of colours used in the system, but the system must be able to project and detect the colours without error in the given work environment. In our case, this freedom of the number of colours used in the grating pattern is limited by the size of the application and the slide making process. Unlike traditional binary encoded transmission gratings that are fabricated by electromagnetic waves and have a resolution of *13,500 lines per inch*, the colour encoded gratings are just prototypes generated by the 'imggen' program and digitally fabricated onto *35mm* colour slides. These slides have a very low resolution of *1,300 lines per inch*, and therefore only low frequency gratings of approximately *6 lines/mm* could be fabricated. The CESL gratings used for Part II and Part III of the research had only considered the colours in the RGB space, and from literature, RGB space will only yield good results when dealing with unsaturated colours, while the HSI (hue, saturation, intensity) space allows saturated colours and variable intensities. Although, the solder paste inspection applications before reflowing might not experience any saturated colour images, it would however be interesting to develop an algorithm possibly, with the use of HSI space, to handle this phenomenon for similar inspection of saturated images. Another interesting idea is to project a colour grating with a combination of a set of different fringe width of the primary colours. This is similar to the binary light-stripe pattern approach of variable spatial frequencies [62] with the difference that binary combined encoding requires several number of frames. A brief example is shown in Figure 8.2 to clarify the idea. This idea is quite effective for measuring objects with various heights, it uses the fine grating channel image (blue) to determine the height accuracy, and then the lower frequencies grating channel images (green and red) to determine the actual slope of the phase shift as to solve the ambiguity problem caused by the phase. For large objects, a liquid crystal projector maybe used to project the combined colour light stripes. It should able to achieve an adequate resolution. But for objects as small as solder paste pads, tremendous difficulty would lie on the manufacture of the actual colour grating.

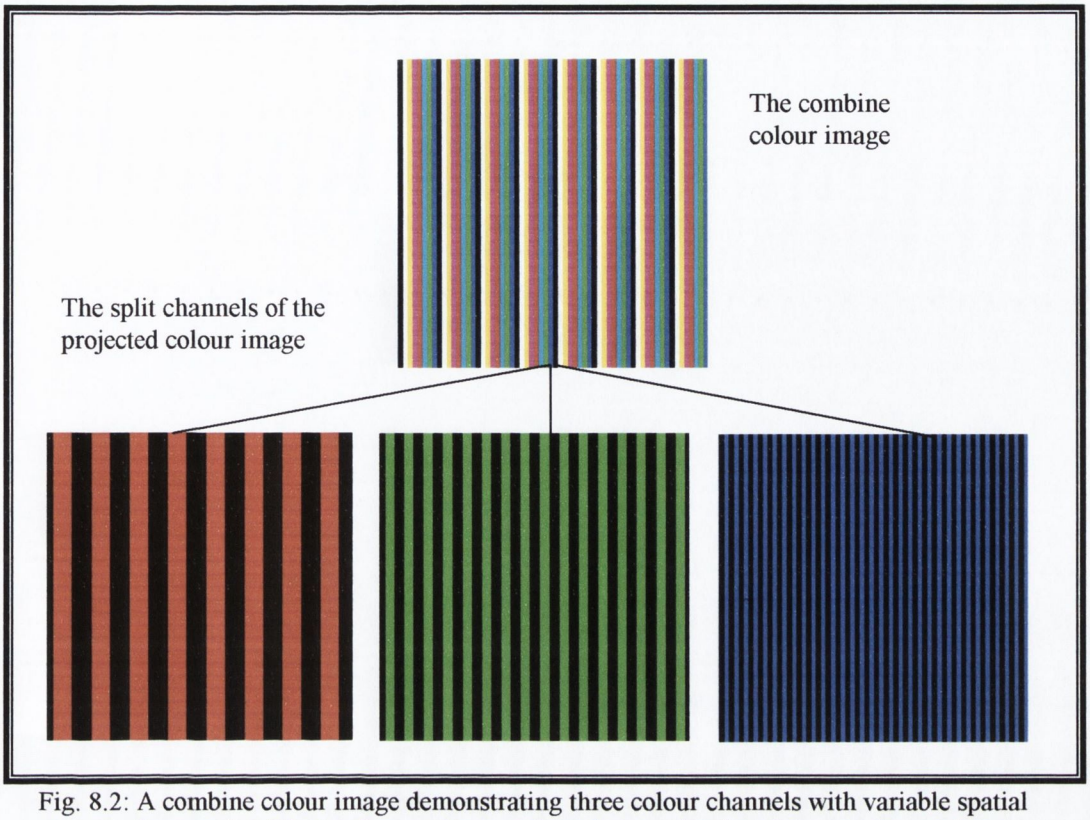

Fig. 8.2: A combine colour image demonstrating three colour channels with variable spatial frequencies. The top image shows eight colours – the six primary and secondary colours, and black and white.

One expert [6] has written a report concerning the key to success in solving machine vision based systems and it is to adopt an approach widely known as KISS – **K**eep **I**t **S**imple, **S**tupid, a fundamental approach with 'low-tech' rather than 'high-tech' in mind towards solving the vision problems. In his paper, he mentions

> '*the existing standard vision techniques, such as edge detection, segmentation, blob analysis, feature extraction and classification will remain key to the success of PCB applications.*'

It is also worth noting that the final accuracy of a volumetric inspection system depends on the accuracy of the underlying image acquisition, processing and analysis as well as on proper calibration of the geometrical, mechanical and projection parameters of the complete system.

It is difficult to predict what will be required in vision technologies in PCB inspection in the future. However, one fact is clear: the electronics industry continues to increase component densities and reduce circuit board sizes. With such a trend, it

can be predict in-line process control with very high-resolution image acquisition system will surely be mandatory. Table 8.1 shows the specifications for all the profilometries studied in this research.

SPECIFICATIONS	Binary Encoded Pattern			Colour Encoded Pattern	
	FTP	SDP	NFP	Geometric Profilometry	Rectangular Pulse Phase Profilometry
Allows low frequency grating with good accuracy	✓		✓	✓	✓
Allows high frequency grating with good accuracy	✓	✓	✓	✓	✓
Arbitrary number of fringes (no specific requirement on the number of fringes used)	✓	✓		✓	✓
Consists of odd or even harmonics	**Odd**	**Odd**	**Odd**	**N/A**	**Odd & even**
Maximum Lateral Deviation	2π	2π	2π	**Upto the no. of colours ***	**Upto the no. of colours**
Distance between two consecutive spectral components	$2f_o$	$2f_o$	$2f_o$	**N/A**	f_o
Filters	Hanning Window Functions	FIR	Moving avaeragers,Comb Filters, Mean Value Subtraction	Pixel & Colour manipulation, Image Processing	Pixel & Colour manipulation, Image Processing, Hanning Window Function
Phase Unwrapping	✓	✓	✓		✓
Depth of view ratio IO_{ratio}				✓	
Computation time *(ms)*	530	340	263	180	600 per channel
Resolution for a *32* frequency grating	0.0393	0.0642	0.0571	N/A	0.0333

Table 8.1: Specifications of all the Profilometry in the research

Bibliography

1. Griffin P., Villalobos J, Foster J, and Messimer S, "Automated Visual Inspection of Bare Printed Circuit Boards", in *Computers Ind. Engineering,* vol. 18, pp. 505-509, 1990.
2. MVT, "To the Point", in *MVT Quaterly Newsletter*, Issue 1, July/August 1998.
3. Prime Research Group, "Automatic Test Equipment Industry Service, Imaging Test System Module", *Prime Research Group,* 1999.
4. Hawthorne J., Owen M. and Allain P., "Automated Optical Inspection for SMT", *Future EMS,* August 1999.
5. "AOI under the microscope", in *The European Test Industry Journal,* March 1998.
6. Siemens Components, Inc., "Surface Mounting", in *www.sci.siemens.com* , 1995.
7. Riddle Michael E., "Solder Paste Measurement: A Yield Improvement Strategy that helps Improve Profits", in *International Business - ASC International.*
8. Jalkio J., "Choosing Solder Paste Inspection Equipment", in *Surface Mount Technology Magazine,* pp. 46-48, September 1995.
9. Vernon D., "Automated Visual Inspection and Robot Vision", in *Machine Vision book, Prentice Hall.*
10. Leonard M., "Colour Machine Vision for the Electronics and Food Industries", in *M. Leonard thesis*, pp. 71-82, October 1995.
11. Hara Y., Akiyama N and Karasaki K, "Automatic Inspection System for Printed Circuit Boards", *IEEE Trans. Pattern Analysis Machine Intelligence,* PAMI-5, 1983.
12. Owen M. and Hawthorne J., "Process Control of Solder Paste Deposition", in *SMTA International Conference, San Jose, CA,* September 1999.
13. Vernon D., "Machine Vision in the Electronics and PCB Inspection Industry, the Current Position and Future Directions", *a short report in www-prima.imag.fr/ECVNNet/policy/ electronics.inspection.html.*
14. Davy J., "How should PWA solder defect detection be performed", in *Proceedings Tech. Program National Electronic Packaging and Production Conference,* pp. 451-465, 1988.
15. Habib T., "Automated Vision Inspection of Solder Paste and Flux", *Testronics,* May 1999.
16. Tong Patrick, "Using visual inspection in your PCB test strategy", in *Electronics Engineer*, September, 1998.
17. Texas Instruments, DS&EG (Raytheon TI Systems), "Best Practice: Using X-Ray Laminography for Solder Volume Measurement", *Best Manufacturing Practices Surveys,* Janurary 1991.
18. Colin Charette, "Automated X-ray Inspection", in *A Test and Inspection Technology Seminar by Hewlett Packard,* 1999.

19. Klette Reinhard, "Structured Lighting", in *415.775 Auckland University, New Zealand.*
20. Curless Brian, "Active Vision", in www.cs.wright.edu/people/faculty/agpsjtas3.activevis/ActiveVis.html, Lecture notes, University of Washington.
21. Doemans G., "Automated Inspection of Printed Circuit Boards", in *TRIOS*, November 1995.
22. Jarvis R.A., "A perspective on range finding techniques for computer vision", in *IEEE Transactions on Pattern Analysis and Machine Intelligence,* vol. 5, pp. 122-139, March 1983.
23. Nitzan D., "Three-dimensional vision structure for robot applications", in *IEEE Transactions on Pattern Analysis and Machine Intelligence,* vol. 10, pp. 291-309, May 1988.
24. Besl P.J., "Active, optical range imaging sensors", in *Machine Vision and Applications,* vol. 1, pp. 127-152, 1988.
25. Poussart D. and Laurendau D., "3-D sensing for industrial computer vision", in *Sanz J (ed) Advances in Machine Vision,* Springer, Berlin Heidelberg, New York, 1989.
26. Nitzan et al., Laser.
27. Takasaki H., "Moiré Topography", *Applied Optics,* vol. 9, pp. 1467-1472, 1970.
28. Meadows D.M., Johnson W.O. and Allen J.B., "Generation of Surface Contours by Moiré Patterns", *Applied Optics,* vol. 9, pp. 942-947, 1970.
29. Moore Duncan T. and Traux Bruce E., "Phase locked Moiré fringe analysis for automated contouring of diffuse surfaces", Applied *Optics,* vol. 18, no. 1, pp. 91-96, 1 January 1979.
30. Duncan, J.P., Dean, D.P. and Pate, G.C., "Moiré contourography and computer aided replication of human anatomy", in *Engrg. In Medicine,* vol. 9, no. 1, pp. 29-36, 1980.
31. Takeda M., Ina H. and Kobayashi S., "Fourier-transform method of fringe pattern analysis for computer based topography and interferometry", *J. Optical Society America,* vol. Am 72(1), pp. 156-160, 1982.
32. Takeda M. and Mutoh K., "Fourier transform profilometry for the automatic measurement of 3-D object shapes", *Applied Optics,* vol. 22(24), pp. 3977-3982, 1983.
33. Tang Shouhong and Hung Yau Y., "Fast profilometer for the automatic measurement of 3-D object shapes", *Applied Optics,* vol. 29, No. 20, July 1990.
34. Di Stefano L and Boland F, "Three-Dimensional Inspection of Printed Circuit Boards using Phase Profilometry", in *Ramponi G, Sicuranza GL, Carrato S, Marsi S (eds) Proceedings of EUSIPCO-96, Lint, Trieste,* 10-13 September 1996, pp1805 –1808.
35. Di Stefano L and Boland F, "A new phase extraction algorithm for phase profilometry", in *Machine Vision and Applications*, vol 10: pp.188-200, 1997.

36. Boyer K and Kak A, "Colour-encoded structured light for rapid active ranging", in *IEEE Transactions on Pattern Analysis and Machine Intelligence*, vol. 9, pp14-28, January 1987.
37. Boyle Roger, Hlavac Vaclav and Sonka Milan, "Image Processing, Analysis and Machine Vision", *Chapman &Hall Computing*, 1995.
38. "Ultrasonic: Revolution timeline", in *http://www.sonosite.com/media_presskit_files/timeline.pdf.*
39. Brown M K, "Feature extraction techniques for recognising solid objects with ultrasonic range sensor, in *IEEE J. Robotics and Automation* RA-1, pp 191-105, December 1985.
40. Owen Mark, "2-D and 3-D Inspections Catch Solder-Paste Problems", in *Test & Measurement World*, February 2000.
41. Petrou and Bosdogianni, "Image Processing The fundamentals", *Wiley,* 1999 Edition.
42. Keller Kurtis and Ackerman Jeremy, "Real-time Structured Light Depth Extraction", *UNC Computer Science, Sitterson HallDepartment*, 2000.
43. Levine MD, O'Handley D A and Yagi G M, "Computer determination of depth maps", in *Computer, Graphics and Image Processing 2*, pp. 134-150, 1973.
44. Yakimovsky Y and Cunningham R, "A system for extracting three-dimensional measurements from a stereo pair of TV cameras, in *Computer, Graphics and Image Processing 7*, pp. 195-210, 1978.
45. Marr D, "A computational investigation in human representation and processing of visual information", pp. 240-250, 1981.
46. Grimson W.E.L, "From images to surfaces – A computational study of the human visual system" *MIT Press, Cambridge*, pp. 15-61, 1981.
47. Wechsler Harry, "Computational Vision", in *Computer Science and Scientific Computing Book.*
48. Yachida M, M. Asada, and S. Tsuji, "Automatic analysis of moving images", in *IEEE Transactions on Pattern Analysis and Machine Intelligence*, volume 3, number 1 pp. 12-20, 1981.
49. Shirai Y. and Suwa M., "Recognition of polyhredrons with a range finder", *Int'l Joint Conf. Artificial Intelligence*, 2nd, 80-87, Sep 1971.
50. "Point Matching with Structured Light", in *www-dsp.elet.polimi.it.*
51. Cunningham Edward P, "Finite Impulse Response (FIR) and Non recursive Filters", in *Digital Filtering: An introduction*, Chapter 5, 1992.
52. Matlab, "Unwrapping", *Signal Processing Toolbox User's Guide.*
53. Wang Yinyan, "Shadow Moiré Sensitivity Increase by Fringe Shifting: Fringe Multiplication", in *web - AkroMetrix LLC*, May 2001.

54. Lyons Richard, "Windowing Functions Improve FFT Results Part I", in *Test & Measurement world*, pp. 3744, June 1998.
55. Lyons Richard, "Windowing Functions Improve FFT Results Part II", in *Test & Measurement world*, pp. 53-60, September 1998.
56. Rabiner l, Mc Clellan Parks T, "FIR Digital Filter Design using weighted Chebyshev Approximations", in *IEEE Proceedings,* vol. 63, pp 595 –610, 1975.
57. Macy William W, "Two-dimensional fringe-pattern analysis", in *Applied Optics*, vol. 22, No. 23, December 1983.
58. Shadle C H, Carter J. N, and Monks T.P, "Colour-encoded structured light for real-time 3d digitisation", in *IEE 4th International Conference on Image Processing: Maastricht, The Netherlands*, 7 –9 April 1992.
59. Munn Kyle, "Evaluation of Three Segmentation Algorithms on Poorly Illuminated Images", in web - *Engineering Dept. University Iowa,* May 1997.
60. Liu John, Bobick Aaron and Ivanov Yuri, "Fast Lighting Independent Background Subtraction", in *www MIT Media Laboratory,* May 1999.
61. Davis Larry, Harwood David and Elgammal Ahmed, "Non-parametric Model for Background Subtraction", in *Computer Vision Lab, University of Maryland, College Park,* July 1999.
62. Daley Raymond C. and Hassebrook Laurence G, " Channel Capacity model of binary encoded structured light-stripe illumination", in *Applied Optics,* vol. 37, No.17, June 1998.
63. Kampel M, "Shape from Structured Light", in *web Research, Projects and Publications*, September 2000.
64. Woolley Ron F., "General Bitmap Image Colour- Bitmaps, Channels, plus the CMYK process", in *www.dtp-aus.com/bitintro.htm*, October 1998.
65. Funnell R., "Basic Computer Notions", in http://funsan.biomed.mcgill.ca/~funnell/InforMed/ Bacon/Graph/graph.hml, 1999.
66. Sonka, Hlavac and Roger Boyle, "Imag Processing, Analysis and Machine Vision", *Chapman and Hall*, 1995 Edition.
67. Kreyszig, "Advanced Engineering Mathematics", Wiley, 7th Edition.
68. Gonzalez Rafael C and Woods Richard E, "Digital Image Processing", *Addison Wesley* 1993 Edition.
69. Bores Signal Processing, "DSP Introductory & Advanced Courses", *in* http:// www.bores.com online course.
70. TechOnline University, "Overview of DSP", in www.dsptutor.freeuk.com online course.

Appendix A - System Hardware

In this section, a brief summary of the specifications and performance of the equipment used in the research are described. Only a short topic is delicate for the description of the hardware, since the main objective of the research is to inspect an algorithm, which would measure the height of the solder paste accurately.

Appendix A.1 - Grating for fringe generation

Binary encoded transmission grating : In part I of the experiment, binary encoded gratings were used to produce the fringes required in the structured light technique. The graticules (also known as transmission gratings) used in our experiment were supplied by Graticules Ltd, the rulings (groove frequency) are *8 lines/mm* and *20 lines/mm* respectively. There are many different types of diffraction gratings in the current market and most gratings have a resolution of *13,500 lines per inch*. Types of diffraction gratings and their geometry are briefly described below.

A *diffraction grating* is a collection of reflecting (or transmitting) elements separated by a distance comparable to the wavelength of light under study. It may be thought of as a collection of diffracting elements, such as a pattern of transparent slits (or apertures) in an opaque screen, or a collection of reflecting grooves on a substrate. A *reflection grating* consists of a grating superimposed on a reflective surface, whereas a *transmission grating* consists of a grating superimposed on a transparent surface. An electromagnetic wave incident on a grating will, upon diffraction, have its electric field amplitude, or phase, or both, modified in a predictable manner.

When monochromatic light is incident on a grating surface, it is diffracted into discrete directions. We can picture each grating groove as being a very small, slit-shaped source of diffracted light. The light diffracted by each groove combines to form a diffracted wavefront. The usefulness of a grating depends on the fact that there exists a unique set of discrete angles along which, for a given spacing d between grooves, the diffracted light from each facet is in phase with the light diffracted from any other facet, so they combine constructively.

Diffraction by a grating can be visualized from the geometry in Figure (A.1), which shows a light ray of wavelength λ incident at an angle α and diffracted by a grating (of groove spacing; *groove spacing d*) along angles β_m. These angles are measured from the grating normal, which is the dashed line perpendicular to the grating surface at its center. The sign convention for these angles depends on whether the light is diffracted on the same side or the opposite side of the grating as the incident light. In diagram (a), which shows a *reflection grating*, the angles $\alpha > 0$ and $\beta_1 > 0$ (since they are measured counter-clockwise from the grating normal) while the angles $\beta_0 < 0$ and $\beta_{-1} < 0$ (since they are measured clockwise from the grating normal). Diagram (b) shows the case for a *transmission grating*. By convention, angles of

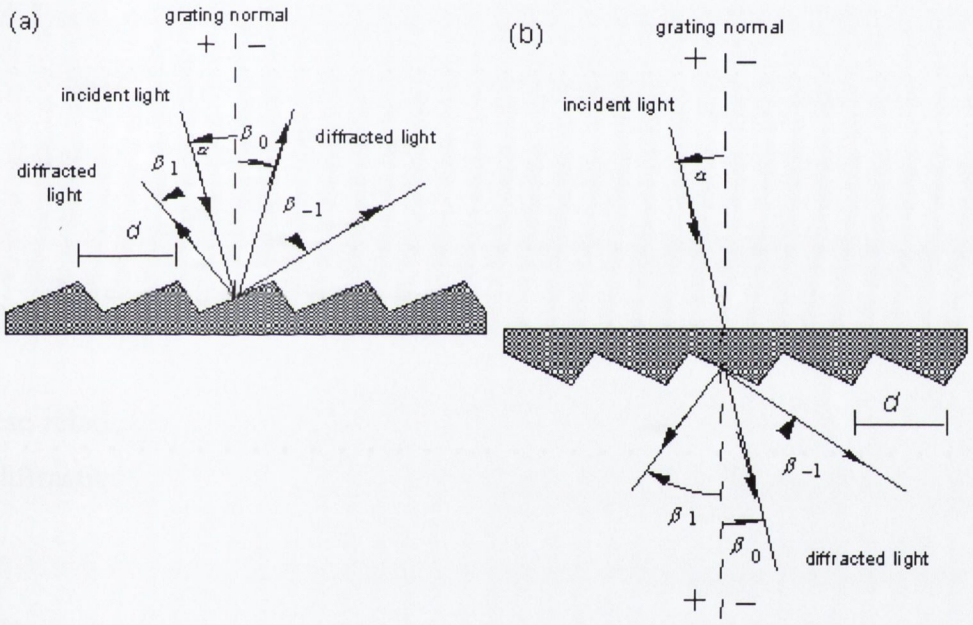

Fig. A.1: *Diffraction by a plane grating*. A beam of monochromatic light of wavelength l is incident on a grating and diffracted along several discrete paths. The triangular grooves come out of the page; the rays lie in the plane of the page. The sign convention for the angles α and β is shown by the + and – signs on either side of the grating normal. (a) A *reflection grating*: the incident and diffracted rays lie on the same side of the grating. (b) A *transmission grating*: the incident and diffracted rays lies on opposite sides of the grating.

incidence and diffraction are measured *from* the grating normal *to* the beam. This is shown by arrows in the diagrams. In both diagrams, the sign convention for angles is shown by the plus and minus symbols located on either side of the grating normal. For either reflection or transmission gratings, the algebraic signs of two angles differ if they are measured from opposite sides of the grating normal.

Another illustration of grating diffraction, using wavefronts (surfaces of constant phase), is shown in Figure (A.2). The geometrical path difference between light from adjacent grooves is seen to be $d \sin\alpha + d \sin\beta$. [Since $\beta < 0$, the latter term is actually negative.] The principle of interference dictates that only when this difference equals the wavelength λ of the light, or some integral multiple thereof, will the light from adjacent grooves be in phase (leading to constructive interference). At all other angles β, there will be some measure of destructive interference between the wavelets originating from the groove facets.

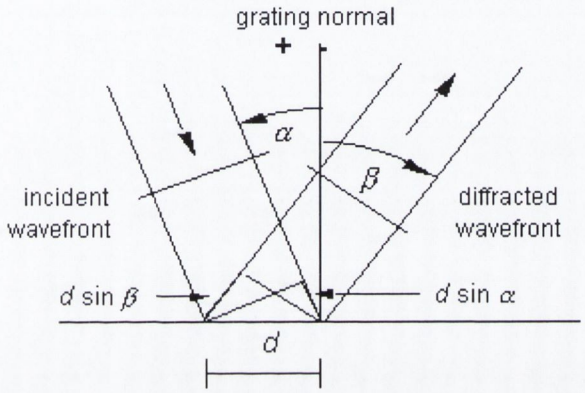

Fig A.2: *Geometry of diffraction, for planar wavefronts.* The terms in the path difference, $d \sin\alpha$ and $d \sin\beta$, are shown.

These relationships are expressed by the *grating equation,* which governs the angles of diffraction from a grating of groove spacing d.

$$m\lambda = d\,(\sin\alpha + \sin\beta) \qquad \text{(A-1)}$$

where

m – the diffraction order (an integer)

λ – the wavelength

α – the angle of incident

β – the angle of diffraction

d – the groove spacing

For a particular wavelength λ, all values of m for which $|ml/d| < 2$ correspond to physically realizable diffraction orders. It is sometimes convenient to write the grating equation as

$$Gm\lambda = \sin\alpha + \sin\beta \qquad \text{(A-2)}$$

where

$G = 1/d$ is the groove frequency, groove pitch, it is measured in grooves per millimeter

Equation (A-1) and its equivalent equation (A-2) are the common forms of the grating equation, but their validity is restricted to cases in which the incident and diffracted rays are perpendicular to the grooves (at the center of the grating). The vast majority of grating systems falls within this category, which is called *classical* (or *in-plane*) *diffraction*. If the incident light beam is not perpendicular to the grooves, then, the grating equation must be modified:

$$Gm\lambda = \cos\varepsilon\,(\sin\alpha + \sin\beta) \qquad \text{(A-3)}$$

where

ε is the angle between the incident light path and the plane perpendicular to the grooves at the grating center (the plane of the page in Figure A.2).

If the incident light lies in this plane, $\varepsilon = 0$, then equation (A-3) reduces to the more familiar equation (A-2).

Colour encoded grating : In the 2nd part of the research, *35mm* colour slides with fine lines are produced for the purpose of inspecting the modulation caused by the object's height. These colour fringe patterns images are generated by the '*Imggen*' program as described in section 5.3, which was designed in C programming language to generate different number of colour lines readily. The images are then exported into *Microsoft Powerpoint* so they can be digitally fabricated into *35mm* colour slides. The slides are made *on Kodak Ektachrome 5058 "100 Colour Reversal Professional"* film and are quoted a resolution of *4000 lines (4096 pixels wide x 2731 pixels high), with 24 bit colour*. The colour slides are mounted in glass mount. The *35mm* slides provide much lower quality compare to the binary encoded gratings but due to the low budget granted for this research and the unavailability of such on-shelves colour gratings in the current market, we could only generate our own slides for testing the experiment. Several grating manufacturers tailor makes special gratings for special use, it would be interesting to fabricate a grating with high fringe frequency and other defined colours. The colour grating is *6 lines/mm* and the adopted colour pattern of Red-Black-Green-Black was used in the slide grating.

Appendix A.2 – The Monochrome and 3 Chip RGB CCD camera

Monochrome Camera : A *Vantage CM510DC ½* inch high-resolution monochrome camera was used in part I of the experiment for which binary images was captured.

The *CM510DC* has effective picture elements of *752(H) x 582(V) pixels* array, and it can produce images with horizontal resolution over *570 TV lines*. The camera produces images with reduced lag, little geometric distortion and has good resistance to vibration and mechanical shock. The noise to signal ratio is *46dB*. The specification of the *CM510DC* is shown in table A-1 below. A combination of mount and lens were used, and the combined lenses system had a focal length of *41mm*.

Specification CCD Monochrome Camera – *Vantage CM510DC*	
Image Area	7.95mm x 6.45mm
Picture Elements	752(H) x 582(V) Pixels ½" Interline Transfer CCD
Scanning System	2:1 Interlace CCIR
Scanning Frequency	Horizontal : 15.625Hz Vertical : 50Hz
Sync System	Internal DC Internal/Linelock AC
Video Output	1Vpp Composite Output, 75 ohms
Lens Mount	C or CS mount
Resolution	570 TV lines (H)
S/N Ratio	46 dB
Power Requirement	DC 12 V AC 230V
Power Consumption	DC 3.0W(max) AC 6.0(max)

Table A-1: Specification of the Vantage CM510DC Monochrome CCD Camera

Colour Video Camera : For the 2nd part of the research, a colour camera was required for the capturing of the images. In choosing a colour camera a choice exists between three chip CCD cameras and single chip CCD cameras, with three chip CCD cameras currently giving a three-fold increase in quality resolution and also costing more than seven to ten-fold in price. Single chip colour cameras use similar technology as monochrome cameras, but with a coloured mask applied to the CCD sensing array, which allows the sensing of colours. This means that the resolution in each output colour channel is one third of that in the equivalent monochrome camera. Three chip CCD cameras use three CCD sensors to avoid the reduction of resolution, but cost significantly raises due to the increased in electronics complexity.

A *SONY DXC-930P ½ inch* CCD colour video camera was embedded into the system for acquiring colour images. The high performance of the three chip in *DXC-930P* can obtain about *420,000* effective picture elements. The horizontal resolution is

720 TV lines and its high signal-to-noise ratio is *56 dB*. The specification of the camera is shown in table A-2 below.

Specification 3CCD Colour Video Camera – *SONY DXC-930P*	
Picture Elements	768(H) x 494(V) Pixels ½" Interline Transfer CCD
Scanning System	2:1 Interlace, 625 lines
Scanning Frequency	Horizontal : 15.625 Hz Vertical : 50Hz
Sync System	Internal DC Internal/Linelock AC
Video Output	Composite: 1Vpp, 75 ohms RGB: 0.7 Vpp, 75 ohms Y: 1.0 Vpp, 75 ohms C: Same level as VBS chroma, 75 ohms Sync: 2.0 Vpp, 75 ohms
Lens Mount	½" bayonet mount
Resolution	720 TV lines (H)
S/N Ratio	56 dB
Power Requirement	DC 12 V
Power Consumption	DC 7.8W(max)

Table A-2: Specification of the SONY DXC-930P 3 Colour CCD Camera

Due to shortage of funding, we cannot acquire a proper lens which was recommended for the above *SONY* model camera. As an alternative, a camera lens with variable focal length of *2.8mm – 50mm* was employed. This was also combined with a set of zoom lenses of power +1, +2 and +4 for close-up shots of the PCB board. The zoom lenses are simply mounted in front of the camera lens, permitting the taking of close-ups. The mounting arrangement between the camera and the lens poses a serious issue on the accuracy of the location of the camera's focal point, since the camera lens was a CS-mount and the colour camera's lens mount was a ½" bayonnet mount. Several alterations and adjustments were made to mount the camera lens onto the colour camera as near as possible, while ensure the camera remains in focus. And finally, the total focal length of the camera lens was measured to be approximately *55mm*.

Appendix A.3 – Framestore

In order to accomplish both parts of the experiment, it is convenient to have a framegrabber board that is capable to adopt the capturing of both colour and mono images, so as to avoid going through any tedious procedures of replacing a separate framegrabber board whenever a different camera mode is used. A framegrabber board, which capable to support both RGB and Mono modes is therefore desirable. The *Prism Imascan* framestore with a resolution of *1600 pixels x 1200pixels* was chosen. The Prism system consists of two boards, namely the *Spectrum motherboard* and the *Prism daughter board.* The RGB and Mono modules are located on the daughter board. The Mono module can provide real-time monochrome analog video capture. It supports *8-bit* gray scale display at resolutions up to *1600 x 1200 pixels.* It has a *4MB DRAM* shared frame buffer that provides easier access to captured image data under *Windows NT/95* upwards. Inputs to the Mono module can be:

Analog:	RS-170 CCIR	Digital:	8-bit monochrome video and digital camera input

The RGB module can provide real-time programmable RGB frame capture. It has a *4MB DRAM* shared frame buffer that provides easier access to captured image data under *Windows NT/95* upwards. It also supports *8, 16, 24-bit* colour display at resolutions up to *1600 pixels x 1200pixels* and component RGB video input up to 15 MHz.

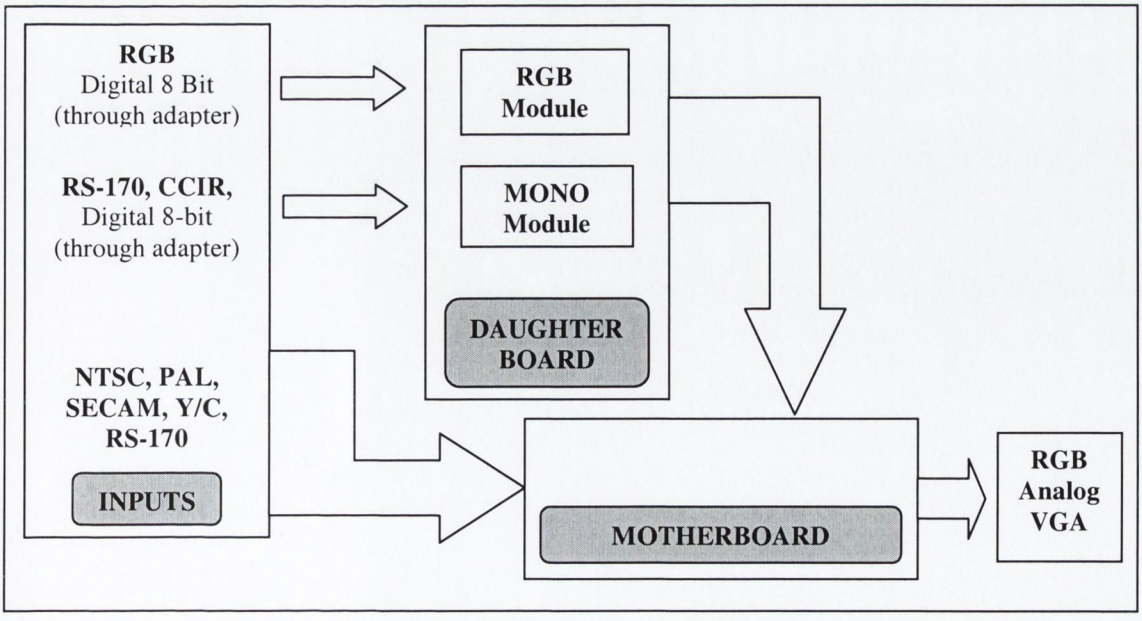

Fig. A.3: *IMASCAN Prism* System block diagram

Appendix A.4 – Computer

A *Gateway 200Hz Pentium* with a *16M* ram was supplied for the research.

Appendix B – Fringe Image Implementation and Windows Interface

Appendix B.1 – Image with a high grating frequency of $0.125\ pixel^{-1}$

Figure B.1 shows a typical image of solder paste deposits with *32* vertical fringes superimposed on them, the red line in the image indicated the chosen reference row.

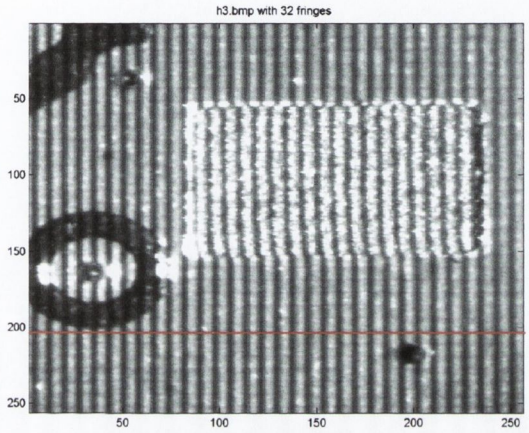

Fig B.1: Sample Solder paste with *32* vertical fringes

To demonstrate the 3D result of the solder paste pad, Fourier Transform Profilometry is used for the implementation. The fundamental grating frequency and the discrete fundamental grating frequency are calculated as,

$$fundamental\ grating\ frequency = \frac{No.of\ fringes}{line\ size}$$

$$= \frac{16}{256} = 0.125\ fringe/pixel$$

$$discrete\ fundamental\ grating\ frequency = \frac{line\ size}{grating\ period} = \frac{256}{8} = 32$$

Figure B.2 shows the FFT of the reference row.

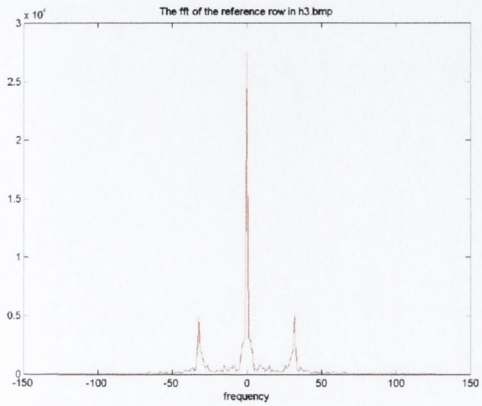

Fig B.2: FFT spectrum of the select reference row in Fig B.1

Figure B.3 shows a modulated row with the Hanning window. The Hanning window is centred at the fundamental discrete frequency of *32* to extract the desired phase deviation

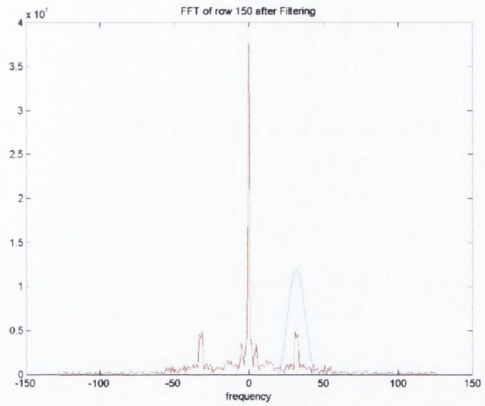

Fig. B.3: The modulated row of a fundamental discrete frequency of 32 with the Hanning window centred at the frequency for phase extraction

The inverse Fourier Transform is applied to the resulting signal containing the phase deviation. The arctangent and phase unwrapping operation are then performed on each row. Figure B.4 shows the resulting phase deviation of the modulated image in 3-dimensional view.

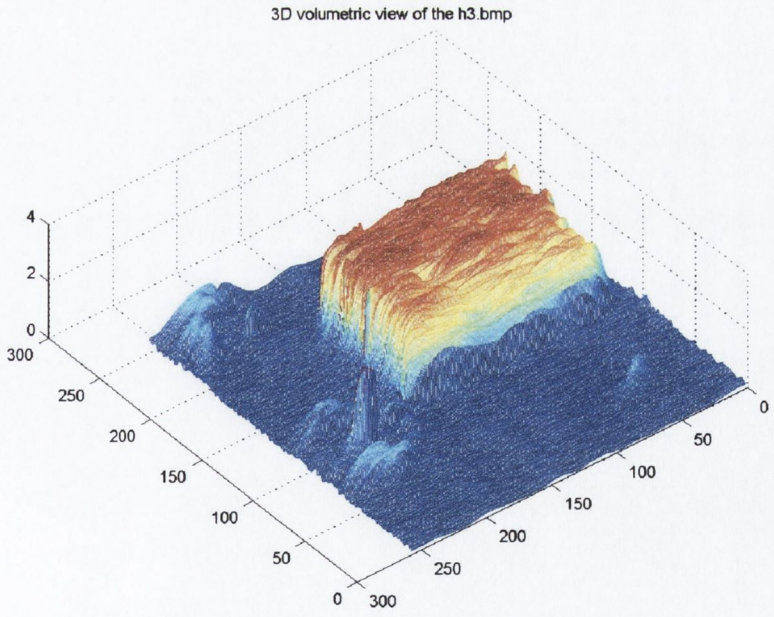

Fig. B.4: The 3D view of the 32 fringe grating image in Figure B.1

The image in Figure B.1 was not pre-processed, thus, the holes and dark parts of PCB were not accounted for as shown in Figure B.4. This can be avoided by processing only the areas where there are solder paste pads according to the CAD layout of the PCB.

Figure B.5 shows the window interface of the image. The phase map is processed by NFP. Figure B.6 shows the actual image with no fringes.

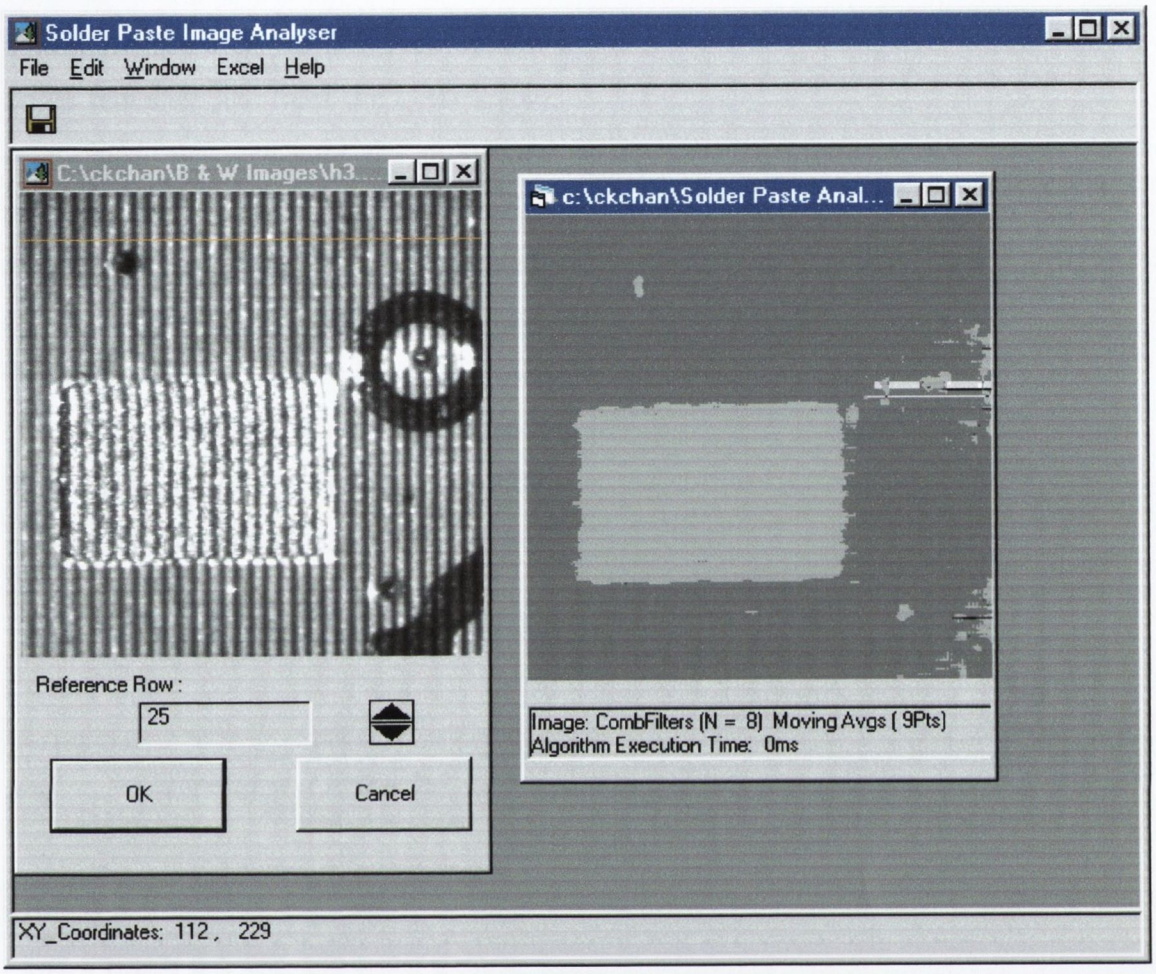

Fig. B.5: the window interface of the image in Figure B.1

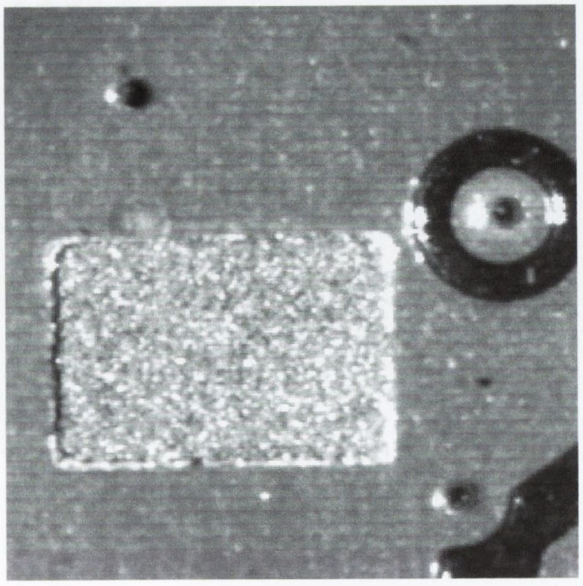

Fig. B.6: shows the solder paste pad image with no fringes projected onto it

Appendix B.2 – Window Interface for Phase Profilometry

The old algorithm requires the use of a reference image for calibrating the phase deviation. However, an advanced system has been established, by selecting only a single reference line from the CAD layout, the phase deviation of each point can be determined, this eliminate the procedure of reading the image data, and hence, reducing computational time dramatically. Figure B.7 shows the window layout of the software, the window is implemented using Visual Basic 5.0. The reference row can be selected with the use of the mouse by pointing to the particular row (guide by the co-ordinates system) or by using the actual row selection as shown.

A filter selection window has also been implemented for different number of fringe images, just by selecting the different parameters and lengths of filters, the optimal filter design is chosen. It is shown in Figure B.8.

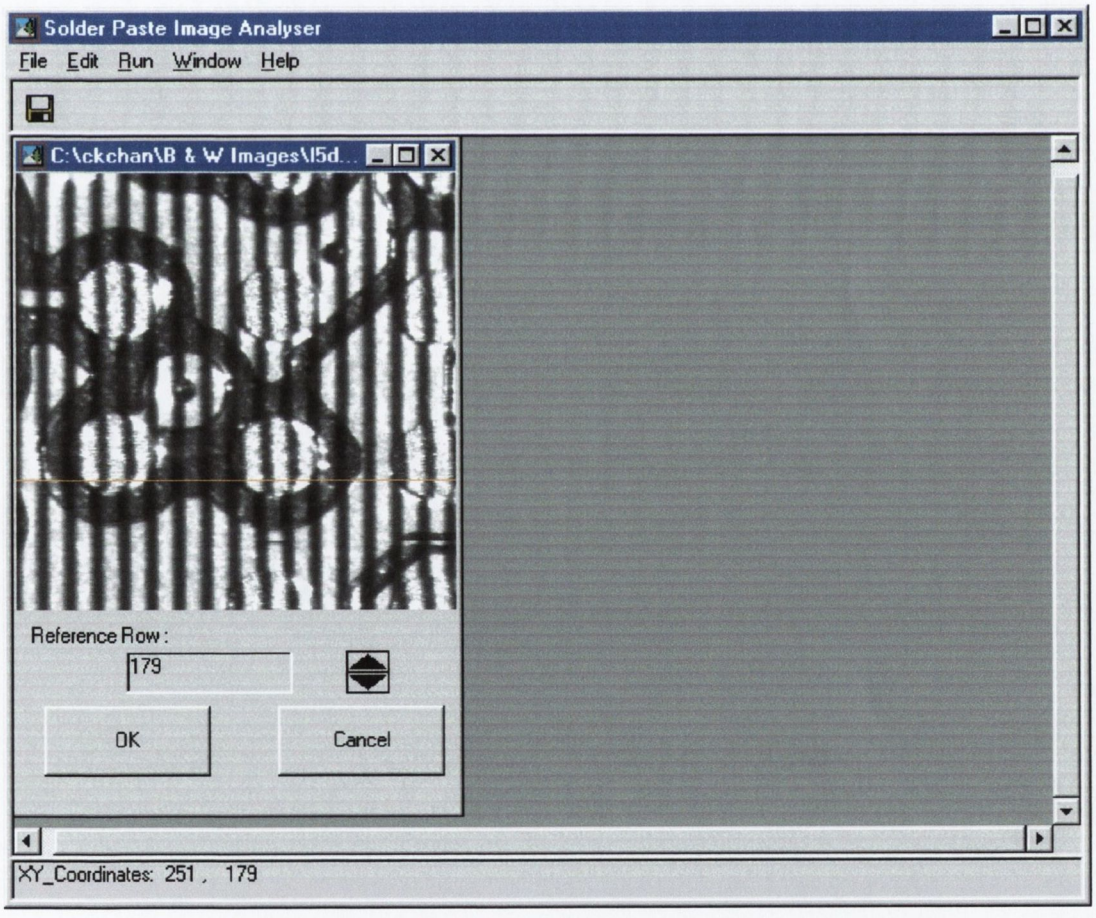

Fig B.7: VB Windows Interface showing how the reference row is selected

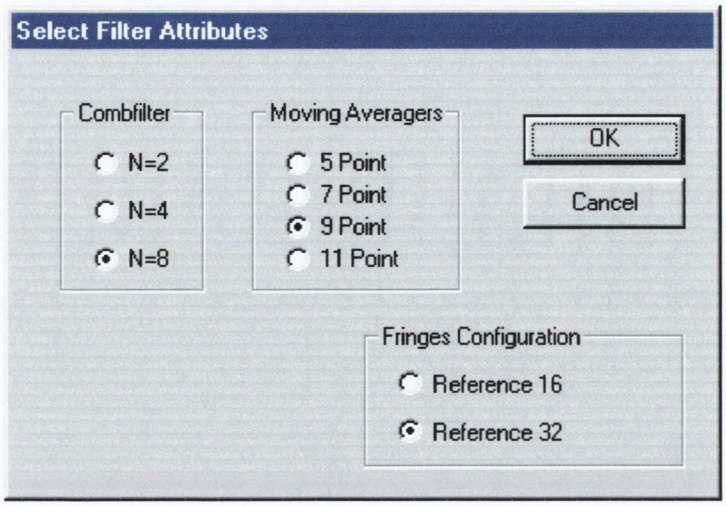

Fig B.8: Filters selection for NFP in a VB Windows Interface

Appendix B.3 – Dual Projection

Figure B.9 shows the user friendly window interface of the Dual Projection system.

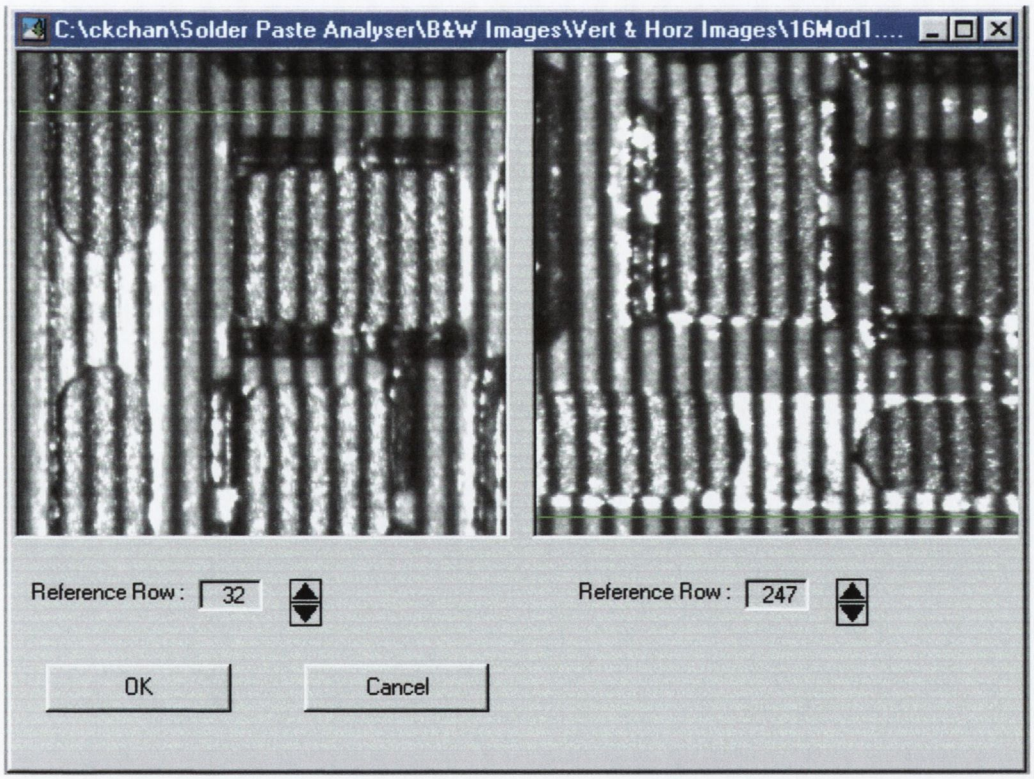

Fig. B.9: Window Interface of the Dual Projection Structured Light technique

Appendix C – Correction of Non Uniform Illumination

Images captured under non-uniform lighting conditions can be problematic for image processing based applications, these variations in background illumination across the field of view in a camera system is quite often caused by the lens and is manifested as an image centre which is to some extent brighter than the periphery. Such non-uniform lighting appears in most cases, unless the light projections are of direct beam types such as laser. In our case, there is no exception; the fringes on the image are generated by an optical fibre with white light going through it. The correction of such non-uniform response to light is known as Photometric Decalibration. Photometric decalibration can sometimes be done during the capturing process to minimise computing time and is required on all AOI inspection application.

Appendix C.1 - Photometric Decalibration using Background Subtraction

Photometric decalibration is a point by point operation applied to an input image to remove the effect of imaging sensor non-linearity. One solution for the removal is by using a technique known as background subtraction. This involves subtracting each pixel of a filtered image containing only the background information from the original interested image. Depending on the application requirements, sometimes it might not be possible to obtain a background image. In that circumstance, a coarse estimate of the background illumination must be determined. The interested image is divided into smaller blocks and the minimum grey-level of each block is identified, this calibration value is then subtracted from each pixel to generate an image, which represents the effective response of the camera.

The algorithm uses the formula below, which is required for the correction of the non-linearity due to background illumination.

$$t = \hat{k} - \hat{r} = \left(\hat{k}^R - \hat{r}^R\ , \hat{k}^G - \hat{r}^G, \hat{k}^B - \hat{r}^B\right) = \begin{cases} 0 & then\ no\ normalisation \\ > 0 & if(\hat{k} \neq \hat{r}) \\ < 0 & if(\hat{k} \neq \hat{r}) \end{cases} \quad \text{(C-1)}$$

$$\hat{r} = \hat{r}^R + \hat{r}^G + \hat{r}^B = \left\{\hat{r}_{x,y} : \forall x, y\right\} \quad \text{(C-2)}$$

$$\hat{k} = \hat{k}^R + \hat{k}^G + \hat{k}^B = \left\{ \hat{k}_{x,y} : \forall x, y \right\} \tag{C-3}$$

where

t – the calibrated resultant image

$\hat{r}$ – the vector for the background RGB image

$\hat{k}$ – the vector for the key inspected RGB image

x – the position of the pixel on the x-axis

y – the position of the pixel on the y-axis

$\hat{r}^R$ – the red component of the vector $\hat{r}$ for the background RGB image

$\hat{r}^G$ – the green component of the vector $\hat{r}$ for the background RGB image

$\hat{r}^B$ – the blue component of the vector $\hat{r}$ for the background RGB image

$\hat{k}^R$ – the red component of the vector $\hat{k}$ for the key inspected RGB image

$\hat{k}^G$ – the green component of the vector $\hat{k}$ for the key inspected RGB image

$\hat{k}^B$ – the blue component of the vector $\hat{k}$ for the key inspected RGB image

The equation given in (C-3) states that for all the pixels *(x,y)* in the key image *k*, subtract each colour component of each pixel *(x,y)* in the background image, *r* from the corresponding colour component of each pixel *(x,y)* in the key image *k*, and the results are stored in the calibrated image, *t*. The background image is split into its RGB channels and they are subtracted from each channels of the key image simultaneously.

An image of the light across the field of view as captured by the camera under our non-uniform lighting system is firstly taken and the data are stored in a file. Figure C.1a shows part of a background image of the light projection, notice how one corner is much darker than the other side due to optical lens. This image is only required to capture once. As the on-line process is capturing the interested image, the recorded data of the background image is retrieved and are used to subtract the data of the interested image, the values of the resultant image are then inverted. Figure C.1b shows the solder paste deposits and tracks on the PCB samples fabricated by Motorola and how the non-uniform lighting affects the actual projection of a PCB with no fringes.

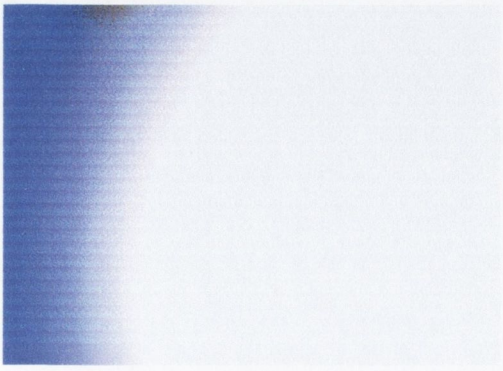

Fig. C.1a: The background image of the light projection

By performing background subtraction as described above with the background image shown in Figure C.1a, the dark side of the image is corrected. This is shown in Figure C.1c.

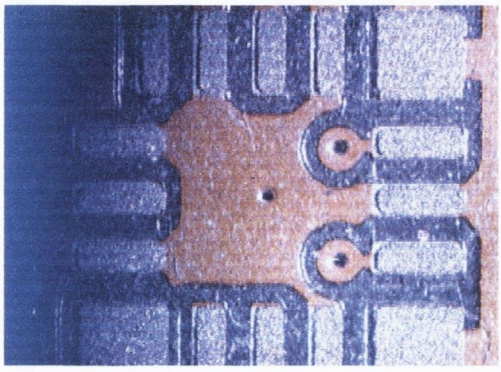

Fig. C.1b: Image of a PCB with the problem of non-uniform lighting

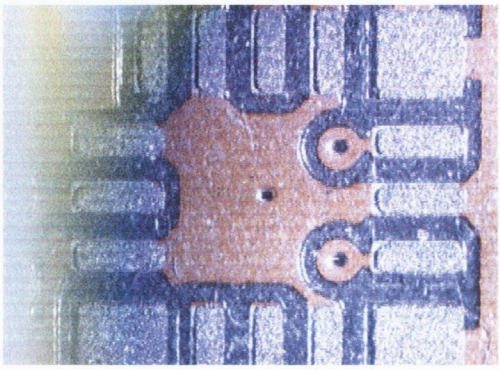

Fig. C.1c: Image of the PCB in Fig. 8.1b with the photometric correction

Although the darker part of the image has became relatively easier to identify after the photometric decalibration correction, but the information in the image still does not provide clear enough information for height measurements. It is possible to reconstruct a better background image by dividing the background image into smaller blocks and compute a more appropriate calibration value for each block by using a median filter. This value is then subtracted from each pixel of the respective block to generate an image that represents the effective response of the camera.

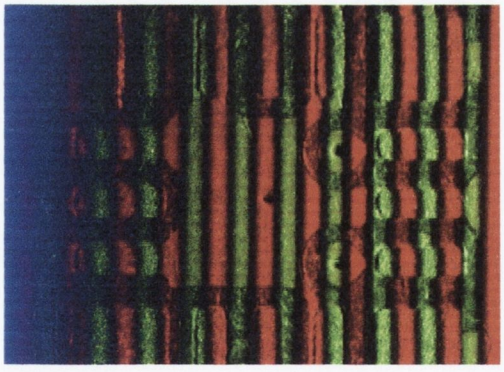

Fig. C.1d: Image with colour stripes projected onto the same part of the PCB

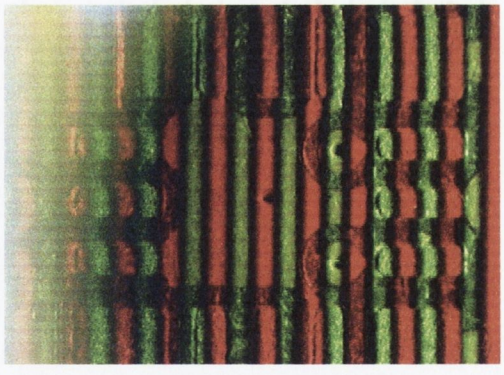

Fig. C.1e: Image with colour stripes projected in Fig. 8.1d with photometric correction.

Alternatively, an adjustment may be set in the actual mechanical inspection system, so that it would re-capture the border part of the image at a more centre view of field as the system moves on-line. Figure C.1f shows an image of part of the PCB board with uniform illumination.